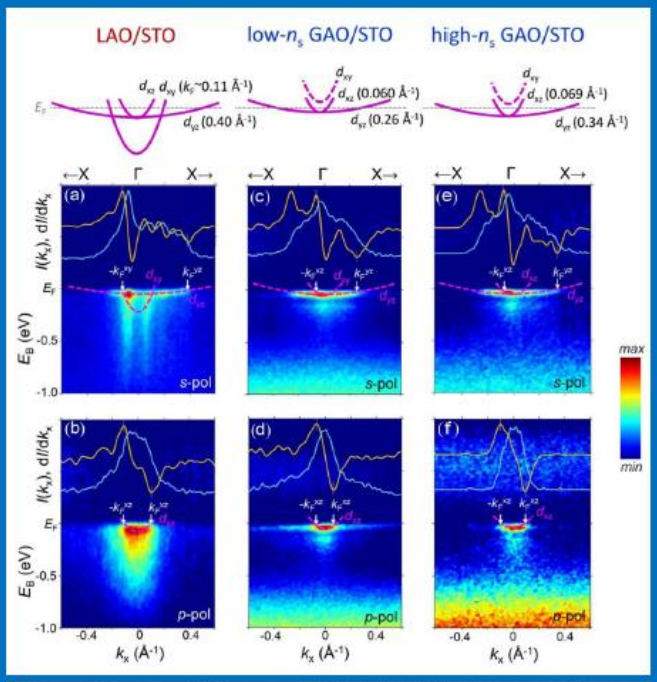


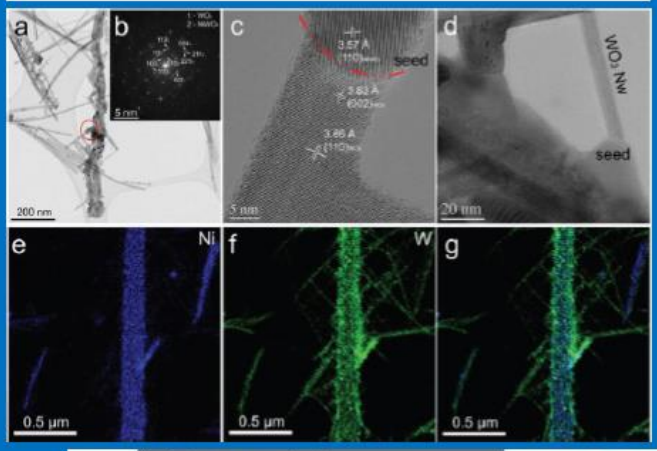


NIMP

**National Institute of Materials Physics**

# ANNUAL REPORT

# 2021

**Ministry of Research, Innovation and Digitalization**

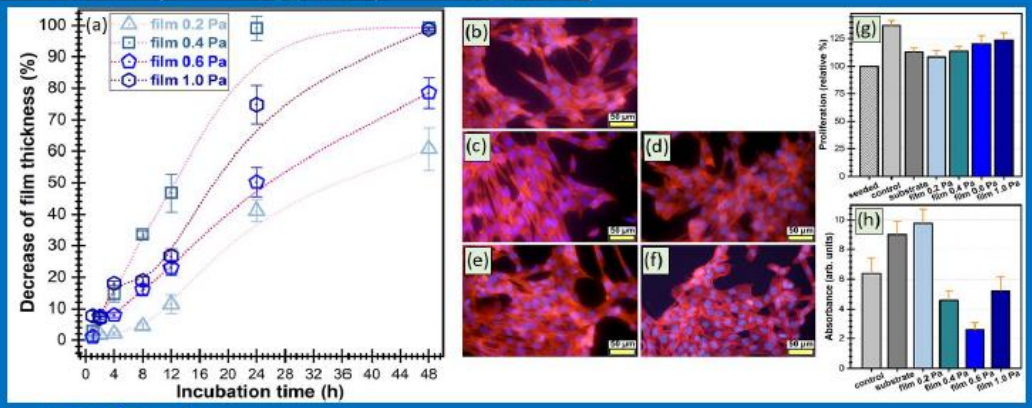



**NATIONAL INSTITUTE OF MATERIALS PHYSICS**
**BUCHAREST-MAGURELE**
Atomistilor Str. 405A, P.O. Box MG-7, 077125 Magurele-Ilfov, Romania
*Phone: +40(0)21 3690185, Fax: +40(0)21 3690177, email: director@infim.ro, http://www.infim.ro*

# Contents

# Laboratories and groups

# Laboratory 10 „**Functional nanostructures**”

**Leader:** Ionut-Marius Enculescu:encu@infim.ro

**Personnel:** 10 CS1, 1 CS2, 7 CS3, 1 CS, 6 ACS, 1 technician

**Main research directions**

The group deals with nanostructure and nanostructured materials preparation and development of applications. Both chemical/electrochemical (chemical bath deposition, electrochemical deposition with and without a template, chemical vapor deposition) and physical (sputtering, thermal evaporation in vacuum, electrospinning and forcespinning) methods are employed for nanostructures and nanostructured materials preparation. Different types of materials are used, including here metals, metal oxides, organometalic compounds and polymers. The nanostructures developed by this approach are used as building blocks for different types of functional devices (transistors or diodes, biosensors, actuators).

- Fabrication of nanostructures and devices based on nanostructures – physical and chemical methods are employed for preparing nanostructures. Electrochemical or chemical deposition are used for preparing semiconductor nanowires of zinc oxide with diameters down to 10 nm. Thermal oxidation of metal foils is used for obtaining metal oxide nanowires with diameters down to 20 nm. Further, the nanowires can be employed as buildingblocks for electronic devices such as diodes and transistors using microlithographic (photolithography and electron beam lithography). Devices complexity can be employed (e.g. core shell devices can be fabricated) by covering the nanowires with thin films employing methods such as sputtering or thermal evaporation. Chemical vapor deposition is employed for preparing thion nanostructured films such as metallic oxides or graphene.

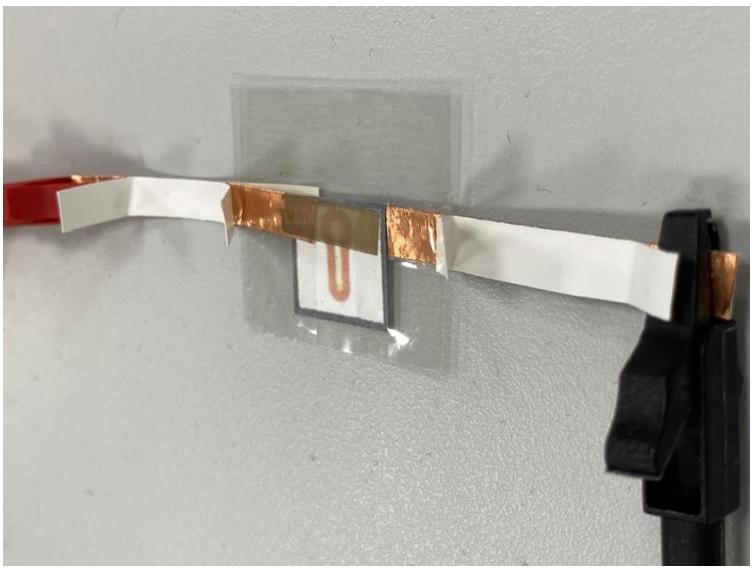

Biosensor on paper based on electrodes obtained by electrospun fibers

- Fabrication of materials suited for applications in optics, optoelectronics and photonics for devices which include diodes and transistors for light emitting applications, glasses or modular composition fibers for photonic applications.
- Fabrication of biosensors and biomedical devices based on nanostructures or on devices containing nanostructures as building blocks. Nanostructures and nanostructured materials

can be exploited successfully in biosensors, mainly due to the high specific surface but also due to other specific functionalities induced by the low dimensionality. Electrochemical sensors are developed based on nanostructured materials and are functionalized with different types of biomolecules in such a way in which both the desired sensitivity and selectivity are obtained. In this context different types of substrates and configurations of functionalization are investigated with the goal of optimizing devices' performances. Novel applications are considered including wearable sensors for physiologic parameters monitoring.

- Sub micrometer fibers: biomimetic devices based on microfiber web electrodes. In our group methods of fabricating polymer submicrometric fibers were developed namely electrospinning and centrifugal spinning. By further functionalization transparent and flexible electrodes based on metal covered polymer fiber webs are obtained. These electrodes can be applied on a wide range of substrates including here materials such as textiles and paper and can become the functional element of devices such as biosensors or for applications such as artificial muscles. Functionality can be increased by covering with electroactive polymers, leading to devices with highly superior performances when compared to classic architectures.
- Biocompatible materials represent another research direction of the group, being developed several approaches, including both biopolymeric fibers (collagen or cellulose), natural membranes (eggshell membrane) or nanostructured materials such as hydroxyapatite. Further functionalization includes covering with different compounds or nanostructures or doping and leads to multiple fields of applications the main one being that of medical devices.

The research directions presented in the group are mostly interconnected for developing devices with direct applications. Equipment for fabricating fibers by means of electrospinning and centrifugal spinning were designed and developed in the group with the support of the engineers from the application department.

**Relevant infrastructure**

The groups activity is based on several chemistry and electrochemistry laboratories dedicated to different types of applications. For obtaining the desired nanostructures or nanostructured materials several chemistry and electrochemistry laboratories are used including specific equipment such as chemistry hoods, ovens, potentiostats and so on.

Left – high resolution SEM Gemini 500; right - liquid chromatograph with mass spectrometer.

Clean room equipment is essential for devices fabrication:

- Electron beam nanolithography equipment with Raith Elphy systems with laser interferometers and Hitachi S3400 and Zeiss Merlin Compact electron microscopes;

- EVG 620 NT equipment with nanoimprint capabilities;
- CVD equiment for preparation of carbon based nanostructures;
- CVD equipment for semiconducting materials deposition;
- Laboratory for optical characterization including UV – vis absorption spectrometers (Carry 5 and Perkin Elmer 35), photoluminescence spectrometers (Edinburgh and Perkin Elmer LS55), near field photoluminescence microscope, plasmonic resonance spectrometer with potentiostat;
- Liquid chromatography equipment with mass spectroscopy;
- Laboratory for biocompatibility testing including cell culture, flux citometry, fluorescence miccroscope.

**Available services:**

- Scanning electron microscopy characterization of materials (micromorphology, composition)
- Optical characterization by means of optical spectroscopy
- Development of equipment for producing micrometric and submicrometric fibers by means of electrospinning and forcespinning;

## Laboratory 20 "**Complex Heterostructures and Multifunctional Materials (HeCoMat)"**

**Leaders:** Dr. Lucian Pintilie, Senior Researcher rank 1 (pintilie@infim.ro); Dr. Geoge Stan Senior Researcher rank 1 (geoge_stan@infim.ro)

**Personnel:** 34 members, 29 with permanent contracts and 5 with short-term contracts. From the 29 members with permanent contracts, 6 are Senior Researchers rank 1 (SR 1), 5 are Senior Researchers rank 2 (SR 2), 8 are Senior Researchers rank 3 (SR 3), 3 are Senior Researchers (SR), 3 are Junior Researchers (JR), 2 are sub-engineers, and 2 are technicians. From the members with permanent contracts, 24 possess PhD titles (in physics, chemistry, materials engineering) – including 1 PhD supervisor – and 2 are PhD students.

**Main research directions:**

- ferroelectric materials and related structures for electronic, optoelectronic and sensing applications (including non-volatile memories, UV and IR detectors, piezoelectric devices);
- materials and devices with application in microelectronics, photovoltaic conversion and light/particle detection (including field-effect transistors, hybrid perovskite and kesterite solar cells, and silicon-based particle detectors);
  - superconducting and magnetic materials, strongly correlated electron systems;
  - dielectric and ferroelectric materials for microwave devices (*e.g.*, dielectric resonators, ferroelectric varactors, filters, antennas).
  - materials for healthcare applications.

**Relevant infrastructure:**

Laboratory 20 possesses a noteworthy infrastructure, covering the entire technological chain from the preparation of materials in the form of powders, bulk and thin layers and their complex physico-

chemical characterization, to the integration of the optimized materials into functional devices. Amongst the most important systems and equipment one can mention:

- SURFACE & SCIENCE systems+technology GmbH pulsed lased deposition (PLD) work station (**Fig. 1a**) equipped with: 2 deposition chambers, each with 4-target carousels; a KrF excimer laser with 248 nm wavelength, repetition rate of 1 – 10 Hz, and maximum energy of 700 mJ; control of laser fluence; substrate heating up to 1000 °C; control of working gases pressure; *in-situ* reflection high-energy electron diffraction (RHEED) capabilities. One reaction chamber is used to deposit ferroelectric layers based on perovskites and other metal oxides (*e.g.*, doped ZnO, $HfO_2$), whilst the other chamber is used to prepare superconductor thin films.
- SURFACE & SCIENCE systems+technology GmbH hybrid system for thin films synthesis from temperature-sensitive materials by (*i*) matrix assisted pulsed laser deposition (MAPLE) and (*ii*) PLD, constituted of: a deposition chamber with *in-situ* freezing facilities for targets (*e.g.*, frozen suspensions of organic materials or inorganic nanoparticles in a support matrix); a KrF excimer laser with 248 nm wavelength, 1 – 10 Hz repetition rate, and 700 mJ maximum power; maximum heating temperature of the substrate: 600 °C.
- Multi-cathode radio-frequency (RF), direct current (DC) and pulsed direct current (p-DC) magnetron sputtering (MS) systems with various facilities: bias, etching and heating (up to 800 ° C) of substrates; vacuum load-lock for sample transfer; vacuum systems (down to ~$10^{-6}$ Pa); computerized control and process automation. The late st MS equipment, AJA PHASE II J, purchased in 2016, is shown in **Fig. 1b**. Each MS system in Laboratory 20 is dedicated to a distinct class of materials: metallic contacts; semiconductor and dielectric materials; biocompatible materials.
- Chemistry laboratory for the preparation of powders and thin films by chemical (wet) methods, equipped with high-temperature annealing furnaces; spin-coating and doctor-blade systems; glove-boxes; *etc*.
- Laboratory for the preparation of piezoelectric and superconducting materials, polycrystals and single crystals.
- Ceramic materials 3D printing laboratory, equipped with a NORDSON EFD, EV series, robocasting (direct ink writing) printing system, with Ultimus V dispenser (**Fig. 2a**); an ANTON PARR MCR302e modular rheometer (**Fig. 2b**); and a THINKY ARE-250 ceramic mixing & degassing machine.

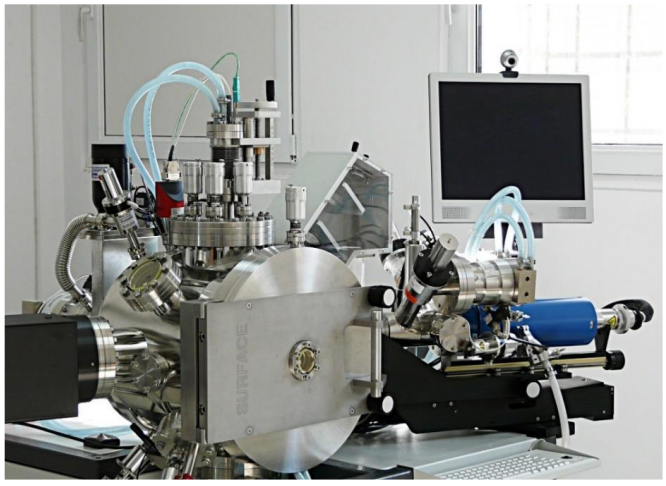


**Fig. 1a** PLD workstation assembly, SURFACE & SCIENCE systems+technology GmbH, for the deposition of ferroelectric thin films.


**Fig. 1b** RF, DC and p-DC magnetron sputtering system, AJA PHASE II, for the deposition of semiconductor thin films.

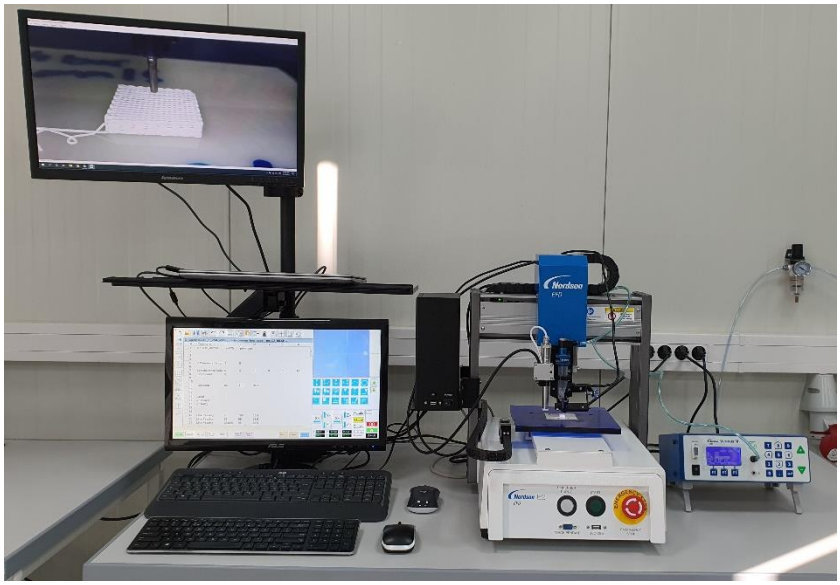

**Fig. 2a** 3D printing system by robocasting (direct ink writing) technology, NORDSON EFD, EV series, with Ultimus V dispenser.

**Fig. 2b** ANTON PARR MCR302e modular rheometer.

- X-ray diffraction systems for structure analysis of thin films (a RIGAKU SmartLab 3 kW/2017 from room-temperature to 1100 °C – **Fig. 3a** and a BRUKER D8 Advance/2006) and powders (BRUKER D8 Advance/2007).
- Optical and structural characterization systems, including a (*i*) variable angle spectroscopic ellipsometer (WOOLLAM) with wavelength range 200 – 1700 nm (6.2 – 0.73 eV), angle of incidence (35 – 90°), automated sample translation stage (for mapping) 150 mm × 150 mm, and an Instec temperature control stage (-160 – 600 °C) and (*ii*) a near infrared (NIR), infrared (midIR) and far infrared (farIR) Fourier transform infrared (FTIR) JASCO spectrometry platform, encompassing the 12000 – 50 $cm^{-1}$ spectral range (**Fig. 3b**).
- Surface investigation by scanning probe microscopy (SPM) in contact or non-contact mode with piezoelectric (PFM), magnetic (MFM) or conductive (C-AFM) response.

**Fig. 3a** RIGAKU SmartLab 3 kW high-resolution XRD system for thin films analysis.

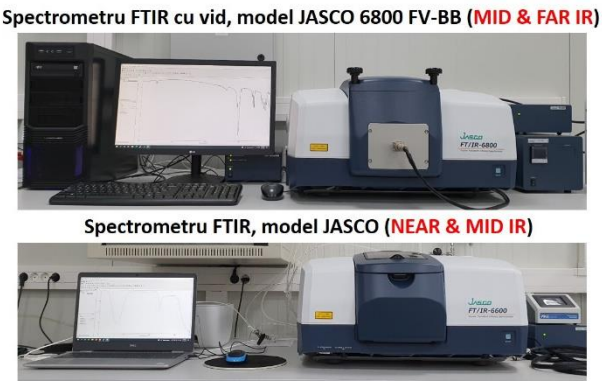


**Fig. 3b** FTIR spectroscopic platform with extended NIR – MID – farIR spectral range, 12000 – 50 $cm^{-1}$.

- Electrical measurements laboratory (see **Fig. 4**), including: 2 LAKE SHORE cryo-probers for electrical measurements in the temperature range of 10 – 400 K; one with vertical magnetic field up to 2.5 T, and one with horizontal magnetic field up to 1.5 T, each with at least 3 micro-manipulated arms with contact needles allowing electrical measurements from liquid helium to 400 K under various electric/magnetic fields and illumination conditions; 4 cryostats, covering a temperature range between 10 – 800 K; DLTS (deep-level transient spectroscopy) and TSC (thermally stimulated current) systems for the investigation of electrically active defects (charge carrier traps) in materials and MOS-like structures; set-up for pyroelectric

measurements; ferritesters; various instruments for measuring currents, resistances and voltages (electrometers, nanovoltmeters, Lock-In amplifiers); voltage and current sources; RLC bridges; and impedance analyzers. These facilities are used to perform complex characterization of electrical (hysteresis loops; CV and I-V characteristics; impedance spectroscopy; defect spectroscopies; *etc*.) and superconductive properties (electron transport, thermodynamics, magnetic-field penetration depth measurements); determination of the $d_{33}$ piezoelectric coefficient.

- Solar cells testing laboratory, with two NEWPORT LED solar simulators (aperture 50 mm × 50 mm), one system for measuring the Quantum Efficiency/IPCE, and accessories.
- Microwave dielectric materials and devices testing laboratory, including:
    - Vector Network Analyzer PNA 8361A from Agilent (0.01 – 67 GHz) for two-ports complex S parameters. It uses electronic calibrator Agilent N4694-60001 in the range of 0.01 – 67 GHz. For access, 1.9 mm, 2.9 mm, 2.4mm, 3.5 mm, SMA or N connectors or adaptors are used.
    - Vector Network Analyzer PNA-X N5245A from Agilent (0.1 – 50 GHz standalone) with 4 ports and dual sources. It allows measurements of the S and X non-linear parameters. By using the millimeter wave extensions, the system covers a wide frequency band up to 500 GHz. Each extension pair allows the measurement of the two-ports parameter of waveguide devices.
    - Anechoic chamber with internal dimensions 3040 mm × 4100 mm × 2800 mm, for antenna characterizations (*e.g.*, directivity parameter) in the range of 0.9 – 40 GHz.
    - Microprobe station for direct *on-wafer* measurements of two-ports in the frequency range 0.1 – 67 GHz by using GSG probes with 150 µm and 100 µm pitches.
    - THz-TDS spectrometer from AISPEC Pulse IRS 2000 Pro, operating in the range of 200 GHz – 5 THz.

- In the framework of collaborative research activities, Laboratory 20 can access other NIMP infrastructures, such as: TEM and SEM equipment; XPS characterization (including at Elettra Synchrotron Trieste); magnetic measurements (SQUID, PPMS); other optical spectroscopy techniques (Raman, UV-Vis-NIR, luminescence); clean-room (photolithography, dry etching); and *in-vitro* preliminary biological testing of materials.

**Fig. 4.** Laboratory for electrical characterization of dielectric, ferroelectric and semiconductor materials.

**Available services:**

- Preparation of materials (nano-powders; bulk ceramics; fabrication of thin films by various techniques, including PLD, chemical methods, CVD and PVD techniques);
- Investigation of charge carrier traps by DLTS and TSC;
- Electric characterization of materials in a wide temperature range, under electric and magnetic fields;
- Investigation of pyroelectric properties;
- Fabrication and characterization of perovskite solar cells;
- Fabrication and characterization of microelectronic devices (*e.g.*, FET, MOS);
- Characterization of microwave, millimeter waves and terahertz materials and devices;
- Antenna characterization (antenna directivity) in anechoic chamber in the frequency band from 900 MHz to 40 GHz;
- Electromagnetic design for microwaves devices/structures by using high accuracy software packages such as CST Studio Suite, Ansoft HFSS, and Ansoft Designer;
- Deposition of biocompatible (ceramic and glass) coatings on metallic implants;
- Characterizations by (*a*) reflection ellipsometry on semiconductor/dielectric thin films or multilayers (thicknesses, refractive index, extinction coefficient, absorption coefficient, dielectric function, band gap, critical point energies, electrical parameters for degenerate semiconductors – resistivity/conductivity, carrier density, scattering time, carrier mobility, phase transition in the temperature range -160 – 600 °C); and (*b*) transmission ellipsometry on uniaxial/biaxial crystals, glasses and glass ceramics (optical constants, linear birefringence and linear dichroism, Verdet constant/ Faraday rotation).
- XRD characterizations for crystalline phase identification and their quantitative analysis; determination of the lattice parameters, average size of crystallites, macro- and micro-strains, preferred orientation, *etc*; analysis of homo- and hetero-epitaxial structures; X-ray reflectometry analyzes for inferring the thickness, density and roughness of the surface and interfaces of amorphous and crystalline layers and multi-layers; *etc*.
- FTIR spectroscopy analyses in transmission, specular reflectance (including at grazing incidence), attenuated total reflectance – ATR (RT – 180 °C), diffuse reflectance – DRIFT (RT – 500 °C) and integrating sphere modes.
- Morpho-compositional analyses by HR-SEM – EDXS;
- Surface characterization of materials by AFM, PFM, MFM and C-AFM.

## Laboratory 30 **„Magnetism and Superconductivity"**

**Group name**: Electronic Correlations, Magnetism and Superconductivity (recently formed by joining the former group of Electronic Correlations and Magnetism and the group of Superconductivity)

**Group leader**: Dr. Victor Kuncser, Senior Researcher rank 1 (kuncser@infim.ro)

**Personnel:** 5 Senior Researchers rank 1 (Research Professor), 5 Senior Researcher rank 2, 9 Senior Researchers rank 3, 4 Scientific Researchers, 6 Research Assistant, 1 engineer for technological development and 3 technicians. Except for the scientific activity, the group is also involved in educational and training activities. There are 3 PhD advisers coordinating 2 to 3 PhD students yearly as well as master and undergraduate students performing their scientific training.

**Main research directions:**
Envisage fundamental and applied research in the field of magnetic and magneto-functional materials for actuator and sensoristic applications as well as in the field of superconductivity, mainly targeting materials with superconducting properties with potential for practical applications. The research process covers all stages, from preparation (bulk materials, thin films or nanostructures) to structural

and electronic characterization, completed with a deep analysis of the magnetic and respectively superconducting properties.
Related to the magnetic behavior, mainly the functionalities mediated by magnetic reconfiguration controlled by temperature, magnetic and electric fields, applied or from interface interactions, are envisaged. The research is focused especially on the study of 0D,1D and 2D nanostructures. In the case of magneto-functional structures, magnetic systems of nanoparticles, thin films and multilayers, materials for colossal magnetoresistance (CMR), giant magnetoresistance (GMR) and tunnelling magnetoresistance (TMR), soft and hard magnetic materials, Heusler compounds with spin polarization, heterogeneous multiferroic systems, magneto-caloric materials, diluted magnetic oxides/semiconductors, thermo-electric systems, etc. are envisaged. In addition, bulk materials, advanced hybrid systems and composites / nanocomposites destined to operate in extreme conditions such as the ones in fusion and fission reactors, particle accelerators and in space, are investigated. Interactions at the interface and functionalities induced by them in nanostructured hybrid systems such as soft magnet / hard magnet (exchange-spring), ferromagnet/antiferromagnet (exchange-bias), ferromagnet-ferroelectric (magneto-electric coupling) represent another field of interest related to fundamental and applicative aspects of smart multi-functional systems. In specific cases, the experimental studies are completed by theoretical studies approaching electronic configurations based on Density functional theory (DFT) and magnetic configurations based on finite-element simulation programs.
Related to the superconducting behavior, studies of vortex matter, dynamics and pinning and nano-engineering of artificial pinning centres for high-magnetic field applications are envisaged. Exploration of fields of applicability of these materials and related ones considering, beyond superconductivity, other that may be important for applications, such as mechanical, biological, optical are also considered. The studied materials are mainly cuprate high temperature superconductors Y (rare earth) $Ba_2Cu_3O_7$ (RE123) with nano-engineered pinning centres, Bi- and La-based superconducting cuprates, MgB2 (with various additions for increasing pinning properties), iron-based pnictide and chalcogenide multicomponent superconductors and low temperature (classic) metallic and intermetallic superconductors. Other materials of interest are CeO2, SrTiO3, LiPdPtB, PdO, boron/carbide composites, selected steels, and archaeological ceramic materials. Most of the materials are obtained in the laboratory in various morphologies: powders, polycrystalline bulk samples, single crystals, wires/tapes, nanostructures, heterostructures and nanocomposites. The group uses advanced techniques for obtaining or processing materials: conventional powder synthesis in controlled atmosphere, cryochemistry or energy milling, crystal growth in flux or by melting zone, growth of thin films by laser ablation, sintering by Spark Plasma, lamination, arc melting, etc. Advanced analysis of superconducting properties aims in particular to determine vortex phase diagrams vortex dynamics and vortex pinning. Temperature dependence of magnetization and resistivity, isothermal hysteresis magnetization and magnetic relaxation, current-voltage characteristics, bulk pinning force and pinning potential etc. are analysed within the existing theoretical models or using recognized practical and theoretical methodologies developed by some members of the group, for example pinning potential determined from frequency-dependent AC susceptibility response, or the use of normalized magnetic relaxation rate to determine the cross-over between elastic and plastic vortex creep, and various field-m and temperature-dependent creep exponents.

**Relevant infrastructure:**
Among important research equipment, considering preparation facilities as well as characterization ones, the following can be listed: spark plasma sintering, hot press sintering, microwave sintering and melt spinning equipment, nanoparticle preparation systems by hydrothermal / solvothermal synthesis in autoclave and centrifugation for separation by sizes), RF/DC sputtering deposition system for magnetic thin films and multilayers with 4 sources and base pressure in the range of $10^{-9}$ mbar, facility for inducing thermal transfer in radiofrequency magnetic field to determine specific absorption rates in dispersed nanoparticle systems, thermogravimetric and differential scanning calorimetry systems,

Vibrating Sample Magnetometry system in magnetic fields up to 9 Tesla, Mossbauer spectrometers with different accessories to perform measurements at variable temperatures (4.5 K –1000 K) and in applied fields, via the detection of gamma radiation / X- rays / conversion electrons (the only group in Romania active in Mossbauer Spectroscopy), complex system for measurements of physical properties (PPMS) with magnetic fields up to 14 Tesla and a SQUID type magnetometer working in 7T down to 2K from Quantum Device with the corresponding facility for liquid He production (18 l /24 h). Magnetic texturing of thin films is investigated by vectorial MOKE magnetometry. For high temperature domain, the laboratory possesses a Laser Flash Analyzer system that allows the determination of thermal diffusivity, specific heat and thermal conductivity of the volume materials or multilayers (3 layers, including liquids) in the range 25-1100 C, a dilatometer (Netzsch 402 C, 2015) to determine thermal expansion coefficients (25-1600 C) and an equipment (Netzsch, Nemesis 2015) to determine electrical conductivity and Seebeck coefficient (25-800 C). In order to determine the composition in bulk / powder systems, an X-ray fluorescence device is available, while for very low concentrations/quantities the group possesses an inductively coupled plasma mass spectrometer (ICP-MS), with an extension for thin film analysis by laser ablation (LA), the last one being aquired in 2019, in collaboration with Laboratory 10. Mechanical properties are determined in quasistatic regime up to 1700 °C, using a recently-acquired equipment (INSTRON).

ICP-MS with LA for thin films (upper left), Mossbauer spectrometers with closed circuit He cryostats (lower left) and SQUID device – Quantum Design, of high sensitivity (middle). Spark plasma sintering plant (FCT Systeme GmbH) used to obtain high density bulk materials (right).

**Available services:**

- preparation of metallic and intermetallic compounds in the geometry of thin films, ribbons or bulk,
- synthesis of materials that are important for applications using state-of-the-art powder metallurgy techniques,
- lyophilisation from frozen materials,
- treatment of powders and thin films at high pressures and temperatures in non-corrosive gas atmosphere (hydrogen, nitrogen, methane, carbon dioxide, helium) and measurement of the formation kinetics and thermodinamics of the materials obtained by gas-solid reaction,
- high sensitivity magnetometry to characterize the magnetic properties of the elements (bulk, powders and nano-powders, ribbons and nanocomposites, 0-, 1- and 2-dimensional nanostructures),
- characterization of the thermodinamic and transport properties (thermal, electric) of the materials in a large temperature domain,
- determination of the Debye temperature, specific heat and entropy variation of solid materials in the temperature range of 2-300 K and in a magnetic field between 0 and 14 T,

- determination of thermal conductivity of solid materials in the temperature range of 2-300 K and in a magnetic field between 0 and 14 T,
- complex characteristics and specific properties of materials with iron evidenced by powerful nuclear gamma resonance investigation methods (Mossbauer spectroscopy),
- specific temperature-dependent properties evidenced by modern differential thermal analysis methods, differential calorimetry and mass spectrometry,
- atomistic simulation within the density functional theory (DFT) of the materials for advanced applications and finite element micromagnetic modelling,
- preparation / processing by various techniques of powders, single-crystals, thin films / heterostructures / nanostructures, bulks, composites;
- magnetic and transport measurements on superconducting materials;
- analysis of experimental data obtained on superconductors with the determination and modeling of critical parameters (critical temperature, critical current density, irreversibility field, pinning force and pinning mechanisms, trapped field, vortex pinning energies, Debye temperature, and others)
- mechanical measurements in quasistatic regime up to 1700 °C (bending / compression of hard materials);
- analysis of mechanical properties and correlation with fractography aspects;
- targets fabrication for thin layer deposition.

The group also develops materials and technologies for a number of applications: superconducting thin layers and coated conductors from high critical temperature cuprates containing nano-engineered pinning centres; superconducting $MgB_2$ wires/tapes in metallic sheath; $MgB_2$-based magnetic storage devices, magnetic concentrators and magnetic shieldings; $MgB_2$-based powders, coatings and bulks for biomedical applications; boron-based super-hard materials for tools and extreme high temperature applications, integrated multifunctional devices.

## Laboratory 40 **„Surface and Interface Science”**

**Leader**: Dr. (habil.) Cristian Mihail Teodorescu, Senior Researcher rank 1 (teodorescu@infim.ro)

**Personnel**: 2 SR1, 3 SR2, 7 SR3, 1 TDI3, 2 Researchers, 6 Research Assistants, 2 technicians, total = 23

**Main research directions:**

- Surface and interface analysis by photoelectron spectroscopies (XPS–ESCA, ARUPS, spin-resolved PES, PED) in situ electron diffraction (LEED, RHEED), AES, scanning tunneling microscopy and spectroscopy STM–STS, photoelectron spectromicroscopy, low energy and photoemission electron microscopy (LEEM–PEEM);
- Surfaces, thin films and heterostructure preparation by molecular beam beam epitaxy (MBE);
- Analysis of ferroelectric surfaces, band bending in heterostructures;
- Molecular reactions at ferroelectric surfaces;
- In plane conduction properties of 2D systems on ferroelectric surfaces;
- ‘2D nanoreactors', molecular reactions with reactants stabilized between graphene layers and substrates;
- Spin asymmetry in band structure of 2D systems;
- Photocatalysts with internal junctions;
- Multiferroic structures with indirect exchange or coupling through charge accumulation;
- Theoretical developments in the area of ferroic thin films (ferroelectric, ferromagnetic);
- Development of new devices operating in ultrahigh vacuum (effusion cells, evaporators, manipulators);

- Development of software packages for data analysis.

**Relevant infrastructure:**

- A complex cluster for surface and interface science (Specs, Fig. 1), composed by: (i) a chamber for photoelectron spectroscopy (XPS, ESCA, UPS, AES); (ii) a molecular beam epitaxy (MBE) chamber with in situ follow-up by low energy electron diffraction (LEED) and reflection high energy electron diffraction (RHEED) and residual gas analysis; (iii) a chamber for scanning tunneling microscopy and spectroscopy (STM/STS); (iv) load-lock and storage of samples in ultrahigh vacuum.
  - An installation for X-ray photoelectron spectroscopy with possibilities of restricted area analyses (lateral resolution 2 micrometers) and automated change of samples / measuring areas, coupled to a reaction cell at high pressures and temperatures (Kratos, Fig. 2).
- A complex cluster for surface and interface science (Specs, Fig. 3), delocalized actually on the SuperESCA beamline at the Elettra synchrotron radiation facility in Trieste (Combined Spectroscopy and Microscopy on a Synchrotron – CoSMoS), composed by: (i) a chamber for photoelectron spectroscopy (XPS, ESCA, UPS, AES) with angle and spin resolution (ARPES, XPD, ARUPS, SR-UPS); (ii) a molecular beam epitaxy (MBE) chamber with in situ follow-up by low energy electron diffraction (LEED) and reflection high energy electron diffraction (RHEED) and residual gas analysis; (iii) a chamber for scanning tunneling microscopy and spectroscopy (STM/STS); (iv) load-lock and storage of samples in ultrahigh vacuum. This installation have allocated each semester from Elettra 5 days of „in-hous research" beamtime and 6 days of beamtime allocated based on research projects, reserved only from projects from Romania. In addition to synchrotron radiation beamtime, photoelectron spectroscopy using laboratory sources, or other experiments STM/STS, LEED, RHEED, Auger, etc.are possible at any time, provided the personnel is able to travel at Elettra.

- An installation for low energy and photoemission electron microscopy: LEEM – PEEM, micro LEED, micro ARUPS (Specs). The installation is able to perform simultaneous imaging (i. e. without scanning) of surfaces by using low energy electrons or photoelectrons produced by UV radiation. In the LEEM mode, the lateral resolution is about 5 nm, and in the PEEM mode about 50 nm. The advantages of using this installation are (i) the possibility to record immediate imaging, to realize movies, to fllow-up in real time surface modifications; (ii) the fact that one uses low energy electrons makes this method suitable for delicate surfaces, which otherwise would be damaged by high energy electrons such as the ones used in scanning electron microscopy (SEM); (iii) one may obtain structural or electronic structure (densities of states, dispersion laws) information on nanometer scale.

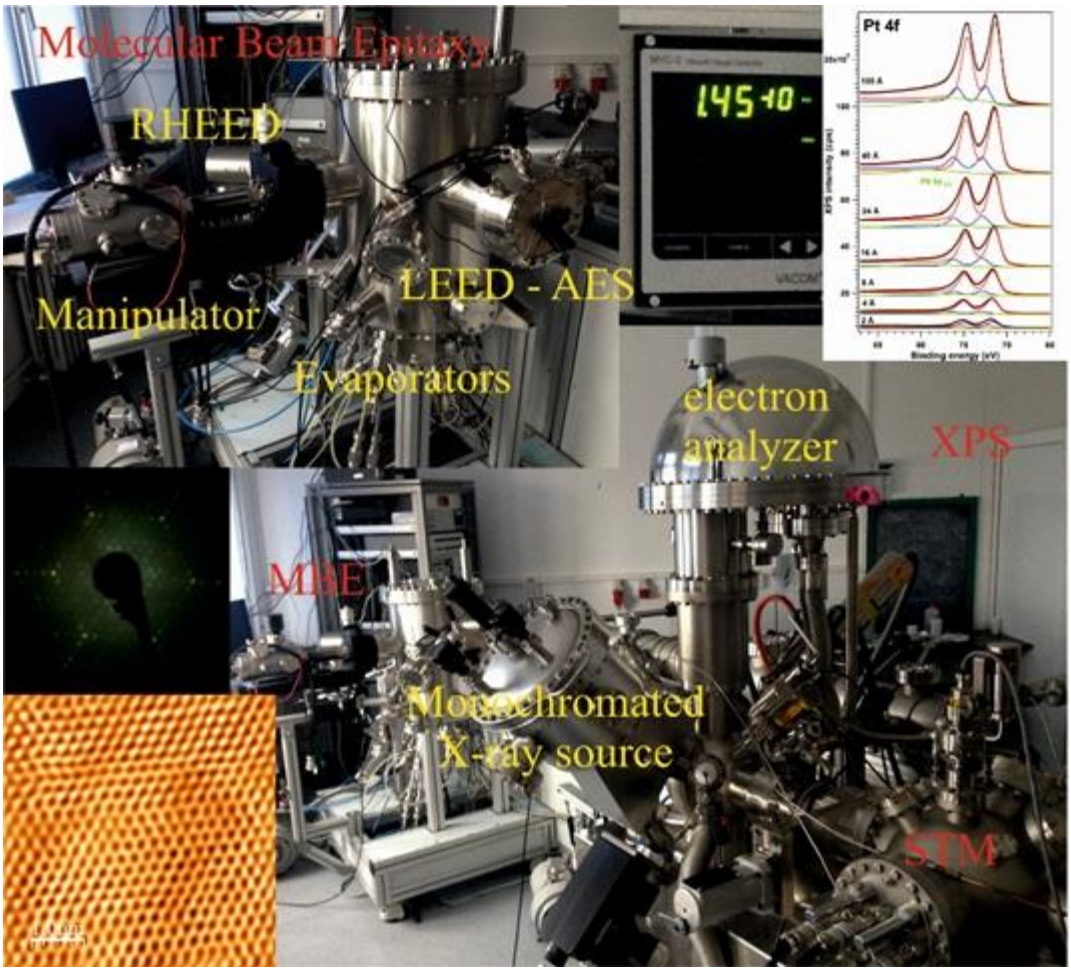


**Fig. 1**. The first cluster of surfaces and interfaces (the „multi-method system" coupled to MBE), located in NIMP. With red, the principal components are denoted (XPS, STM, MBE). With yellow, the main devices. Other photographs from this panel plot the working pressures, the quality of XPS spectra, LEED and STM images. Produced by Specs, Berlin, Germany.

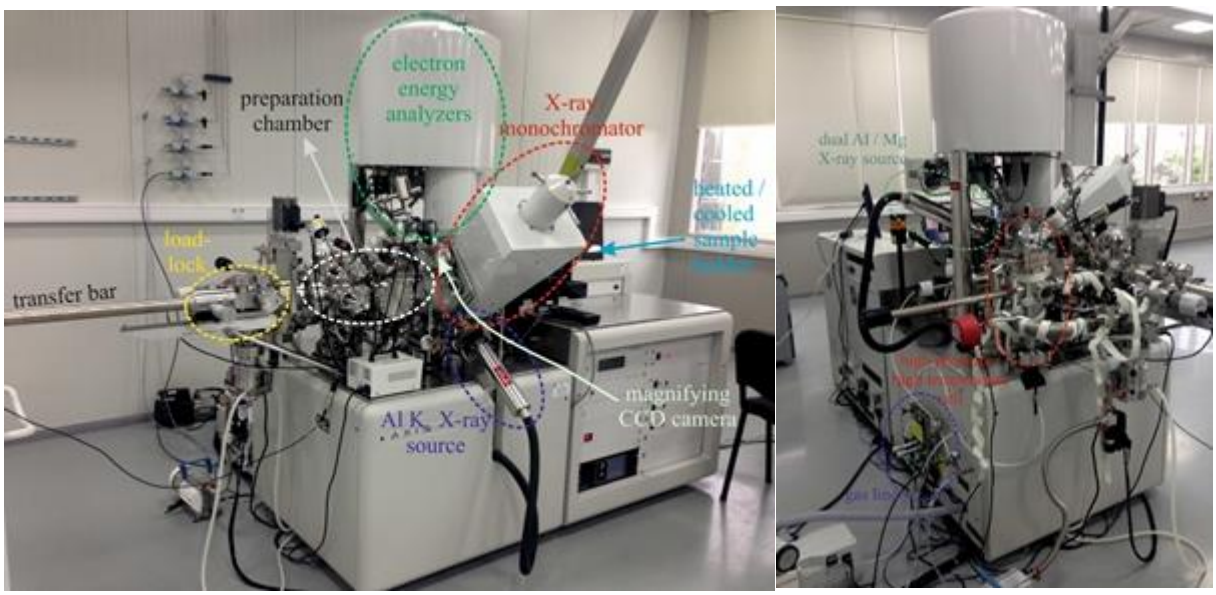


**Fig. 2**. The installation for photoelectron spectroscopy with possibilities of analysis on micrometer areas and provided with a cell for sample treatment at elevated pressures and temperatures (4 bar / 1000 °C). Produced by Kratos, Manchester, Marea Britanie.

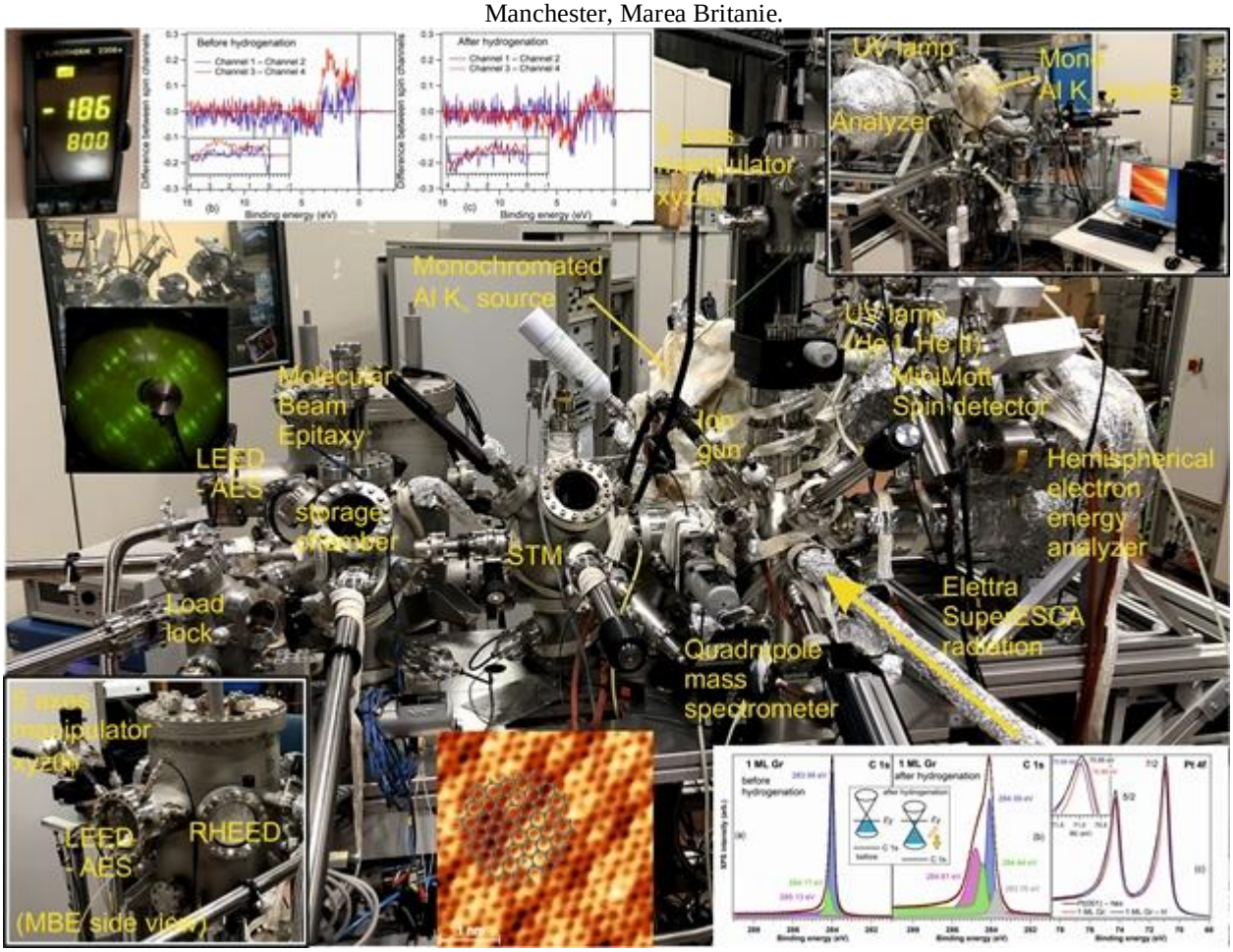


**Fig. 3**. The CoSMoS (combined spectroscopy and microscopy on a synchrotron) cluster coupled to the SuperESCA beamline at Elettra, Trieste.

- Setup for extended X-ray absorption fine structure (EXAFS). Excitations: Mo Kalpha (17479.34 eV), W Lalpha (8397.6 eV), power 3 kW (40 kV, 75 mA); Ge(220), Ge(400), Ge(840) monochromators; detectors: proportional counters, scintillation detectors; measurement in transmission or fluorescence; simulation and analysis software. Produced by Rigaku, Tokyo, Japan.

- Installation for positron annihilation-induced Auger electron spectroscopy, CNCAN certification in process.

**Available services:**
- Photoelectron spectroscopy-based techniques: X-ray photoelectron spectroscopy (XPS) and diffraction (XPD), ultraviolet photoelectron spectroscopy (UPS), angle-resolved UPS (ARUPS), spin-resolved ARUPS.
- Auger electron spectroscopy (AES) and diffraction (AED).
- Low energy electron diffraction (LEED) and reflection high energy electron diffraction (RHEED) characterization of surfaces.
- Scanning tunneling microscopy (STM) and spectroscopy (STS) at variable temperature.
- Sample depth profiling by ion sputtering assisted by XPS or AES.
- Surface cleaning and synthesis of epitaxial thin films by molecular beam epitaxy (MBE).
- Thermally-programmed desorption of molecules from surfaces by residual gas analysis (RGA).
- Low energy electron microscopy (LEEM) and photoemission electron microscopy (PEEM), micro-LEED and micro-ARUPS.
- Extended X-ray absorption fine structure (EXAFS).
- Positron annihilation-induced Auger electron spectroscopy (PAES).

## Laboratory 50 **"Theoretical Physics"**

**Leader:** Dr. Valeriu Moldoveanu, Senior Researcher rank 1 (valim@infim.ro)

**Personnel**: 7 researchers (1 senior researcher 1st degree (SR 1), 1 SR2, 3 SR3, 1 SR, 1 research assistant & PhD student.)

**Main research directions:**
A. Topological and transport properties of 2D materials and lattices
B. Hybrid quantum systems for nano-electronics and nano-optomechanics
C. Correlation effects in 2D lattices and artificial molecules

## Laboratory 60 **„Optical processes in nanostructured materials"**

**Leader:** Dr. (habil.) Mihaela Baibarac, Senior Researcher rank 1 (barac@infim.ro)

**Personnel:** 4 SR 1, 6 SR 2, 2 SR 3, 7 SR, 10 RA and one technician.

**Main research directions:**
- optical properties of composite materials based on macromolecular compounds and carbon nanoparticles (graphene, including graphene oxide and reduced graphene oxide, carbon nanotubes, fullerene) and phosphorene, respectively, for applications in the field of eco-nanotechnologies, health and energy storage (supercapacitors, rechargeable batteries);
- photoluminescence of 2D inorganic materials (including dichalcogenides) and their applications in information technology, sensors and energy storage;
- optical properties of plasmonic materials, quantum dots and their applications in the field of eco-nano-technologies and the pharmaceutical field;
- optical properties of the inorganic micro/nano-particles for applications in the field of heritage and optoelectronic.

**Relevant infrastructure:**

- an UV-VIS-NIR spectrophotometer, Lambda 950 model, from Perkin Elmer;
- a FTIR spectrophotometer, Vertex 80 model, from Bruker,
- a FTRaman spectrophotometer, MultiRam model, from Bruker;
- a Fluorolog FL-3.2.2.1 model with upgrade for the NIR range, from Horiba Jobin Yvon,
- a triple Raman spectrophotometer T64000 model, from Horiba Jobin Yvon, equipped with the lasers for the excitation in visible range;
- a FTIR imaging microscope SPOTLIGHT 400 from Perkin Elmer,
- a thermoluminscence reader Harshaw TLD 3500,
- a system for photoconductivity and I-V characteristics;
- a Scanning Near Field Optical Microscope (Multiview 4000 SNOM/SPM system from Nanonics) coupled with Atomic Force Microscope (AFM),
- Fluoromax 4P with quantum efficiency and colorimetry options, for luminophores characterization, o system to measure surface/interfacial tension, contact angle and density;
- Langmuir-Blodgett instruments, KSV 2000 system and KSV 5003 model;
- a potentiostat/galvanostat, Voltalab 80, from Radiometer Analytical;
- multi-channel potentiostat/galvanostat, Origaflex model, from Origalys;
- equipment for deposition by vacuum evaporation of organic materials;
- broadband dielectric spectroscopy system from Novocontrol;
- an infrared spectro-microscope, Carry 600, from Agilent Scientific;
- a surface plasmons resonance (SPR) equipment from Reichert;
- Hybrid Magnetron Sputtering – Pulsed Laser Deposition equipment for thin films and
- Physical Vapor Transport equipment for transition metal dichalcogenides.

**Available services:**

Analyzes by the UV-VIS-NIR and IR absorption spectroscopy, Raman scattering, photoluminescence, cyclic voltammetry, atomic force microscopy and the assessing of the hydrophobic/hydrophile properties.


Surface Plasmon Resonance equipment from Reichert

MultiRam FTRaman spectrophotometer from Bruker

Physical Vapor Transport equipment for transition metal dichalcogenides

Hybrid Magnetron Sputtering – Pulsed Laser Deposition equipment for thin films

# Laboratory 70 **„Atomic Structures and Defects in Advanced Materials (LASDAM)"**

**Leader:** Dr. Corneliu Ghica, Senior Researcher rank 1 (cghica@infim.ro)

**Personnel:** LASDAM counts 36 research and technical personnel (44% female, 56% male) including 22 Senior Researchers (7 SR1, 5 SR2, 8 SR3, 2 SR), 8 research assistants (PhD students), 3 engineers and 3 technicians.

**Main research directions:**

- Atomic scale structure-functionality correlations in advanced materials (nanostructures, thin films, ceramics and special alloys);
- Paramagnetic point defects, either intrinsic or induced by impurities or radiations in insulators and wide-bandgap semiconductors;
- Investigation of the physical-chemical mechanisms underpinning the detection process in nanostructured materials for gas sensing applications;
- Dielectric and semiconductor thin films for microelectronic applications of interest for environment, security, space, biomedicine, food safety;
- Cellular and non-cellular in vitro interactions and biomedical applications of inorganic nanomaterials and hybrid nanostructures.

**Main research infrastructure:**

- Aberration-corrected analytical transmission electron microscope (HRTEM/HRSTEM) provided with EDS and EELS microanalytical facilities for sub-Ångström resolution imaging and atomic-resolution elemental mapping;
- High-resolution analytical electron microscope for electron tomography, *in situ* and *operando* experiments by specimen heating/cooling/electrical biasing;
- SEM-FIB dual analytical system used for morpho-structural and microanalytical investigations (SEM, EDS, EBSD) as well as for ion beam micro- and nanoprocessing;
- Continuous wave (cw) X-band (9.8 GHz) EPR spectrometer with variable temperature (VT) accessories in the 80÷500 K range; cw Q-band (34 GHz) EPR spectrometer with ENDOR (Electron-Nuclear Double Resonance) and VT accessories (5÷300 K);
- Pulse X-band (9.7 GHz) EPR spectrometer equipped with pulse ENDOR, pulse ELDOR (Electron-Electron Double Resonance) and VT accessories (5÷300 K);
- Automatic liquid He plant completed with a helium recovery system; computer-controlled gas mixing station and associated electrical measurements chains for materials testing under controlled atmosphere;
- Chemical reactor and autoclave for hydrothermal and co-precipitation chemical synthesis;
- Magnetron sputtering installation for thin films deposition, with *in situ* characterization/monitoring by Auger electron spectroscopy (AES), low-energy electron diffraction (LEED) and ellipsometry;
- Installation for rapid thermal annealing, oxidation and nitriding; horizontal furnace with 3 temperature zones for thermal treatments and physical vapour deposition (PVD);
- Measurement chains for electrical, ferroelectric and photoelectric characterization, Hall effect and magnetoresistance measurements.


a. Bruker EPR spectrometer in X band (9.7 GHz) in pulsed regime with ENDOR accessories;
b. Bruker EPR spectrometer in CW Q-band with ENDOR accessory;
c. Setup for electrical measurements under controlled atmosphere gas mixing station.
d. JEM 2100 high-resolution analytical transmission electron microscope;
e. Tescan Lyra III analytical SEM-FIB dual system;
f. Magnetron sputtering installation for thin films deposition, provided with in situ AES, LEED and ellipsometry;
g. Installation for rapid thermal processing (RTA, RTO, RTN), horizontal furnace with 3 temperature zones for thermal treatments and PVD;
h. Measurement chains for electrical, ferroelectric and photoelectric characterization, Hall effect and magnetoresistance measurements

**Available services:**

- SEM morphological characterization of advanced materials;
- TEM characterization of nanostructured materials, thin films, ceramics, alloys;
- Chemical elemental composition and elemental mapping by SEM-EDS and STEM-EDS;
- Multifrequency EPR characterization of bulk and nanostructured insulating and semiconductor materials: nature, concentration, localization, formation mechanism and stability of the paramagnetic centers in materials; chemical processes, structural or magnetic transitions;
- Controlled simulation of toxic and explosive gas environments (CO, $CH_4$, $NO_2$, $H_2S$, $NH_3$, $SO_2$) for gas sensors testing and calibration; temperature-voltage calibration for the optimization of power consumption for substrates and gas sensors.
- Growth of thin films and multilayers by magnetron sputtering;
- Rapid thermal annealing (RTA) and controlled oxidation (RTO) at temperatures within 200-1250 $^oC$, heating rates up to 200 $^oC/s$ in gas flow ($N_2$, $O_2$, Ar, $H_2$) and thermal treatments using the horizontal furnace with 3 temperature zones up to 1200 °C in vacuum or flow of Ar, $N_2$;
- Electrical characterization under dark/illumination conditions, Hall effect measurements and modelling of experimental curves current-voltage (I–V) at varying temperature, in DC and AC, capacity-voltage (C–V), capacity-frequency (C–f), capacity-time (C–t), polarization-voltage (P–V), I–T and R–T; spectral characteristics of the photocurrent (I–λ) in modulated and continuous illumination; Hall measurements: V-I curves as a function of current, magnetic field and temperature.

LASDAM operates as Partner Facility within CERIC-ERIC (https://www.ceric-eric.eu/) on behalf of NIMP, the Romanian Representing Entity in the consortium along with research institutes and universities in Austria, Croatia, Czech Republic, Hungary, Italy, Poland, Slovenia.

## Laboratory 80 **"Catalytic Materials and Catalysis (MATCA)"**

**Leader:** Dr. (habil.) Mihaela Florea, Senior Researcher rank 1 (mihaela.florea@infim.ro)

**Personnel:** MATCA group has been set up in 2021, and has, at present time, 6 members with permanent contract. From the 6 members with permanent contracts, 2 are Senior Researchers rank1 (SR 1), 1 is Senior Researcher rank 2 (SR 2), 1 is Senior Researchers rank 3 (SR 3), 1 is Senior Researcher (SR), 1 is Assistant Researcher. There are 5 holders of PhD title, 1 PhD students and 1 PhD supervisor.

**Main research directions:**

- Development of heterogeneous catalytic and photocatalytic materials (preparation and characterization);
- Catalytic reactions: selective oxidation reactions, hydrogenation reactions, synthesis of polymers from renewable/alternative resources, depolymerisation of plastics, reduction of volatile organic compounds;
- Photocatalysis: water splitting, photocatalytic CO2 transformation and artificial photosynthesis;
- Energy: synthesis of materials used as electrocatalysts in fuel cells.

**Relevant infrastructure:**

MATCA Group has an infrastructure covering various methods of catalytic material preparation and physico-chemical characterization.

Among the important infrastructures one can mention:

- Chemistry lab (Figure 1): equipped with all necessary small equipment's for catalytic materials synthesis (ovens working in air or vacuum, rotavapors, magnetic stirrers, autoclaves for hydrothermal treatments, chemical niche, apparatus for miliQ water production, centrifuge,

balances) and catalytic reactors (in house reactors for solid-gas phase and liquid-solid phase reactions)

- Thermo-programmed desorption and reduction equipment (TPD-TPR) – for determining the adsorption capacity and redox properties (Figure 2)
- Spectroscopy analysis: UV-Vis and Raman portable (Figure 2)
- Thermal analysis – to study the relationship between a sample property and its temperature as the sample is heated or cooled in a controlled manner. (Figure 2)
- Analysis of the reaction products- gas chromatograph with three detectors (TCD, FID and BID) gas chromatograph coupled with mass spectrometer (Figure 2)


**Fig 1.** Chemistry lab

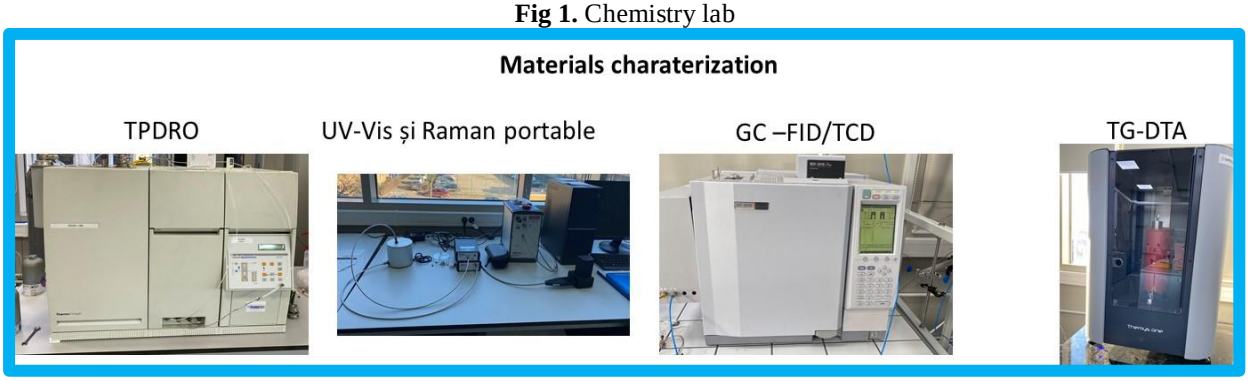


**Fig. 2.** Equipment for materials characterization and analysis

The group has access to other infrastructures located at NIMP, through collaborative research activities, such as: TEM and SEM equipment's; XPS characterization; other optical spectroscopies (Raman, UV-Vis-NIR, FTIR); X-ray diffraction, ICP-MS, photoluminiscence.

**Available services:**

- Catalytic materials preparation
- Gas-solid and gas-liquid catalytic reaction
- Water splitting
- Surface characterization
- Structural and textural characterization of the catalytic materials
- Investigation of acid-base and redox properties

# Materials modeling, preparation and characterization

# Conductance zeros in complex molecules and lattices from the interference set method

**M. Niţă[a], M. Ţolea[a], and D. C. Marinescu[b]**
[a]National Institute of Materials Physics, Atomistilor 405A, Magurele 077125, Romania
[b]Department of Physics, Clemson University, Clemson, SC 29634

We study the occurrence of conductance cancellations in transport through molecules and certain lattices, as a result of destructive quantum interference (DQI) - a phenomenon without correspondence in classical electricity. The DQI has been previously studied in different physical and chemical systems, such as quantum dots [1,2], graphene-type structures [3,4,5], benzene and other carbon-based molecules [6,7]. Controlling the conductance cancellations is important in all transistor-like applications.

Here, we summarize our results published in the paper Phys. Rev. B 103, 125307 (2021). A method was developed for determining the conductance zeros that result from destructive electron state interference in certain complex systems derived from more simple bipartite systems. The method starts by finding a smaller system which includes an interference set, whose points are such that any pair of them is associated with zero conductance (GII = 0, including the diagonal terms, when both leads are connected to the same site). The remaining points from this initial system, outside the interference set, are called rigid points R. A complex system is then obtained by connecting new, external points X to the I points (but never to the R points) or by adding any on-site or hopping energies related to the I points. We prove that the new system obtained in this way retains all the initial conductance cancellations between the I points (GII = 0) and, in addition, exhibits new zeros between points I and points X (GIX = 0). The proposed algorithm is sketched in Fig.1.

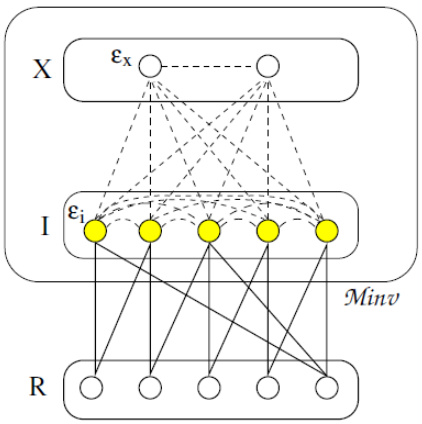


**Fig.1** A complex system is built by perturbing the I points from the set $M_I$ or by connecting external points X from the set $M_X$ to the interference points I. The R points are not affected during the construction of the new system. The larger contour enclosing the two sets $M_X$ and $M_I$ defines the invariance set $M_{inv}$.

One must mention that not all molecules/lattices have interference sets with the conductance cancelations property that we mentioned, they are rather an exception. A particular class of systems with known conductance cancellations are the bipartite systems: i.e. which can be divided into two sub-systems (say A and B) with hoppings only between sites from different sub-sets (A-B) but not between sites from the same sub-set (A-A or B-B). In such systems, if they are half-filled with electrons (which is the case in grahene sheets, for instance), the conductance always vanishes between sites from the same sub-lattice (A-A or B-B), and therefore the A or B sets can be used as starting set in our construction described above (see the previous paragraph and Fig.1). Among the simplest examples of bipartite systems with non-singular Hamiltonians we mention the linear chains with 2N sites and circular molecules with 4N + 2 sites. In the example given in Fig.2 for instance, about the fulvene molecule, we identify in 6 possible ways bipartite sub-systems (they are all linear chains, except for the case in Fig.2c).

Our proof is based on the Dyson equation and the Landauer-Buttiker transport formalism:

$$G'_{II} = G_{II} + G_{II}h_{II}G'_{II} + G_{II}h_{XI}G'_{XI}$$
$$G'_{IX} = G_{II}h_{II}G'_{IX} + G_{II}h_{IX}G'_{XX} \qquad (1)$$

In the above equations G' denotes the Green function of the full system while G denotes the Green function of the initial system, composed only of the interference set I. The formulas show that if the supplementary hoppings are allowed only between I points or between I and X points, then, the cancellation of the conductance in the larger system (G'II and G'IX) results from the cancellations in the initial system ($G_{II}$). The discussion above is made in terms of Green functions, however they are directly connected to the electronic conductance through the Landauer-Buttiker transport formalism (see, e.g. [1,4]).
Below we give an example of how the described formalism was used to predict all conductance cancellation for the fulvene molecule.

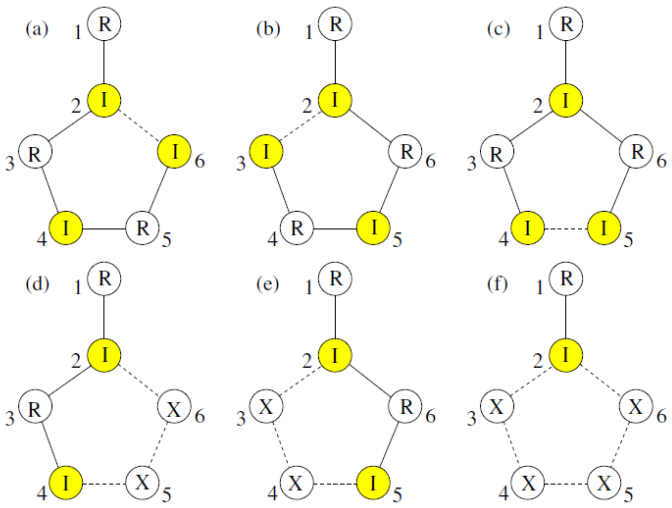


**Fig.2** Interference points in fulvene molecule and the decomposition of its lattice sites: I+R+X, where I and R are the interference and rigid points of the starting bipartite molecule and the X are the "extra" points added so that the fulvene molecule is recovered. In (a)-(f) the dashed lines correspond to the new hopping energies, while the X circles in (d)-(f) designate the new external sites X added to the initial bipartite molecule (composed of I and R circles).

One can notice that the fulvene molecule is not bipartite, however the finite chains which we use as starting systems are bipartite and we can use one sub-lattice as the starting interference set. Also, we mention again that the choice of the starting bipartite system is not unique, but in fact making different initial choices help find different conductance cancellations. Apart from predicting conductance cancellations, our scheme also offers information about the robustness of the zeros – telling what perturbations affect them and which do not. Being an interference effect, and taking place at a precise energy (of the incoming electrons), the DQI is in particular independent of the coupling strength with the leads, which provides a certain robustness to be used in potential applications.
Our study contributes to the understanding of the destructive interferences and their invariance properties for an appropriate class of physical systems that have bipartite lattices or contain subsystems with bipartite lattices. They can be relevant for transport experiments on molecules, nanostructures and various finite lattices, for designing of logical gates or for projection of quantum interference transistors at the nanoscale.

*References*


1. A. Levy Yeyati and M. Buttiker, Scattering phases in quantum dots: An analysis based on lattice models, Phys. Rev. B 62, 7307 (2000).
2. I. Rotter and A. F. Sadreev, Zeros in single-channel transmission through double quantum dots, Phys. Rev. E 71, 046204 (2005).
3. T. Tada and K. Yoshizawa, Quantum transport effects in nanosized graphite sheets, Chem. Phys. Chem. 3, 1035 (2002).
4. M. Nita, M. Tolea, and B. Ostahie, Transmission phase lapses at zero energy in graphene quantum dots, physica status solidi (RRL) Rapid Research Letters 08, 790 (2014).
5. A. Valli, A. Amaricci, V. Brosco, and M. Capone, Interplay between destructive quantum interference and symmetry-breaking phenomena in graphene quantum junctions, Phys. Rev. B 100, 075118 (2019).
6. P. Sautet and C. Joachim, Electronic interference produced by a benzene embedded in a polyacetylene chain, Chemical Physics Letters 153, 511 (1988).
7. D. Nozaki and C. Toher, Is the antiresonance in metacontacted benzene due to the destructive superposition of waves traveling two different routes around the benzene ring, Journal of Physical Chemistry C 121, 11739 (2017).
8. M. Nita, M. Tolea, D.C. Marinescu, Conductance zeros in complex molecules and lattices from the interference set method, Phys. Rev. B 103, 125307 (2021).

# Spin-mechanical coupling effects in single-molecule magnets

**V. Moldoveanu,[a] R Dragomir[a]**

[a]National institute of Materials Physics, Bucharest-Magurele, Atomistilor 405A Romania, Magurele 77125

Single molecular magnets are conveniently described as large localized spins which can be used as qubits in spintronic devices. In a cornerstone experiment, Ganzhorn *et al.* studied the subtle coupling between this spin and the mechanical motion [1]. More precisely, a $TbPc_2$ molecule with localized spin $S = 6$ was grafted on a suspended carbon nanotube (see the sketch in Fig. 1). The latter supports quantized longitudinal stretching modes (LSM) called vibrons which are activated by an electronic current. It turns out that by matching the vibron energy $\hbar\omega$ one can drive transitions between two energy levels corresponding to different values of the localized spin. These measurements confirm the existence of the spin-vibron coupling and provide a way to tune the spin of the molecular magnet. On the theoretical side, the vibron-assisted spin transitions in freely rotating or rigidly coupled nanomagnets were only studied in special cases [2]. First, one considers only the transitions corresponding to the ground state (GS) doublet $S_z = \pm S$. Secondly, the theoretical studies disregard the electronic occupation of the suspended nanostructure, which means that the effect of the electron-vibron coupling cannot be captured. Here we go beyond these limitations and provide a theoretical study of the interplay between the electron-vibron and spin-vibron interactions in open nano-electromechanical systems with grafted nanomagnets.

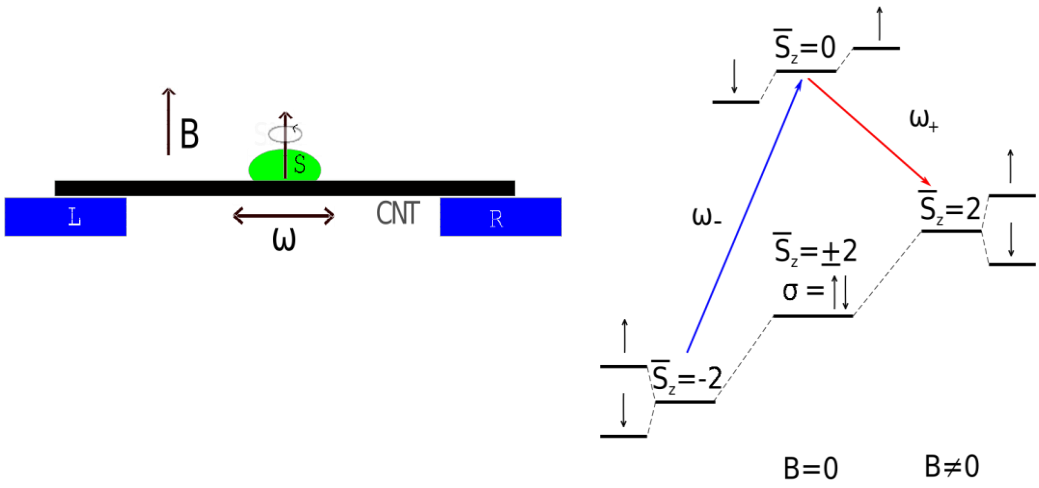


**Fig. 1** Left panel - the sketch of the hybrid system. A localized spin grafted on a carbon nanotube which supports longitudinal stretching modes and is connected to source (L) and drain (R) contacts. Right panel - the Λ configuration of the single-particle states in the case $S = 2$.

The horizontal lines mark the energy levels in the absence of vibrons and the arrows indicate transitions between states with $z$-projection of the spin $\overline{S_z} = 0$ and $\overline{S_z} = \pm 2$. One has two resonant frequencies $\omega_+$ and $\omega_-$ . The blue/red arrows show resonant/off-resonant transitions. The dashed line describes Zeeman splittings and the vertical arrows correspond to the electronic spin orientation. The bar placed over the spin component reminds the fact that and $\overline{S_z}$ is in fact a dominant quantum number in a state which is in fact a mixture of many spin components. This is a consequence of the transverse anisotropy term.

We find that even in the simplest case of a small molecular spin $S = 2$ the vibron-assisted transitions $S_z = \pm 2 \rightarrow S_z = 0$ (represented in the right panel of Fig.1 and neglected in previous theoretical studies) have a large probability, as the corresponding matrix element is of first order in the spin-vibron coupling. Last but not least, these transitions induce much faster operations on the localized spin than in the case of GS transitions. Notably, apart from the additional energy splitting associated to the Zeeman terms involving both molecular and electronic spins the spectral structure depicted in Fig. 1 resembles the so called Λ-configuration encountered in quantum optics. In particular, our

numerical simulations (see the results in Ref. [3]) predict the existence of vibronic Rabi oscillations in the transient regime.

Let the system be submitted to a bias $eV = \mu_L - \mu_R$, where $\mu_{L,R}$ are the chemical potentials of the source/drain reservoirs. Then one should study the simultaneous effects of the electron-vibron and spin-vibron interctions, which are introduced as follows:

$$H_{el-vb} = \lambda \hat{N}(a + a^{\dagger}), \qquad H_{sp-ph} = -i\alpha E(S_{+}^{2} - S_{-}^{2})(a + a^{\dagger}). \tag{1}$$

Here $\lambda$ and $\alpha$ are coupling constants, $\hat{N}$ is the charge operator associated to the hybrid system, $\hat{S}_{\pm}$ are the jump molecular spin operators and $a,a^{\dagger}$ are the operators of the vibronic mode. The spin-rotation coupling is defined as $\alpha = \sqrt{\hbar/2\, I_z \omega_0}$ , where $I_z$ is the inertia moment of the nanomagnet and $\omega_0$ is the fixed frequency of the LSMs. From Eq. (1) one notices that the electron-vibron coupling does not depend on the molecular spin while the spin-vibron coupling does not depend on the electronic occupation of the system. We recall that molecular magnets posses axial magnetic anisotropy $DS_z^2$ as well as a transverse anisotropy component $E(\hat{S}_x^2 - \hat{S}_y^2)$.

The dynamics of the SMM spin, the electron currents and the expectation value of the vibron number are found by solving the generalized Master equation (GME) for the reduced density operator (RDO). The GME is solved in a Markovian approximation (i.e. in a Lindblad form) and has the advantage of allowing an exact treatment of the electron-vibron and spin-mechanical interactions. We calculated the transient currents, the statistical average of the molecular spin and of the vibron number, as well as the occupations of various spin states. Full details are given in Ref. [3].

Fig. 2 summarizes some of the main results. The frequency of the vibrational mode is set such that the transition $S_z = -2 \rightarrow S_z = 0$ is resonant. The effect of the spin-vibron coupling is confirmed by the increase of the average molecular spin from its initial value $S_z = -2$. We also discern two time scales of the spin evolution. In the resonant regime the spin increases abruptly in just a few nanoseconds, then the system enters a second regime in which the increase of the average spin slows down and it takes at 150 nanoseconds until it approaches the stationary state.

In Fig. 2(a) one also sees that as the ratio E/D decreases, the stationary regime is reached at longer times (e.g., at t ~ 400 ns for E/D = 1/7.5). This is the expected behavior, given the fact that a smaller spin-vibron coupling leads to less effective off-resonant transitions between pairs of states carrying spin quantum number value $S_z = 0$ and value $S_z = 2$, whereas the resonant transitions between the states value $S_z = 0, -2$. remain active. In Fig. 2(b) we also identify small but systematic signatures of the spin-vibron coupling on the time-dependent output current. More precisely, we compare the fully interacting currents corresponding to the three ratios E/D considered before and the noninteracting currents (i.e., in the absence of the spin-vibron coupling, $\alpha = 0$). In the latter case all currents display a sharp peak once the leads are coupled to the hybrid system and then decrease uniformly to the steady-state values (see the dashed lines in Fig. 2(b)). In contrast, for $\alpha = 0.15$ (solid lines) one notices a non-monotonous behavior, namely the sharp peak is followed by a slow but noticeable increase of the transient current as it slowly approaches the steady-state value. The time range on which this smooth increase appears becomes longer if the ratio E/D decreases and roughly corresponds to the slower off-resonant spin dynamics shown in Fig. 2(a). Also, the steady-state values of the currents are slightly reduced in the presence of the spin-vibron coupling.

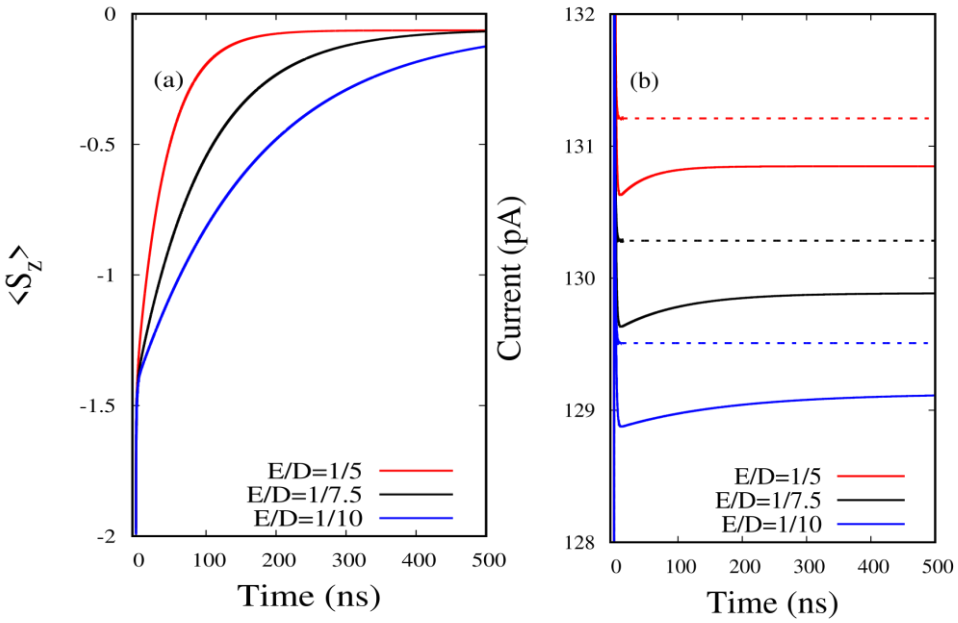


**Fig. 2** (a) Average molecular spin for different values of the ratio E/D. The frequency of the vibrational mode is set to the resonant value $\omega = \omega_-$ , and $\hbar\omega_- = 0.267$ meV. (b) The time-dependent current in the drain lead. The solid lines correspond to the spin-vibron coupling $\alpha = 0.15$ and the dashed lines to the noninteracting case $\alpha = 0$.

*References*

1. M. Ganzhorn, S. Klyatskaya, M. Ruben and W. Wernsdorfer, Nature Communications 7, 11443 (2016).
2. E. M. Chudnovsky and D. A. Garanin, Phys. Rev. B 81, 214423 (2010).
3. V. Moldoveanu and R. Dragomir, Phys. Rev. B 104, 075441 (2021).

# Band-Order Anomaly at the γ-$Al_2O_3$/$SrTiO_3$ Interface Drives the Electron-Mobility Boost

**M. A. Husanu,[a,f]** in collaboration with
**A. Chikina,[a,b] D. V. Christensen,[c] V. Borisov,[d,e] Y. Z. Chen,[c,g] X. Q. Wang,[a] T. Schmitt,[a] M. Radovic,[a] N. Nagaosa,[h,i] A. S. Mishchenko,[h] R. Valenti,[d] N. Pryds,[c] V. N. Strocov[a]**

[a] Paul Scherrer Inst, Swiss Light Source, CH-5232 Villigen, Switzerland
[b] Aarhus Univ, Inst Phys & Astron, DK-8000 Aarhus, Denmark
[c] Tech Univ Denmark, Dept Energy Convers & Storage, DK-2800 Lyngby, Denmark
[d] Goethe Univ Frankfurt Main, Inst Theoret Phys, D-60438 Frankfurt, Germany
[e] Uppsala Univ, Dept Phys & Astron, S-5120 Uppsala, Sweden
[f] Natl Inst Mat Phys, Magurele 077125, Romania
[g] Chinese Acad Sci, Inst Phys, Beijing Natl Lab Condensed Matter Phys, Beijing 100190, Peoples R China
[h] RIKEN, Ctr Emergent Matter Sci, Wako, Saitama 3510198, Japan
[i] Univ Tokyo, Dept Appl Phys, Tokyo 1138656, Japan

The results obtained in soft X-ray angle resolved photoelectron spectroscopy (SX-ARPES) studies performed at Swiss Light Source synchrotron facility in Switzerland explain the mechanism of mobility enhancement by orders of magnitude at the interface of $SrTiO_3$ (STO) with γ-$Al_2O_3$ (GAO) [1]. The metallic conductivity at the STO-based interfaces is best illustrated by the prototype two-dimensional electron system (2DES) which appear in STO when covered with $LaAlO_3$ at a critical thickness of 4 unit cells [2]. Although the electron concentration accumulated by such interfaces is typically a couple of orders of magnitude larger than that at the semiconductor interfaces, the electron mobility ($\mu_e$) is however orders of magnitude less [3] due to defect scattering, electron-correlation phenomena, and, for the STO-based interfaces in particular, a strong electron–phonon interaction (EPI), resulting in the polaronic nature of the interfacial charge carriers [4]. Unlike the LAO/STO where electronic reconstruction occurs at the interface in order to prevent a "*polar catastrophe*" [1], the mechanism of metallic conductivity at the GAO/STO interface relies on accumulation of oxygen vacancies, highly confined in the interface region [5].

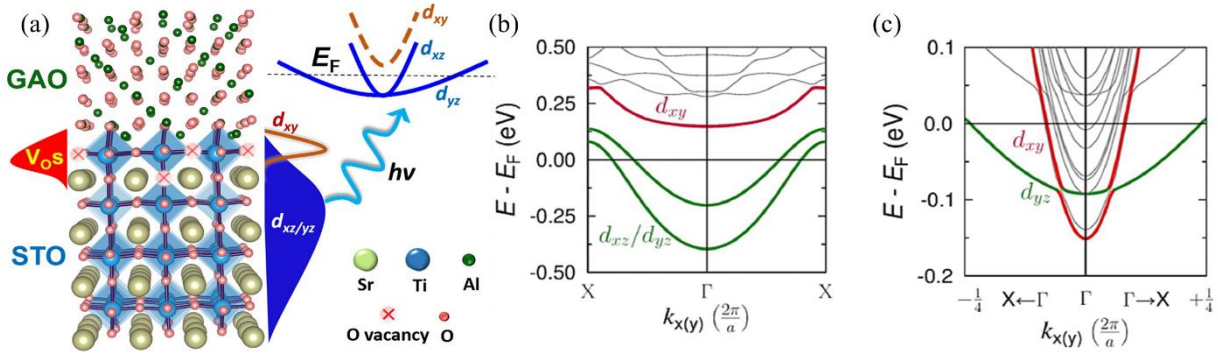


**Fig. 1** Scheme of the GAO/STO interface probed with **k**-resolved photoemission to directly image electron dispersions. The ARPES experiment finds the band-order anomaly $d_{xy} > d_{xz}/d_{yz}$ which promotes spatial separation of the oxygen vacancies from the 2DES to boost $\mu_e$ (a). (b,c) Calculated band structures for the oxygen-deficient GAO/STO and defect-free LAO/STO interfaces (the latter is adapted from J. Zabaleta *et al* , Phys. Rev. B **93** (2016) 235117) along the XΓX direction. The dominant orbital character is encoded by color: red ($d_{xy}$) and green ($d_{xz}/d_{yz}$).

Fig. 1(a) presents the general idea of the SX-ARPES experiment, where the interface electronic states are probed through a thin 2.5 nm of GAO deposited by pulsed laser deposition by resonantly exciting the Ti L edge photoelectrons with X-rays with the energy of ~460 eV. This extends the probing depth towards the buried interface and singles-out the signal of the Ti $t_{2g}$ derived bands of the 2DES. Samples with low and high carrier concentrations and mobilities were investigated.
DFT calculations have revealed the different band order at the GAO/STO interface compared to the LAO/STO system (Fig. 1b,c). It is observable that unlike LAO/STO 2DES, the metallic conductivity

of the GAO/STO interface is mostly due to heavy $d_{xz,yz}$ derived bands, whereas the light $d_{xy}$ band stays unoccupied.
Such band anomaly is due to the breaking of the symmetry and tilting of the oxygen octahedral which lifts the $t_{2g}$ orbital degeneracy and modify the crystal field at the spinel-perovskite interface compared to the perovskite-perovskite case [1]. This effect results in increasing energy separation between the lowest occupied $d_{xz}/d_{yz}$ states and the $d_{xy}$ –derived band.

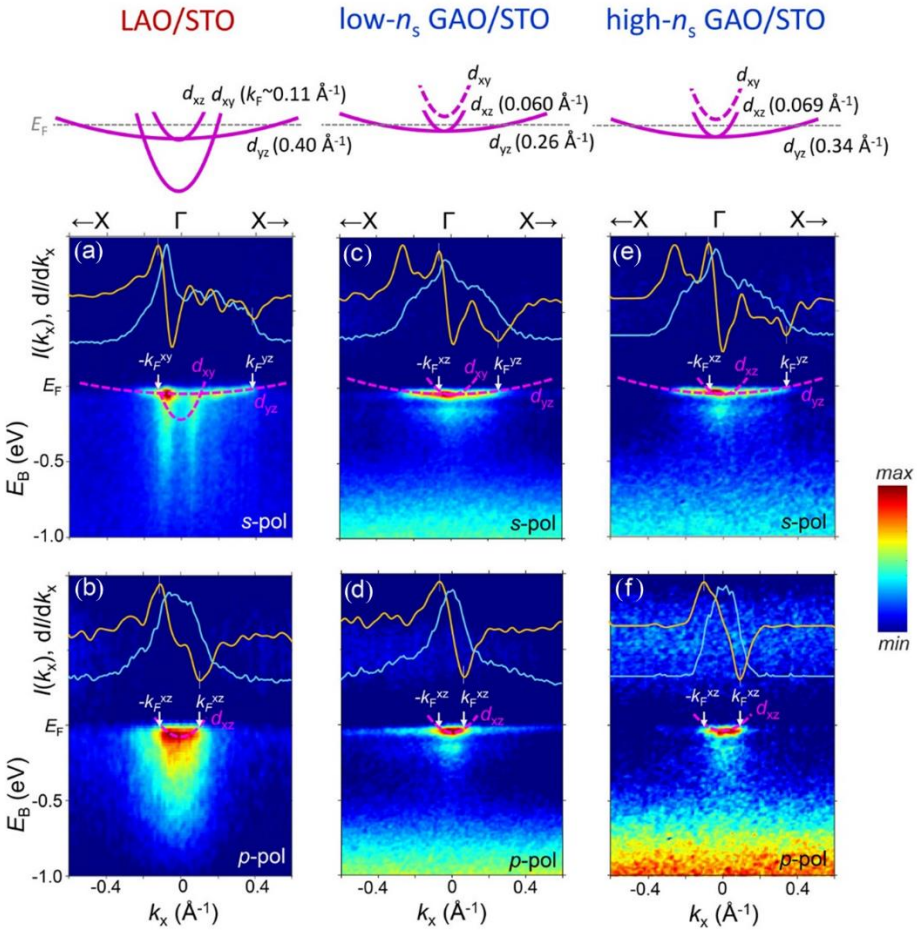


**Fig. 2** Experimental $E(\mathbf{k})$ images along ΓX for the oxygen-deficient LAO/STO interface (a,b) and low- and high-electron density GAO/STO interfaces (c,d and e,f, respectively) measured at $h\nu$ = 460.4 eV. For LAO/STO, *s*-polarized X-rays select the $d_{xy}$ and $d_{yz}$ bands (top panels) and *p*-polarized X-rays the $d_{xz}$ bands (bottom panels), and for GAO/STO these selection rules relax. The momentum-distribution curves at $E_F$ (blue curves) and their gradients (yellow) are shown on top of each panel, with extremes of the latter (dashed lines) locating the $k_F$ values (arrows). The sketches on top of the figure schematize the band order for the three samples, where GAO/STO shows the anomalous $d_{xy} > d_{xz}/d_{yz}$ band order with complete depopulation of the $d_{xy}$ band.

Indeed, the ARPES images recorded on both LAO/STO (Fig. 2a,b) and GAO/STO (Fig.2c-f) with different motilities identifies the different band structures of the two interfaces. Whereas the hybridization between the light and heavy bands characteristic of LAO/STO system [4] is clearly seen at the Fermi energy (Fig. 2a), at the GAO/STO interface it completely disappears indicating that the $d_{xy}$ bands are empty, consistent with the scenario of different band occupation induced by the different symmetry at this interface.
Moreover, the polaronic signature of the GAO/STO is much weaker (Fig. 2d,f) compared to the standard LAO/STO system (Fig. 2b). This signature is normally seen as either a distinct replica separated by energies matching the phonon modes, or as fading intensity extending 0.2-0.4 eV below the electron band if several polaronic mechanisms (different vibration modes or impurity scattering) are involved.
In fact, the experimental spectral function derived from the ARPES images features not only the decrease of the polaronic replica which accompany the quasiparticle peak but also sharpening of the

spectral features which is inversely proportional to the coherence length of the charge carriers. Such behavior reflects the effective disorder they experience due to scattering on impurities, in this case on oxygen vacancies which at the GAO/STO interface is diminsihed.

As shown in Fig. 1, oxygen vacancies relative to the depopulated $d_{xy}$ and populated $d_{xz}/d_{yz}$ electron density in GAO/STO accumulate more at the interface region reducing their concentration and thereby the associated defect scattering in the deeper STO region. This further propagates into mobility increase by two orders of magnitude at the GAO/STO interface compared to the LAO/STO one.

Equally interesting, further increase of the mobility upon increasing the carrier concentration in the interface 2DES (Fig. 2e,f) is due to electron-density accumulation in higher-order $d_{xz}/d_{yz}$-derived states located in STO beyond the top 2–3 u.c. reached by ARPES. This situation can be viewed as a transformation of the 2DES into a quasi-three-dimensional system expanding deep into $V_O$-free STO. In this case, the increase of $n_s$ should be associated with an increase of $\mu_e$, and it indeed increases by a factor of ~8 between the two GAO/STO samples.

*References*


1. A. Chikina et al., "Band-Order Anomaly at the γ-$Al_2O_3$/$SrTiO_3$ Interface Drives the Electron-Mobility Boost" ACS Nano. 15(3), 4347–4356 (2021)
2. A. Ohtomo and H.Y. Hwang, Nature 427, 423 (2004)
3. J. A. Sulpizio et al. "Nanoscale Phenomena in Oxide Heterostructures" Annu. Rev. Mater. Res. 44, 117– 149 (2014)
4. C. Cancellieri et al. "Polaronic Metal State at the $LaAlO_3$/$SrTiO_3$ Interface", Nat. Commun. 7, 10386 (2016Y. Z. Chen et al. "A high-mobility two-dimensional electron gas at the spinel/perovskite interface of γ-$Al_2O_3$/$SrTiO_3$", Nature Commun. 4, 1371 (2013P. Schutz et al. "Microscopic Origin of the Mobility Enhancement at a Spinel/Perovskite Oxide Heterointerface Revealed by Photoemission Spectroscopy", Phys. Rev. B 96, 161409 (2017)

# A corrected band model and a new criterion for ferromagnetism

**Cristian Mihail Teodorescu**[a]

[a]National Institute of Materials Physics, Atomiștilor 405A, 077125 Măgurele–Ilfov, Romania

Ferromagnetism is usually treated starting with several models, and the most widely used are the Heisenberg model for the interaction of the spins localized on neighboring atoms, induced by the exchange interaction, and the Stoner model for band ferromagnetism, in which electrons are considered delocalized over the whole crystal. It is first shown that in the Curie-Weiss model starting with the Heisenberg interaction, the coercive fields obtained are several orders of magnitude higher than the observed experimental values. The actual view to explain this discrepancy is that ferromagnetic domains are formed and their relative spatial extent varies in an applied external field, up to the stabilization of the single domain state at saturation [1]. However, a complete description of this variation is still lacking and is currently under investigation.

The band theory of ferromagnetism considers electrons in the conduction and valence band spin-split according to their spin orientation, with a rigid shift between these two bands. The band with 'majority' spin orientation is shifted towards lower energies, while the band with 'minority' spin orientation is shifted towards higher energies. One should consider the variation of average kinetic energy of the electrons together with a stabilization energy which is proportional to the product of the densities of spin up and spin down electrons $-Un_{\uparrow}n_{\downarrow}$ (whose origin may be traced down to the on-site Coulomb repulsion of electrons, yielding the Hubbard term in the Hamiltonian). $U$ is called the 'Hubbard' energy and has an atomic origin. By estimating the relative influence of the stabilization energy and the increase of the kinetic energy, one obtains the well-known 'Stoner criterion' for ferromagnetism $Ug_0(\varepsilon_F) > 1$, where $g_0(\varepsilon_F)$ is the density of states at the Fermi level in the paramagnetic state [2]. The main drawback of the Stoner model is the fact that it predicts unreasonably high Curie temperatures, on the order of $k_B T_C \sim U \sim$ several electronvolts.

However, a more detailed estimate of the kinetic energy variation between the spin polarized and unpolarized state (Figure 1) yields the fact that, if one assumes the constancy of the Fermi level amongst the two sub-bands with majority and minority spins, the kinetic energy in the spin polarized state is always lower than in the paramagnetic state [3]. One needs to consider the total electron energy, while also considering the shift of the bottom of the conduction band, and not only the kinetic energy! Thus, even in the absence of the stabilization Hubbard energy, the spin polarized state would be favored and hence *all metals should be ferromagnetic!*

A more detailed estimate in Ref. [3] of the variation of the total energy between the spin-split and the paramagnetic state yields that ferromagnetism is favored when the following criterion is fulfilled:

$$\left(\frac{dg_0}{d\varepsilon}\right)(\varepsilon_F)\int_0^{\varepsilon_F} g_0(\varepsilon)d\varepsilon < {g_0}^2(\varepsilon_F) \quad (1)$$

Hence, a subtler influence of the shape of the density of states has to be considered for stabilization of the spin-split state. It seems, in particular, that when the Fermi level lies on a decreasing part of the density of states $(dg_0/d\varepsilon)(\varepsilon_F) < 0$, the metal is ferromagnetic. The next step was to propose a simplified model for the density of states for 3d metals; this model consists of two triangular shapes, one corresponding to $e_g$ and the other to $t_{2g}$ sstates, the first being occupied by maximum 4 electrons and the second by maximum 6 electrons (Figure 2). For body cubic centered (*bcc*) structures, the energy of $e_g$ states is lower in energy than the $t_{2g}$, while for face cubic centered (*fcc*) and hexagonal close packed (*hcp*) structures, $t_{2g}$ states are lower in energy that $e_g$. Computing the energies in these bands allows one to derive that for the first 3d elements (Sc, Ti) the most stable structures are *fcc*, then for intermediate elements (V, Cr) the *bcc* structure has lower energy; Mn is a special case since it does not have a simple crystal structure, but it seems that the *fcc* structure is more stable in this simple model. Problems occur with Fe, whose most stable structure yields to be *fcc–hcp*. But considering the fact that it is magnetic, in the bcc ferromagnetic state Fe has a lower energy than in

the fcc paramagnetic state and, according to the above criterion, for *fcc* Fe the paramagnetic state is the most stable and for *bcc* the ferromagnetic state is the lowest in energy. Thus, *bcc* ferromagnetic Fe is the most stable structure. And Co and Ni in both paramagnetic and ferromagnetic states have fcc as the most stable structure. Thus, this simple model is able to predict which are the most stable structures along most 3d metals.

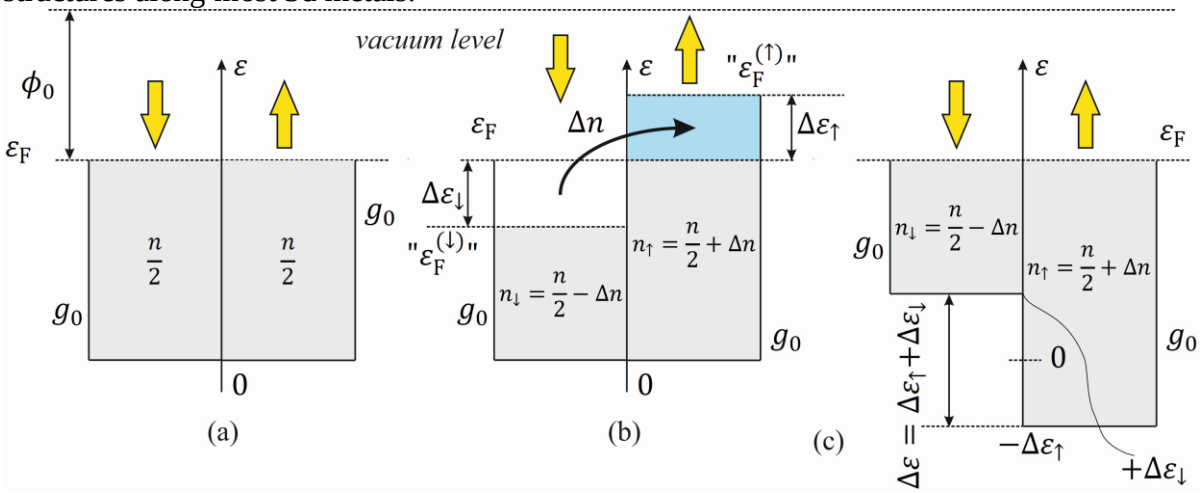


**Fig. 1**. Sub-band splitting in the case of a constant density of states $g_0$. (a) densities of states for spin up (majority) and down (minority) sub-bands in absence of spin polarization; (b) transfer of $\Delta n$ electrons from the minority and majority sub-band, which are filled up to spin-dependent Fermi levels "$\varepsilon_F^{(\uparrow)}$" and "$\varepsilon_F^{(\downarrow)}$", with the energy of the bottom of the conduction band unchanged. (c) The situation obtained with the same Fermi level for both sub-bands, assumed to be located at the same position as in the case of unpolarized sub-bands. With respect to (b), the majority spin sub-band is shifted to lower energies by $\Delta\varepsilon_\downarrow$, and the minority spin sub-band is shifted to higher energies by $\Delta\varepsilon_\uparrow$. The total electron energy in this state is lower than in (a).

The above simple theory also allows one to predict that only *bcc* Fe, *fcc* and *hcp* Co, *fcc* Ni are ferromagnetic. The theory allows one also to justify why some metastable phases are ferromagnetic, such as *bcc* Co, *hcp* Cr or *fcc* V. Also, a temperature dependent development of the model allows one to predict reasonable Curie temperatures for Fe and Co, in agreement with the experimental values. Note also that in this model there is no need to introduce any Hubbard-like stabilization energy, all properties may be derived just by starting with the shape of the density of states.

Low coercive fields in metals appear in this model as a simple consequence of the conservation of the total electron density, according to Figure 2. Applying a field parallel with the sample magnetization shifts the majority spin sub-band towards even lower energies, while the minority spin sub-band is shifted towards higher energy, hence the Fermi level also shifts by the Zeeman energy. When the field is applied in the opposite direction, the free states occurring in the majority spin sub-band are not compensated by the newly occupied states in the minority spin sub-band, hence the electron density is not conserved. As a consequence, the system shifts suddenly in the state with opposite magnetization.

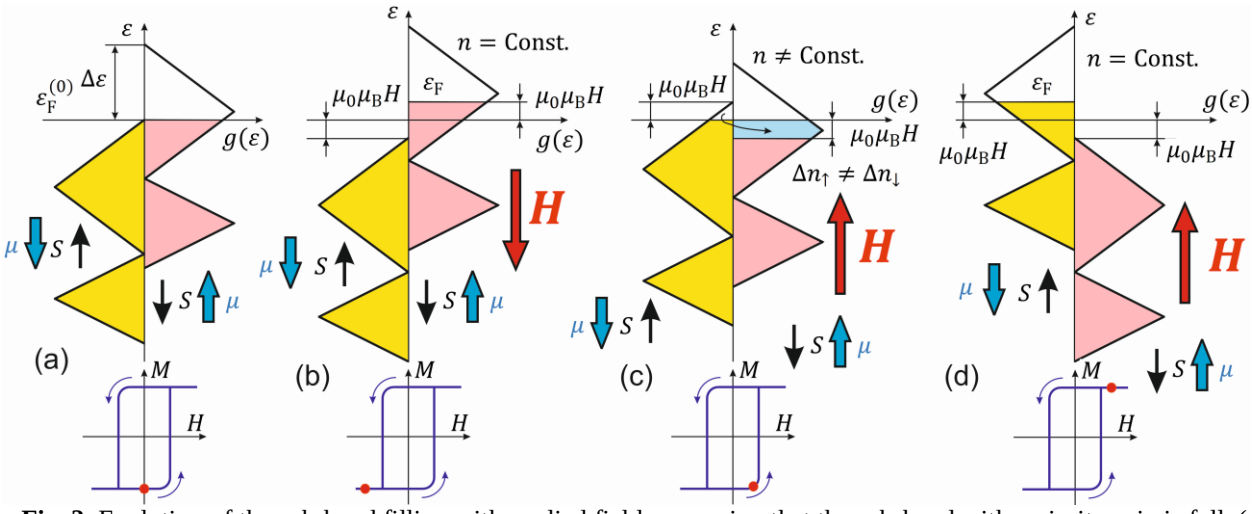


**Fig. 2**. Evolution of the sub-band filling with applied field, supposing that the sub-band with majority spin is full. (a) situation with no applied field and remnant polarization approximately equal to the saturation magnetization. (b) Applied field in the direction of the existing magnetization: the initial band splitting increases, the minority spin sub-band is shifted towards higher energies, the total electron density may be the same as in the initial case provided the position of the Fermi level increases by the Zeeman energy corresponding to one minority electrons. (c) Applied field opposite to the direction of the existing magnetization: the electron density cannot be conserved with similar Zeeman shifts of the two sub-bands. (d) Sudden change of spin polarization: the initial minority sub-band becomes majority sub-band and vice versa.

One fascinating hypothesis comes from the investigation of the temperature evolution of the second derivative of the energy with respect to the spin asymmetry at very high temperatures. It turned out that at temperatures above about 6000 K, Fe becomes again ferromagnetic. This phenomenon is called 're-entrant ferromagnetism'. The temperature of the Earth's inner ore is in this range; hence, the actual corrected model for band ferromagnetism may propose also the fact that the Earth's inner core is at least partially ferromagnetic. Thus, the Earth's magnetic pole inversion might proceed by simple rotation of the magnetization and not by a lowering of the absolute value of the geomagnetic field. In these condition, the Earth's surface will permanently be protected from cosmic radiation; the evolved organisms and our electrically-based civilization is not expected to suffer any harm during such magnetic pole inversion.

The temperature for re-entrant ferromagnetism in Co is predicted to be even lower than that of Fe (about 2500 K) and one might think about its experimental verification with the actual technology.

*References*


1. C. Kittel, "Physical theory of ferromagnetic domains", *Rev. Mod. Phys.* **21**, 965 (1949). [doi: 10.1103/RevModPhys.21.541]
2. E. C. Stoner, "Collective electron ferromagnetism", *Proc. Roy. Soc. London* **165**, 372–414 (1938). [doi: 10.1098/rspa.1938.0066]
3. C.M. Teodorescu, "Spin asymmetry originating from densities of states: Criterion for ferromagnetism, structures and magnetic properties of 3d metals from crystal field based DOSs", *Res. Phys.* **25**, 104241 (2021). [doi: 10.1016/j.rinp.2021.104241]

# Microscopic model for ferroelectricity and its statistical treatment

**Cristian Mihail Teodorescu**[a]

[a] National Institute of Materials Physics, Atomiștilor 405A, 077125 Măgurele–Ilfov, Romania

Unlike ferromagnetism which benefits of several microscopic models, with magnetic moments either localized on individual atoms, or magnetization associated to the spin of electrons in the conduction and valence band, accompanied by a spin asymmetry, ferroelectricity until recently lacked such a microscopic moment, which may constitute the basis for a statistical treatment and derivation of the equations of state of such system. In ferromagnetism, the basic entity for any model is the electron spin; in ferroelectricity, there is no such basic entity whose interaction with the environment (similar entities or external fields) may be modelled and treated statistically.

For a sample which shows a non-vanishing polarization inside its bulk and no free charges, the Maxwell equation $\boldsymbol{\nabla} \cdot \boldsymbol{D} = \boldsymbol{\nabla} \cdot (\epsilon_0 \boldsymbol{E} + \boldsymbol{P}) = 0$ ($\boldsymbol{D}$ is the electric induction, $\boldsymbol{E}$ the intensity of the electric field, $\boldsymbol{P}$ the polarization, $\epsilon_0$ the vacuum permittivity) may be written by evidencing a 'density of fixed charges' $-\boldsymbol{\nabla} \cdot \boldsymbol{P}$. It is easy to show that towards the external surfaces of the film oriented perpendicular to the polarization (say the $z$ direction), this density has pronounced positive and negative peaks; integrating it over $z$ across these surface yields to surface 'fixed charges' densities numerically equal to $\pm P$. This implies that the bulk of the sample is subject to a field whose order of magnitude is about $P/\epsilon$, where $\epsilon$ is the permittivity of the material. Numerically, this field is on the order of $10^8$–$10^{10}$ $\mathrm{Vm}^{-1}$, and oriented opposite to the polarization of the material. Since this 'depolarization field' exceeds the coercive field of the material and is oriented against the polarization, its presence would destroy the ferroelectric polarization of the material. Thick materials form domains where, according to Kittel's theory, the depolarization field decreases exponentially towards the bulk [1]. But thin films quite often show a single-domain structure with the polarization oriented perpendicular to the film, and for such systems Kittel's theory cannot provide the cancellation of the depolarization field away from the film's surface or interface. Thus, the hypothesis formulated almost two decades ago to explain the single domain state of thin ferroelectric films is that these materials are usually wide band gap semiconductors, and charges are generated and accumulated towards the surfaces or interfaces of the films, with the surface charge density numerically equal to the polarization, such as to compensate the depolarization field [2]. So, the main idea is that charges accumulated at surfaces or interfaces of a single domain thin ferroelectric films occur in order to compensate the depolarization film. Experimental investigations by X-ray photoelectron spectroscopy of the surface band bending in ferroelectric thin films confirmed this hypothesis; moreover, in Ref. [3] a complete picture of the nature of these charges accumulated was listed, these charges being either free charge carriers (electrons or holes), or charges accumulated on the sandwiching layers (e. g. electrons in metal electrodes, or charged radicals adsorbed on the surfaces), or layers of ionized impurities left when the mobile charges migrate towards the opposite surface or interface.

In Ref. [4], the above paradigm was inverted as follows: instead of regarding charge accumulation at surfaces or interfaces of a ferroelectric thin film as a *consequence* of the establishment of the ferroelectric state, it was proposed as a *cause* of it. By investigating all interactions that might be applied to a virtual elemental dipole in the material, it turned out that the dipole-dipole interaction with the other dipoles in the material does not compensate the interaction with the accumulated charges at surfaces and interfaces. Hence, the interaction of a dipole in the material with charges accumulated at surfaces or interfaces may be regarded as a *stabilization* energy for the ferroelectric state, since the field generated by the accumulated charges is oriented parallel to the polarization. As soon as a polarizable material or the heterostructure which comprises it may stabilize charges at its surfaces and interfaces, these charges are accumulated, producing the polarization of the material, such that the total energy of this system is lower than in the unpolarized state. This situation, for a ferroelectric thin film with perovskite structure, is summarized in Figure 1. Thus, the stabilization energy may be simply written, for an elemental dipole in the material whose magnitude is $p_0$ such as:

$$\varepsilon_{\text{micro.}} = -\frac{GPp_0}{\epsilon_0 \kappa_0} \tag{1}$$

where $\kappa_0$ is the dielectric constant of the material and $G(\approx 0.5)$ a 'geometric factor' introduced to consider the dipole-dipole interactions and which depends weakly on the tetragonality of the film and on its thickness.

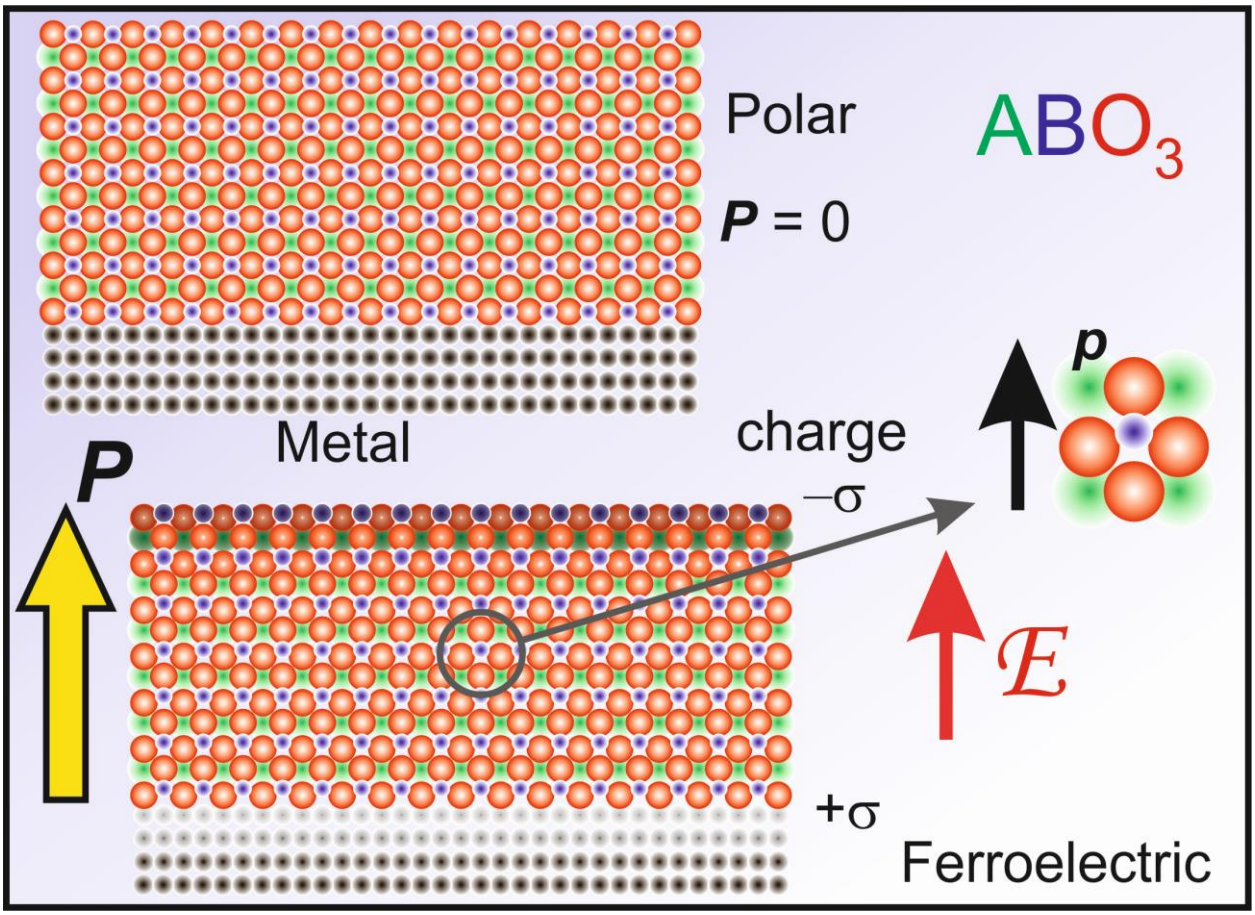


**Fig. 1**. Charges accumulated at the outer surfaces and interfaces of thin films stabilize the permanent polarization of a polar material. If a dipole moment is attributed to each unit cell, its interaction with charges accumulated at outer surfaces and interfaces prevails upon dipole-dipole interactions and allows one to apply the Curie-Weiss mean field theory

Starting with the microscopic energy from the above equation, one may then apply usual statistical mechanics as in the standard Curie-Weiss theory and derive the equations of state, more particularly the $P - E$ curves at different temperatures. At temperatures below the Curie temperature, hysteresis is obtained with non-vanishing polarization in zero applied electric field, whereas above the Curie temperature, the paraelectric state is obtained. According to the way the possible states of the 'elemental dipole' are considered (summing over two discrete states $\pm P/n_0$, where $n_0$ is the density of elemental dipoles, or integrating from $-P/n_0$ to $+P/n_0$) two models may be developed, one involving the tanh function, the other involving the Langevin function. Also, starting with the $P - E$ dependencies and integrating $EdP$, one may recover stabilization free energies, which are derived on a microscopic basis and not just on general considerations, as in Landau-Ginsburg-Devonshire model. All parameters of the free energy then have well-defined meanings; at the same time, the coercive fields, remnant polarization and their dependence on temperature may be calculated starting with microscopic parameters and they yield reasonable values.

A question arising concerns the constancy of the dielectric constant $\kappa_0$. For a ferroelectric material both the global and the differential permittivity depend on the temperature and on the polarization. This raises the question whether such a non-constant permittivity should be used in the stabilization

energy of the ferroelectric phase, and whether it can be self-consistently identified with the function resulting after applying the statistics based on the microscopic model. A model is then built up in Ref. [5], able to predict coercitivity. Nevertheless, the coercive fields and the Curie temperature yield values several orders of magnitude higher than the experimental ones. Therefore, one has to introduce a background dielectric constant of several hundreds to accommodate the result of the model with the experimental data. The poling history of the film has to be considered, together with the presence of a small bias field. The last model is able to predict self-consistently the equation of state of a ferroelectric, and in particular the linear decrease of the coercive field with temperature. The microscopic parameters, in particular the background dielectric constant and the density of elemental dipoles may be expressed directly from experimental quantities.

*References*


1. C. Kittel, "Theory of the structure of ferromagnetic domains in films and small particles", Phys. Rev. 11–12, 965 (1946).
2. L. Pintilie and M. Alexe, "Metal-ferroelectric-metal heterostructures with Schottky contacts. I. Influence of the ferroelectric properties", J. Appl. Phys. 98, 124103 (2005).
3. L. C. Tănase, L. E. Abramiuc, D. G. Popescu, A.-M. Trandafir, N. G. Apostol, I. C. Bucur, L. Hrib, L. Pintilie, I. Pasuk, L. Trupină, and C. M. Teodorescu, "Polarization orientation in lead zirco-titanate (001) thin films driven by the interface with the substrate", Phys. Rev. Applied 10, 034020 (2018).
4. C. M. Teodorescu, "Ferroelectricity in thin films driven by charges accumulated at interfaces", Phys. Chem. Chem. Phys. 23, 4085–4093 (2021).
5. C. M. Teodorescu, "Self-consistently derived sample permittivity in stabilization of ferroelectricity due to charge accumulated at interfaces", *Phys. Chem. Chem. Phys.* **24**, 5419–5430 (2022).

# Electron trapping in twisted light driven graphene quantum dots

**Adrian Pena**[a,b,*]
[a]National Institute of Materials Physics, Atomiştilor 405A, Măgurele –Ilfov, Romania, 077125
[b]Faculty of Physics, University of Bucharest, Atomiştilor 405, Măgurele – Ilfov, Romania, 077125

Twisted light (TL) is a novel type of electromagnetic field which carries a finite orbital angular momentum oriented on the propagation direction, besides its spin [1]. As the wave front goes by, the wave vector k rotates around the propagation direction, describing a cone with a well-defined opening angle $\boldsymbol{\theta_k = arctan(q/k_z)}$, where q and $k_z$ are the transversal and, respectively, longitudinal components of k (see Fig. 1).

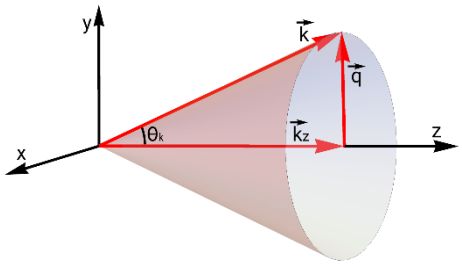


**Fig. 1** Twisted light propagation.

The presence of TL is introduced in the problem via its vector potential [2]

$$\boldsymbol{A}(\boldsymbol{r},t) = A_0\left(J_m(qr)e^{im\varphi}\boldsymbol{\epsilon}_\Lambda - \Lambda i\frac{q}{k_z}J_{m+\Lambda}(qr)e^{i(m+\Lambda)\varphi}\hat{\boldsymbol{z}}\right)e^{i(k_z z-\omega t)},$$

where $\boldsymbol{r} = (\boldsymbol{r}, \boldsymbol{\varphi})$ is the position vector in polar coordinates, $\boldsymbol{A_0}$ is a constant real amplitude, $\boldsymbol{J_m(x)}$ is the Bessel function of the first kind of order *m*, *m* is the topological charge, $\boldsymbol{\epsilon_\Lambda}$ is the polarization vector in the transversal plane (perpendicular on the propagation direction), $\boldsymbol{\Lambda = \pm 1}$ is the helicity quantum number and $\boldsymbol{\omega}$ is the frequency.
We investigated an elastic scattering process of an electron on a TL driven circular graphene quantum dot (GQD) of radius R, as sketched in Fig. 2. The incident electron, represented by the wave $\boldsymbol{\Psi_k^i}$, propagates freely towards the dot with energy $\boldsymbol{E = v_F \hbar k}$, where $\boldsymbol{v_F = 10^6\, m/s}$ is the Fermi velocity, $\hbar$ is the reduced Plank constant and $\boldsymbol{k}$ is the associated wave number.

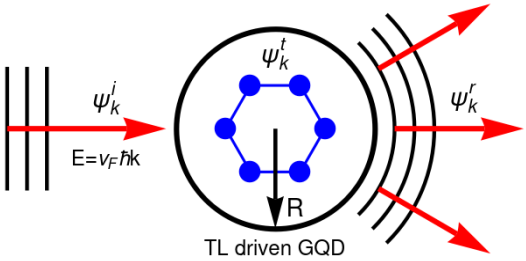


**Fig. 2** Schematic representation of the scattering process.

As the incident electron interacts with the GQD, it is either reflected (wave $\boldsymbol{\Psi_k^r}$) or transmitted inside the dot (wave $\boldsymbol{\Psi_\kappa^t}$), where κ is the associated wave number inside the GQD.
The analysis is performed in terms of scattering efficiency (Q) defined as scattering cross section divided by the geometric cross section [3], density and current. The wave functions we discussed about, represent states of well defined orbital angular momentum, but it is conveniently to perform the investigation in terms of scattering modes *n* = 0, 1, 2, 3 … Each scattering mode couples two orbital angular momentum states. For instance, *n* = 0 includes 0 and -1 orbital angular momentum states, *n* = 1 includes 1 and - 2 and so on.

The scattering analysis was performed for $\boldsymbol{m = 1}$, $\boldsymbol{\omega = 10^{14} s^{-1}}$ and $\boldsymbol{\theta_k = 30°}$. It was observed that in the case of $\boldsymbol{\Lambda = -1}$ the scattering efficiency presents resonances [4], depending on the total averaged TL power received by the dot ($\boldsymbol{P_{GQD}}$) and GQD radius R. In Fig. 3 it can be observed that for $\boldsymbol{R = 220}$ nm (red curve) only the $\boldsymbol{n = 0}$ mode is resonantly excited, with the scattering efficiency resonance peak centered on $\boldsymbol{P_{GQD} = 4.95}$ mW (see marker 2). For the case of $\boldsymbol{R = 280}$ nm, we also observe the resonant excitation of $\boldsymbol{n = 1}$ mode with the peak centered on $\boldsymbol{P_{GQD} = 32.36}$ mW (see marker 3).

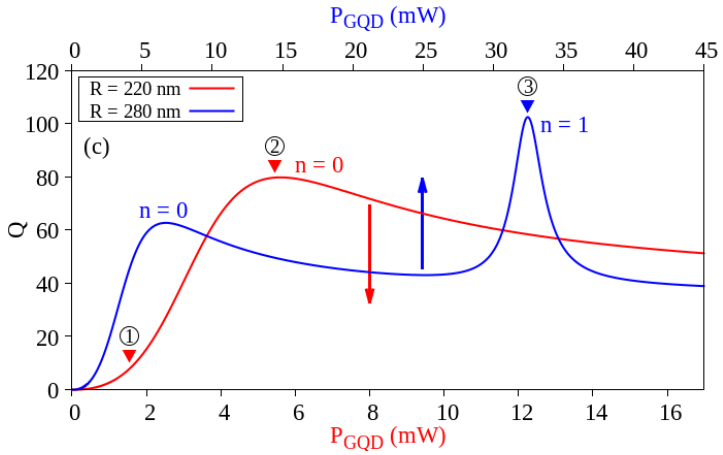


**Fig. 3** Scattering efficiency for an incident energy $\boldsymbol{E = 0.5}$meV and $\boldsymbol{\Lambda = -1}$.

The scattering regimes indicated by markers 1, 2 and 3 in Fig. 3 were analyzed in terms of density and current (see Fig 4). The first scattering regime investigated corresponds to $P_{GQD}$= 1.53 mW, where the scattering is non-resonant (see marker 1). In this case, the density values and the current flow are not affected, since the TL power is not high enough [see panels (a) and (b)]. For a higher power (marker 2), the presence of TL induces so-called *quasi-bound states* [5], associated with the resonant excitation of$n$ = 0mode, characterized by high density values inside the dot [see panel (c)]. On the other hand, these states are associated with the formation of two counter-rotating current vortices inside the GQD, as can be observed in panel (d). For the case of an even higher power of TL (marker 3), where $n = 1$ mode is resonantly excited, the density reaches values up to four times as high compared to the previous case. The current flow generates six counter-rotating vortices inside the dot, which trap the electron inside.

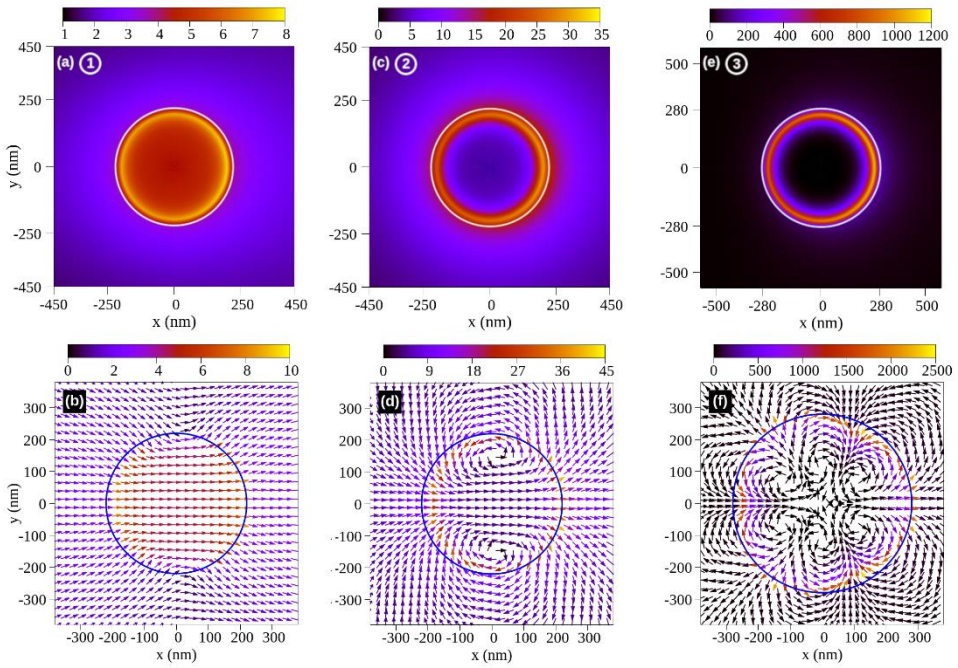


**Fig. 4** Density and current corresponding to scattering regimes indicated by markers (1, 2 and 3) in Fig. 3.

In low-excitation regimes around K-points, the charged particles in graphene behave as massless Dirac fermions, having a well-defined helicity (chirality). Due to this peculiar property, the localization of an electron inside a GQD is forbidden, as a manifestation of Klein tunneling [6]. The most important finding reported in this paper is the possibility to control the trapping features of a GQD by TL driving and suitably adjusting the scattering parameters.

*References*

1. O. Matula, A. G. Hayrapetyan, V. G. Serbo, A. Surzhykov, and S. Fritzsche, J. Phys. B: At. Mol. Opt. Phys 46, 205002 (2013)
2. G. F. Quinteiro, C. T. Schmiegelow, D. E. Reiter, and T. Kuhn, Phys. Rev. A 99, 023845 (2019)
3. R. L. Heinisch, F. X. Bronold, and H. Fehske, Phys. Rev. B 87, 155409 (2013).
4. P. Hewageegana and V. Apalkov, Phys. Rev. B 77, 245426 (2008)
5. H.-Y. Chen, V. Apalkov, and T. Chakraborty, Phys. Rev. Lett. 98, 186803 (2007)
6. M. I. Katsnelson, K. S. Novoselov, and A. K. Geim, Nat. Phys. 2, 620 (2006)

# Room temperature adsorption and oxidation of carbon monoxide on graphene synthesized on atomically clean Pt(001)

**Nicoleta G. Apostol, Ioana C. Bucur, George A. Lungu, Cristian A. Tache, Cristian M. Teodorescu***

National Institute of Materials Physics, Atomistilor 405A, Magurele, Romania, 077125

Ref. [1] describes first results in room temperature intercalation of carbon monoxide beneath graphene (Gr) layer synthesized in ultrahigh vacuum (UHV) conditions by chemical vapor deposition (CVD), starting from ethylene, on atomically clean Pt(001) surface. Graphene formation at high-temperature has been studied *in-situ* using high-resolution X-ray photoelectron spectroscopy (HRPES), and low-energy electron diffraction (LEED) and near-edge X-ray absorption fine structure (NEXAFS) spectroscopy, meanwhile CO adsorption and oxidation have been studied *in-situ* using only HRPES.

The main reasons for studying adsorption and oxidation of CO on this particular system, involving graphene above the well-known catalytic platinum metal were: (i) a previous proof that chemical bond of Gr with Pt(111) surface is one of the weakest graphene-metal bonds [2] makes one to expect that its chemical bond with Pt(001) surface to be even weaker, due to the incommensurable character of Pt(001) surface with respect to Gr structure; (ii) existence of a rich *hex* reconstruction of atomically clean Pt(001) surface [3] promotes this particular surface as affinity enhancer for adsoption of CO molecules with respect to the more compact and lacking superstructure Pt(111) surface; (iii) the need for investigation of all possible crystallographic orientations of the Pt substrate, since one cannot ensure a single orientation of the films for practical applications in real catalytic systems, when Pt films synthesized by low-cost methods are to be used in conjunction with graphene; (iv) CO oxidation reaction on Pt(001) appear to occur even at 500-800 K at $10^{-5}$ Torr CO pressure [4], and our previous STM studies confirmed that Gr/Pt(001) preserves the (reactive) *hex* reconstruction and protects it against reaction while $O_2$ dosing at pressures up to $10^{-4}$ hPa and CO dosing at pressures up to $10^{-6}$ hPa (at room temperature); at higher pressures, CO is observed to intercalate under the graphene coating layer, thus lifting the reconstruction, leaving intact the Gr layer; *ab initio* DFT calculations also prove the stability of graphene; the stripe structure of the *hex* reconstruction is preserved under graphene, even across step edges and domain boundaries, but such studies require confirmation and supplement by XPS analyses of the chemical states, and NEXAFS spectroscopy has to be used to check for the complete in-plane bonding of carbon atoms forming the graphene layer and to detect if defects are present in the graphene layer.

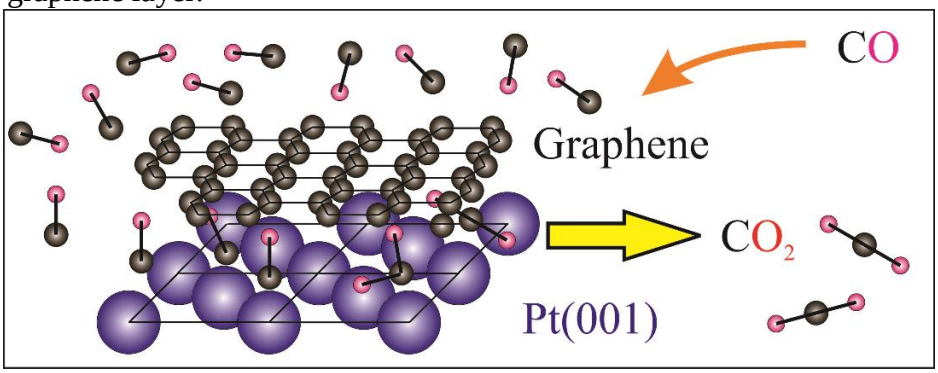


**Fig. 1** Graphical abstract of the published paper [1]. Intercalation of CO molecules between graphene and metal Pt(001) surface enhances its oxidation yield.

The entire experiment has been performed in the Combined Spectroscopy and Microscopy on Surfaces (CoSMoS) facility belonging to host institute of the authors of Ref. [1], in UHV conditions, having base pressure within $10^{-9}$ Pa, and being connected to the SuperESCA beamline at Elettra synchrotron radiation facility in Trieste, Italy.

NEXAFS spectroscopy performed at carbon K edge enable one to detect if deposited carbon p orbitals hybridize into planar $sp^2$ molecular orbitals only, or into both planar $sp^2$ and spatial $sp^3$ orbitals.

NEXAFS spectra recorded at various incidence angles for the graphene for which HRPES spectra encountered very sharp (only 0.230(5) eV full width at half maximum) line at proper binding energy (BE) of 284.000(5) eV, are well fit with $\cos^2\alpha$ and $\sin^2\alpha$ functions, a sign that most of the carbon 2p orbitals form in-plane σ bonds. This is a sign of a 'perfect' local structure around carbon atoms and possibly also a sign of low corrugation, but one has to note that the 'fingerprint region' between σ* and π* resonances exhibits some peaks, which may be due to double-vacancy or line defects, possibly acting as capture and insertion centers for later deposited carbon monoxide.

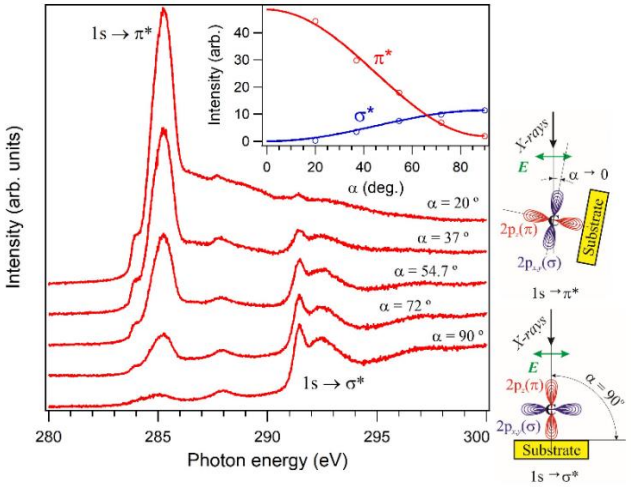


**Fig. 2** Near-edge X-ray absorption fine structure (NEXAFS) at the carbon K-edge for 1 monolayer graphene grown on Pt (001). The insert represents the variation of intensities corresponding to transitions to σ* and π* unoccupied electronic states as function on the angle α between the direction of the soft X-rays and the sample surface. The lines are fits with $\cos^2\alpha$ for the transition to π* and $\sin^2\alpha$ for the transition to σ*. The drawing at the right shows the orientation of the 2p σ* and π* orbitals with respect to the linear polarization of the incoming X-rays in two extreme cases: normal incidence (bottom) and nearly grazing incidence (top).

After 4500 Langmiur of CO deposited, C 1s and Pt 4f core levels in HRPES spectra exhibit rigid chemical shifts of 36 meV (to lower BEs) and 96 meV (to higher BEs), respectively, values consistent with prevalence of CO molecules adsorbed atop of Pt topmost atoms of the substrate, with carbon atoms bound to platinum and being relatively positively ionized from charge transfer processes, and oxygen atoms more negatively ionized due to back-donation process. The generated potential difference of $\Delta V = 132$ meV by summing up the chemical shifts of carbon and platinum may give an estimation for a dipole moment $p$ of the CO molecule as

$$p = \frac{\varepsilon_0 \Delta V}{\theta_a n_s} \approx 0.27\,\mathrm{D}, \qquad (1)$$

a value in close agreement to 0.29 D, reported by Engel and Ertl in 1979 [5], where $\varepsilon_0$ is the electric permitivity of vacuum, $\theta_a \approx 0.1$ ML is CO coverage, and $n_s$ is the surface density of CO molecules; this value helps us conclude that graphene plays no significant role on charge transfer processes occuring among CO molecules and platinum substrate.

The novelty of the summarized study is the time evolution of the CO-related C 1s and O 1s peaks, suggesting a progressive desorption of CO, together with alterations of the [O]:[C] ratios corresponding to both adsorption sites, namely increase of this ratio for 'atop' adsorbed molecules and decrease of it for molecules adsorbed on 'bridge' sites (Fig. 3). While for the definition of 'atop' oxygen-rich CO one may imagine a mixture of CO and $CO_2$, each having the carbon bound to a platinum atom, the definition of a 'bridge' oxygen-poor CO would imply some adsorbed carbon without any binding oxygen. One may imagine that such carbon atoms, after just having lost their oxygen, are still located in the same adsorption sites on Pt(001) and should probably induce components in the XPS spectra close to their initial position in 'bridge' configurations, before the dissociation of the molecule.

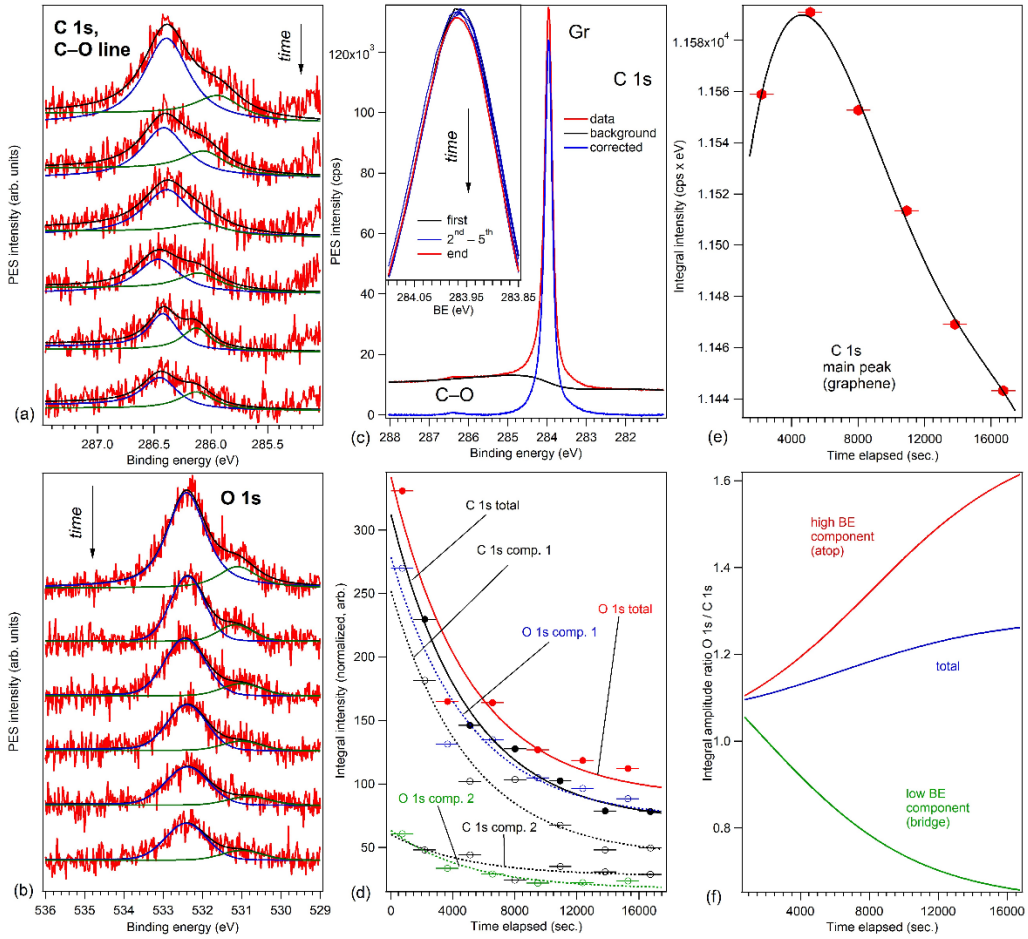


**Fig. 3** (a) C 1s (photon energy **h**$\nu$ = 400 eV, only in the region of the C–O line) and (b) O 1s (**h**$\nu$ = 650 eV) photoelectron spectra obtained successively, after dosing 4500 Langmuir CO on graphene grown on Pt(001). The spectra are 'deconvoluted' each one with two Voigt lines. (c) The total C 1s signal, with a procedure for background removal, in order to evaluate its integral intensity. The insert represents the evolution of the total integral intensity of the C 1s signal corresponding to the graphene peak at about 284 eV, normalized by the photoionization cross section, the sample current and by the total Au photoionization cross section (see text for details). (d) Time evolution of integral intensities for C 1s corresponding to C–O bonding (separated components, open black circles; total integral intensity, full black circles) and for O 1s (separated components, open blue and green circles; total integral intensity, full red circles). The intensities are corrected by the photoionization cross section, the different pass energies employed and by the beam intensity, such that their ratio is similar to the atomic ratio. (e) Time evolution of the main C 1 peak. (f) Derived hypothetical time evolution of the [O]:[C] ratio, where the blue line is obtained by dividing fits of the time evolution of the total integral intensities, and the red and green lines are obtained by dividing fits of the time evolution of the components with higher and, respectively, lower binding energies from (a, b).

*References*


1. N. G. Apostol et al., "CO adsorption and oxidation at room temperature on graphene synthesized on atomically clean Pt(001)," Catal. Today 366, 155-163 (2021).
2. M. Gao et al., "Epitaxial growth and structural property of graphene on Pt(111)", Appl. Phys. Lett. 98(3), 033101 (2011).
3. R. Hammer et al., "Surface reconstruction of Pt(001) quantitatively revisited," Phys. Rev. B 94(9), 95406 (2016).
4. F. Gao et al., "CO oxidation on Pt-group metals from ultrahigh vacuum to near atmospheric pressures. 2. Palladium and platinum," J. Phys. Chem. C 113(1),174-181 (2009).
5. T. Engel and G. Ertl, "Elementary steps in the catalytic oxidation of carbon monoxide on platinum metals", Adv. Catal. 28, 1-78 (1979).

# Adsorption, reduction and oxidation of CO molecules on PZT(001) surfaces with Au nanoparticles

**Nicoleta G. Apostol,[a] Marius A. Huşanu,[a] Daniel Lizzit,[b] Ioana A. Hristea,[a,c] Cristina F. Chirilă,[a] Lucian Trupină,[a] Cristian M. Teodorescu[a,*]**

a National Institute of Materials Physics, Atomistilor 405A, Magurele, Romania, 077125
b Elettra Sincrotrone Trieste, SS 14 Km 163.5, Area Sci. Pk., Trieste, Italy, 34169
c Univ Bucharest, Fac. Phys., Atomiştilor 405, Măgurele, Ilfov, Romania, 077125

Ref. [1] brings again into attention of scientific community the investigated catalytic properties of the ferroelectrics, based on knowledge that their polarization may be easily switched by external parameters (electric fields, strain, or temperature), provide the ability to modulate adsorption or desorption energies for the molecules as the harmful carbon monoxide, our previous work showing: (i) a straightforward correlation between the amount of CO adsorbed and the polarization state of the substrate, (ii) evidence for considerable dissociation of the molecule upon its fixation on the ferroelectric surface; (iii) carbon release from the surface in the form of $CO_2$ with temperature increase up to the loss of the surface ferroelectric polarization [2], results in line with previous results concerning noticeable differences in adsorption energetics of CO or $CO_2$ on ferro-electric surfaces [3]. In paper [1] we present a follow-up by *in situ*, time and temperature dependent XPS of CO adsorption and desorption of a $Pb(Zr,Ti)O_3(001)$ (PZT) surface with gold nanoparticles pre-deposited on it. These nanoparticles are visualized by *ex situ* atomic force microscopy. With respect to Ref. 2, a higher amount of carbon monoxide is found to adsorb, but with a lower dissociation rate. Gold is found in a negative ionization state, and this state is proposed to enhance the catalytic activity of the heterosurface.

The preparation experiments for the ferroelectric PZT thin films via pulsed laser deposition (PLD), and their routinely characterization via atomic force microscopy (AFM) and X-ray diffraction (XRD) were performed in the affiliation institution 1. The dosing and in situ characterization using high resolution photoelectron spectroscopy (HRPES) experiments were performed in the CoSMoS facility connected to the SuperESCA beamline at the Elettra synchrotron radiation facility in Trieste.

Usually PZT(001) is not stable with respect to the release of neutral (metallic) Pb under intense synchrotron radiation beam, fact observed also for the present data, but only after the Au deposition. Au nanoparticles, especially in a relative negative state (as found using HRPES spectra, not shown here), might have a beneficial effect on the back-donation mechanism when CO molecules interact with the surface of a negatively charged Au nanoparticle. Fig. 1 presents AFM scans on the sample surface, performed after *in situ* CO adsorption-desorption experiments. Structures resembling 'fortifications' with walls of 2 nm together with 'towers' of 4-6 nm height surrounding 'pools' of about 20 nm depth are identified (Fig. 1(c, d)). The root mean square (RMS) roughness for an extended area ($10\times10$ $\mu m^2$) is 1.34 nm, while the RMS roughness for a restricted area containing a significant part of Au nanoparticles exceeds 3 nm (Fig. 1(d, e)). Note that the RMS roughness of the 50 nm PZT(001) sample recorded before Au deposition is of about 1 nm (Fig. 1(a)), and such surfaces are in principle saturated by the naturally attached contaminant molecules. The significantly larger RMS roughness in areas where we suppose that Au nanoparticles are formed is in line with the amount of gold deposited, 1 nm if the film was completely flat. The lateral size of these structures varies between 50 and 100 nm, and they occupy roughly one half of the surface. The origin of the 'pools' is probably connected to the substrate disruption and consumption of Pb. It might be possible that 'consumed' Pb mixes with Au to build up the walls of the 'fortifications'. Indeed, Pb with Au forms solid solutions over the whole range of compositions, with well-defined intermediate compounds $Au_2Pb$, $AuPb_2$ and $AuPb_3$.

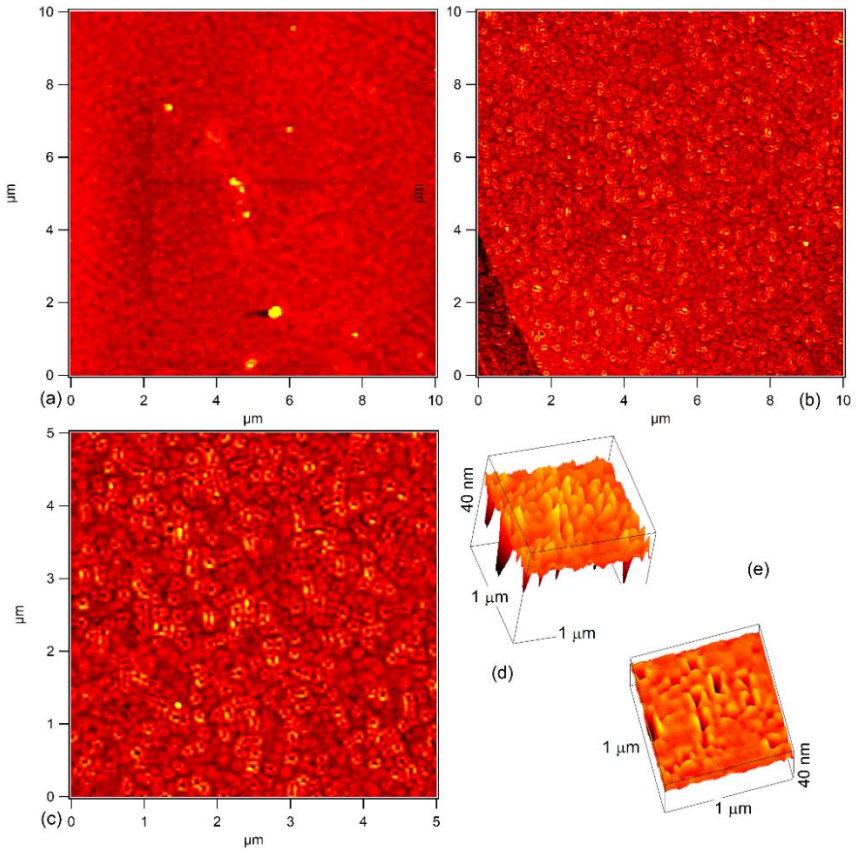


**Fig. 1** AFM images obtained in air on Au/PZT(001) surfaces after their preparation by PLD (a) and after cleaning in UHV followed by Au deposition, CO adsorption and synchrotron radiation experiment (b-e). Areas investigated: (a, b) 10 × 10 µm$^2$, (c) 5 × 5 µm$^2$. (d, e) 3D plots of a 1 × 1 µm$^2$ area, to reveal the size and shape of Au nanoparticles. RMS roughness: 1.08 nm for (a), 1.34 nm for (b), 1.44 nm for (c) and 3.46 nm for (d, e).

From the time- and temperature-resolved HRPES spectra on Au 4f core level (not shown here, but in paper [1]), one can then infer that negatively charged gold may be found at the surface of the gold nanoparticles. Also, it might happen that these areas are progressively 'discharged' by photoemission. These two phenomena may justify a considerably lower proportion of negative gold, but it is still present on the sample in the temperature induced desorption scan. These observations are synthesized in Fig. 2, where the carbon coverage derived from all core level evolution (in fact, from the interpolated curves) is represented as function of the Pb $4f_{7/2}$ binding energy, hence on the average value of the inwards polarization. The fact that negatively charged gold is found mostly at the outer surface of gold nanoparticles may be corroborated with the extrinsic compensation mechanism implying the creation of positive charges in gold at the interface with the ferroelectric substrate. Also, the fact that most neutral carbon is desorbed when the polarization is lost at higher temperatures together with a lower desorption of oxidized carbon implies (as a rough model) that CO reaching the free ferroelectric substrate are dissociated owing to the strong field in this region, a polarization mechanism which is discussed in more details in Ref. [2]. Briefly, the electric field in the outer region is

$$\mathcal{E} = \frac{P}{\varepsilon_0}, \tag{1}$$

and the molecular polarizability $\alpha$ of carbon monoxide molecule is written by introducing a 'polarization volume' $V_p$ [4]:

$$\alpha = 4\pi\varepsilon_0 V_p\ . \tag{2}$$

If we estimate the interaction energy W between CO molecule and the external field, we obtain

$$W = \int p\, d\mathcal{E} = \frac{\alpha\mathcal{E}^2}{2} = \frac{2\pi P^2 V_p}{\varepsilon_0} \tag{3}$$

yielding 8.7 eV for polarization volume $V_p$ = 1.95 Å$^3$ and polarization value $P$ = 1 Cm$^{-2}$. This value approaches the dissociation energy of CO (9.6–9.9 eV [5]). For an increase of 10 % in polarization, the electrostatic interaction energy exceeds the dissociation energy.

Carbon monoxide adsorbed on Au (and then on Au + Pb) nanoparticles seems to be found mostly in an oxidized (bound CO molecules) state and is less sensitive to the polarization decrease of the substrate. It seems that even though the Au 5d $t_{2g}$ orbital positions might have some influence on the π* backbonding, the fact that the 5d occupancy is the same in neutral or negative gold does not influence in a considerable way the back-donation such as to render the carbon-oxygen bond weaker and eventually to dissociate the molecule.

Decrease in oxygen content is found of about 0.05 oxygen atoms per formula unit at 250 °C, when the desorption of neutral carbon was about 0.2 ML. Thus, in order to build up CO to be desorbed, the substrate must be depleted by 0.05 oxygens on about 4 unit cells; and to build up $CO_2$, the oxygen depletion must arrive on 8 unit cells. This is a lower oxygen depletion with respect to Ref. 2; however, one cannot imagine a mechanism for the desorption of graphitic carbon in ultrahigh vacuum other than the oxygen uptake from the substrate. This moderate oxygen depletion was found to be completely recoverable by new treatments in oxygen atmosphere, thus the catalytic heterosurface may be easily regenerated.

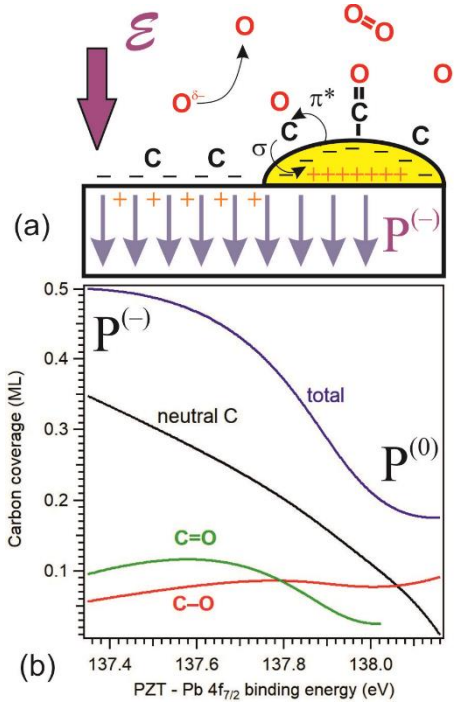


**Fig. 2** Schematics of the PZT(001) surface with inwards polarization prone to adsorb dissociated carbon and of a Au nanoparticle with surface negative charge, prone to adsorb molecular CO *via* back-donation processes.

*References*


1. N. G. Apostol et al., "CO adsorption, reduction and oxidation on Pb(Zr,Ti)$O_3$(001) surfaces associated with negatively charged gold nanoparticles," Catal. Today 366, 141-154 (2021)
2. L. C. Tănase et al., "Ferroelectric triggering of carbon monoxide adsorption on lead zirco-titanate (001) surfaces," Sci. Rep. 6, (2016) 35301.
3. M. A. Khan, M.A. Nadeem, and H. Idriss, "Ferroelectric polarization effect on surface chemistry and photo-catalytic activity: a review," Surf. Sci. Rep. 71(1), 1-31 (2016).
4. C. M. Teodorescu, "Image molecular dipoles in surface enhanced Raman scattering," Phys. Chem. Chem. Phys. 17(33), 21302-21314 (2015).
5. H.G. Howell, "Dissociation energy of carbon monoxide," Nature 163(4150), 773-773 (1949).

# Novel results in the field of ferroelectric thin films and nanostructures

**L. Pintilie[a], A. G. Boni,[a] C. F. Chirila,[a] V. Stancu,[a] L. Trupina,[a] C. M. Istrate,[a] C. Radu[a], I. Pintilie,[a] I. Pasuk,[a] F. Neatu,[a] S. Neatu,[a] M. Florea,[a] L. Amarande,[a] A. Tomulescu[a]**

[a] National Institute of Materials Physics, 405A Atomistilor Street, Magurele, Romania, 077125

In recent years, the National Institute of Materials Physics has started researching in the field of ferroelectric nanomaterials [1]. Nanosized $BaTiO_3$ (nano-BTO) of cuboid shape can be assembled in ordered thin films, that can be used for example as gate dielectric in field effect transistors or in multilayer capacitor structures due to their large dielectric constants and low dielectric losses. The ferro-paraelectric phase-transition temperature of BTO is about 120°C, but its ferroelectricity becomes unstable at room-temperature (RT) when particle size decreases below a critical size. This critical size as well as some details of the crystal structure and the phase-transition mechanism of nano-BTO are still under debate. Our study published in Nanomaterials [1] addresses these controversial structural issues.

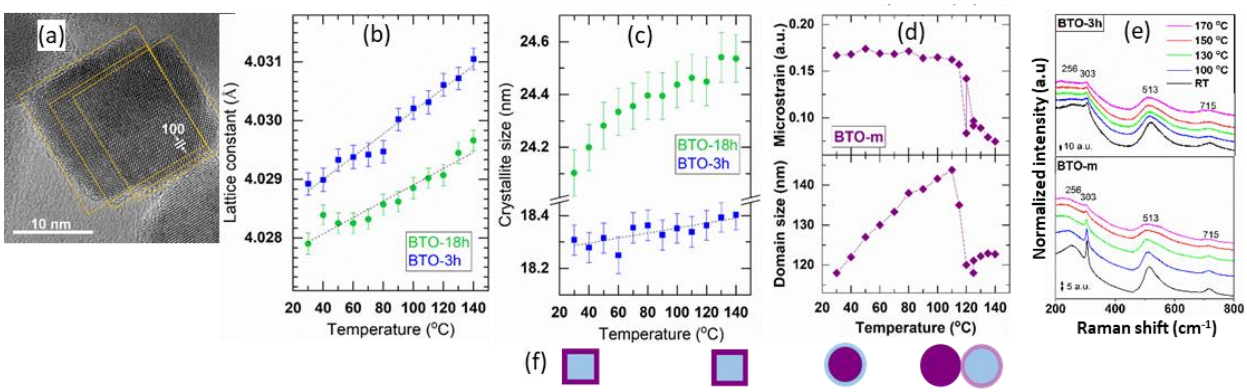


**Fig. 1** (a) TEM image of the cubic crystallites; (b) the cubic lattice constant and (c) the average crystallite size of the prepared nano-BTO powders as a function of temperature; (d) the coherence domain size and microstrain of BTO-m function of temperature; (e) Raman spectra at different temperatures; (f) sketches of the crystallites at the corresponding temperatures, blue – cubic phase, purple – tetragonal phase. Reproduced from Ref. [1].

We have studied the temperature dependent structural properties of BTO nanocubes compared with those obtained for a BTO powder with crystallite (domain) size of about 120 nm (BTO-m). The nano-BTO powders were prepared using a solvothermal method at two different reaction times: 3h (BTO-3h) and 18h (BTO-18h). The cuboid crystallite shapes of the prepared nano-BTO powders, and their sizes were assessed by TEM and XRD, and were found of about 18 nm and 24 nm for the two samples (Fig.1a). X-ray diffraction (XRD) analysis showed that the crystal lattice symmetry is apparent cubic for the nano-BTO samples at RT, with no evidence of any phase transition up to 130 °C (Fig. 1b,c), in contrast to BTO-m (Fig. 1d). Raman spectroscopy results indicated the existence of tetragonal symmetry in nano-BTO at RT, with no significant structural changes up to 170 °C (Fig. 1e). We succeeded to resolve this controversy by performing a deeper XRD analysis, that clearly revealed the presence of tetragonal deformation in nano-BTO at RT, and, surprisingly, also in BTO-m above the ferro-paraelectric transition temperature. The set of experimental results obtained in this study can be interpreted within the core-shell model both for the nano-BTO samples and for the BTO-m, and are summarized in Fig. 1f. At RT the core has a cubic structure in the first case and a tetragonal one in the second, and *vice versa* for the shell. The shell structure is deformed tetragonal for nano-BTO and deformed cubic for BTO-m, and there are clues that the deformation is due to the surface relaxation phenomenon.

Based on our experience on preparing and characterizing epitaxial PLD-deposited PZT thin films, we performed a study regarding the influence of the target purity on the structural and electrical characteristics of the epitaxial PZT thin films. We used two targets: (1) a commercial one with 99.9% (3N) purity and (2) an in-house manufactured one with 99.99% (4N) purity.

It was found that the thin films obtained from the commercial target had a larger *c* lattice parameter which was associated with a larger polarization value (Fig. 2a). The larger dielectric constant

measured in thin films obtained from pure target (Fig. 2b) was associated to a different PZT domain structure [2]. Furthermore, these samples elicited a leakage current with one order of magnitude smaller than the films derived from the commercial target (Figure 2b). These findings well-correlated with the compositional analysis which revealed that the amount of heterovalent impurities was two times larger in the commercial target [2].

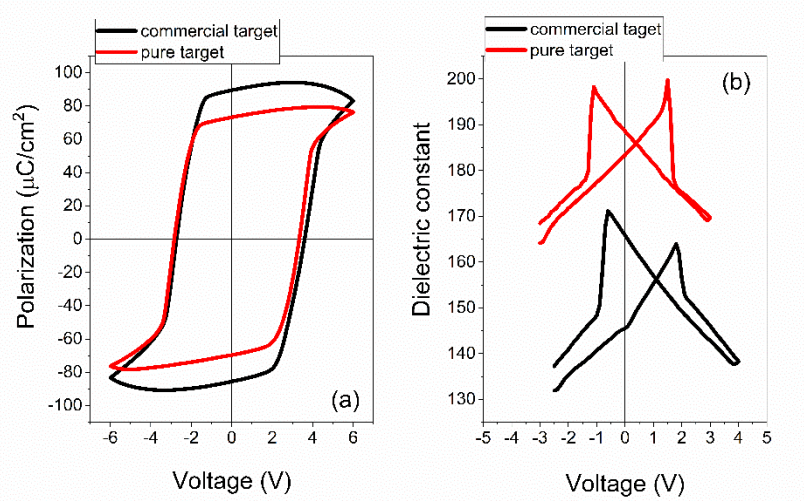


**Fig. 2** The electrical characterization of the epitaxial thin films obtained from the commercial (3N) and in-house manufactured (4N) targets: (a) polarization-voltage hysteresis loops recorded at room temperature, at 1 kHz frequency; (b) the dielectric constant-voltage characteristics obtained from capacitance measurements at 100 kHz with 0.2 V a.c. signal. Reproduced from Ref. [2].

In a subsequent study [3] the relation between the polarization switching and the structural quality, and also the impact on the negative capacitance effect was surveyed. In addition to the previous two thin films structure, two polycrystalline thin films were used: PZT deposited by sol-gel on single crystal STO and Si substrates. The value of the polarization and the leakage current decreased when the structure changed from epitaxial to polycrystalline (Fig. 2a and Fig. 3a,b). Also, the differential negative capacitance decreased (Fig. 4) and the switching changed from homogeneous to inhomogeneous [3]. These results are linked with a faster compensation of the depolarization field during switching in epitaxial thin films compared with polycrystalline thin films.

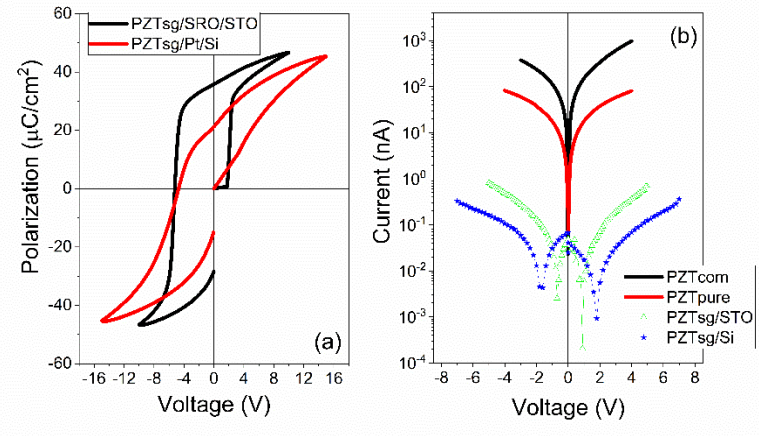


**Fig. 3** (a) Polarization-voltage hysteresis loops recorded at RT, at 1 kHz frequency for polycrystalline thin films deposited by sol-gel on STO and Si substrates; (b) The comparison of the leakage current characteristics for thin films with different structural quality. Reproduced from Ref. [3].

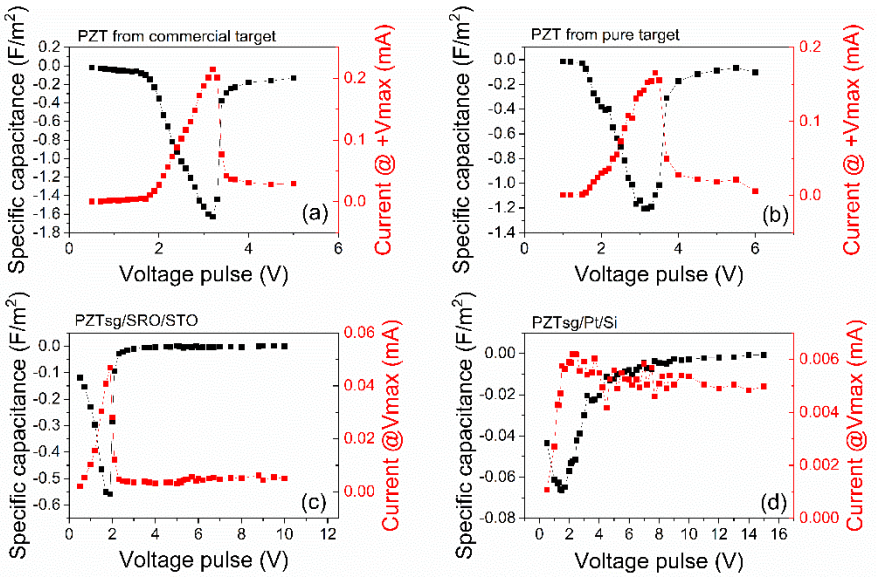


**Fig. 4** The representation of the minimum of the specific capacitance and the values of the maximum current values for different amplitudes of the voltage pulse for epitaxial PZT deposited from: (a) commercial (3N) and (b) in-house manufactured (4N) targets and for polycrystalline thin films deposited on (c) STO and (d) Si substrates. Reproduced from Ref. [3].

*References*


1. I. Pasuk et al., "Structural details of $BaTiO_3$ nano-Powders deduced from the anisotropic XRD peak broadening," Nanomaterials 11(5),1121 (2021).
2. G.A. Boni et al., "Accidental impurities in epitaxial Pb $(Zr_{0.2}Ti_{0.8})O_3$ thin films grown by pulsed laser deposition and their impact on the macroscopic electric properties," Nanomaterials 11(5), 1177 (2021).
3. L. Pintilie et al., "Homogeneous versus inhomogeneous polarization switching in PZT thin films: Impact of the structural quality and correlation to the negative capacitance effect," Nanomaterials 11(8), 2124 (2021).

# Tetragonal-cubic phase transition and low-field dielectric properties of $CH_3NH_3PbI_3$ crystals

**R. E. Patru[a], H. Khassaf[b], I. Pasuk[a], M. Botea[a], L. Trupina[a], C. P. Ganea[a], L. Pintilie[a], I. Pintilie[a]**

[a] National Institute of Materials Physics, 405A Atomistilor Street, Magurele, Romania, 077125

[b] Department of Materials Science and Engineering and Institute of Materials Science, 97 North Eagleville Road University of Connecticut, Storrs, USA, CT 06269-3136

This work was triggered by the currently large efforts for development of clean energy production and for improving the performance of photovoltaic devices based on metalorganic lead-halide perovskite materials, a promising class of materials for fabricating potentially low-cost new type of solar cells, known as perovskite solar cells (PSC), with power conversion efficiencies (PCE) exceeding 25% [1]. Despite the tremendous rapid enhance in the performance of PSCs, there are still issues to be understood for being under control, *e.g.*, how the electrostrictive strain between the perovskite grains impacts their stability/degradation under illumination, the presence of bulk ferroelectricity at room temperature – a property that could explain why these materials are so efficient in converting the light into electricity or the measurement procedures which may strongly impact evaluating the true PCE [2,3]. Accordingly, in order to understand the electrical behavior of hybrid perovskite crystals and establish the connection with the nature of the migrating species, the focus of our study was on the structural, electrical, ferroelectric, dielectric and relaxation properties of $CH_3NH_3PbI_3$ (MAPI) crystals in the temperature range of interest for PSCs, of -30 ÷ +110 °C. MAPI single crystals of 5 mm size were synthesized using inverse temperature crystallization [5]. The structure was analyzed by *in-situ* X-ray diffraction (XRD) between 30 °C and 110 °C on a powder sample. The evolution with temperature of the lattice constants, crystallite sizes and the microstrain was estimated by fitting the diffraction patterns according to the Pawley approach. The resulted temperature dependences are given in Fig. 1a-c. To make easier the comparison between the parameters of tetragonal ($a_t$, $c_t$) and cubic MAPI structure ($a_c$), in Fig. 1a are represented $a_t'=a_t/\sqrt{2}$, $c_t'=c_t/2$ and $\sqrt[3]{V_t'}$ defined by $a_c'=\sqrt[3]{V_t'}$. As the temperature increases, $a_t'$ increases and $c_t'$ decreases, until they approach values that are similar with $a_c$, at approx. 60 °C. Above this temperature $a_t'$ and $c_t'$ are slowly approaching, but do not exactly become equal even at 70 °C. Fig. 1b and 1c show that both the crystallites of the tetragonal MAPI and the lattice disorder slightly decrease upon heating. This shrinking process stops between 55 – 60 °C. Heating further up to 70 °C, the crystallites remain small, but the crystalline ordering rapidly improves. Above 70 °C the size of cubic phase crystallites increases monotonously with temperature, with the symoultaneous improvement of the atomic ordering.

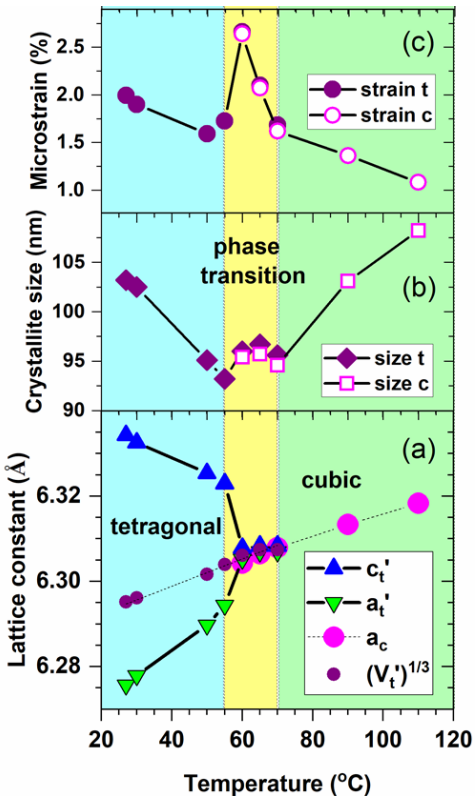


**Fig. 1** Evolution of the structure parameters: (a) lattice constants; (b) crystallite size; (c) microstrain.

These XRD investigations show that the tetragonal-cubic transformation takes place gradually, starting sharply between 55 – 60 °C and being completed at approx. 70 °C. Piezoelectric force microscopy (PFM) studies performed on a MAPI crystal show a strong and clear contrast in the piezoelectric phase images indicating the presence of ferroelectric domains at the surface of the crystals [5]. Impedance spectroscopy measurements in the -30 ÷ +110 °C temperature range, using an AC voltage of 0.1 V and sweeping the frequency from $10^{-2}$ to $10^{7}$ Hz were performed and analyzed in detail with respect to dielectric and relaxation properties of the MAPI crystals. The real part of the dielectric permittivity (ε'), given as a 3D representation in Fig. 2, indicates a dispersive dielectric polarization. The dielectric function exhibits a strongly diffusive character over the whole 10 mHz to 1 MHz frequency range, from where the frequency dispersive relaxation phenomena originate with distinct time constants, each having its own influence on the thermally activated conduction mechanisms. We found two relaxation phenomena that dominantly act in the medium and low frequency regions, producing a cumulative effect in the a.c. conductivity - $\sigma_{ac}(\nu, T)$. They were disjointed by analyzing the complex dielectric function combined with the dielectric modulus approach. In $\sigma_{ac}(\nu)$ , the relaxation phenomena are characterized by energy barriers of ~0.43 eV at low temperatures and 0.48 eV at higher temperatures, approaching the theoretical DFT calculations for interstitial $MA^+$ ions [8]. From $\sigma_{dc}(T)$, activation energies of ~0.85 eV at low temperatures and ~0.62 eV at higher temperatures were determined. In consistence with DFT calculations [6] and experiments [7], the main contributor to the long-range ionic conduction, in this case, are the $MA^-$ vacancies.

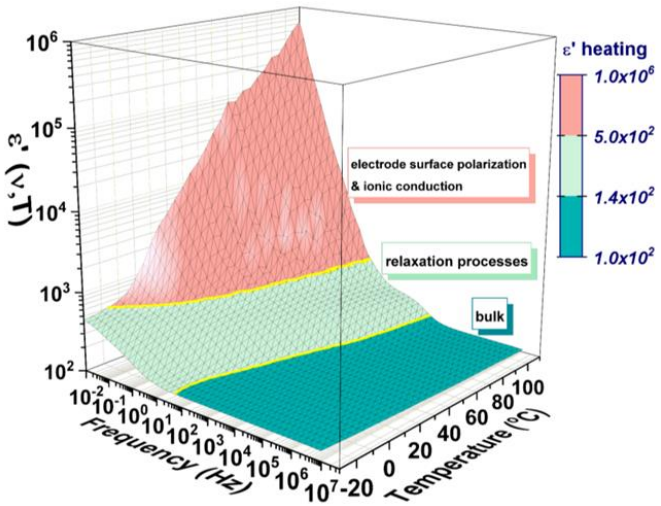


**Fig. 2** The real part of dielectric permittivity represented as a function of frequency and temperature at heating.

The contribution of the iodine ions to the diffusion processes in MAPI crystal was determined by developing an equivalent circuit model, fully describing the experimental data in the whole range of explored temperatures (-30 ÷ +110 °C) and frequencies ($10^{-2}$ ÷ $10^{7}$ Hz) – see Fig. 3. The main regimes of ionic transport in the MAPI crystal were determined by analyzing the impedance spectra and dissociating between the frequency and temperature dependent signals coming from the bulk of crystal, boundaries and interfaces, each contributing to the overall conductivity. The activation energies extracted from Arrhenius plots of the equivalent circuit time constants are found to be in consistence with the lately DFT calculations and previous experiments [6–9]. This way, we conclude that the interstitial $MA^+$ ions, together with their vacancies, produce thermally activated relaxation phenomena related to the grains and interfaces. The polarized vacancies are the main species liable to accumulate at the grain boundaries and interfaces involving distinctive thermally activated relaxation phenomena at long time scales and conduction mechanisms. At the grain boundaries, the prevailing response comes from the $MA^+$ and associated polarized vacancies, even masking the iodine ions contribution in the $\sigma_{dc}(T)$. However, by analyzing the temperature dependence of the equivalent circuit time constant ascribed to the diffusion process at the interfaces, the imprint of the iodine ions was recognized based on its energy barrier of 0.28 eV. The presented results provide insights on the correlation between the properties of the crystal and the interfacial dynamics. The increase of the intrinsic bulk ionic conductivity upon increasing of temperature and the accumulation of mobile ions at interfaces happen in the absence of light, due only to the application of an external small a.c. electric field.

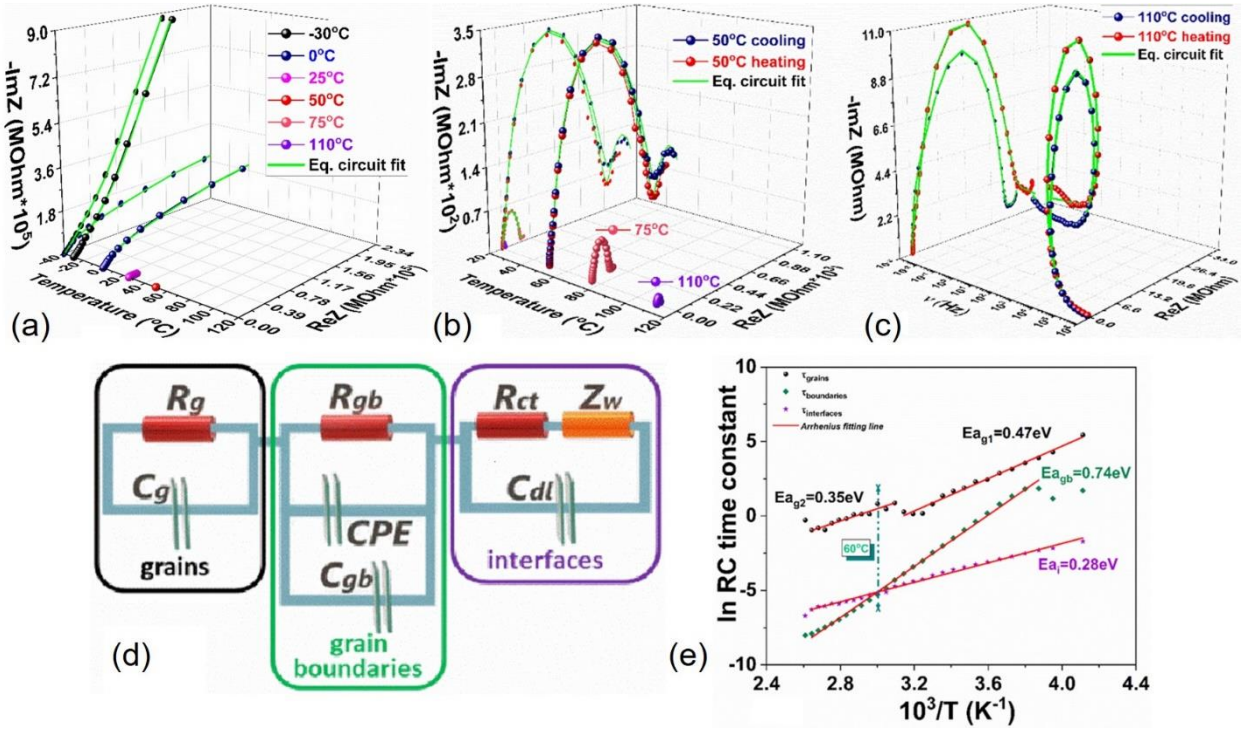


**Fig. 3** (a) Nyquist spectra for temperatures in the range of -30 ÷ +110 °C together with (b) zoom for higher temperatures, and (c) zoom for 110 °C for both paths of heating and cooling; (d) The equivalent circuit used for fitting the Nyquist spectra; (e) Activation energies of the time constant related to grain, grains boundary and interfaces.

*References*


1. https://www.nrel.gov/pv/cell-efficiency.html; accessed 19 January 2022.
2. B. Chen et al., "Large electrostrictive response in lead halide perovskites," Nat. Mater. 17(11), 1020–1026 (2018)
3. G. A. Nemnes et al., "How measurement protocols influence the dynamic J-V characteristics of perovskite solar cells: theory and experiment," Sol. Energy 173, 976–983 (2018)
4. R. E. Patru et al., "Tetragonal–cubic phase transition and low-field dielectric properties of $CH_3NH_3PbI_3$ crystals," Materials 14, 4215 (2021).
5. D. Yang et al., "Fast diffusion of native defects and impurities in perovskite solar cell material $CH_3NH_3PbI_3$," Chem. Mater. 28, 4349–4357 (2016)
6. O. Almora et al., "Ion-mediated hopping electrode polarization model for impedance spectra of $CH_3NH_3PbI_3$," J. Appl. Phys. 128, 075104 (2020).
7. S. Meloni et al.; "Ionic polarization induced current-voltage hysteresis in $CH_3NH_3PbX_3$ perovskite solar cells," Nat. Commun. 7, 10334 (2016).
8. M. H. Futscher et al., "Quantification of ion migration in $CH_3NH_3PbI_3$ perovskite solar cells by transient capacitance measurements," Mater. Horizons 6, 1497–1503 (2019).

# A versatile instrument to address both linear optical properties and Faraday rotation of glasses

**A. C. Galca,[a,*] M. C. Dinca,[b] G. E. Stan,[a] L. Boroica,[b] M. Elisa,[c] V. Kuncser,[a] B. A. Sava,[b]**

[a] National Institute of Materials Physics, 405A Atomistilor Street, Magurele, Romania, 077125

[b]National Institute for Laser, Plasma and Radiation Physics, 409 Atomistilor, Magurele, Romania, 077125

[c]National Institute of Research & Development for Optoelectronics INOE 2000, 409 Atomistilor, Magurele, Romania, 077125

*corresponding author https://infim.ro/@galca/

In a recent paper [1], undoped and co-doped with terbium ($Tb^{3+}$) and dysprosium ($Dy^{3+}$) borophosphate glasses oxides were studied for possible magneto-optical applications. One technique used to characterize the bulk glasses was spectroscopic ellipsometry, known for its versatility and accuracy. A Woollam Vertical Variable Angle Spectroscopic Ellipsometer (V-VASE) was used to perform the experiments.

The dispersions of the refractive index shown in Fig. 1a were inferred by fitting the spectroscopic ellipsometry data in reflection mode (angles of incidence 50° and 60°) using a Cauchy dispersion as optical model. Processing of samples is a prerequisite to suppress the backside reflections which are incoherent with the desired reflection from the front side [2]. Roughening the back surface or using index matching semi-solid materials (tapes) are regarded as the best solutions. Note that the front side should be optically polished, otherwise the optical model which should have an effective medium approximation of the rough layer, while it is not always giving the best results.

Glasses refractive index in the transparency region is directly proportional to mass density, Fig. 1b, as well as to the corresponding electronic density of the materials [3]. In other words, the electric polarization which defines the presented refractive index, is greater in a material having a higher density of electrons. Thus, doping with heavier rare earth (RE) ions increases the electronic density in direct relation to the amount of the doping lanthanides.

The correctness of the refractive index evaluation can be therefore easily checked by verifying the linear relationship with respect to the mass density. This interdependence is also used to qualitatively analyze the densities of thin films, and further to predict the composition of deposited materials [3].

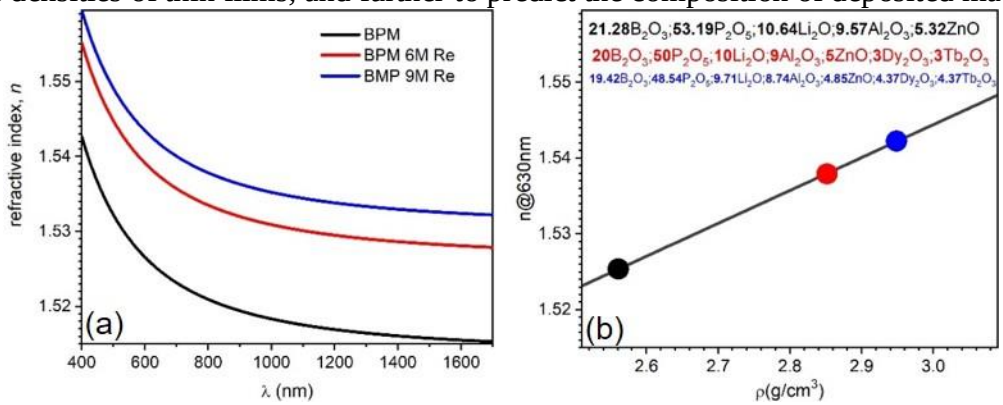


**Fig. 1** (a) Refractive index dispersion of borophosphate glasses with different RE doping and (b) refractive index vs. mass density. Adapted from Ref. [1].

Same equipment was used to measure the Faraday rotation (Fig. 2a) and the conventional transmission measurements [1]. The transmission ellipsometry measurements were performed without and with the aid of a toroidal permanent magnet, the magnetic field being applied parallel to the light beam. By a simple subtraction using the 2 measured ellipsometric parameter Ψ (inset Fig. 2a), the Faraday rotation can be easily determined [4], while applying a simple equation, the Verdet constant (Fig. 2b) can be also calculated. Note the extremely low experimental error of ~ 0.01° in the determination of Ψ.

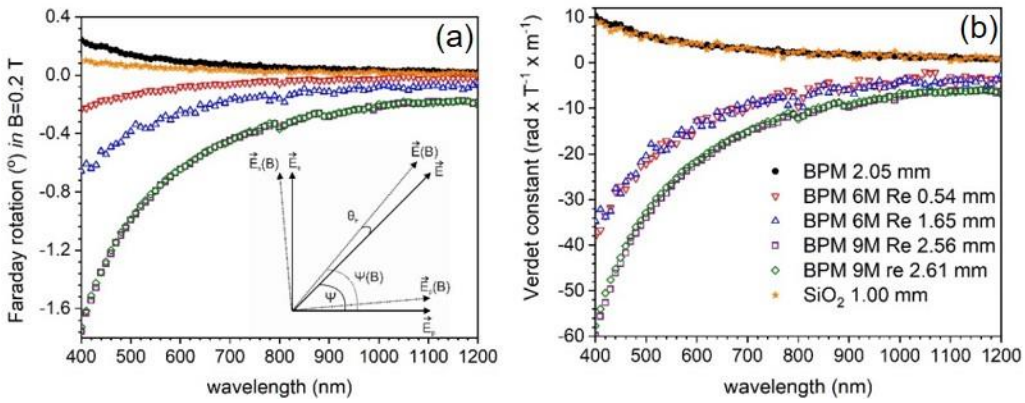


**Fig. 2** Magneto-optical results: (a) Faraday rotation (inset: principle of measurement [4]) and (b) Verdet constant. Adapted from Ref. [1].

The Verdet constants (positive for diamagnetic materials and negative for paramagnetic ones) can be assumed as proportional to the magnetic susceptibilities [4]. Thus, the Verdet constant of glasses co-doped with RE ions consists also of a superposition of the diamagnetic and paramagnetic contributions. The conformity of the deduced Verdet constant can be done by measuring glasses with different thicknesses, while the assessment of paramagnetic contribution which is relatively linear to the rare earth concentration [4,5] can be used to state on the homogeneity (distribution of RE in the diamagnetic host).

Designing magneto-optical materials (glasses) should be done also by considering other factors such as solubility limits of RE ions in the diamagnetic matrix and glass transition temperature, since RE tends to depolymerize the glassy network.

*References*


1. M. C. Dinca et al., "Magneto-optical properties of borophosphate glasses co-doped with $Tb^{3+}$ and $Dy^{3+}$ ions", *J. Non-Cryst. Solids* 568 (6), 120967 (2021).
2. R. A. Synowiki, "Suppresion of backside reflections from transparent substrates", Phys. Status Solidi (C) Curr. Top. Solid State Phys. 5 (5), 1085–1088 (2008).
3. T. Tite et al., "Phosphate bioglass thin-films: Cross-area uniformity, structure and biological performance tailored by the simple modification of magnetron sputtering gas pressure", Appl. Surf. Sci. 541, 148640 (2021).
4. M. Valeanu et al., "The relationship between magnetism and magneto-optical effects in rare earth doped aluminophosphate glasses", J. Phys. D Appl. Phys. 49 (7), 075001 (2016).
5. G. Gao et al., "Faraday rotation and photoluminescence in heavily $Tb^{3+}$-doped $GeO_2$-$B_2O_3$-$Al_2O_3$-$Ga_2O_3$ glasses for fiber-integrated magneto-optics", Sci. Rep. 5, 8942 (2015).

# Structural, functional properties and enhanced thermal stability of bulk graded (Ba,Sr)$TiO_3$ structures obtained by spark plasma sintering

**M. Botea,[a] I. Pintilie,[a] V. A. Surdu,[b] C. A. Stanciu,[b] R. D. Truşcă,[b] B. S. Vasile,[b] R. Patru,[a] M. Udrea,[c] A. C. Ianculescu,[b,*] L. Pintilie [a,*]**

[a]National Institute of Materials Physics, 405A Atomistilor Street, Magurele, Ilfov, 077125, Romania

[b]Department of Oxide Materials Science & Engineering, Faculty of Applied Chemistry and Materials Science, "Politehnica" University of Bucharest, 1–7 Gh. Polizu Street, Bucharest, 011061, Romania

[c] Apel Laser SRL, 15 Vintila Mihailescu Street, Bucharest, Romania

Many of the properties of ferroelectric materials can be conveniently changed by doping or by the use of compositional gradients, in order to improve or obtain new functionalities [1,2]. Graded structures can be obtained by successively depositing films with different compositions of Zr/Ti or Ba/Sr ratios into Pb(Zr,Ti)$O_3$ (PZT) or (Ba,Sr)$TiO_3$ (BST) films [3,4]. Some applications, such as energy and power measurements of laser beams, require a thick ceramic layer as the active pyroelectric element. An important aspect in the case of pyroelectric detectors is that of the thermal stability of the generated signal, which implies the stabilities of the dielectric constant and pyroelectric coefficient. Structures with a composition gradient are used for this purpose, since the temperature variation of the two parameters will not manifest itself due to the difference in phase transition in the layers. Our study focused on symmetrical and asymmetrical bulk ceramics, based on solid solutions of BST, in which the concentration gradient was preserved by a new method of preparation, which involves cold pressing of the successive layers with different Sr content derived from sol-gel $Ba_{1-x}Sr_xTiO_3$ nanopowders (x=0.10, 0.20 and 0.30) followed by spark plasma co-sintering (SPS).

The phase composition and crystal structure of BST sol-gel powders were investigated by X-ray diffraction (XRD) and the particle morphology was analysed by transmission electron microscopy (TEM). The microstructure and graded composition of the BST ceramics were investigated by field emission gun scanning electron microscopy (FE-SEM) coupled with energy-dispersive X-ray spectroscopy (EDX). To evaluate the purity of perovskite phases and the structural parameters of BST graded ceramics, micro-X-ray diffraction (μXRD) was used.

It was shown that the BST powder contained nanometre-sized particles, uniform in shape and size, with a tendency to cluster especially when the Sr content increases. For all structures, the presence of a single perovskite phase was observed in all analysed regions, with an obvious shift of the main reflection corresponding to the crystalline plane (110) to higher angular values with increasing Sr content, which further endorse the compositional gradient. As the number of layers increased, the densification in the symmetrical samples increased and a microstructural gradient appeared, by changing the size of the grains.

Electrical and pyroelectric measurements were performed by function of temperature (Fig. 1a,b). The dielectric constant ($\varepsilon_r$) was extracted from the capacity measured at 1 kHz during cooling and heating between –245 and +200 °C. The value of the dielectric constant decreased with increasing number of component layers, contrary to what was reported in previous studies on multilayer structures [5]. This is most likely owned to the diffusion of Ba/Sr species at interfaces or the variation of crystalline grain size and of the c/a ratio in the graded structures. The temperature dependence of $\varepsilon_r$ became less pronounced as the number of layers increased. For the 6-layer symmetrical sample, BST3, the variation of $\varepsilon_r$ in the range 0 – 100 °C was only 8%, thus indicating a remarkable thermal stability. The value of the pyroelectric coefficient estimated from pyroelectric current measurements was around $10^{-6}$ C/m$^2$K, lower compared to other studies performed on ungraded BST ceramics [6]. This is likely due to the appearance of a polarization gradient resulting from structural change. Component layers with different Sr content had successive phase transitions during heating, which lead to changes in the crystal structure. Internal electric fields appeared, which locally affected the value and orientation of the ferroelectric polarization, resulting in changes in both the size and the sign of the pyroelectric coefficient. The temperature dependence of the pyroelectric coefficient is reduced

between 0 °C and 80 °C to less than 6%, around $3 \cdot 10^{-7}$ C/m$^2$K, a result comparable to previous studies on thin film graded structures [7].

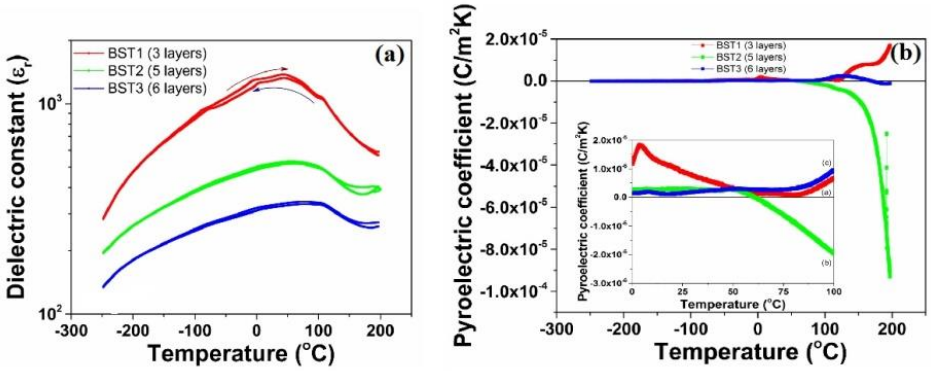


**Fig. 1** The temperature dependence of the (a) dielectric constant and (b) pyroelectric coefficient for the graded BST1, BST2 and BST3 samples.

Pyroelectric measurements were performed at room-temperature (RT), in voltage mode, on different concentration gradient configurations: parallel and perpendicular to the electrodes. A laser diode with a wavelength of 800 nm and an optical power of 25 mW was used as the radiation source. Heating the sample evenly is only possible at low modulation frequencies of the IR beam, when the pyroelectric signal does not depend on the frequency [6]. At high frequencies, because the heating is non-uniform and the sample sizes are different, it was necessary to normalize the signal to the thickness of the sample in Fig. 2a,b.

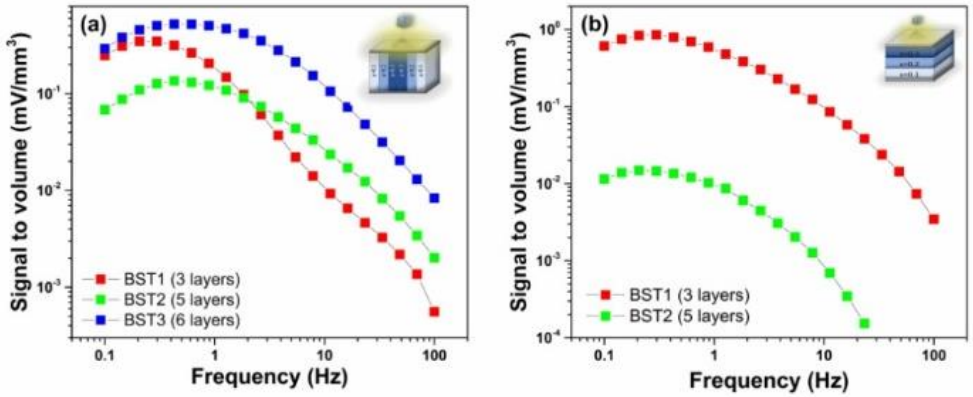


**Fig. 2** The frequency dependence of the pyroelectric signal measured at RT on samples with concentration gradient: (a) parallel to the electrodes – BST1, BST2, BST3; (b) perpendicular to the electrodes – BST1, BST2.

For a concentration gradient parallel to the electrodes, all layers contributed to the generation of the total pyroelectric signal, the symmetric 6-layer sample, BST3, having the best result. If the concentration gradient is perpendicular to the electrodes, the pyroelectric coefficient differed depending on the Sr concentration of the layer exposed to IR radiation. The largest pyroelectric signal was obtained on the 3-layer asymmetric sample when it was exposed to the Sr 30% layer in the incident radiation. The comparison of the volume-normalized pyroelectric signal between the two types of configurations showed that the asymmetric sample with the gradient perpendicular to the electrodes (BST1), has a twofold higher signal compared to BST3. The latter had a gradient parallel to the electrodes and the signal decreased faster with frequency, which can be beneficial for applications where large temperature ranges are required. The pyroelectric signal decreased as the sample temperature increased and was recovered when it is cooled to RT (see Fig. 3), behaviour which was assigned to internal electrical fields that occur when the component layers have phase transitions that lead to changes in lattice parameters, strain, dielectric constant and polarization.

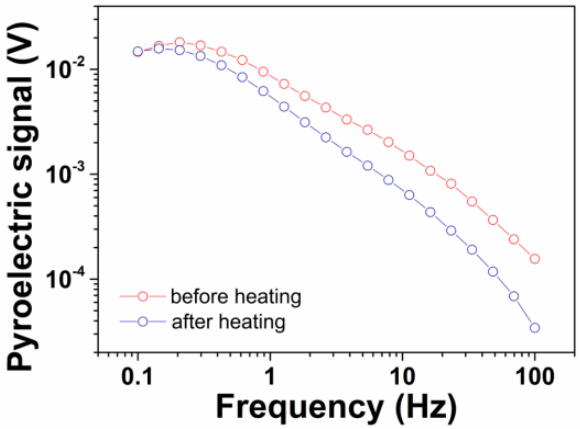


**Fig. 3** The frequency dependence of the pyroelectric signal for asymmetric sample BST1 (3 layers) before and after heating to 80 °C and subsequent cooling to RT.

The low temperature dependence of both the dielectric constant and the pyroelectric coefficient is an important property for applications that require a constant response over a wide range of operating temperatures.

*References*


1. L. Pintilie, I. Pintilie, "Ferroelectrics: new wide-gap materials for UV detection," Mater. Sci. Eng. B 80, 388–391 (2001).
2. B. Misirlioglu, S. P. Alpay, "Compositionally graded ferroelectrics as wide band gap semiconductors: Electrical domain structures and the origin of low dielectric loss," Acta Mater. 122, 266–276 (2017)
3. X. Tang et al., "Dielectric and pyroelectric properties of compositionally graded $Pb(Zr_{1-x}Ti_x)O_3$ thin films prepared by sol-gel process", Chin. J. Chem. Phys. 20, 665 (2007).
4. V. N. Shut et al., "Compositionally graded ceramics based on $Ba_{1-x}Sr_xTiO_3$ solid solutions," Inorg. Mater. 47 87–92, (2011).
5. L. Pintilie et al., "Capacitance tuning in antiferroelectric–ferroelectric $PbZrO_3$–$Pb(Zr_{0.8}Ti_{0.2})O_3$ epitaxial multilayers," New J. Phys. 10 013003 (2008).
6. A. Ianculescu et al., "Intrinsic pyroelectric properties of thick, coarse grained $Ba_{1-x}Sr_xTiO_3$ ceramics," Ceram. Int. 42 10338–10348, (2016).
7. H. He et al., "Advances in lead-free pyroelectric materials: a comprehensive review," J. Mater. Chem. C 8, 1494–1516 (2020).

# Tuning of the morphology, structure and biological response of sputtered phosphate bio-glass films by the working gas pressure

**T. Tite,[a] A.C. Popa,[a,b] I.M. Chirica,[a] B.W. Stuart,[c] A.C. Galca,[a] L.M. Balescu,[a] G. Popescu-Pelin,[d] D.M. Grant,[c] J.M.F. Ferreira,[e] G.E. Stan[a,*]**

[a] National Institute of Materials Physics, Magurele, RO-077125, Romania
[b] Army Centre for Medical Research, Bucharest, RO-010195, Romania
[c] Advanced Materials Research Group, Faculty of Engineering, University of Nottingham, NG7 2RD, UK
[d] National Institute for Lasers, Plasma and Radiation Physics, Magurele, RO-077125, Romania
[e] Department of Materials and Ceramics Engineering, CICECO, University of Aveiro, 3810-193 Aveiro, Portugal

The coating of metallic implants with biofunctional (*e.g.*, controlled release of therapeutic ions, match of biomaterial degradation – bone growth rates, antimicrobial efficiency) layers represents a highly promising solution for orthopedics and dentistry. As third-generation biomaterials, phosphate bioactive glasses (PBGs) are capable to stimulate specific biological responses at molecular level, successfully accomplishing the coupling of the bioactive and resorbable material designs [1]. Surprisingly, little attention has been payed to date to the application of PBGs as implant-coatings. Of paramount importance is the discovery of new paths to tune the morphology, physical-chemical properties and biodegradability of PBG coatings for obtaining specific biological responses. Having these challenges in mind, PBG films have been synthesized by radio-frequency magnetron sputtering (RF-MS) at different argon working pressure (0.2–1 Pa). The target was constituted of a PBG powder with a 50–$P_2O_5$, 35–CaO, 10–$Na_2O$ and 5–$Fe_2O_3$ composition (mol%). The PBG films were deposited onto silicon (Si) wafers with a diameter of 3-inches. The engineered modification of physical-chemical and biological features of the films was multi-parametrically surveyed by atomic force microscopy (AFM), energy-dispersive X-ray spectroscopy (EDXS), spectroscopic ellipsometry (SE), grazing incidence X-ray diffraction (GIXRD), Fourier transform infrared (FTIR) spectroscopy measurements and *in-vitro* degradation and cytocompatibility assays.
The performed researches showed that the morphology, composition, and structural properties of the PBG films can be modified by simply tuning the working pressure in the deposition chamber (Fig. 1).

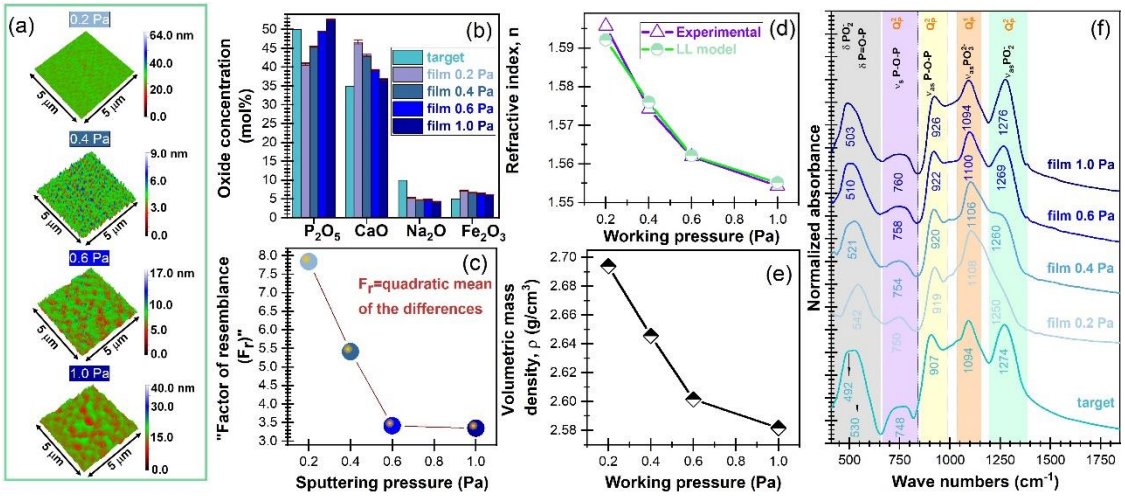


**Fig. 1** (a) 3D AFM micrographs; (b) compositional variation; (c) evolution of the "$F_r$" for each PBG film with respect to the target; (d) experimental and simulated refractive indexes; (e) evolution of the volumetric mass density; and (f) FTIR spectra of PBG films at different argon working pressures. Reproduced from Ref. [2].

The AFM analyses revealed the presence of pits on the surface of the all PBG samples, whose diameter and height enlarged with the argon pressure ($P_{Ar}$), leading thereby to an increase of the surface porosity (Fig. 1a). The diameter and height of the pits were on the average of ~200 nm and ~3 nm at 0.2 Pa, respectively, and were of ~690 nm and 9 nm at 1.0 Pa. The EDXS results (Fig. 1b) revealed a progressive augmentation of the $P_2O_5$ content at the expense of CaO concentration with the increase of $P_{Ar}$. The best compositional target-to-substrate transfer, as also indicated by the "resemblance factor" ($F_r$) (Fig. 1c), was obtained at 0.6 and 1.0 Pa. SE and FTIR techniques are important tools, capable to unveil structural

modification insights. SE analysis showed a decrease of the refractive index (RI) by increasing $P_{Ar}$, with a value of ~1.596, 1.574, 1.562 and 1.554 for films deposited at 0.2, 0.4, 0.6 and 1 Pa, respectively (Fig. 1d). The results were found in excellent agreement with the Lorentz-Lorentz (LL) prediction without introducing any adjustable parameters. Concomitantly, derived from the LL model, it was found that the volumetric mass density of PBG films was decreasing with $P_{Ar}$ (Fig. 1e). FTIR analysis has evidenced a notable increase of the glass network connectivity (NC), as indicated by the intensity augmentation of the band associated to the $\nu_{as}$ vibration modes of bonds in $Q_P^2$ units at ~919−926 $cm^{-1}$and ~1250−1276 $cm^{-1}$ (Fig. 1f) [2]. It has to be mentioned that the glass NC is a crucial parameter for PBGs, as it governs the fate of the degradability and overall biological performance [2].

The aforementioned results were inferred to measurements taken at the center of the PBG samples. However, the large area of the substrate used (3 inches) has allowed us to investigate the cross-area uniformity of deposited films, generally overlooked in the literature. In this prospect, SE, EDXS, and FTIR spectroscopy measurements were carried out at consecutive positions along the samples' diameter, at a step of ~2 mm. Our results have indicated the thickness (Fig. 2), composition, refractive indexes, density and structural features are preserved (irrespective of $P_{Ar}$) for a diameter between 14 to 20 mm [2]. The ability to produce coating layers with large-area uniformity, *i.e.* taking into consideration the geometrical constraints of dental implants, will positively influence the chances for a successful transfer of technology to industrial level.

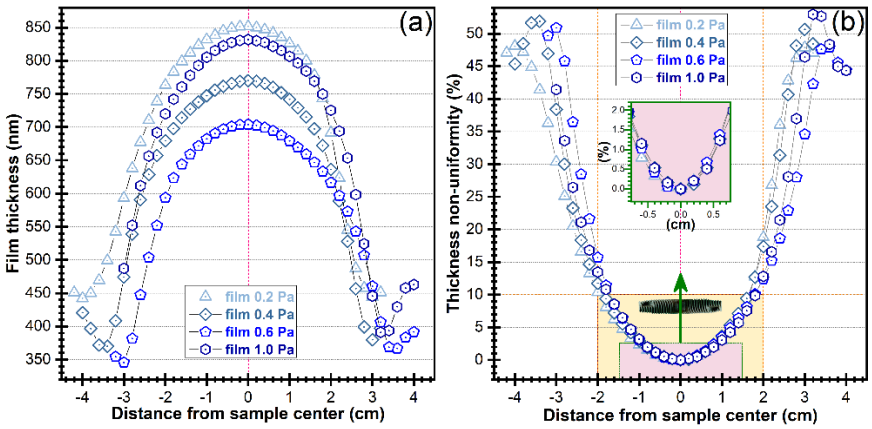


**Fig. 2** (a) The thickness evolution of PBG films deposited at different working pressures with the distance from centre. (b) Percentage decrease of film thickness starting from the center of maximum uniformity. Reproduced from Ref. [2].

The design of resorbable implant coatings is of paramount importance in biomedical research and point of care application. A degradable coating is envisioned to gradually disappear in a body after its mission would have been fulfilled (*e.g.*, for bone regeneration, drug delivery and sensing). Thereby, degradation assays were performed for PBG films selected within the high uniformity region. These tests were carried out under high biomimicry *in-vitro* conditions that best reproduce the microenvironment found in the intercellular fluid [2]. The mass/thickness loss was assessed, before and after immersion of the PBG films in DMEM+10% fetal bovine serum fluid for periods of time of 1, 2, 4, 8, 12, 24 and 48 h, either by FTIR spectroscopy (by calculating the integral area evolution of the $\nu_{as}$ convoluted prominent band) or by SE (on the basis of the thickness evolution). Fig. 3a displays the relative film loss (in percentages) deduced by FTIR analyses prior and after *in-vitro* testing. After 48 h of incubation, a film loss of ~60%, 100%, 80% and 100% was evidenced for the films synthetized at 0.2, 0.4, 0.6 and 1.0 Pa, respectively. It is suggested that the degradation of the PBG sputtered coatings is influenced by two antagonistic factors: (*i*) the network connectivity of the phosphate glass and (*ii*) the degree of surface porosity of the films [2].

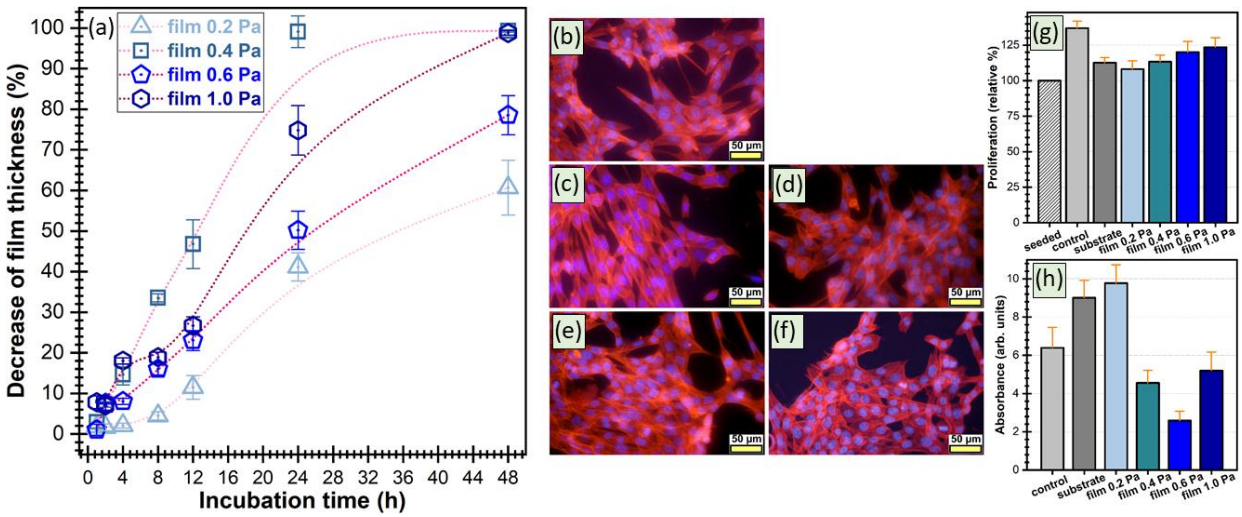


**Fig. 3 (a)** Evolution of PBG films loss with immersion time; (b–f) Epi-fluorescence microscopy images emphasizing the morphology of the Hs27 fibroblast cells grown onto: (a) bare and (b–e) coated Si substrates with (b) 0.2 Pa, (c) 0.4 Pa, (d) 0.6 Pa, and (e) 1.0 Pa type films. Bar-charts displaying the (f) cell proliferation (MTS assays) and (g) cytotoxicity results after 24 h of culturing (LDH assays). Reproduced from Ref. [2].

Cytocompatibility was assessed *in-vitro* at 24 h using human fibroblasts (Hs27) by investigating their morphology by epi-fluorescence microscopy (Fig. 3b–f) when grown on PBG films. The results indicated that the cells were well-spread and had normal fusiform polygonal fibroblast-type morphology (cell cytoskeleton red labelled with phalloidin-AlexaFluor546 fluorochrome). Furthermore, the nuclei (blue labelled with DAPI) had normal shapes and sizes, without apoptotic chromatin condensations. *In-vitro* cytocompatibility assays (Fig. 3g,h) have shown that all PBG films were biocompatible, with slightly increased biological performance in the case of 0.6 Pa and 1.0 Pa sputtered films.

A path towards the engineering of PBG sputtered films properties is suggested, which, in turn, can enable the fine tuning of the *in-situ* degradation and release speed of the therapeutic ions. The reported results might serve as a useful benchmark for developing phosphate bio-glass materials with controlled properties and tunable biodegradability.

*References*

1. D. S. Brauer, "Phosphate glasses", in Bio-Glasses: An Introduction, pp. 45–64 John Wiley & Sons, Ltd, Chichester, UK (2012).
2. T. Tite et al., "Phosphate bioglass thin-films: Cross-area uniformity, structure and biological performance tailored by the simple modification of magnetron sputtering gas pressure," Appl. Surf. Sci. 541, 148640 (2021).

# A unitary study on the physico-chemical properties and exploratory real-time cell analysis of hydroxyapatite nanopowders substituted with Ce, Mg, Sr and Zn (0.5–5 at.%)

**I.M. Chirica,[a,b] A.M. Enciu,[c,d] T. Tite,[a,*] M. Dudau,[c,d] L.Albulescu,[c] S.L. Iconaru,[a] D. Predoi,[a] I. Pasuk,[a] M. Enculescu,[a] C. Radu,[a,b] C.G. Mihalcea,[a,b] A.C. Popa,[a] N. Rusu,[e] S. Nita,[e] C. Tanase,[c,f,*] G.E. Stan[a,*]**

[a]National Institute of Materials Physics, RO-077125 Magurele, Romania
[b]Faculty of Physics, University of Bucharest, RO-077125 Magurele, Romania
[c]"Victor Babes" National Institute of Pathology, RO-050096 Bucharest, Romania
[d]Department of Cellular Biology and Histology, "Carol Davila" University of Medicine and Pharmacy, RO-050047 Bucharest, Romania
[e] National Institute for Chemical Pharmaceutical Research and Development, RO-031299 Bucharest, Romania
[f]"Nicolae Cajal" Institute, "Titu Maiorescu" University, RO-004051 Bucharest, Romania

Currently, one prominent healthcare research domain focuses on bioceramics for the regeneration [1] of hard connective tissues (*e.g.*, bone and teeth), with emphasis on the design of innovative and highly efficient bone graft substitutes and biofunctionalization solutions for endosseous and dental implants. The production of cation-substituted hydroxyapatite (SHA) has recently attracted a significant interest since such bioceramics are able to mimic the composition of the bone and teeth mineral component and yield superior mechanical performance and biological responses with respect to pure stoichiometric HA. However, in spite of a rich scientific literature, divergences over the physico-chemical properties of SHAs are evident, being associated to a rather systemic lack of homogeneity with concerns of their synthesis and testing protocols [1,2]. This is why the aim of this work was to compare in a single study, for the first time, the physico-chemical properties and the preliminary biological responses of SHAs doped with some of the most promising biofunctional cations (*i.e.*, Ce, Mg, Sr, Zn). The co-precipitation method was selected for the synthesis of SHA-based bioceramics in nanoparticle (NPs) form, due to its recognized advantages (*e.g.*, control over the particle size, simplicity, lower fabrication costs and industrial scalability) [2,3]. Several important outputs of this multi-parametrical study will be highlighted in the following.

The structural changes, induced by the $Ca^{2+}$ substitution in HA, are characteristically caused by differences in ionic radius, electronegativity, and effective charge of the substituting cation [2,3]. Irrespective of type of cation (Ce, Mg, Sr, or Zn), the SHA crystalline quality was incrementally reduced, although at different paces. Important structural modifications have been observed starting with a dopant of ~2.5 at.% (Fig. 1a,b). A single discontinuity in the crystalline quality decreasing trend emerged in the case of HA-Sr2.5 (Fig. 1c). A possible explanation resides in the higher ionicity/electropositivity of Sr with respect to both Ca and the other employed cation substituents, being thus able, in some circumstances, to form more readily bonds with non-associated oxygen ions, without necessarily cleaving already formed Ca–O bonds. At the highest cation substituent concentration (*i.e.*, 5 at.%) a more marked decrease in crystalline quality was noticed for Ce and Sr. An important lattice distortion effect was to be expected in the case of Ce (having higher positive charge than $Ca^{2+}$, and being able to induce vacancies formation) and Sr (being by far the bulkiest dopant). A complementary factor contributed to the crystallinity decay of HA-Ce5.0 samples, *i.e.* $CeO_2$ presence as secondary phase (Fig. 1b), further hinting towards exceeding the Ce-doping limit in HA.

The concentration of therapeutic ions to be released from SHAs into biological environment can be influenced by a number of independent or interconnected factors: composition, long-range order (*e.g.*, crystalline quality, lattice alterations), ionic radii, specific surface area and bond strength formed by ions in the host matrix lattice. The inductively coupled plasma mass spectrometry (ICP-MS) results (Fig. 2a) indicated that the crystalline quality played a prominent role on the dopant release. A material with higher crystalline quality possesses lower free energy and molecular mobility which could consequent in more reduced degradation rates. However, it needs to be stressed that significant lower (with one order of magnitude) ion release concentrations were attained in the case of Sr- and Zn-substituted HAs (Fig. 2a) with respect to Mg-HA (Fig. 2b). Thereby, it is suggested that besides the decrease of crystalline quality of HA, other factors of influence could be at play, and impact the therapeutic ion release rates in the

biomimetic environments. For instance, the bond dissociation energy is higher for Ce–O (795 kJ·mol$^{-1}$) and Sr–O (454 kJ·mol$^{-1}$) with respect to Mg–O (394 kJ·mol$^{-1}$) and Zn–O (284 kJ·mol$^{-1}$), and thus it is expected that once Ce–O and Sr–O bonds are formed within HA, they should be more stable and harder to break apart. The inferior release of Zn ions in comparison to Mg ones seems to be contradictory if one considers the lower dissociation energy of Zn–O bonds with respect to the Mg–O ones. Nevertheless, one should not dismiss the fact that Zn does not substitute into the same Ca occupation sites as Mg [4]. The lower release of Zn ions with respect to Sr ions, can be linked to the higher crystalline quality of Zn-HA as compared to Sr-HA.

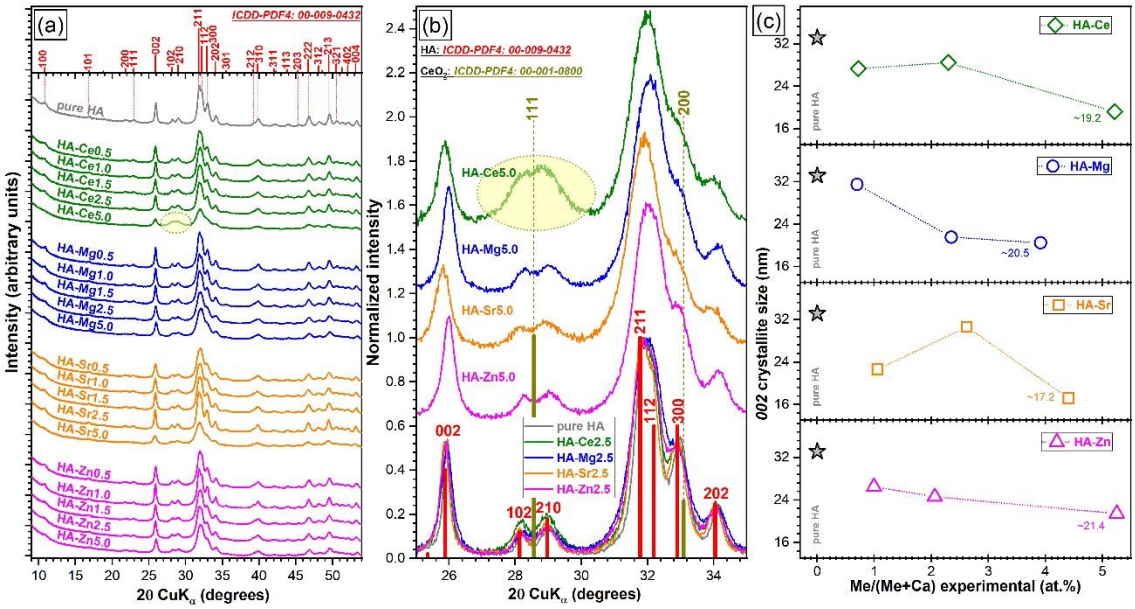


**Fig. 1** (a) X-ray diffraction patterns of all pure and SHAs (0.5–5 at.%). (b) Comparison of XRD patterns for HAs with substituent concentrations of 2.5 and 5 at.%, zoomed in the 2θ angular region ≈24–35°. (c) Evolution of the crystallite size (as determined on the basis of the Scherrer equation applied to the 002 XRD peak) with the increase of the dopant concentration. The values inferred in the case of pure HA NP are presented for comparison. Reproduced from Ref. [4].

The *in-vitro* cytocompatibility screening tests performed in mouse fibroblast cell (NIH/3T3, ATCC® CRL−1658™) cultures indicate that SHA NPs elicited similar cell viability results as compared to the pure HA, with one exception, the HA-Ce5.0 Ce (Fig. 2c). This is owned to the presence of the secondary nano-sized $CeO_2$ phase (Fig. 1a,b). The cell death data (Fig. 2d) indicated that HA NPs substituted with Ce, Mg, Sr or Zn determined similar biological responses with respect to pure HA.

Further, the bio-functional effects of SHA NPs were explored by Real-Time Cell Analysis (RTCA), a technology that enables a real-time monitoring of cell behavior with accuracy and good practice protocols without altering the cells (*e.g.*, avoiding to manipulate the medium or labelling); RTCA is currently envisaged to become a future asset for the study of the biological properties of materials. Two types of cells were investigated by RTCA in the framework of this study, *i.e.*, human osteoblast hFOB 1.19 (ATCC® CRL-11372) and endothelial EAhy 926 (ATCC ® CRL-2922™) cells. Osteoblasts play an important role in the bone matrix production, whilst endothelial cells are involved in the vascularization process by regulating the release of vasodilator molecules. None of the studied SHA materials elicited inferior cell adhesion values with respect to pure HA (see Ref. [4]). The best composition dependent adhesion (for both osteoblast and endothelial cells) was obtained in the case Mg-HAs (with emphasis on the HA-Mg0.5). This is in good agreement with other studies which conveyed a Mg-mediated increased cell adhesion for osteoblast and dermal fibroblast and keratinocyte cells [5]. However, to the best of our knowledge there are no reports to date on the effect of Mg-HA on endothelial cells, and thereby, this positive effect (particularly at a low Mg dosage) needs to be emphasized. An adequate adhesion of the cells to the SHA bioceramics could have concomitantly an important impact on the other expressions of the cells (*e.g.*, proliferation, differentiation). From proliferation point of view, the RTCA investigations indicated that all SHAs returned superior responses with respect to HA in the case of osteoblast cells, whilst this was valid only for Ce- and Sr-containing SHAs in the case of endothelial cells. Thereby, following RTCA

assessments, one should consider whether a time-related, two-step intervention would mimic natural cell behavior – firstly a Mg-based formulation to increase local adherence of cells, followed by a long-term consolidation of cell proliferation, based on Ce/Sr substitutes or a material with low degree of Mg and Zn substitution syncronous with higher degree of Ce/Sr substitution would stimulate the proliferation of both osteoblasts and endothelial cells.

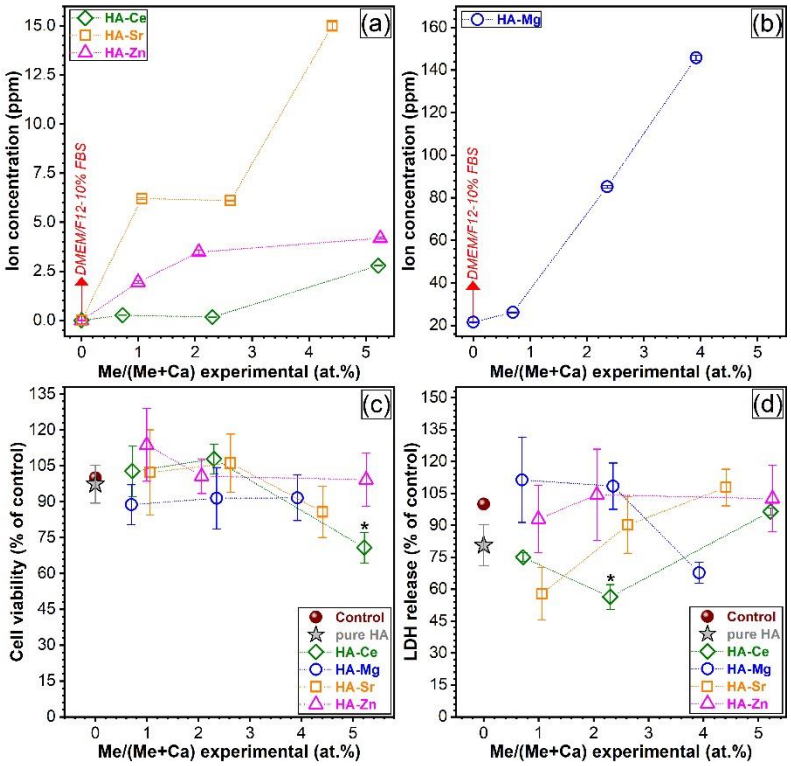


**Fig. 2** The concentrations of the (a) Ce, Sr, Zn and (b) Mg ions leached after 48 h in the DMEM/F12-10%FBS solution by the SHA NPs, as determined by ICP-MS. The NIH/3T3 (c) cell viability (evaluated by a 3-(4,5-dimethyl thiazol-2-yl) 5-(3-carboxymethoxyphenyl)-2-(4-sulfophenyl)-2H-tetrazolium assay—MTS assay) and (d) cytotoxicity (inferred by a lactate dehydrogenase release test—LDH) evaluated after 48 h for the pure and substituted HA NPs. Reproduced from Ref. [4].

In summary, monophasic nano-crystalline pure and single-substituted HA materials can be synthesized by co-precipitation method for concentrations of at least up to ~5 at.% for Mg, Sr, and Zn and of ~2.5 at.% for Ce. Most substituted HA nano-powders presented good cytocompatibility, comparable or even superior with respect to the pure HA and the biological control. The results suggested that Zn and Mg ions are useful as first intervention, for cell adherence, whereas Ce and Sr could sustain a long-term cell proliferation. This work could pave the road for future developments in this field of knowledge, supporting a more decisive delineation of HA-based materials with controlled therapeutic effects (*e.g.*, osteogenesis, angiogenesis, extended antimicrobial activity) suitable for a more effective generation of bone graft substitutes and implants. In the near future, a special focus will be put on the design and integration of multi-substituted HA-based bioceramics with controlled therapeutic ion release into implant coatings and bone graft substitutes (porous scaffolds), and on their insightful mechanical and complex biological evaluation.

*References*


1. H. Qu et al., "Biomaterials for bone tissue engineering scaffolds: A review," RSC Adv. 9(45), 26252–26262 (2019).
2. M. Šupova, "Substituted hydroxyapatites for biomedical applications: A review," Ceram. Int. 41(8), 9203–9231 (2015).
3. T. Tite et al., "Cationic substitutions in hydroxyapatite: Current status of the derived biofunctional effects and their in vitro interrogation methods", Materials 11(11), 2081 (2018).
4. I. M. Chirica et al., "The physico-chemical properties and exploratory real-time cell analysis of hydroxyapatite nanopowders substituted with Ce, Mg, Sr, and Zn (0.5–5 at.%)," Materials 14(14), 3808 (2021).
5. T. S. Lange et al., "$Mg^{2+}$ and $Ca^{2+}$ differentially regulate β1 integrin-mediated adhesion of dermal fibroblasts and keratinocytes to various extracellular matrix proteins," Exp. Cell Res. 214(1), 381–388 (1994).

# Hard/soft effects of multivalence co-dopants in correlation with their location in PZT ceramics

**L. Amarande, M.C. Cioangher, V. Toma, C.F. Miclea, M. Stefan, I. Pasuk, A.R. Iuga, C. Negrila, E. Matei, A.M. Palici,[a] A.C. Joita**

National Institute of Materials Physics, 405A Atomistilor Street, Magurele, Romania, 077125

[a]Horia Hulubei National Institute of Physics and Nuclear Engineering, 077125 Bucharest–Magurele, Romania

Lead titanate zirconate (PZT) is a ferroelectric material well known for its excellent piezoelectric and electromechanical characteristics. Hence, it was extensively used for many applications, such as: sensors, actuators, electro-optical devices, ferroelectric memories, etc. This work is focused on the effect of the relative concentrations and valence states of two co-dopants, manganese and antimony, on the piezoelectric and ferroelectric properties of PZT ceramics. Manganese is a multivalence (2+, 3+, 4+) element, which enters the B-site ($Ti^{4+}$/ $Zr^{4+}$) of the perovskite lattice, as an acceptor or isovalent dopant, easily changing its valence state under different preparation/thermal treatments conditions. Antimony has two possible valences (3+ and 5+) and can enter the both cationic sites, the B-site [1] and the A-site, as a substitute of $Pb^{2+}$ [2, 3]. This work provides a detailed insight into the antimony localization in the PZT lattice, by correlating the valence of the co-dopants and their mutual charge compensation, with the lattice parameters and the ferroelectric and piezoelectric hard/ soft properties of the ceramics.

PZT ceramics with the following compositions: $Pb_{0.98}Sr_{0.02}((Ti_{0.49}Zr_{0.51})_{1-0.015-x}Mn_{0.015}Sb_x)O_3$ where x = 0, 0.005, 0.01, 0.02, 0.03, were prepared, with and without 2 wt.% excess PbO, by conventional ceramic method: solid state reaction at 900 °C/2h, between precursors powders (oxides and carbonates), followed by sintering, at 1250 °C/2h, of the compacted samples. The ceramics composition formula was calculated assuming that antimony enters the lattice as $Sb^{3+}$ at B-sites only. Ceramics were poled in a DC electric field of 35 kV/cm, at 110 °C, in silicon oil.

The structure of PZT, investigated by XRD, is predominantly tetragonal, with a small amount of rhombohedral phase (below 10%) and monoclinic $ZrO_2$, for all compositions, as shown in Fig. 1a. The lattice constants are represented, as a function of Sb concentration, in Fig. 1b,c.

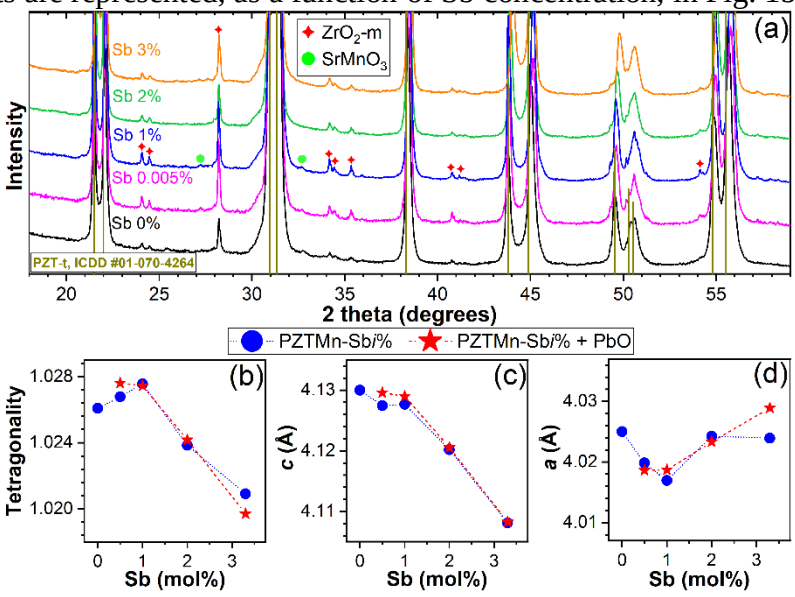


**Fig. 1** (a) XRD diffractograms; (b,c) Lattice parameters and (d) tetragonality and as a function of Sb concentration (in mol%) for the PZT co-doped ceramics. Reproduced from Ref. [4].

The *c* constant shows a decreasing trend, while *a* presented a slightly increasing trend by average, both leading to the decrease of the tetragonality (Fig. 1d), being an indirect evidence of the incorporation of Sb in the PZT lattice. The lattice parameters variation, correlated with the crystal radii of the ions, suggests that antimony is localized at the A-site of the perovskite cell, with a possible charge compensation by $Mn^{2+}$ or $Mn^{3+}$ from the B-site. According to the XPS results (Fig. 2a),

antimony has only the 3+ valence state in these materials. The valence of the Mn ions and their position in the PZT lattice was investigated by EPR measurements, which evidenced a steep increase in the $Mn^{2+}$ spectra intensity, with increasing amount of antimony, explained by a charge compensation mechanism, between the $Sb^{3+}$ ions substituting $Pb^{2+}$ in the A-sites and the $Mn^{2+}$ ions, localized at the B-sites (Figs. 2b,c).

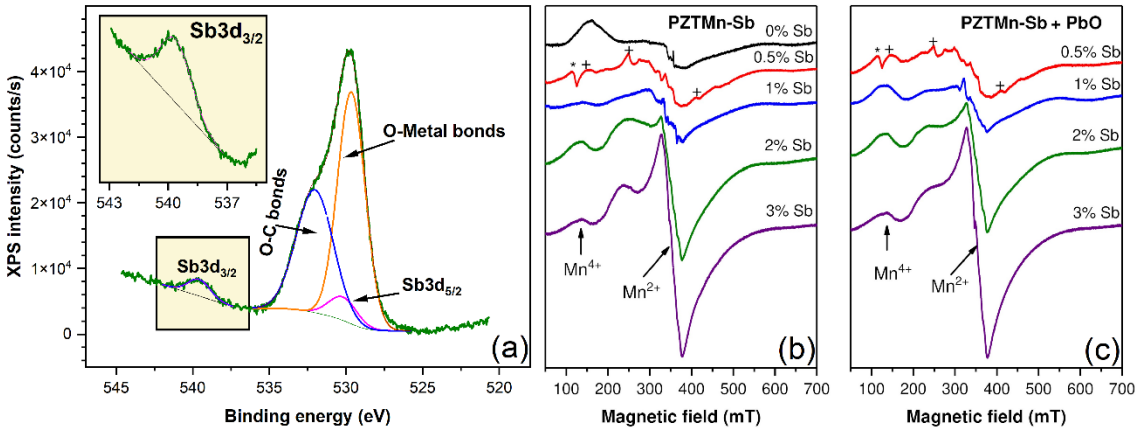


**Fig. 2** (a) XPS spectra of PZTMn-Sb2% samples; (b) and (c) EPR spectra of the PZTMn-Sb*i*% and PZTMn-Sb*i*% + PbO samples, respectively. *****: Fe3+ impurity ions. +: EPR lines of $Mn^{4+}$ ions in $ZrO_2$. Reproduced from Ref. [4].

The ferroelectric properties were studied by measuring the polarization *P* as a function of the applied electric field *E*, with a ferroelectric test system. Before poling, non-saturated "pinched" hysteresis loops were obtained, as shown in Fig. 3a, with low maximum and remnant polarizations, typical for hard piezoelectric materials. After poling, the shape of the hysteresis loops drastically changed, as shown in Figs. 3b,c. Thus, the aria of the loops, as well as the coercive fields, the maximum and remnant polarizations increased. The loops are no longer "pinched", but have an asymmetrical shape and position with respect to the vertical axis.

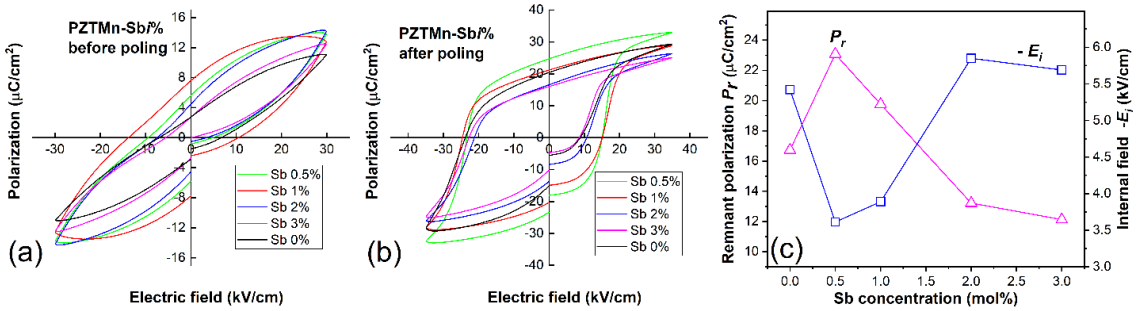


**Fig. 3** *P-E* hysteresis loops (a) before poling and (b) after poling, (c) remnant polarization and internal field *vs.* Sb concentration. Reproduced from Ref. [4].

This asymmetry is the consequence of the internal field, generated as a result of a stable domain configuration achieved by poling. The remnant polarization (see Fig. 3c) abruptly decreases with increasing Sb concentration, while the absolute value of the internal field $E_i$ (derived as the arithmetic mean of the positive and negative coercive fields) increases mostly for the samples with 2 and 3 mol% Sb, as can be seen in Fig. 3c. These features of the hysteresis loops, especially their qualitatively different shapes before and after poling, represent a proof for piezoelectric hard behavior of the Mn and Sb co-doped PZT ceramics.

The electromechanical response of the disc shaped piezoceramic resonators, in the resonance-antiresonance band of the radial vibration mode, was studied by determining the electromechanical coupling factor $k_p$, and the mechanical quality factor $Q_{mp}$, as a function of Sb doping level.

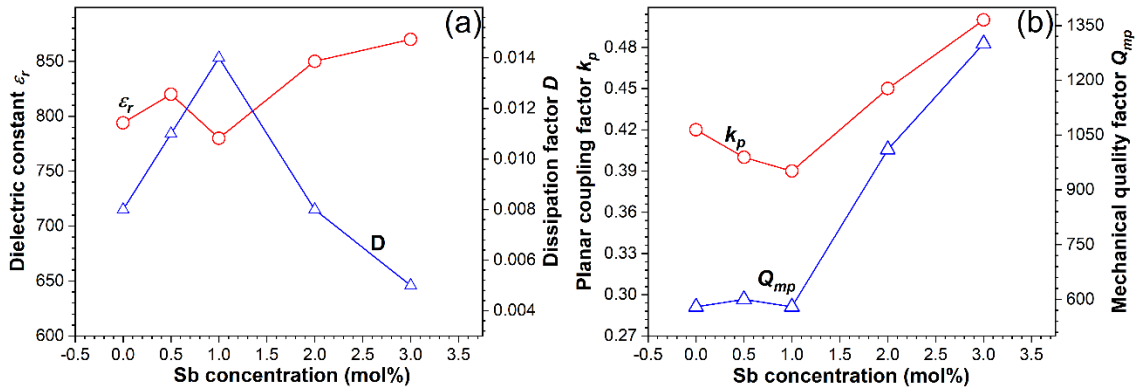


**Fig. 4** (a) Dielectric constant with dissipation factor and (b) planar coupling factor with mechanical quality factor *vs.* Sb concentration. Reproduced from Ref. [4].

As shown in Figs. 4a,b, $\varepsilon_r$, $k_p$ and $Q_m$ have a similar trend relative to the Sb concentration, with a minimum at 1 mol% Sb and a steeper increase for higher doping levels, as a result of the lower ceramic density, and the very low dielectric constant, of $ZrO_2$ secondary phase, with higher concentrations in samples with lower antimony doping levels. The increasing values of the mechanical quality factor, correlated with the steeper decrease of the dissipation factor, upon increasing the Sb concentration above 1 mol%, indicate that samples with 2 and 3 mol% Sb manifest hard piezoelectric behavior, in agreement with their ferroelectric properties.

Despite the predominant A-site location of $Sb^{3+}$, as a donor substitute for $Pb^{2+}$, which would normally lead to a soft piezoelectric behavior, these ceramics exhibited hard characteristics, enhanced by the increasing amount of Sb, due to the associated presence of the $Mn^{2+}$ ions. The large size of the $Mn^{2+}$ ions, has a pinning effect on the domain walls' mobility. The manganese valence state, evidenced by EPR measurements, made it possible to ascertain Sb location in the lattice. Besides, the lack of Pb vacancies, caused by the lead excess with respect to the ceramic formulas, created by $Sb^{3+}$ substitution of $Pb^{2+}$, additionally reduced the soft characteristics. All these results prove that the correlation between multiple valence states and locations of the co-dopants decisively influences the piezoelectric hard/soft response and provides indirect information about the location of some co-dopants, which presumably could substitute for both cationic sites in the PZT based ceramics.

*References*


1. S. Eitssayeam et al., „High dielectric and piezoelectric properties observed in annealed $Pb_{0.88}Sr_{0.12}Zr_{0.54}Ti_{0.44}Sb_{0.02}O_3$ ceramics," Ferroelectrics 451(1), 48–53 (2013).
2. T. Zhou et al., „The effect of doping $Sb_2O_3$ in high d33 • g33 PZT piezoelectric ceramics," Ferroelectrics 195(1), 101–104 (1997).
3. S. Dutta et al., „Electrical properties of antimony doped PLZT ceramics prepared by mixed-oxide route," J. Alloys Compd. 426(1–2), 345–351 (2006).
4. L. Amarande et al., "Hard/soft effects of multivalence co-dopants in correlation with their location in PZT ceramics," Ceram. Int. 47(23), 33382–33389 (2021).

# Intrinsic losses in microwave dielectrics assessed by terahertz time domain spectroscopy: A case study on $Zr_{0.8}Sn_{0.2}TiO_4$ ceramics

**L. Nedelcu, C. D. Geambasu, M. Enculescu, M. G. Banciu**
National Institute of Materials Physics, 405A Atomistilor Street, Magurele, Romania, 077125

Modern communication systems rely on a series of devices such as oscillators, antennas, filters and multiplexers. These passive devices take advantage of the advanced dielectric materials, which exhibit low loss and high dielectric constant and allow the enhancement of the system reliability and a significant size reduction. Many microwave (MW) dielectrics show appropriate features for improved devices [1]. However, the production of the microwave dielectrics on a large scale is limited due to the fabrication costs and to the technological limitations. As a consequence, ceramic materials became the most employed in passive MW devices due to the simplicity, cost effectiveness and scalability of their large-scale fabrication.

The various types of losses, which occur in dielectrics, are classified in two classes: (*i*) intrinsic losses, which correspond to the electromagnetic field interaction with phonons in the ideal crystalline lattice; and (*ii*) extrinsic losses, which are due to defects such as secondary phases, grain boundaries, lattice local or extended defects, *etc*. Fortunately, the total losses of polycrystalline materials can be reduced to the limit of the intrinsic ones by appropriate tuning of the "synthesis-microstructure-properties" cycle. The extrinsic dielectric loss is an important feature, which can limit the use of ceramics in MW applications. This drawback became particularly restrictive for filters or multiplexers.

Over time, many attempts for estimation of the intrinsic losses of many MW dielectrics by using Fourier Transform Infrared (FTIR) spectroscopy, Backward Wave Oscillator (BWO), and Whispering Gallery Mode resonators techniques [1] have been made. Of these, FTIR spectroscopy was the most employed because it enables the identification of the polar phonons, which contribute to the complex relative permittivity ($\varepsilon = \varepsilon' - j\varepsilon''$) in MWs and millimeter-waves (MMWs); the anharmonic interaction between electromagnetic field and lattice vibrations is the dominant mechanism for losses, these being attributed to the damping of phonon modes. Based on this supposition, the extrapolation of losses to MWs and MMWs was made by using the proportionality between $\varepsilon''$and frequency [1].

Highly sensitive, easy and wideband measurement of low-loss dielectrics in MMWs and submillimeter waves can be achieved by using the terahertz time-domain spectroscopy (THz-TDS) [2]. Compared to FTIR spectroscopy and BWO methods, THz-TDS has the advantage of a better signal-to-noise ratio and allow the direct determination of $\varepsilon'$ and $\varepsilon''$ without using the Kramers–Kronig relations.

During the last decades, $Zr_{0.8}Sn_{0.2}TiO_4$ (ZST) ceramics have been extensively investigated as low-loss MW materials for substrates and dielectric resonator (DR) applications. ZST ceramics were fabricated by various methods and, analyzing the data published in the literature, it is worth mentioning that $\varepsilon'$ varies between 35 and 40, while $Q \times f$ product ($Q$ is the inverse of dielectric loss tangent and $f$ is the measurement frequency) is ranging from 10 to 100 THz. However, the intrinsic losses values, expressed as $Q \times f$ product, were estimated to 60 THz by using FTIR spectroscopy and BWO techniques [1]. Given these inconsistencies, we used the THz-TDS technique in order to determine the intrinsic dielectric loss of ZST ceramics. Three batches of DRs with different extrinsic losses were fabricated [3], as defined in Table 1, under similar to the optimal (batch ZST A), close to optimal (batch ZST B), and far from optimal (batch ZST C) conditions.

The ZST powders, prepared by the solid-state reaction method from high purity oxides ($ZrO_2$, $SnO_2$ and $TiO_2$), were sintered into cylinders by using the conventional ceramic technology. Ceramics with relative density higher than 96.5% of the theoretical density (5.195 g/cm$^3$) were achieved for all three batches (Table 1) [3].

**Table 1** The bulk density and lattice constants (*a*, *b* and *c*) of ZST ceramics for different sintering conditions [3].

| Batch | Sintering temperature (°C) | Sintering time (h) | Bulk density (g/cm$^3$) | *a* (nm) | *b* (nm) | *c* (nm) |
|---|---|---|---|---|---|---|
| **ZST A** | 1300 | 2 | 5.08 | 0.4774 | 0.5517 | 0.5044 |
| **ZST B** | 1300 | 4 | 5.05 | 0.4773 | 0.5516 | 0.5042 |
| **ZST C** | 1350 | 4 | 5.03 | 0.4772 | 0.5515 | 0.5401 |

The morpho-structural characterization of the ZST ceramics was performed by X-ray diffraction (XRD) and scanning electron microscopy (SEM). Fig. 1a shows the XRD patterns indexed with respect to the ICDD 01-081-2214 reference file and, within the detection limit, no secondary phases were observed. The determined lattice constants values (Table 1) indicated that the sintering conditions had a slight influence on the orthorhombic unit cell. Despite the fact that the SEM images of the fractured ceramics looked similar, the ZST sample sintered at 1300 °C / 2h (Fig. 1b) is characterized by a significant number of pores of small dimensions. The segregation of the pores is taking place when heat-treatment dwell time increases (Fig. 2c), while the increase of the sintering temperature leads to the decrease of the pores' number and the increasing of their volume (Fig. 2d).

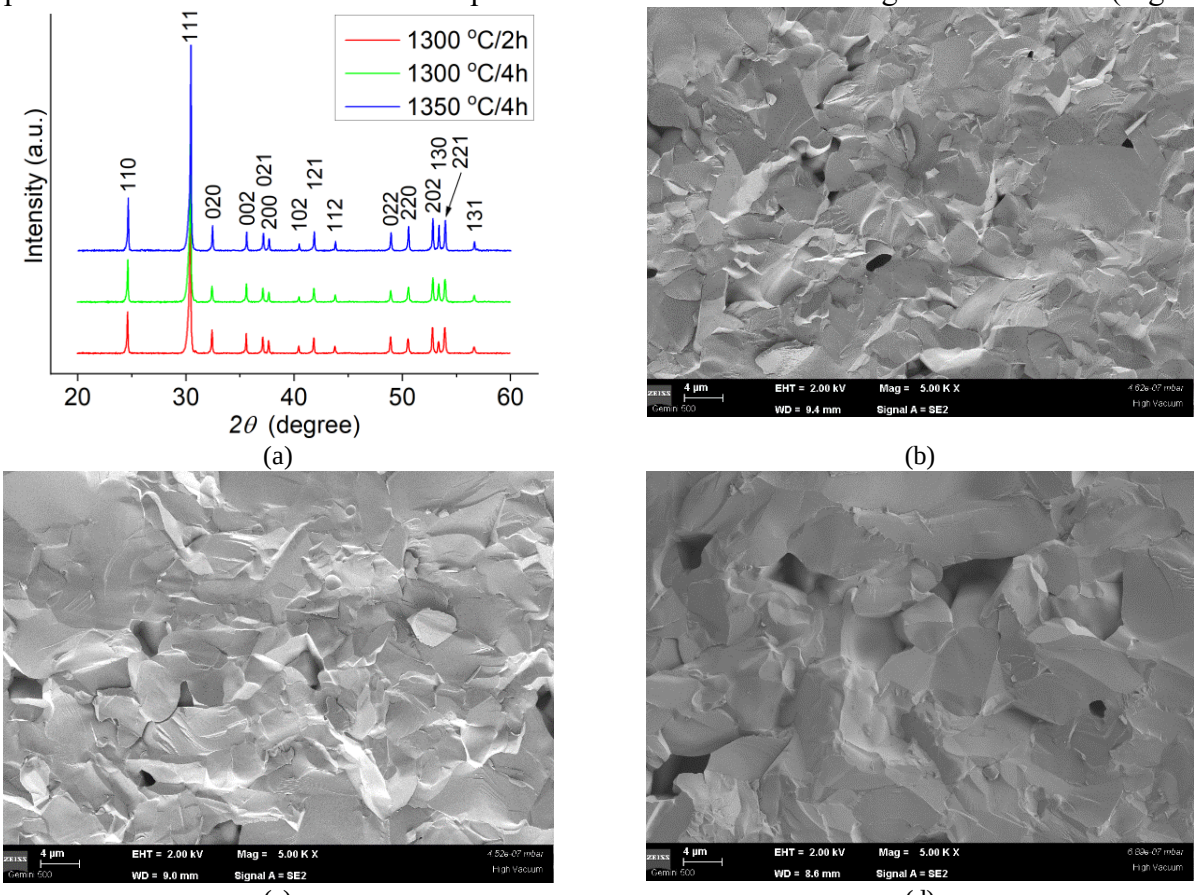


**Fig. 1** (a) XRD patterns vs. sintering temperature and (b–d) SEM images of the ZST samples sintered at (b) 1300 °C/2h, (c) 1300 °C/4h (c), and (d) 1350 °C/4h. Reproduced from Ref. [3].

The sintered cylinders were employed as DRs, then characterized in MWs and the effect of the sintering conditions on their dielectric properties is presented in Table 2. It is shown that the sintering conditions have a strong impact on the sample densification (Table 1), morphology (Fig. 1b–d) and finally, on the dielectric constant $\varepsilon'$. In addition, the dielectric loss $\varepsilon''$varies between $4.3 \times 10^{-3}$ and $14.7 \times 10^{-3}$ when the sintering conditions are changed. Since the porosity does not significantly change, the strong variation in the dielectric loss cannot be caused by the losses due to the pores. Hence, the cause of the dielectric losses consists in such factors for extrinsic losses as impurities, vacancies, aggregation of Sn, granular interfaces, *etc.*, which explain the dielectric response of the close to optimal condition (ZST-B batch) and far from optimal condition (ZST-C batch).

The terahertz measurements were carried out on 0.5 mm thick disks sliced from ZST DRs. For the investigated ZST samples, variation of the absorption coefficient, $\varepsilon'$ and $\varepsilon''$ with frequency is given in Fig. 2. It is shown that, for frequencies up to 0.8 THz, the dielectric constant $\varepsilon'$ is the highest for the ZST-A batch. Moreover, the ZST-A batch exhibits the lowest absorption and dielectric losses when compared to the ZST-B and ZST-C batches. From the data given in Table 2, one can see that the extrinsic losses are much higher in MWs than in THz.

**Table 2** Real part ($\varepsilon'$) and imaginary part ($\varepsilon''$) of the complex relative permittivity and $Q$ x $f$ product of ZST ceramics measured in microwave (@ 6 GHz) and terahertz (@ 0.4 THz) domain [3].

| Batch | $\varepsilon'$ @ 6 GHz | $\varepsilon''$ @ 6 GHz | $Q$ x $f$ @ 6 GHz (THz) | $\varepsilon'$ @ 0.4 THz | $\varepsilon''$ @ 0.4 THz | $Q$ x $f$ @ 0.4 THz (THz) |
|---|---|---|---|---|---|---|
| **ZST A** | 37.3 | $4.3 \times 10^{-3}$ | 50 | 38.2 | $2.5 \times 10^{-1}$ | 60 |
| **ZST B** | 37.2 | $7.4 \times 10^{-3}$ | 30 | 38.1 | $2.7 \times 10^{-1}$ | 55 |
| **ZST C** | 37.1 | $14.7 \times 10^{-3}$ | 15 | 37.6 | $2.9 \times 10^{-1}$ | 50 |

As it can be seen from Table 2, values of $\varepsilon'$slightly increase when the frequency is increased from MWs to THz. However, this increase is very small, which confirms the theoretical frequency invariant values [1]. In addition, the $Q \times f$ product exhibits a significant increase from MWs to THz. This increase is larger for ZST-B and ZST-C batches and lower for ZST-A batch. This indicates that the intrinsic factor plays a lower role for the optimal batch, ZST-A than for the other two batches; therefore, the intrinsic losses ($Q \times f \sim 60$ THz) of the ZST ceramics can be assessed from THz data.

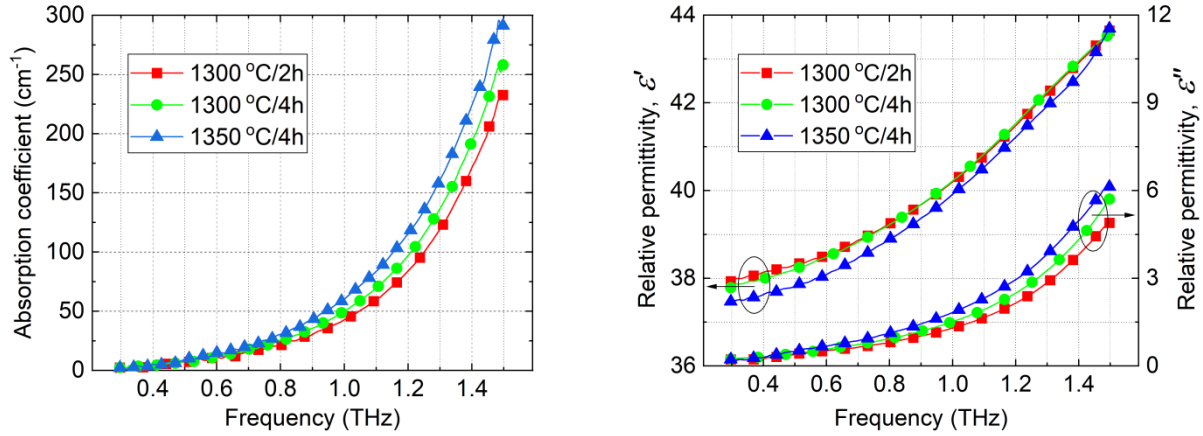


(a) (b)

**Fig. 2** Frequency dependence of the (a) absorption coefficient and (b) complex relative permittivity *vs.* sintering condition for ZST ceramics. Reproduced from Ref. [3].

One can conclude that the THz-TDS is a versatile measurement technique, which can allow for the determination of intrinsic dielectric loss of low-loss MW ceramics. The THz losses are less sensitive to the sample preparation than the MW losses. Therefore, THz-TDS it is useful for tailoring of the synthesis parameter in an optimization cycle. Furthermore, the THz - TDS gives $\varepsilon'$ and $\varepsilon''$ without any requirement of additional calculation (*e.g.*, Kramer-Kronig analysis), being very attractive for fast screening of new low-loss dielectric materials.

*References*


1. M.T. Sebastian, R. Ubic, and H. Jantunen, Microwave materials and applications, John Wiley & Sons, Chichester, UK (2017).
2. J. Neu, C. A. Schmuttenmaer, "Tutorial: An introduction to terahertz time domain spectroscopy (THz-TDS)," J. Appl. Phys. 124(23), 231101 (2018).
3. L. Nedelcu et al., "Intrinsic dielectric loss in $Zr_{0.8}Sn_{0.2}TiO_4$ ceramics investigated by terahertz time domain spectroscopy," Materials 14(1), 216 (2021).

# Electroactivity and spin related functionalities of organic systems

**B. Borca, L. Trupina, A.-C. Galca, C. Chirila, G. E. Stan, A.-M. Vlaicu, A. E. Stanciu, A. G. Boni, M. Botea, A. Stanculescu, L. Pintilie**

[1]National Institute of Materials Physics, Atomistilor 405A, 077125, Magurele, Ilfov, Romania

The realization of functional and multifunctional systems based on organic materials and/or biomolecules that are presenting various advantages related to their low cost, versatile preparation, flexibility, large area, low dimensionality, chemical selectivity, lightweight, biocompatibility, is actually of major scientific and technological interest for applications in the fields of molecular electronics, spintronics, bioelectronics, therapeutic techniques, energy convectors, actuators, neuromorphic computing, *etc.* Therein, new research contributions on systems that contain organic molecules and reveal new properties and functionalities are of great importance in material sciences and innovative technologies. Here, two different studies on molecular systems are summarized in the following. One is focused on the electroactive properties of thin films of biomolecules, comprising ferroelectricity and piezoelectricity of guanine and cytosine nucleobases [1]. The other one reports the synthesis of a double-decker cyclophane and single molecule investigations of hybridization and spin polarization effects at metal-organic interfaces. This last research topic [2] is based on the collaboration of B. Borca with Peter Grünberg Institut from Forschungszentrum Jülich, Germany including M. Metzelaars,[1] S. Schleicher,[2] T. Hattori,[2] F. Matthes,[2] S. Sanz,[2] D. E. Bürgler,[2] J. Rawson,[1,2] C. M. Schneider[2] and P. Kögerler[1,2] ([1]Institute of Inorganic Chemistry, RWTH Aachen University, 52074 Aachen, Germany, [2]Peter Grünberg Institute (PGI-6), Forschungszentrum Jülich, 52428 Jülich, Germany).

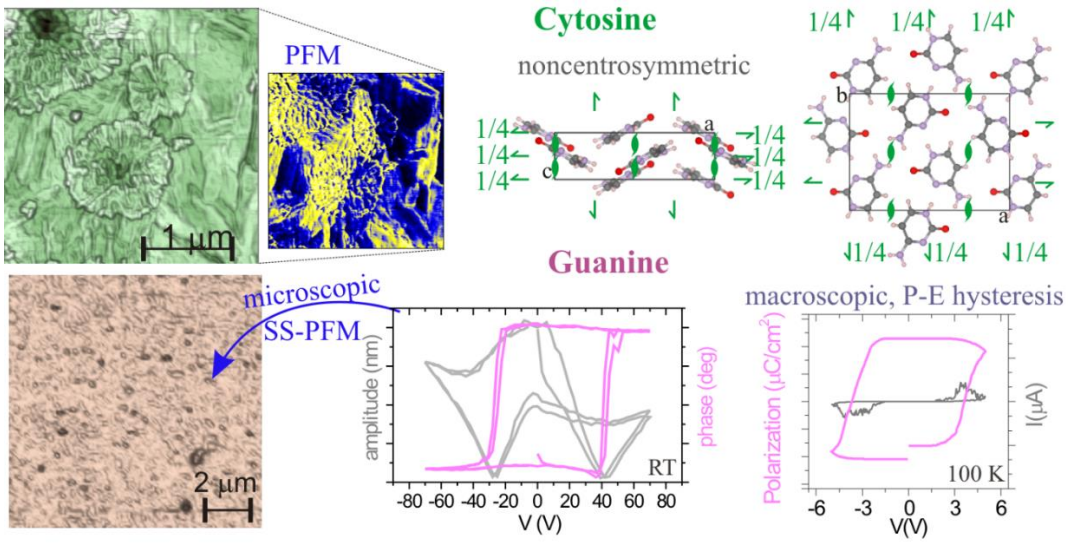


**Fig. 1 –Top row:** Experimental results on cytosine films. Left panels: Atomic Force Microscopy (AFM) and Piezoresponse Force Microscopy (PFM) images, showing two types of interconnected fractal features and the corresponding polar domains with opposite contrast. Right panels: Ball-and-stick models of the cytosine non-centrosymmetric orthorhombic unit cell. **Bottom row:** Experimental results on guanine films. Left panel: AFM image on guanine with a densely nano-grained morphology. Right panels: Polarization switching hysteresis curves, characteristics of ferroelectricity, acquired locally by single point switching spectroscopy SS-PFM and macroscopically by P-E measurements, respectively. Figure adapted with panels and results published in Ref. 1.

A ferroelectric material which is in the same time pyroelectric and piezoelectric (but the reverse situation is not always valid) is characterized by a spontaneous electrical polarization and by the possibility to switch its polarity by an electric field, or to generate electricity by small temperature variations (pyroelectricity), or by mechanical forces (piezoelectricity), or to change its dimensions by applying an electric field (converse piezoelectricity) and have a large spectra of possible applications. Our investigations on the the „Electro-active properties of nanostructured films of cytosine and guanine nucleobases" [1] reveal such properties in thin nanostructured anhydrous films of thermally

evaporated guanine and cytosine nucleobases, that are known for their fundamental role in organisms, being interacting components of DNA and RNA nucleic acids. Our anhydrous films of cytosine have interconnected fractal features, of nearly equal proportion and with lateral sizes of hundreds of nanometers to micrometers as revealed by morpho-structural characterizations using room temperature Atomic Force Microscopy (AFM). The corresponding Piezoresponse Force Microscopy (PFM) images on the cytosine films exhibit large piezoresponse domains with opposite polarization (Figure 1-top row, left panels), that are effects of the non-centrosymmetric structure with an orthorhombic $P2_12_12_1$ space group (Figure 1-top row, right panels) determined by crystallographic measurements. The orientation of the domains of the cytosine films in the direction of an applied electric field strongly depends on the local molecular assembly.

The anhydrous guanine films have a few nanometer-size densely grained morphology (Figure 1-bottom row, left panel). The guanine films display characteristic ferroelectric hysteresis loops showing large remnant polarization (Figure 1-bottom row, right panel) up to 200 K. Above this temperature, a thermally induced size-dependent transition to a paraelectric phase, containing residual or locally induced nanoscopic ferroelectric domains by single point switching spectroscopic SS-PFM measurements even at room temperature, occurs (Figure 1-bottom row, middle panel). The discovery of the multifunctional properties related to electro-activity of the nucleobases systems opens routes for further applications, especially for devices in the domain of biocompatible sensors and/or bioactuators.

In the following, the description is focused on the „ Cyclophane with eclipsed pyrene units enables construction of spin interfaces with chemical accuracy" [2]. The organization of molecules on metal surfaces and the interactions at the metal-organic interface determine the characteristics of devices in molecular electronics and spintronics. Scanning Tunneling Microscopy and Spectroscopy (STM/STS) is one of the most powerful techniques that allows the investigation of structural, electronic and spin-related phenomena (with the spin polarized SP-STM/SP-STS versions) at the atomic scale on a variety of different emerging materials including individual atoms and molecules, biomolecules, surfaces and subsurface defects, 2D materials and artificial structures. Here, research studies are briefly presented that are realised in a close international collaboration with Forschungszentrum Jülich, exploiting the synthesis of a metal-organic double-decker cyclophane complex enclosing Fe in ferrocene pillars that are connecting two planes of pyrene moieties at van der Waals (vdW) interacting distance in an AA-stacked graphene-like rare configuration (Figure 2). Single double-decker cyclophane molecules are investigated with STM/SP-STM/SP-STS techniques operated in ultra-high vacuum conditions and at cryogenic temperatures on magnetic Co and non-magnetic Cu surfaces.

The STM investigations allow the study of individual cyclophane molecules, excluding other fragment molecules that may be found on the surface after thermal deposition on a substrate of Cu(111) covered with submonolayer coverage of Co(111) nanoislands. The double-decker cyclophane molecules adsorb with a face-on geometry having the pyrene molecular planes parallel to the Cu and to the Co surfaces (Figure 2). On Cu(111) the molecules are physisorbed, while on Co(111) they are chemisorbed. The strong hybridization of the lower pyrene group to Co reduces its interaction with the top pyrene. This decoupling between the pyrene planes is consistent with the SP-STM/SP-STS measurements that reveal no spin polarization above the pyrene moiety of the cyclophane molecules (Figure 2 top row). The spin asymmetry measurements over the ferrocene groups of the cyclophane on Co(111) leads to a spin polarization of comparable strength, but opposite direction, to that of the pristine Co surface (Figure 2 top row, right panel).

This result shows that the ferrocene groups efficiently transmit spin polarization by the spin-dependent hybridization mechanism, and covalent extensions of these groups can be used as an approach to enforce the hybridization to ferromagnetic surfaces. This opens a path to the construction of more complicated metal-organic spintronic systems.

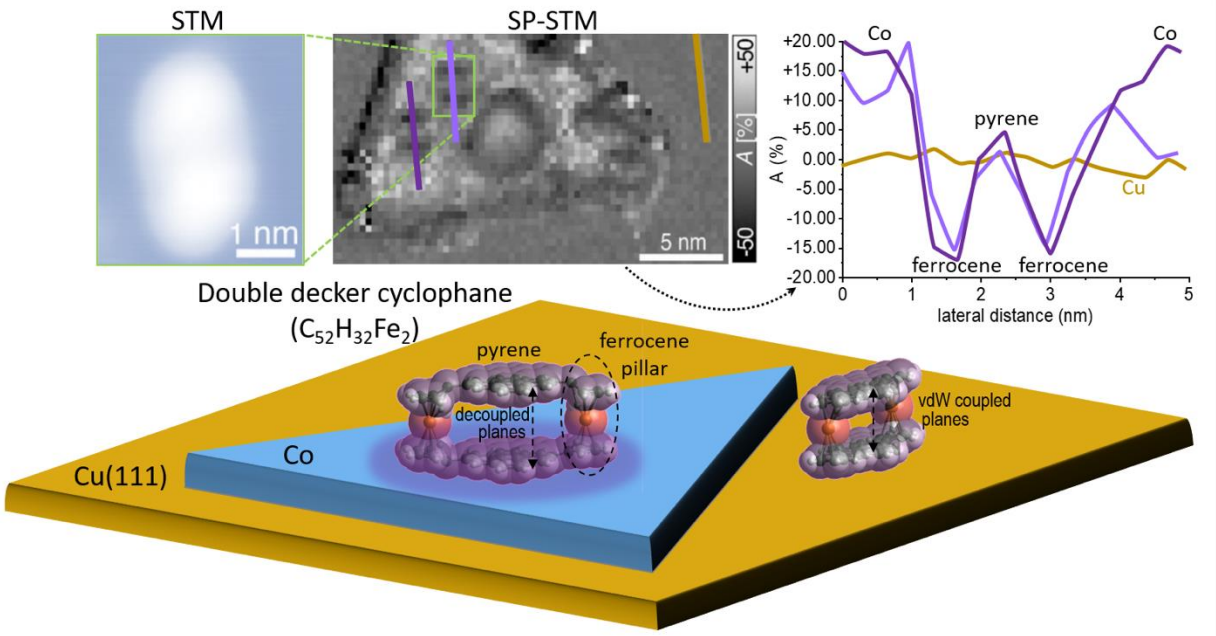


**Fig. 2** - **Top row**: Experimental results on cyclophane/Co/Cu(111). Left panel: STM image of a single cyclophane molecule. Middle panel: SP-STS extracted spin-asymmetry-map of cyclophane/Co/Cu(111). Right panel: spin-asymmetry profiles along the lines marked in the middle panel. Panels adapted and recolored from Ref. 2. **Bottom row**: Schematic representation of the cyclophane molecules physisorbed on Cu(111) and chemisorbed on Co(111).

*References*

1. M Socol, L Trupina, A-C Galca, C Chirila, G E Stan, A-M Vlaicu, A E Stanciu, A G Boni, M Botea, A Stanculescu, L Pintiliea and B Borca. Electro-active properties of nanostructured films of cytosine and guanine nucleobases. Nanotechnology 32, 415702 (2021)
2. M Metzelaars, S Schleicher, T Hattori, B Borca, F Matthes, S Sanz, D E Bürgler, J Rawson, C M Schneider and P Kögerler. Cyclophane with eclipsed pyrene units enables construction of spin interfaces with chemical accuracy. Chem. Sci. 12, 8430 (2021)

# Thickness dependent magnetic and magneto-functionalities of thin films and multilayers

**S.G Greculeasa, C. Locovei, A.E. Stanciu, N. Iacob, G.Schinteie, A. Leca, A. Kuncser, L. Hrib, C.Chirila, I.Pasuk, and V.Kuncser**
National Institute of Materials Physics, 077125 Magurele, Romania

Magnetic, magneto-transport, and magneto-optical properties of different films and multilayers were investigated with regards to thickness, composition and temperature dependencies. In this respect, epitaxial $La_{0.7}Sr_{0.3}MnO_3$ (LSMO) films with different thicknesses (9-90 nm), Fe-Gd amorphous thin films of different compositions (Gd content 20-29 at. %) and thicknesses (40-90 nm) and [Fe/Permalloy]/FeMn/Permalloy multilayers with different thickness of the antiferromagnetic FeMn spacer (6 and 15 nm) were prepared.
Magnetic hysteresis loops of the LSMO films were collected in parallel geometry and perpendicular one (relative to the applied field and the film plane). Magnetic contributions with different switching mechanisms were evidenced, depending on the perovskite film thickness. Two spin structures of different in-plane and out of plane anisotropies were evidenced in the hysteresis curves of the LSMO 90, 60 and 36 samples (with suffix representing the sample thickness, in nm), which may be assigned to an interface component and a main film component. The first component is characterized by a higher coercive field (interface component), while the second component presents a softer magnetic behavior (main component). The interface spins are harder to rotate, suggesting a disordered spin structure, relative to the main film. These features are more clearly observed in the perpendicular geometry, where spins cannot be saturated at lower temperatures. For samples LSMO 9 and LSMO 30, the two different magnetic contributions are clearly evidenced in the parallel geometry. However, considering the hysteresis curves in the perpendicular geometry, the two magnetic phases are no longer distinctly observed, suggesting that the out-of-plane anisotropies are similar.

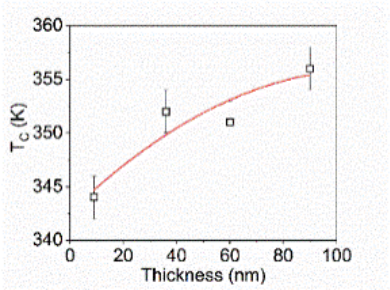


**Fig.1** Thickness dependent Curie temperature of LSMO thin films.

The transition temperature dependence on the film thickness (fig. 1), shows an overall increase with the film thickness, however with a saturation tendency for thicknesses above 60 nm. The values are typical for LSMO thin films and lower than the bulk-like transition temperature of 369 K. In the parallel geometry, the coercivity values (shown in fig. 2) are considerably reduced (few tens of Oe) in relation to the values in the perpendicular geometry (more than 600 Oe).
Typical colossal magnetoresistance (CMR) effects in manganites are clearly observed up to 29 % (see fig. 3), with specific features depending on geometry as a result of the different magnetic reversal processes. The magnetoresistance effect is more pronounced in the perpendicular geometry and at high temperatures for sample LSMO 30, while it decreases for higher film thickness (e.g. in case of sample LSMO 60). Generally, the MR effect is enhanced at 300 K due to electron scattering on paramagnetic regions that become dominant when approaching room temperature. MR curves of LSMO 30, 36 and 60 samples in perpendicular geometry present a plateau near 0 field region at temperatures in (50 – 330 K), (300 – 325 K) and, respectively, (50 – 150 K) intervals, at variance to the case of parallel geometry, where only a maximum at 0 T applied field is observed, more pronounced at higher temperatures. This temperature dependent feature was previously associated (and supported by electron microscopy data) to the prevalence of insulating regions and of ferromagnetic domains in the corresponding temperature range. As a general observation, the MR

effect increases sharply at higher temperatures, approaching $T_C$. This behavior is more evident in case of the thinner films with a sharper metal-insulator transition.

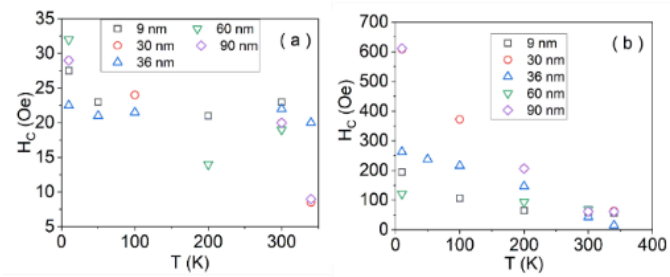


**Fig. 2** Temperature dependence of the coercivity of the main magnetic phase in parallel (a) and perpendicular (b) geometry for the LSMO samples.

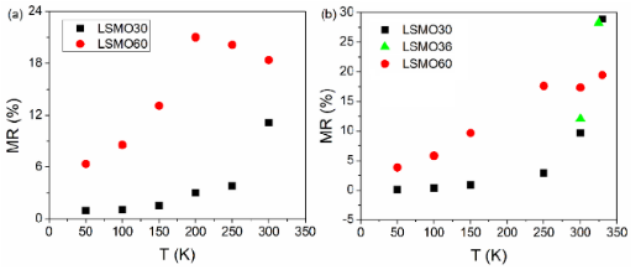


**Fig. 3** MR effect at various temperatures in parallel (a) and perpendicular (b) geometry for LSMO 30 and LSMO 60.

In Fe-Gd films, the magneto-optical curves are reversed for samples with a higher amount of Gd that cross the concentration compensation point (see fig. 4). Because Gd atoms have zero local orbital momentum, and hence a negligible spin-orbit coupling (as well as a negligible magneto-optical rotation power), just the iron magnetic moments rotate the polarization plane of the incident laser light. As a consequence, reversed hysteresis loops will be obtained when the magnetic moment of Gd sub-lattice overpass the magnetic moment of the Fe sub-lattice, taking into consideration the antiferromagnetic alignment between each other and the orientation of the net magnetic moment of Gd along the field. The small coercive field ($H_c$) values increase with the film thickness for fixed elemental ratio. The in plane magnetic anisotropy effect is noticeable mainly in the $Fe_{80}Gd_{20}$_60 film, having the closest composition to the compensation point in the magnetic frozen regime. At this particular elemental ratio, two magnetic phases are present in MOKE measurements when the field is oriented along the easy axis. The drastic change of the hysteresis loop to an almost linear shape when the field is oriented perpendicular to the easy axis may suggest that the saturation is achieved in a linear coherent spin rotation manner. Taking into consideration the cumulative effects of competition between Fe-Gd magnetic moments, the differences in the absolute values of the exchange integrals (J (Fe-Fe) > J(Fe-Gd) > J(Gd-Gd)) as well as the negative value of J (Fe-Gd), a later in field reorientation is expected for that magnetic phase closer to the compensation point and characterized therefore by a smaller net magnetic moment due to uncompensated Fe moments. In case of sample with 29 at % of Gd, the formation of two magnetic phases (this time slightly richer in Gd) might be supported only by the sensible different shifts of the hysteresis loops collected under different orientations of the field with respect to an in-plane axis, reminding possible exchange bias effects due to interfacial couplings.

The FeGd films are oxidation free, as observed from the Mössbauer spectroscopy results (depicted in fig. 5). For samples $Fe_{80}Gd_{20}$_90 and $Fe_{80}Gd_{20}$_60, an average atomic configuration is supported: the main peak is related mainly to the Fe sites with an average number of 2-3 Gd atoms among the 12 neighbors, and secondary peak accounts for an increased number of Gd. The average hyperfine magnetic field slightly increases for the thinner film due to compositional modifications (25 T for 60 nm relative to 22 T for 90 nm). The collapse of the broad sextet pattern in samples of higher Gd content, $Fe_{71}Gd_{29}$_60, is due to the decrease of the average exchange interactions and not to the enhanced magnetic relaxation effects. The two narrow hyperfine field distributions were used, of average fields of about 5 T and 21 T, respectively, present relatively closed contributions and hence, comparable effects in the magnetic hysteresis loops. Nevertheless, the component with the average hyperfine field of 21 T is much closer in composition to the compensation point whereas the one of

5 T has a Gd content much higher than the one corresponding to the compensation point. Being magnetically dominant, this last configuration is also responsable for the inverse hysteresis loop evidenced by MOKE.

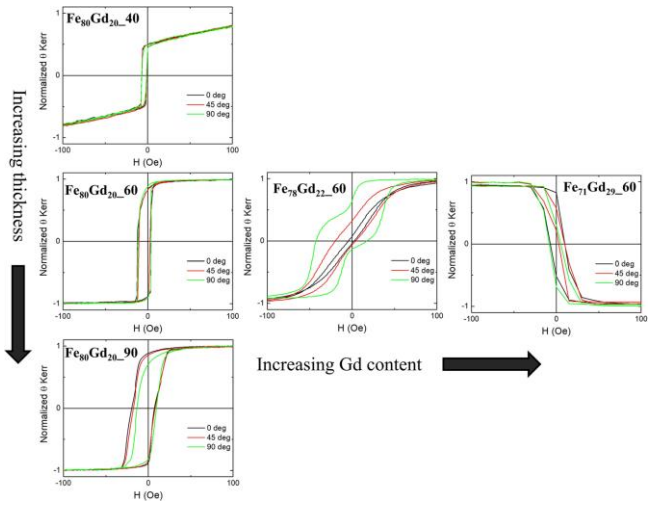


**Fig. 4** Magnetization curves taken at MOKE on Fe-Gd amorphous samples at azimuthal angles of 0°, 45°, and 90°.

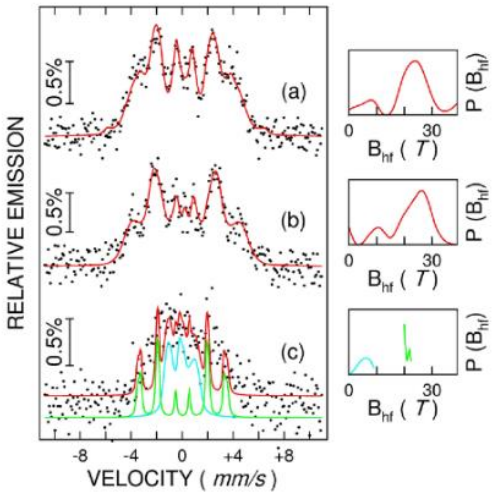


**Fig. 5** $^{57}$Fe CEM spectra taken at room temperature for samples: $Fe_{80}Gd_{20}$_90 (a), $Fe_{80}Gd_{20}$_60 (b), and $Fe_{71}Gd_{29}$_60 (c). The corresponding hyperfine magnetic field distributions are presented on the right hand of each spectrum.

The thickness of the spacer layer plays a crucial role in the magnetic properties of the [Fe/Py]/FeMn/Py (Py = Permalloy) samples. A 15 nm FeMn structure exhibits exchange pinning of both ferromagnetic layers (5-300 K), negligible interlayer coupling, strong exchange-bias field and enhanced coercivity for both ferromagnetic layers at low temperatures. On the contrary, a 6 nm FeMn structure becomes exchange de-pinned in the vicinity of room temperature. The depinned state is characterized by a single hysteresis loop centered at zero field and having enhanced magnetic coercivity.

In conclusion, more insight into the influence of thickness of LSMO and Fe-Gd films and of FeMn spacer layer in [Fe/Py]/FeMn/Py multilayers on the magnetic, magneto-transport and magneto-optic properties is given.

*References*


1. S.G. Greculeasa, A.-E. Stanciu, A. Leca, A. Kuncser, L. Hrib, C. Chirila, I Pasuk, V. Kuncser, "Influence of thickness on the magnetic and magnetotransport properties of epitaxial $La_{0.7}Sr_{0.3}MnO_3$ films deposited on STO (0 0 1)", Nanomater. 11, 3389 (2021).
2. C. Locovei, N. Iacob, G. Schinteie, A.E. Stanciu, A. Leca, V. Kuncser, "Tuning the magnetic properties of amorphous Fe-Gd thin films by variation of thickness and composition", Hyperf. Interact. 242, 44 (2021).
3. D.M. Polishchuk, O.I. Nakonechna, Y.M. Lytvynenko, V. Kuncser, Y.O. Savina, V.O. Pashchenko, A.F. Kravets, A.I. Tovstolytkin, V. Korenivski, "Temperature and thickness dependent magnetostatic properties of [Fe/Py]/FeMn/Py multilayers", Low Temp. Phys. 47, 483 (2021).

# Advanced characterization of ferromagnetic shape memory alloys obtained by various methods

**F. Tolea, M. Sofronie, B. Popescu, M. Enculescu, D. Macovei, M. Tolea**
National Institute of Materials Physics, Atomistilor 405A, 077125, Magurele, Ilfov, Romania

The shape memory alloys (SMA) have triggered an increasing interest due to their attractive multifunctional properties, with potential for applications in the biomedical field [1], miniature devices and robotics [2, 3] and non-medical applications [4]. Specific to SMA is the martensitic transformation (MT): a reversible and thermoelastic structural phase transition that takes place between a phase of high symmetry (austenite) and one of low symmetry (martensite) [5]. Advanced characterizations of SMAs is a key step in optimizing their properties for possible future devices. Scanning Electron Microscopy (SEM), Energy Dispersive X-Ray Spectroscopy (EDS), X-Ray Diffraction (XRD), high-energy X-ray (HEX) diffraction and extended x-ray absorption-edge fine structure (EXAFS) spectroscopy, on beamline BW5 at DORIS III, DESY, Germany, Differential scanning calorimetry (DSC), Magnetometry via Quantum Design—Superconducting Quantum Interference Device (SQUID) and the Quantum Design-Physical Properties Measurement System (PPMS), magnetostrictive measurements, temperature and magnetic field dependences of the electrical resistivity were used for complete characterization. The samples were rapidly quenched ribbons obtained using the melt spinning technique [6-8] or ingots subjected to High Speed, High Pressure Torsion (HSHPT) [9, 10].

Ribbons with the $Ni_{50}Mn_{20}Ga_{27}Cu_3$ nominal composition have been prepared by melt-spinning and characterized by different methods [6], both as-prepared (AP) and after a 20 min at 400ºC thermal treatment (TT). SEM images evidenced that the preparation route induces a mixture of cellular and dendritic structures on surface, with grain sizes of few μm, having a columnar aspect in cross-section. The thermal treatment favors the growth of the dendritic structures, a reduction of defects and a promotion of the ordered $L2_1$ phase (evidenced by XRD – see Fig.1a). Thermo-magnetic, strain and resistivity measurements confirm a martensitic transformation at low temperatures (below 90K) preceded by a premartensite transformation (starting at around 190K – see Fig.1b). Indications that there is a premartensitic phase - formed on cooling from austenite, before the martensite phase is stabilized - are seen in magnetic measurements, strain measurements, and in resistivity measurements (both for the Mn-AP and Mn-TT samples). The magnetostriction have negative values (of about 10-20 ppm in 5T), comparable with previously reported data on the undoped polycrystalline Ni2MnGa. For the thermal treated samples, the parabolic dependence of $\lambda_P$ at low fields suggests a spin rotational mechanism while at high fields a saturation tendency can be noticed, except for the temperatures close to the transformation, where a saturation is not noticed and a volume magnetostriction can be assumed. While the unusual behavior of magnetostriction for Fe67.5Pd30.5Si2 in the technically saturated domain is based on the coexistence of the ordinary and forced magnetostrictions, the last one increasing faster with the temperature decreasing [7].

The crystalline structure and Fe local environment of the $Ni_{52}Co_2Fe_{20}Ga_{26}$ Heusler alloy, prepared by melt spinning have investigated by XRD, HEX and EXAFS spectroscopy in [8]. XRD could clearly establish the $L2_1$ structure of the alloy by the presence of the maxima with all (*hkl*) indices odd. EXAFS was less conclusive about a clear distinction between $L2_1$ and an alternative B2 structure. The EXAFS spectrum of the austenite was equally well fitted with B2 and $L2_1$, with only a larger shrink of the B2 lattice constant by comparison with that of the lattice constant of $L2_1$, as reported to the reference $Ni_{54}Fe_{19}Ga_{27}$ alloy.

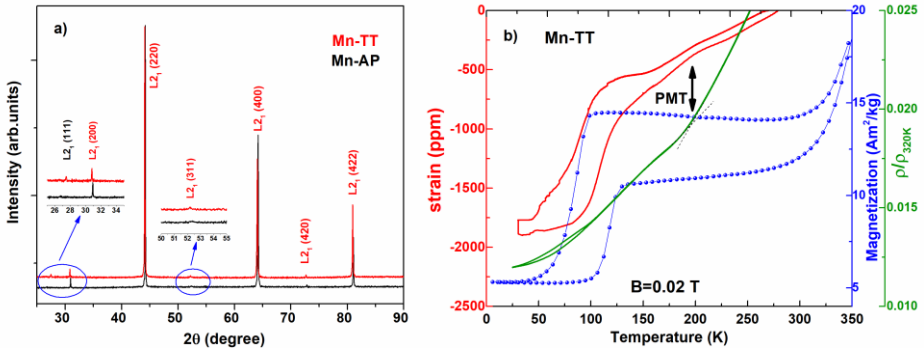


**Fig.1** a) XRD patterns recorded for Mn-AP and Mn-TT ribbons at room temperature. b) The thermo-magnetic, thermo-resistivity and thermal expansion measurements to identify MT interval and also the value of the PMT start temperature (at 190 K) for the Mn-TT sample.

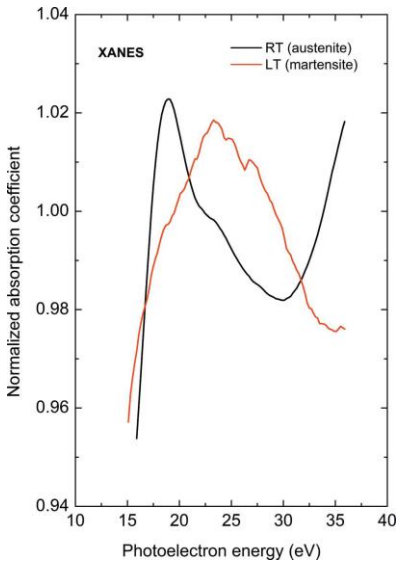


**Fig.2** Fe K-edge XANES of $Ni_{52}Fe_{20}Ga_{26}Co_2$ at 300 K (RT) and 180 K (LT).

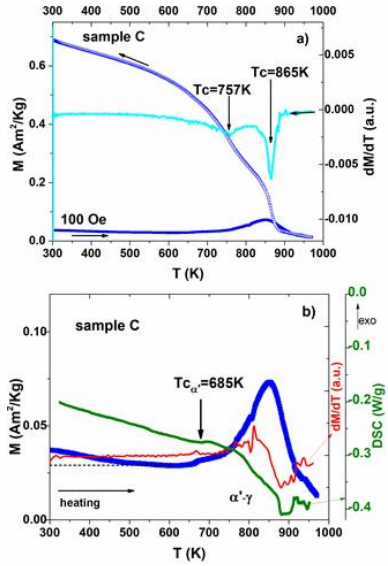


**Fig.3** a) M(T) at high temperatures for sample C; b) Magnetization behavior superposed with DSC scan and dM/dT on the heating the sample C

The synchrotron-based HEX diffraction of the low-temperature martensite has evinced its modulated structure. Nevertheless, the corresponding EXAFS spectrum could be reliably fitted with the tetragonal $L1_0$ structure of the non-modulated martensite. This proves that the martensite modulation changes the long-range order but leaves the short-range order around the atoms of the alloy components, essentially unmodified. The $L2_1$-to-$L1_0$ symmetry transition of the Fe environment on the martensitic transformation leaves almost undisturbed the nearest Ni neighboring of Fe, but drastically modifies its next-nearest Ga neighboring. The shell of six Ga atoms in austenite splits into two sub-shells with four and two Ga neighbors at shortened and elongated distances from Fe with respect to the initial Fe-Ga distance in austenite. This changes the electronic structure of Fe at the Fermi level, which is reflected by the white line of the Fe-K XANES spectrum (Fig.2). Its broadening upon the martensitic transition indicates the spread of the unoccupied *p* states in a wide energy range above the Fermi level, as an effect of the transition from the high-symmetry cubic ($L2_1$) austenite to the lower-symmetry tetragonal ($L1_0$) martensite.

The influence of the processing by HSHPT technique of the shape memory $Ni_{57}Fe_{18}Ga_{25}$ Heusler alloy [9] and $Fe_{57}Mn_{27}Si_{11}Cr_5$ (at%) [10] on the morphology and magnetic properties was investigated. DSC results and magnetic investigations suggested that moderate applied deformations modify the ratio of the $L1_0$ tetragonal and cubic γ phase in $Ni_{57}Fe_{18}Ga_{25}$ SMA, and generate a reduction of the samples granularity and a rearrangement of the two phases. Which explains the diminishing of the MT temperatures and the decrease of the Curie temperature and the saturation

magnetization when the level of the applied deformation enhances. For the $Fe_{57}Mn_{27}Si_{11}Cr_5$ (at%) alloy crystalline structure, magnetic and transport properties were investigated on samples subjected to room temperature HSHPT incorporating 1.86 degree of deformation and also to hot-compression. Thermo-resistivity as well as thermomagnetic measurements indicate an antiferromagnetic behavior with the Néel temperature ($T_N$) around 244 K, directly related to the austenitic γ-phase. The jump in the temperature dependence of magnetization after the Néel point, on cooling, is explained by the increased phonon-electron interaction. At room temperature, the overall behaviour of magnetisation suggests the existence of two overlaying magnetic phases: the paramagnetic one (associated with austenite and ε martensite) and a magnetic ordered phase which gives a finite magnetization at RT, associated with α' martensite. High temperature measurements act as in situ thermal treatments and lead to the formation of a δ bcc-ferrite type phase with ferromagnetic behaviour, reflected by the temperature dependence of the magnetization (Fig.3a). The correlation of DSC results with thermomagnetometry (Fig.3b) highlighted reverse MT (α'- γ).

*References*


1. Morgan N B, Materials Science and Engineering A 378 (2004), 16-23
2. Nespoli A, Besseghini S, Pittaccio S, Villa E, Viscuso S, Sensors and Actuators A158 (2010) 149–160
3. Furuya Y, Shimada H, Materials & Design 12 (1991) 21-28
4. Frolova L, Mino J, Ryba T, Gamcova J, Dzubinska A, Reiers M, Diko P, Kavecansky V, Milkovic O, Kravcak J, J Alloys Comp 747 (2018), 21–25
5. Otsuka K, Wayman C M, Shape memory materials, Cambridge University Press (1998)
6. M. Sofronie, M. Tolea, B. Popescu, M. Enculescu, F. Tolea, Magnetic and Magnetostrictive Properties of Ni50Mn20Ga27Cu3 Rapidly Quenched Ribbons, MATERIALS 14, 5126 (2021) [DOI: 10.3390/ma14185126].
7. M. Sofronie, B. Popescu, M. Enculescu, Structural, magnetic and magnetostrictive properties of the ternary iron–palladium–silicon ferromagnetic shape memory ribbons Applied Physics A 127:168 (2021),
8. D. Macovei, F. Tolea, Long- and short-range order in the Ni52Co2Fe20Ga26 ferromagnetic Heusler alloy, J. of APPL. CRYST. 54 (4), 1207-1216 (2021) [DOI: 10.1107/S1600576721006415]
9. B. Popescu, C. Gurau, G. Gurau, M. Tolea, M. Sofronie, F. Tolea, Martensitic Transformation and Magnetic Properties of Ni57Fe18Ga25 Shape Memory Alloy Subjected to Severe Plastic Deformation TRANS. of the INDIAN INST. of METALS, (2021) [doi: 10.1007/s12666-021-02293-8]
10. C. Gurau, G. Gurau, F. Tolea, B. Popescu, M. Banu, LG Bujoreanu, The Effect of the In-Situ Heat Treatment on the Martensitic Transformation and Specific Properties of the Fe-Mn-Si-Cr Shape Memory Alloys Processed by HSHPT Severe Plastic Deformation, MATERIALS 14, 4621 (2021) [DOI: 10.3390/ma14164621]

# Development and pinning force aspects in $MgB_2$ superconductor

**P. Badica[a,*], M.A. Grigoroscuta,[a] V. Sandu,[a] G. Aldica,[a] I. Pasuk,[a] M. Burdusel,[a] V. Sandu,[a] A. Kuncser,[a] A.M. Ionescu,[a] T.S. Suzuki,[b] O. Vasylkiv,[b]**

[a] National Institute of Materials Physics, Street Atomistilor 405A, 077125, Magurele, Romania

[b] National Institute for Materials Science, 1-2-1 Sengen, 305-0047, Tsukuba, Ibaraki, Japan

Development and application of $MgB_2$ superconductor is related to its ability to transport high critical current densities. This can be obtained by vortex pinning control and high connectivity, and to achieve this goal, there are different approaches. Among them we mention nano structuring for enhancement of the density of grain acknowledging that boundaries/interfaces are effective pinning centers. Introduction of additives with the purpose to modify the grain boundaries or to modify the electronic structure through chemical substitutions of B or Mg in the crystal lattice of $MgB_2$ is another popular method. One can also use technologies that influence the already mentioned factors and can promote fabrication of $MgB_2$ with high density. Another idea is to take advantage of the $MgB_2$ anisotropy. The crystal structure of $MgB_2$ is composed of alternate stacked layers of B and Mg. The *in-plane* flow of the supercurrent is favored. Hence, textured $MgB_2$ materials are of interest for practical purposes.

Added, partially-oriented $MgB_2$ bulk discs with the starting compositions of $(MgB_2)_{0.99}(B_4C)_{0.01}$ (labeled MBBC, Table 1) and $(MgB_2)_{0.99}$(c-BN)$_{0.01}$ (labeled MBBN, Table 1) were fabricated by slip casting under an intense magnetic field (perpendicular to the disc surface) (HFSC), $H_0$ = 12 T, and subsequent spark plasma sintering (SPS) [1]. Samples are presented in Table 1. XRD was performed on $S_{top}$= top surface of the disc and on $S_{lateral}$ = surface perpendicular to $S_{top}$ and parallel to the thickness of the disc. X-ray diffraction reveals that in sintered samples, $MgB_2$ is partially textured with (001) orientation (Fig. 1). The degree of preferred orientation ($\eta$), orientation angle ($\varphi$), and Lotgering factor (LF) are presented in Table 1. The differences in orientation degree $\eta$ (~13 and ~9 %) and in phase amount (70 and 75 wt. %) when using different additives ($B_4C$ and c-BN) indicate on a synergetic effect of orientation and additions on the evolution of the microstructure. This aspect is reflected on the superconducting properties of the materials.

**Table 1** Samples, preparation, phase content and orientation parameters.

| | Sample | Phase content [wt. %] | | | *r* | *LF* [%] / $\eta$ [%] ($\varphi$) [°] |
|---|---|---|---|---|---|---|
| | | $MgB_2$ | $MgB_4$(Mg) | MgO | | |
| 'a' | $MgB_2$ raw powder | 88.0 | 4.6(0.3) | 7.1 | - | - |
| 'b' | SPS MBBC randomly oriented | 78.9 | 13.3 | 7.8 | - | - |
| 'c' | HFSC+ SPS MBBC; $S_{top}$ | 70 | 20 | 10 | 0.796 | 14 / 13 (50°)* |
| 'd' | SPS MBBN randomly oriented | 81.4 | 10.9 | 7.7 | - | - |
| 'e' | HFSC+ SPS MBBN; $S_{top}$ | 74 | 15 | 11 | 0.847 | 9 / 9.4 (51°) |

*Note:* * The meaning of $\eta$ is: compared to a random sample, an excess of 13% of the $MgB_2$ crystallites have the *c* axes within $\varphi$ = 0-50° from the surface normal.

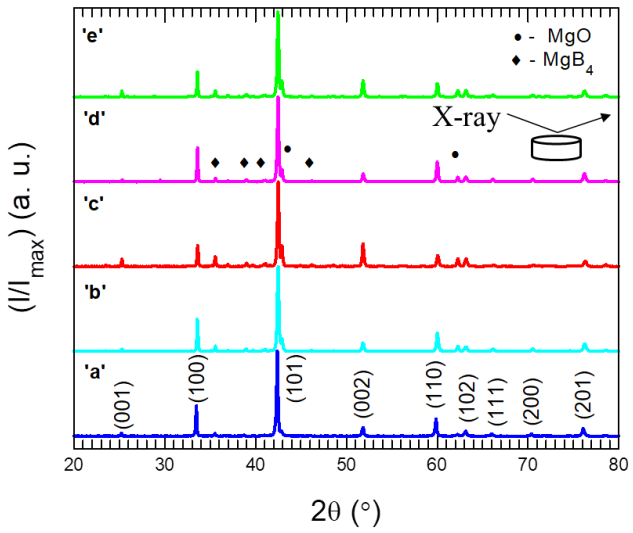


**Fig. 1 (a)** X-ray diffraction patterns of $MgB_2$ samples 'a' – raw $MgB_2$ powder; 'b' – reference MBBC randomly oriented sample obtained by SPS (without slip casting); 'c' – MBBC 12 T oriented sample obtained by SPS; 'd' – reference MBBN randomly oriented sample obtained by SPS (without slip casting); 'e' – MBBN 12 T oriented sample obtained by SPS (in all cases, XRD was measured on $S_{top}$), The peaks' indices are for the $MgB_2$ phase. Secondary phases are: ● – MgO and ♦ - $MgB_4$.
Samples notation is as in Table 1

The magnetic critical current densities at 5 K are presented in Fig. 2. In the partially-oriented samples 'c' and 'e', $J_c$ in the high magnetic fields for an applied magnetic field $H$ // $H_0$ is higher than for $H \perp H_0$ and it is similar or even higher than for the corresponding reference randomly oriented samples 'b' and 'd'. The highest values of $H_{irr}$ are for sample 'c' when $H$ // $H_0$. This result is remarkable since the amount of $MgB_2$ is lower in the oriented samples than in the corresponding randomly-oriented samples 'b' and 'd'.

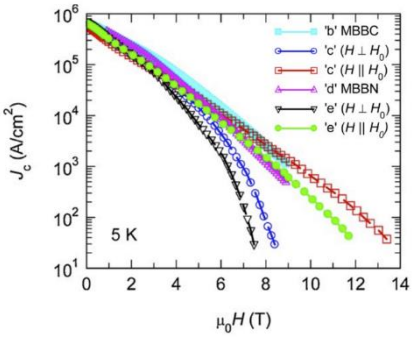


**Fig. 2 (a)** Critical current density curves $J_c(\mu_0 H)$ for $MgB_2$ samples at 5 K. Samples notation is as in Table 1.

The dependence at 20 K of the normalized pinning force $f_p$ (where $f_p = F_p / F_{p,max}$, $F_p = J_c \cdot \mu_0 H$, $F_{p,max}$ is the maximum $F_p$) [2] with the reduced field $h = H/H_{irr}$ (where $H$ is applied magnetic field, $H_{irr}$ is the irreversibility field determined for $J_c$ = 100 A/cm$^2$) is shown in Fig. 3(a). In the partially-oriented samples 'c' and 'e' for $H$ // $H_0$, the maximum is shifted to unusually low values: $h_0$ is around 0.1 at 5 K and 0.18 at 30 K (Fig. 3(b)).

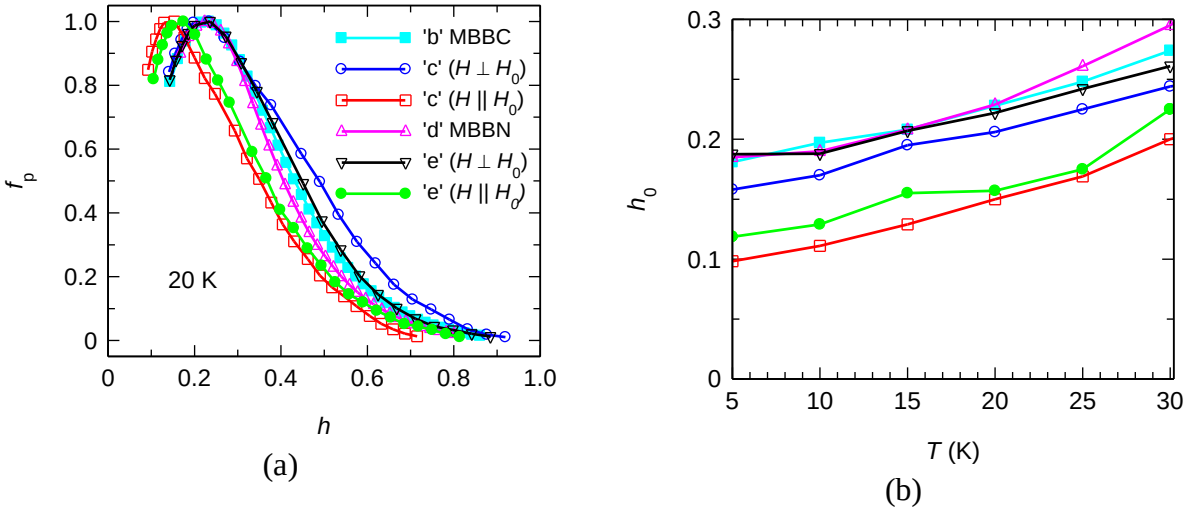


**Fig. 3 N**ormalized pinning force $f_p$ as a function of reduced magnetic field $h$ at 20 K for randomly oriented samples 'b' and 'd' and for (001) partially-oriented samples 'c' and 'e'. Samples notation is as in Table 1.

The abnormal values of $h_0$, far away from theoretical ones, suggest the need to revise the model of the pinning force scaling analysis. Moreover, the curves of pinning force versus magnetic field can present peculiar profiles and application of the typical scaling procedures fails. Based on the percolation model, we show [3] that most features of the field dependence of the critical force that generate dissipation comply with the Dew-Hughes scaling law predictions within the grain boundary pinning mechanism [2] if a factor $g(h, T)$ related to the superconducting connection of the grains is used:

$$f_p(h,T) = h^{\frac{1}{2}}(1-h)^2 g(h,T) \qquad (1)$$

The field dependence of the connecting function, which is dependent on the superconducting anisotropy, is the main factor that controls the boundary between dissipative and non-dissipative current transport in high magnetic field. Experimental data indicate that the connecting function is also dependent on the particular properties (e.g., the presence of slightly non-stoichiometric phases, defects, homogeneity, and others) of each sample and it has the form of a single or double peaked function in all investigated samples. The analytical expression of $g$ is a Gaussian or a log-nomal function.

*References*


1. Grigoroscuta MA, Aldica G, Pasuk I, Burdusel M, Sandu V, Kuncser A, Suzuki TS, Vasylkiv O, Badica P, Partially-oriented $MgB_2$ superconducting bulks with addition of $B_4C$ and cubic BN obtained by slip casting under high magnetic field and spark plasma sintering, (2021) Mater. Res. Bull. 134, 111103
2. D. Dew-Hughes, Flux pinning mechanisms in type II superconductors, Philos. Mag. **30** (1974) 293-305
3. Sandu V, Ionescu AM, Aldica G, Grigoroscuta MA, Burdusel M, Badica P, On the pinning force in high density $MgB_2$ samples, (2021) Scientific Reports 11, 5951

# Optical properties of composites based on conjugated/insulating polymers and carbon nanotubes

**M. Baibarac,[a] M. Daescu,[a] A. Udrescu,[a] E. Matei,[b] D. Nastac,[c] O. Cramariuc,[c] G. Arzumanyan,[d] and K. Mamatkulov,[d]**

[a] National Institute of Materials Physics, Lab. Optical Processes in Nanostructure Materials, Atomistilor str. 405 A, Magurele, Romania, 77125

[a] National Institute of Materials Physics, Multifunctional Materials and Structures Laboratory, Atomistilor str. 405 A, Magurele, Romania, 77125

[c] IT Centre for Science and Technology, 25 no. Av. Radu Beller str., 011702 Bucharest, Romania

[d] Joint Institute for Nuclear Research, 6 Joliot-Curie street, Dubna, Russia, 141980.

The progress recording the optical properties of two composite materials based on i) poly(o-phenylenediamine) (POPD) fibers, poly(vinylidene fluoride) (PVDF) spheres and double-walled carbon nanotubes (DWNTs) [1] and ii) poly(3-hexylthiophene) (P3HT( and single-walled carbon nanotubes highly separated into metallic (M-SWNTs) and semiconducting tubes (S-SWNTs) [2] is recorded. The chemical polymerization of o-phenylenediamine (OPD), in the presence of PVDF has resulted to the POPD fibers assembled with PVDF spheres (Fig.1a). The adding of DWNTs to the reaction mixture consisting from OPD, $FeCl_3$ and PVDF has allowed the adsorption of DWNTs onto the POPD-PVDF aggregates (Fig 1b).

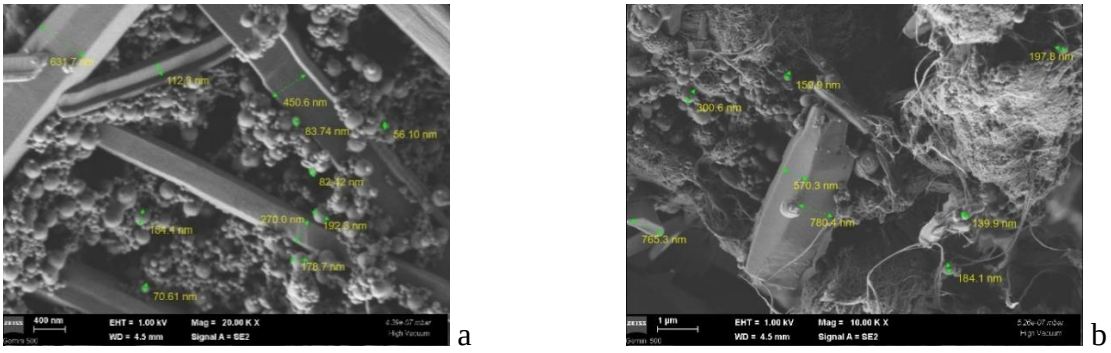


**Fig. 1** SEM images of POPD-PVDF (a) and the POPD-PVDF/DWNTs composite (the DWNT concentration being of 2wt.%) [1]

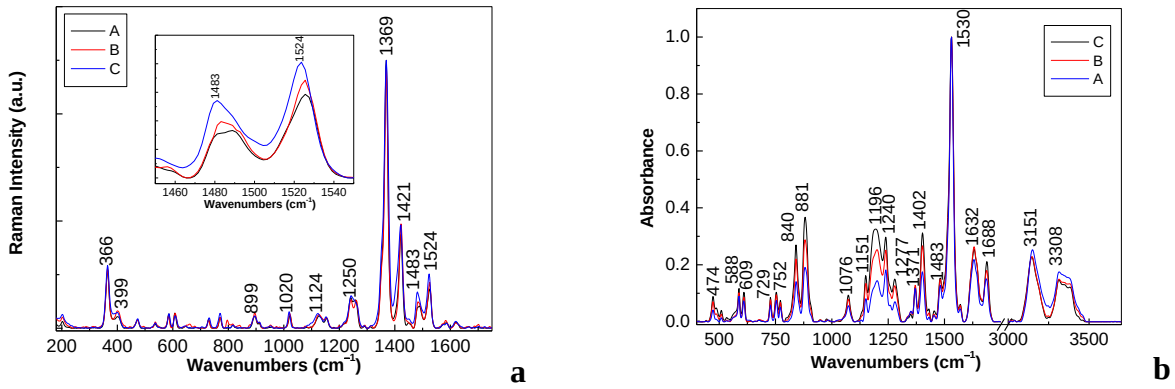


**Fig.2** Raman and FTIR spectra of the POPD-PVDF structures labeled as A, B and C samples [1].

Fig. 2 shows Raman and FTIR spectra of the POPD-PVDF structures which are characterized by the following weights of the two polymers: i) A sample contains 0.045 g POPD and 0.045 g PVDF; (ii) the B sample contains 0.05 g POPD and 0.09 g PVDF, (iii) the C sample contains 0.06 g POPD and 0.18 g PVDF. The Raman and FTIR spectra of the POPD-PVDF/DWNTs composites are shown in Fig.3; the D, E and F samples corresponds to the composites which contain 5, 10 and 20 mg DWNTs [1]. According to Figs. 2a and 3a, the Raman line from 1421 $cm^{-1}$ is shifted to 1415 $cm^{-1}$, this experimental fact being interpreted as evidence of the covalent functionalization of DWNTs with

POPD. The variations of the absorbance in the case of the IR bands at 840 and 881 $cm^{-1}$ were explained considering hindrance steric effects induced of carbon nanotubes to the POPD fibers and the PVDF spheres.

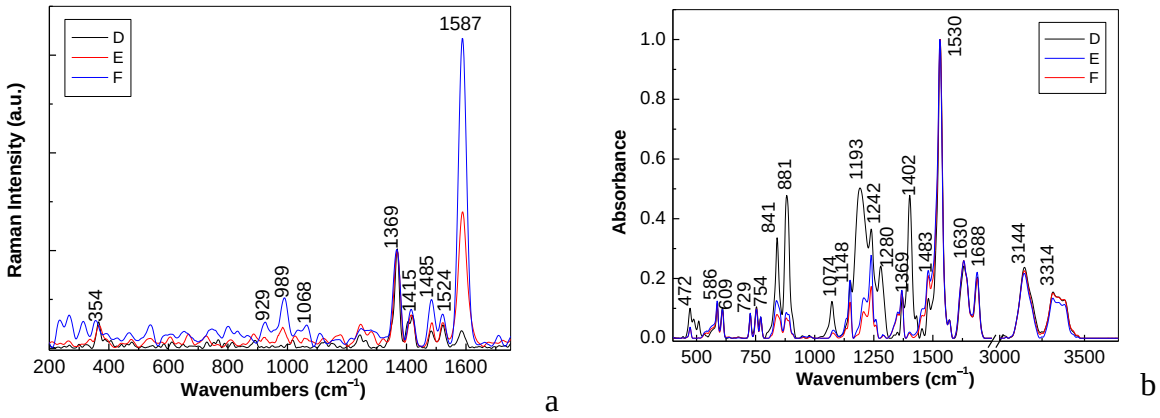


**Fig.3** Raman (a) and FTIR (b) spectra of the POPD-PVDF/DWNTs composites labeled as D, E and F samples [1].

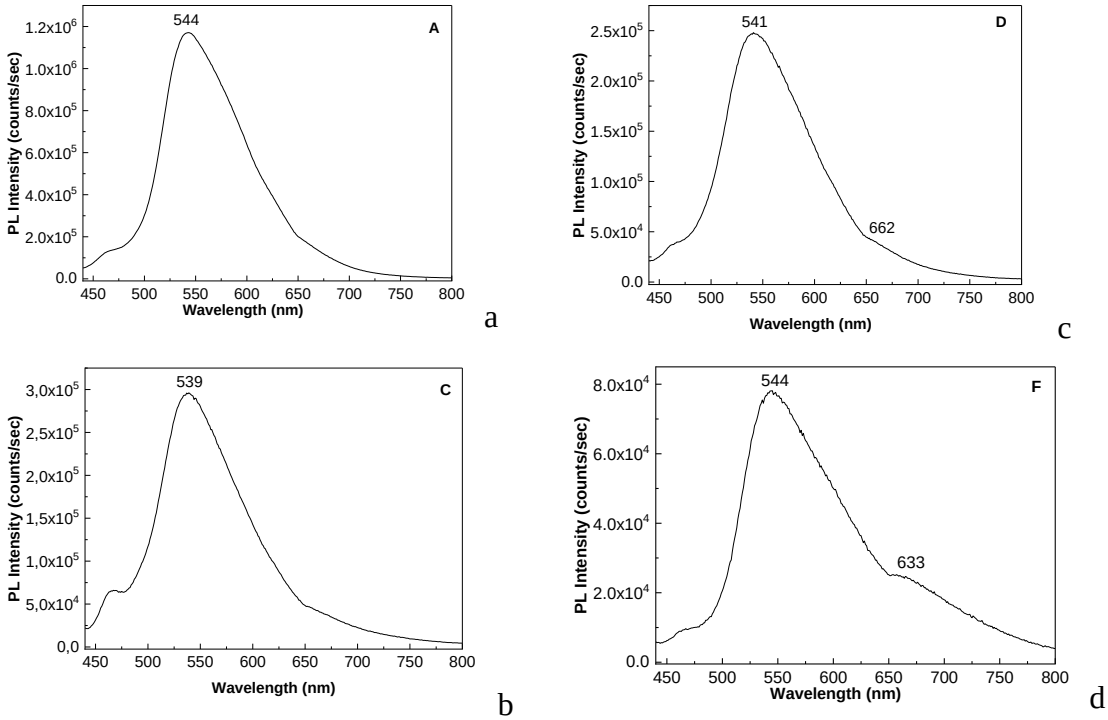


**Fig.4** PL spectra of the POPD-PVDF samples labelled A (a), and C (b) as well as the POPD-PVDF/DWNTs composites labeled D (c) and F (d) samples [1].

Figs. 4a and 4b illustrate the role of PVDF as POPD photoluminescence (PL) quenching agent as a consequence of the assembling of the PVDF spheres onto the POPD fibers. According to Fisg.4c and 4d, DWNTs have the role of the POPD-PVDF quenching agent in the case of the POPD-PVDF/DWNTs composites. The role of the PL quenching agent of macromolecular compound is a feature of carbon nanotubes. In order to prove this sentence, Fig. 5 shows the PL spectra of P3HT interacted with S-SWNT and M-SWNTs.

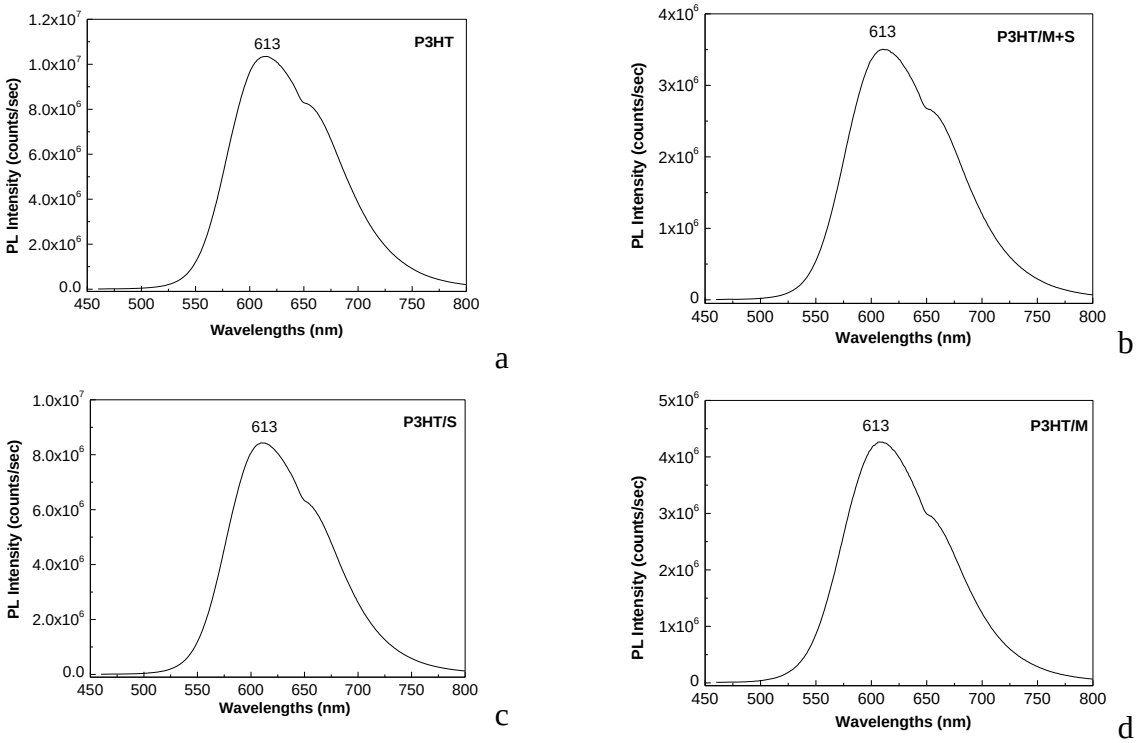


**Fig.5** PL spectra of the solution of P3HT (**a**) and its composites of the type P3HT/M+S-SWNTs (**b**), P3HT/S-SWNTs **c** and P3HT/M-SWNTs (**d**), recorded at $\lambda_{exc}$ = 460 nm. [2]

Our studies focused on the carbon nanotubes and macromolecular compounds have demonstrated: i) the chemical polymerization of ODP in the presence of PVDF and DWNT can lead to the morphological structure based on aggregates consisting from POPD fibers and PVDF spheres and carbon nanotubes, which involve a covalent functionalization of DWNTs with POPD-PVDF; ii) the presence of DWNTs in the POPD-PVDF induce a PL quenching process of macromolecular compound; and iii) the macromolecular compounds PL quenching process can be observed also in the case of other composites such as those based on P3HT and SWNTs.

*References*

1. M. Baibarac, et al., "Optical properties of composites based on poly(o-phenylenediamine), poly(vinylenefluoride) and double-wall carbon nanotubes", Int. J. Molec Sci. 22, 8260 (2021). [ DOI: 10.3390/ijms22158260]
2. M. Baibarac, et al., "Anisotropic photoluminescence of poly(3-hexyl thiophene) and their composites with single-walled carbon nanotubes highly separated in metallic and semiconducting tubes", Molecules 26, 294 (2021) [DOI: 10.3390/molecules26020294 ].

# Photodegradation processes of organic compound used in antipyretic drugs

**M. Daescu[a], M. Iota[a], M. Baibarac[a], Alina C. Ion[b], C. Serbschi[c]**

[a] National Institute of Materials Physics, Optical Processes in Nanostructured Materials, Atomistilor 405A Street, Bucharest, Romania, R-077125

[b] Faculty of Applied Chemistry and Materials Science, University Politehnica of Bucharest, Gh. Polizu 1-7 Street, Bucharest, Romania, 011061

[c] Bioelectronic SRL, Cercelus 54 Street, Ploiesti, Romania, 2000

The role of testing the stability of pharmaceutical compounds is to understand how the quality of an active pharmaceutical ingredient varies when different environmental factors are introduced, such as temperature, humidity and light [1]. In order to exemplify the influence of environmental factors, in Figures 1-3 photoluminescence (PL) and photo-luminescence excitation (PLE) spectra of the aqueous solutions of aspirin in the presence of UV light, phosphate buffer (PB) and alkaline medium, are shown.

Fig. 1 shows the PLE and PL spectra of aspirin in the absence (ASA) and presence of excipients (ASE). The exposure to UV light for 342 min. induced, in the case of ASA and ASE samples, the following modifications in: i) the PLE spectra, a gradual increase in the intensity of the band, peaked at 305 nm from 2.1× $10^7$ counts/sec to 6.55 × $10^7$ counts/sec (Fig. 1a), while in the case Fig. 1c one observes a decrease of the two bands peaked at 305 nm and 327 nm from 6.81× $10^7$ counts/sec and 7.5×$10^7$ counts/sec to 1.13 $10^7$ counts/sec and 5.93×$10^7$ counts/sec; and ii) the PL spectra of ASA, having maximum at 358 nm, a gradual decrease in the intensity from 3 × 105 counts/sec to 5.5×$10^4$ counts/sec (Fig. 1b) while in Fig. 1d one remarks an increase in the intensity of the two emission bands at 358 and 403–400 nm [2].

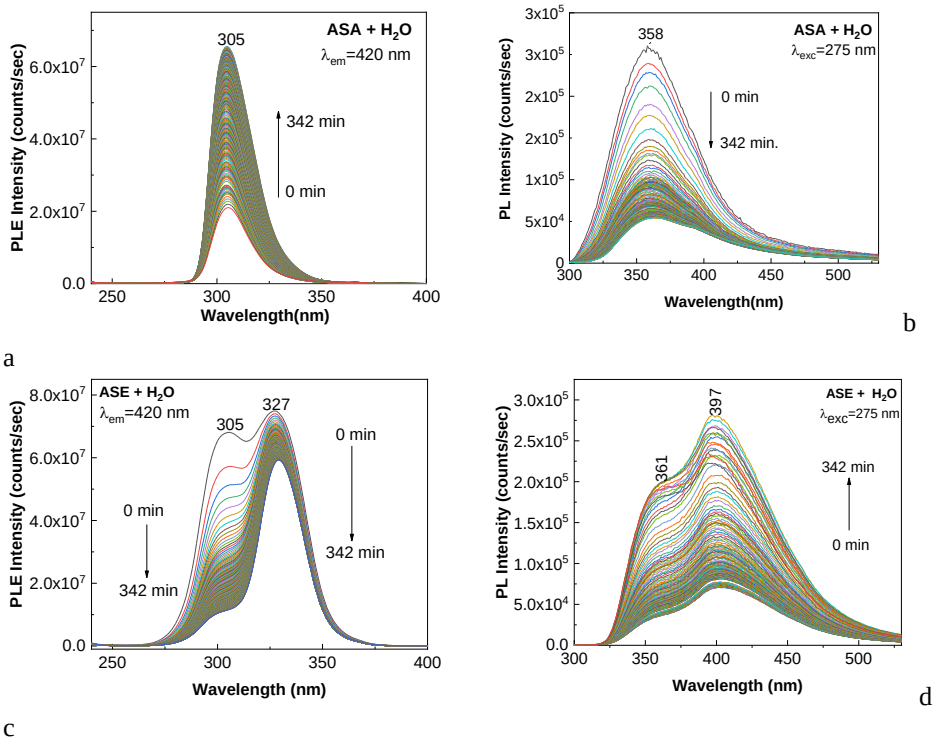


**Fig. 1** PLE and PL spectra recorded under the emission wavelength of 420 nm and the excitation wavelength of 275 nm, respectively, of the aqueous solution of ASA 0.3 M (a, b) and ASE 0.3 M (c, d) [2].

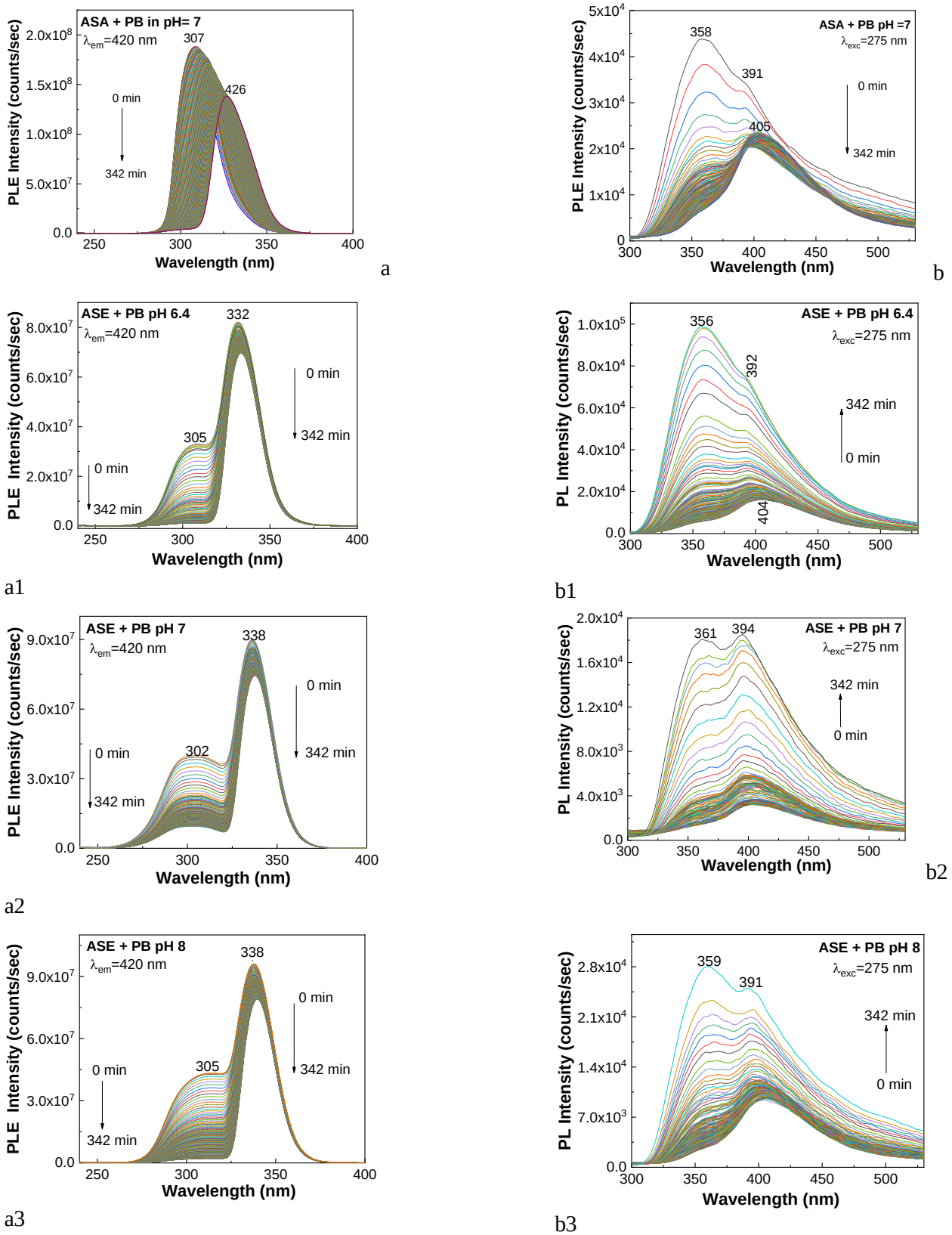


**Fig. 2** PLE and PL spectra of ASA in the presence of PB with pH equal with 7 and ASE in the presence of PB with pH equal to 6.4 (**a**$_1$, **a**$_2$), 7 (**b**$_1$, **b**$_2$) and 8 (**c**$_1$, **c**$_2$). PLE and PL spectra were recorded at the emission wavelength equal to 420 nm and the excitation wavelength equal to 275 nm, respectively [2].

Compared to ASA and ASE in the presence of PB with a pH of 6.4, 7 and 8, the following differences were observed before and after exposure to UV light of these samples: **i)** the PLE spectra of ASA in PB with pH =7 presents an increase in the intensity of the PLE spectra from $1.68 \times 10^8$ counts/sec to

1.88 × $10^8$ counts/sec occurred in the first 17 min, followed by a decrease in intensity to ~1.38 × $10^8$ counts/sec and in the case of ASA in PB with pH=7, the PL spectrum showed two components having maxima at 358 nm and 391 nm, whose intensity gradually decreased from 43.807 counts/sec and 34.644 counts/sec to 6.612 counts/sec and 22.863 counts/sec(Fig. 2 a, b); **ii)** PLE spectra of ASE in PB with pH of 6.4, 7, and 8, presents a decrease in the intensity of the band at 332–338 nm which was observed up to 6.98×$10^7$ counts/sec, 7.45× $10^7$ counts/sec, and 8×$10^7$ counts/sec (Fig.2 a1, b1, c1) while PL spectra for the same samples before the exposure to UV light show two bands having at 356–361 nm and 403–404 nm, whose maximum is shifted to 403–404 nm to 391–394 nm after exposure at UV light (Fig. 2 a2, b2, c2) [2].

Similar variations can be observed in the case of aqueous solutions of ASA and ASE with the solution of NaOH 0.3 M. Figure 3 shows the PLE and PL spectra of the chemical interaction of ASE with NaOH solutions and its evolution under UV light, when a decrease in the intensity of these spectra [2] is reported.

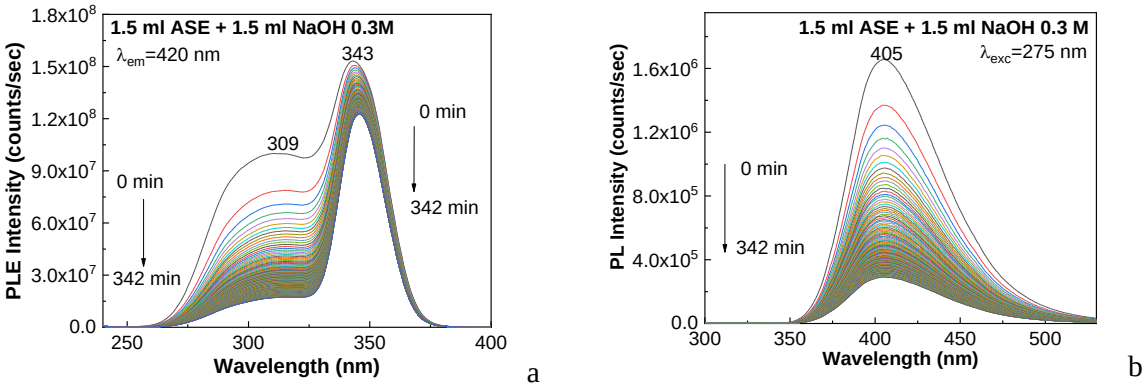


**Fig 3.** PLE and PL spectra of ASE reacted with NaOH 0.3M when the volumetric ratios 1.5:1.5 (a, b), PLE and PL spectra were recorded at the emission wavelength equal to 420 nm and the excitation wavelength equal to 275 nm, respectively [2].

Summarizing above results, these clearly demonstrate that PL is a valuable tool which allows to highlight the photodegradation of aspirin.

*References*


1. H. Khan, M. Ali, A. Ahuja, J. Ali, ''Stability Testing of Pharmaceutical Products—Comparison of Stability Testing Guidelines'', Curr. Pharm. Anal., 6(2), 150 (2010)
2. M. Daescu et al, "The Influence of UV Light on Photodegradation of Acetylsalicylic Acid'', Int. J. Mol. Sci., 22(8), 4046 (2021)

# New insights on the photodegradation of atorvastatin calcium

**M. Daescu[a], M. Oprica[a], M. Iota[a], C. Negrila[a], S. N. Fejer[b], M. Baibarac[a]**

[a] National Institute of Materials Physics, Optical Processes in Nanostructured Materials, Atomistilor 405A Street, Bucharest, Romania, R-077125

[b] National Institute of Materials Physics, Optical Processes in Nanostructured Materials, Atomistilor 405A Street, Bucharest, Romania, R-077125

Atorvastatin calcium (ATC) is a drug that is given to patients with cardiovascular disease, kidney disease, and lowering cholesterol. Recently, in the field of drugs, the subject that has attracted a lot of attention has been their degradation, which has led to the formation of toxic compounds, fact which resulted in a diminution of the therapeutic activity of active compound. The process of photodegradation of ATC is one that can occur both in the preparation of tablets and in their handling by patients. The photodegradation process of ATC in both solid and liquid states was evidenced using photoluminescence (PL) as a complementary tool to the Raman scattering and IR spectroscopy [1].
Fig. 1 shows the photodegradation of ATC in powder and tablet state, when observed in the PLE and PL spectra, before and after exposure to UV light for 216 min., the following differences: i) the PLE spectrum of the ATC in the powder state shows two bands at 288 nm and 315 nm (Fig. 1a$_1$) while in the case of ATC in tablet state two bands at 270 and 318 nm (Fig. 1b$_1$) are remarked; ii) the PL spectra of ATC in the powder and tablet state highlight a band at 369 (Fig. 1a$_2$) and 372 (Fig. 1b$_2$); iii) the exposure to UV light induces a significant decrease in the intensity of the PL and PLE spectra (Fig. 1). These changes indicate that a photodegradation process took place [1].

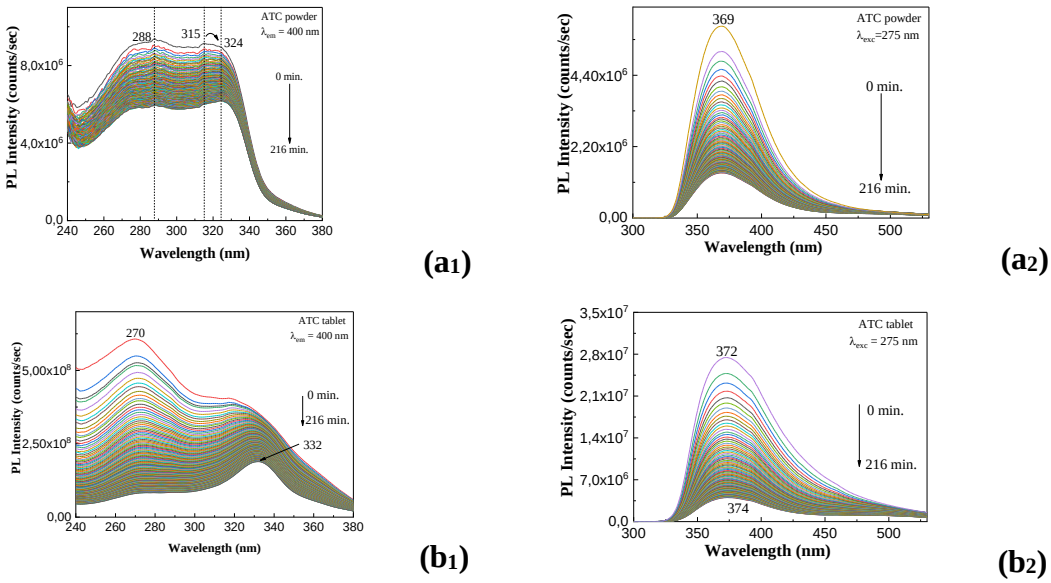


**Fig. 1** PLE (1) and PL (2) spectra of ATC in powder state (**a$_1$**, **a$_2$**) and as tablet (**b$_1$**, **b$_2$**) before and after exposure to UV light for 216 min [1].

A similar behavior is reported in the case of the aqueous solution of ATC. Fig. 2 shows the PLE and PL spectra of the aqueous solution of ATC having the concentration of 2mg/ml. Depending on the pH value of the solution used to dissolve ATC, there are reported changes which involve the change in the profile and intensity of PLE and PL spectra. Fig. 3 shows the evolution of PLE and PL spectra of: i) ATC in the presence of phosphate buffer with pH=8 and ii) the ATC solution interacted with NaOH.

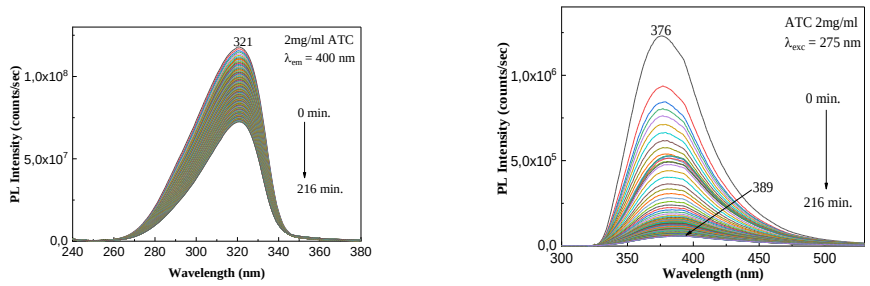


**Fig. 2** PLE (a) and PL (b) spectra of the aqueous solution of ATC (2mg/ml) before and after exposure to UV light for 216 min. [1]

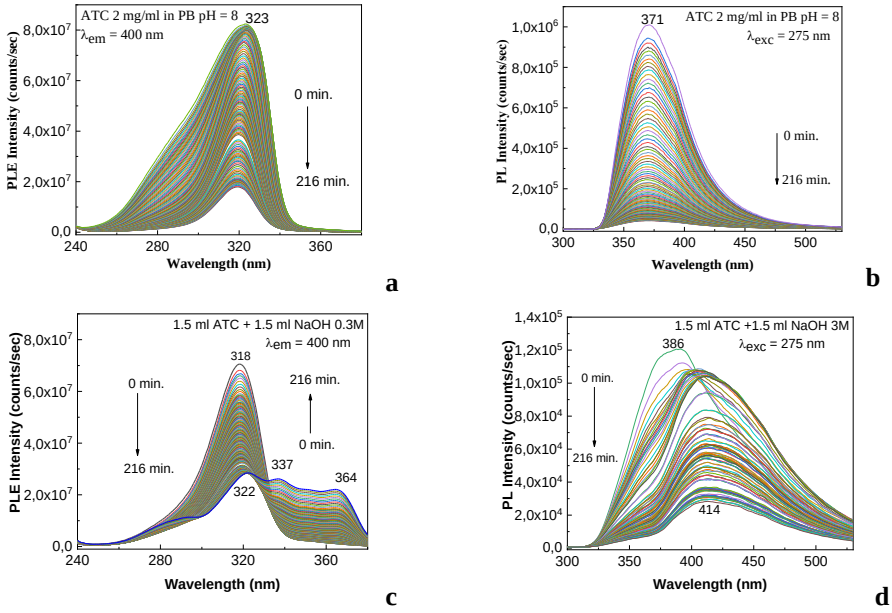


**Fig. 3** PLE and PL spectra of the aqueous solution of ATC (2mg/ml) in PB (pH=8) (a, b) and NaOH-reacted ATC (c, d) before and after exposure to UV light for 216 min. [1]

Fig.3 highlights that in the basic medium, a significant decrease in the intensity of PLE and PL spectra of ATC takes place in comparison with those reported in the case of the aqueous solution of ATC in PB (pH=7) [1]. Considering values of the PLE and PL spectra intensities, before ($I^0_{PLE}$ and $I^0_{PL}$) and after exposure to UV light ($I_{PLE}$ and $I_{PL}$), these become equal to 1.63 and 20.82. According to Ref. [1], these values are smaller than ones reported in the case of the solution of ATC in PB (pH=8) having the concentration of 1mg/ml. A careful analysis of Figs. 3c and 3d illustrates that as increasing the exposure time to UV light, additional to the decrease in the intensity of PLE band one observes the appearance of a new band in the spectral range 330-370 nm and a shift of PL band from 386 nm to 414 nm. In order to explain these variations, Fig.4 shows the Raman and FTIR spectra of ATC before and after interaction with NaOH. Fig. 4a evidences a new Raman line at 1080 $cm^{-1}$ and the increase of the Raman line intensity at 3066-3080 $cm^{-1}$, attributed to NH stretching + OH asymmetrical stretching vibrational mode [1, 2]. An explanation for this increase as well as the presence of IR band at 880, 1159 and 3574 $cm^{-1}$ attributed to the out-of-plane NH bending, C-N/C-O stretching and NH stretching in primary amine [1, 2], can be given taking Scheme 1 into account.

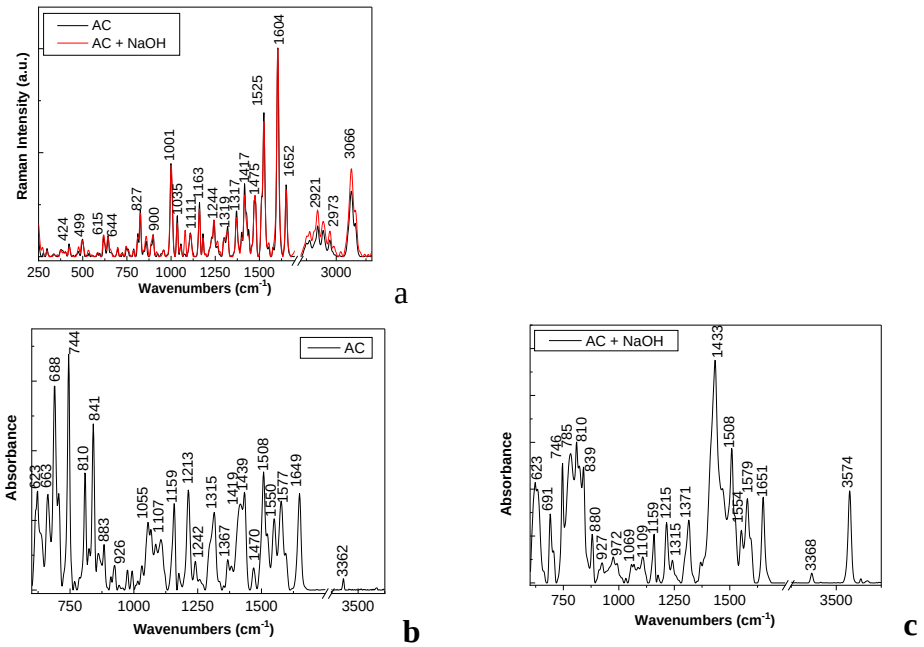


**Fig. 4** Raman spectra of ATC interacted with NaOH (**a**) and IR spectra of ATC before (**b**) and after interaction with NaOH (**c**) [1].

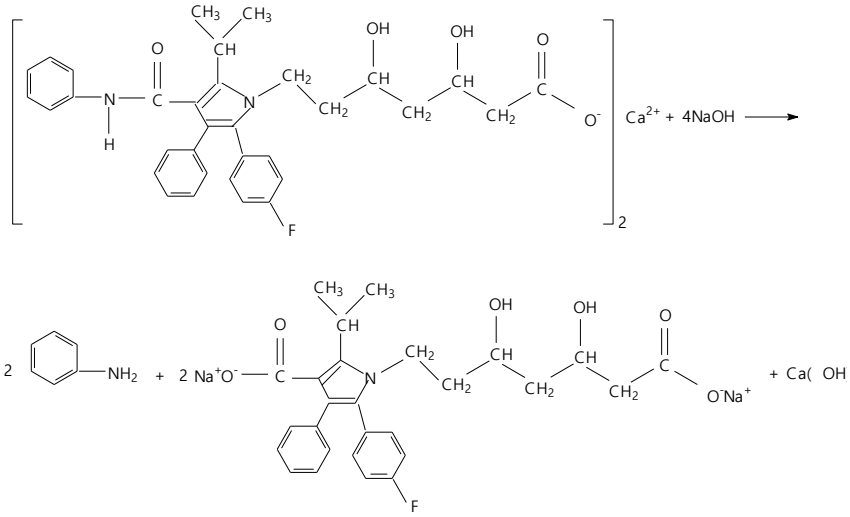

**Scheme 1**. The photochemical reaction of ATC with NaOH when the molar ratio is1:4 (**2**) [1].

In conclusion, above results obtained by PL, Raman scattering and FTIR spectroscopy have demonstrated that the ATC photodegradation is intensified in the presence of $H_2O$ and alkaline medium.

*References*

1. M. Oprica, M. Baibarac et al., "Spectroscopic studies on photodegradation of atorvastatin calcium", Sci. Rep., 11, 15338 (2021) and its references.
2. S. Gunasekaran, T.S.R. Devi, P.S. Sakthivel, FTIR, FTRaman and UV-VIS spectra measurements and analysis on atorvastatin calcium, Asian J. Chem. 19, 335 (2007)

# Optical, structural and dielectric properties of composites based on thermoplastic polymers and ceramic nanoparticles

**I. Smaranda[a], A. Nila[a], M. Stroe[a], L. Stingescu[a], M. Cristea[a], R. C. Cercel[a], M. Daescu[a], A. Lorinczi[a], P Ganea[a], I. Mercioniu[a], C. Bartha[a], I. Zgura[a], A. Trandabat[b], R. C. Ciobanu[b,c], C. Schreiner[b,c], R. G. Garcia[d], M. Baibarac[a]**

[a] National Institute of Materials Physics, Optical Processes in Nanostructured Materials, Atomistilor 405A Street, Bucharest, Romania, R-077125

[b] SC All Green SRL, 8 George Cosbuc, 700470 Iasi, Romania

[c] Faculty of Electrical Engineering, Department of Electrical Measurements and Materials, Technical University Gh. Asachi Iasi, Bd. Professor Dimitrie Mangeron 67, 70050 Iasi, Romania

[d] Izertis, Parque Cientifico Tecnologico, Avda. Del Jardin Botanico, 1345 Edificio Intra, 33203 Gijon, Spain

The influence of ceramic nanoparticles (CNs) of the type $BaTiO_3$, $BaSrTiO_3$ and $SrTiO_3$ on the optical and conductive properties thermoplastic polymers (TPs) such as polyurethane (TPU) and polyolefin (TPO) were investigated [1, 2]. The interest for the composites based on CNs and TPs was given off of their applications as fused filament, profile, the automotive panels, and so on. Figure 1 highlights that: i) chemical interaction of TPU with TPO induces the changes in the intensity and the profile of PL spectrum shown in Fig. 1a, as increasing the TPU weight in the TPU:TPO blends mass and ii) CNs has the role of PL quenching agent of TPU:TPO 2:1, as increasing CNs weight in the TPU:TPO blends, a decrease in the intensity of the PL spectra of TPs, accompanied by a down-shift of the maximum of PL spectrum from 459 to 445, 439 and 420 nm is reported [1].

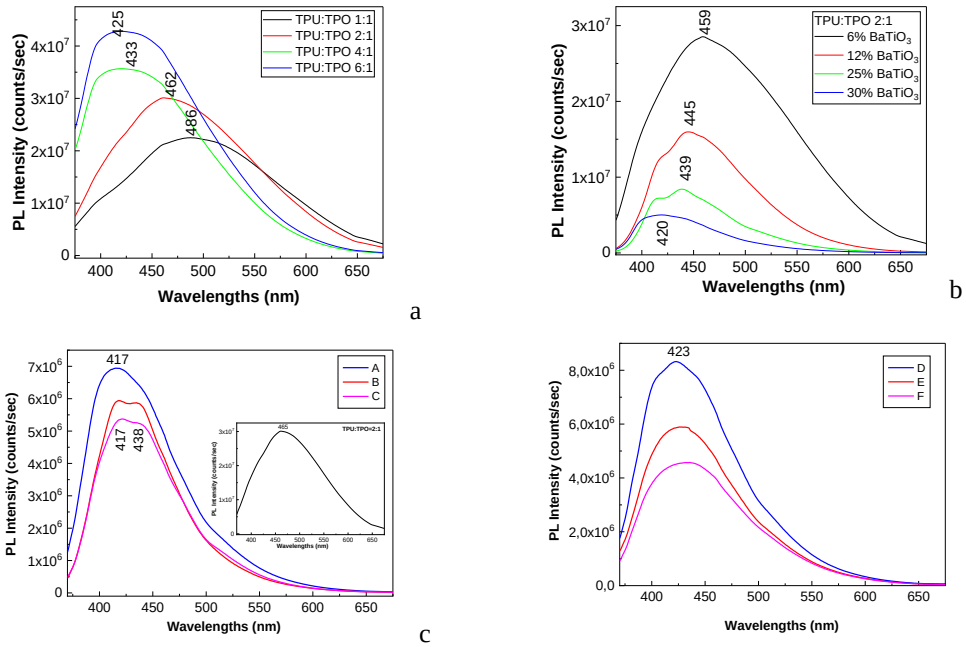


**Fig.1** PL spectra of : a) the TPU:TPO blends, when the mass ratio is 1:1, 2:1, 4:1 and 6:1 and b) the CNs weight in the TPU:TPO 2:1 blend is equal to 6.25 wt.%, 12 wt.%, 25 wt.% and 30wt. %. [1]. Figs. c and d shows PL spectra of the TPU:TPO 2:1 blends, when the $BaSrTiO_3$ and $SrTiO_3$, respectively, when the CNs concentration 6 (blue curves), 12 wt.% (red curves) and 25 wt.% (magenta curves)[2]

Figs.1c and 1d have proved a similar behavior for the CNs of the type $BaSrTiO_3$ and $SrTiO_3$ show in the case of the TPU:TPO 2:1 blends. In order to understand the adsorption of TPs onto CNs, he PL anisotropic analysis were carried out. These analysis have evidenced changes in the binding angle of TPs onto the CNs surface from $23.7^0$ for the TPU:TPO 2:1 blend to: i) $46.9^0$, $51.5^0$ and $49.3^0$, when the $BaSrTiO_3$ concentration is equal to 6, 12 and 25 wt.% (Fig.2) and ii) $66^0$, $52.4^0$ and $53.4^0$ when the $SrTiO_3$ concentration is equal to 6, 12 and 25 wt.% [2]. These differences were correlated with the aggregation of CNs in the TPU:TPO matrix [2].

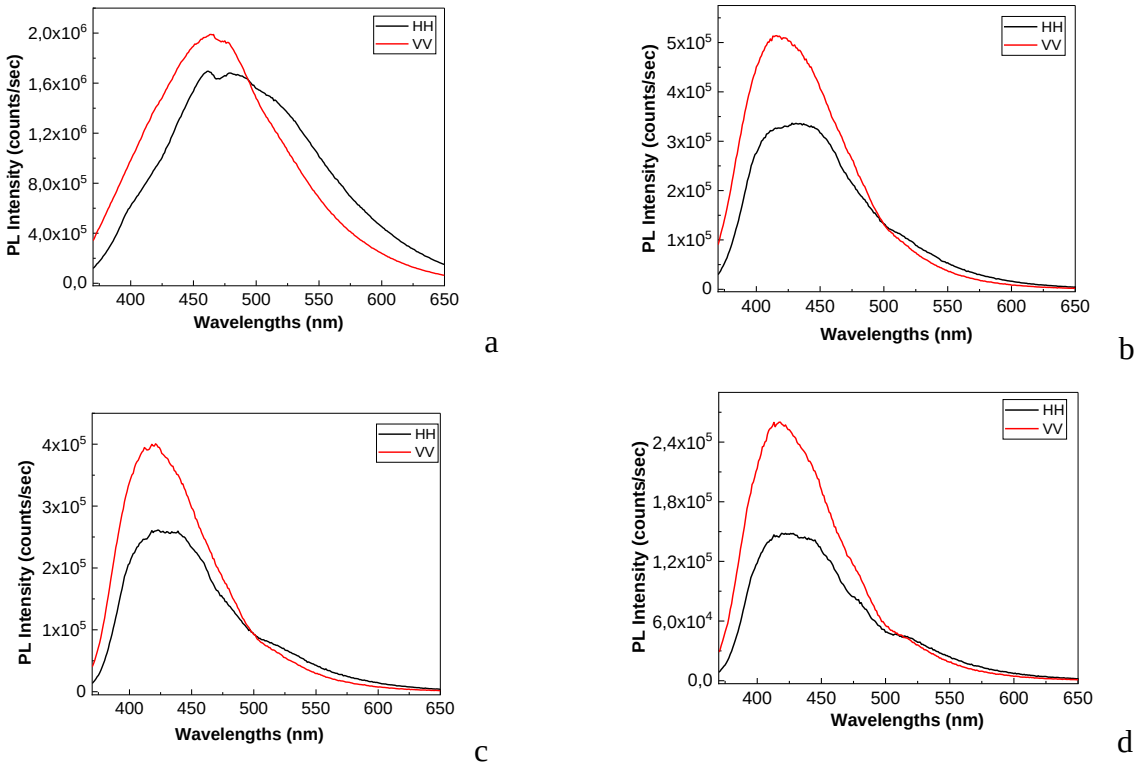


**Fig.2** Anisotropic PL of the TPU:TPO 2:1 blends (a) and their composites with $BaSrTiO_3$, when the CNs concentration is 6 wt.% (b), 12 wt.% (c) and 25 wt.% (d) [2]. Red and black curves correspond to PL spectra recorded when the emission and excitation polarizors are both in horizontal (HH) and vertical (VV) position [2].

The electrical conduction analysis (Fig.3) have indicated two mechanisms which are remarkable by i) the increase of dielectric constant and dielectric losses at low frequencies, simultaneous with the emergence of a plateau region of electrical conductivity when the frequency range is the same; this electrical conduction does not induce the variations in the mechanism of the carriers generation; and ii) an electrical dipolar relaxation at high frequencies [2].

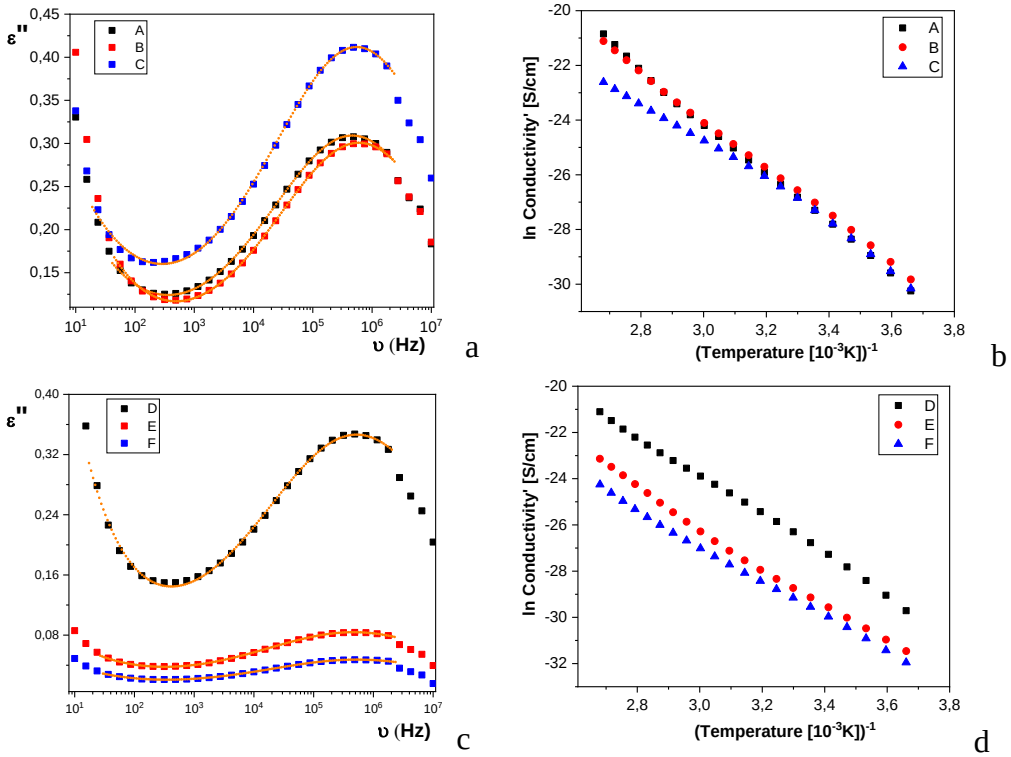


**Fig. 3** Permittivity spectra of the TPU:TPO 2:1/$BaSrTiO_3$ at T=293 $^0$K (a) and electrical conductivity Arrhenius plot (b) - the A, B and C samples correspond to the TPU:TPO2:1 with a CNs concentration of 6, 12 and 25 wt.%. Figs. C and d show the

permittivity spectra and electrical conductivity Arrhenius plot of the TPU:TPO 2:1/$SrTiO_3$ samples, when the CNs concentration is equal to 6, 12 and 25 wt.%.

In conclusion, results published in Refs. 1 and 2 have demonstrated that: i) CNs are the PL quenching agents of the TPU:TPO blends; ii) the change of the binding angle of TPs in the presence of CNs indicates a preferential orientation of TPs onto the CNs surface; and iii) dielectric spectroscopy studies achieved using samples based on TPU:TPO blends and CNs of the type $BaSrTiO_3$ and $SrTiO_3$, have indicated two mechanisms, the former of the type of the electrical conduction and the latter one corresponds to the dielectric-dipolar relaxation processes.

*References*


1. M. Baibarac, et al., "Optical, Structural, and Dielectric Properties of Composites Based on Thermoplastic Polymers of the Polyolefin and Polyurethane Type and $BaTiO_3$ Nanoparticles", Materials (Basel), 14(4), 753 (2021)
2. I. Smaranda, et al., The Influence of the Ceramic Nanoparticles on the Thermoplastic Polymers Matrix: Their Structural, Optical, and Conductive Properties, Polymers, 13(16), 2773 (2021)

# Effect of the nanostructuring on the properties of bio-organic thin films

**A. Stanculescu[1], M. Socol[1], O. Rasoga[1], C. Breazu[1], G. Petre[1], N. Preda[1], A. Costas[1], P. Ganea[1], T. Tite[1], E. Matei[1], M. C. Bunea[1], F. Stanculescu[2], G. Socol[3], A. M. Baracu[4], M. A. Avram[4], A. Dinescu[4], P. C. V. Thrane[5], C. A. Dirdal[5]**

[1]National Institute of Materials Physics, 405A Atomistilor Street, P.O. Box MG-7, Magurele, Romania, 077125
[2]University of Bucharest, Faculty of Physics, 405 Atomistilor Street, P.O. Box MG-11, Magurele, Romania, 077125
[3]National Institute for Laser, Plasma and Radiation Physics, Str. Atomistilor, Nr. 409, PO Box MG-36, Magurele, Romania, 077125
[4]National Institute for Research and Development in Microtechnologies IMT Bucharest, 126A, Erou Iancu Nicolae St, Voluntari, Romania, 077190
[5]SINTEF Microsysemst and Nanotechnology, Gaustadalleen 23C, Oslo, Norway, N-0737

Nowadays, the nanostructures and nanoparticles, a very active area of research and development in the fields of nanotechnology and nanoscience, play a very important role in the materials science. This topic has attracted a growing attention because with nanometers dimension there are correlated interesting and new phenomena related to physical, chemical and biological properties of the materials or the improvement of the existing functions. Nanostructured materials research area refers both to materials that have structural features in the nanometers range and to materials that have been patterned using specific techniques. On the other hand, environmentally-friendly bio-organic materials have become a topic of high interest in organic electronics and a suitable nanostructuring by interfacial modification is a way of improving the devices' performances and development of future applications. In this context we have investigated both the effect of a carbon based nanomaterial and the effect of a periodic network of surface nanostructures on the properties of the bio-organic layers deposited on top, such as polypeptides and nucleic acid bases.

From the polypeptides, the amyloid beta/Aβ(1-42) was selected, which is one of the most important components of the brain plaques, associated with the neurodegenerative diseases through the secondary structure forms developed during the molecular assembling [1]. The investigation of the effect of carbon nanomaterials on the aggregation particularities of Aβ(1-42) layers in the presence/absence of lipids, such as cholesterol (Ch), is important in order to understand the mechanism for the generation of neuronal disorder and how it can be inhibited. Amyloids are also nanomaterials with a wide area of potential applications from nanotechnology to biotechnology. The Langmuir-Blodgett (L-B) and drop cast (DC) methods were used to investigate the formation of the secondary structures associated with Aβ(1-42) cytotoxic effect. The effect of a carbon nanomaterial, for example fullerene (C60), on the morphology and composition in secondary structure of the aggregates developed in the layers during their deposition was analyzed [1].

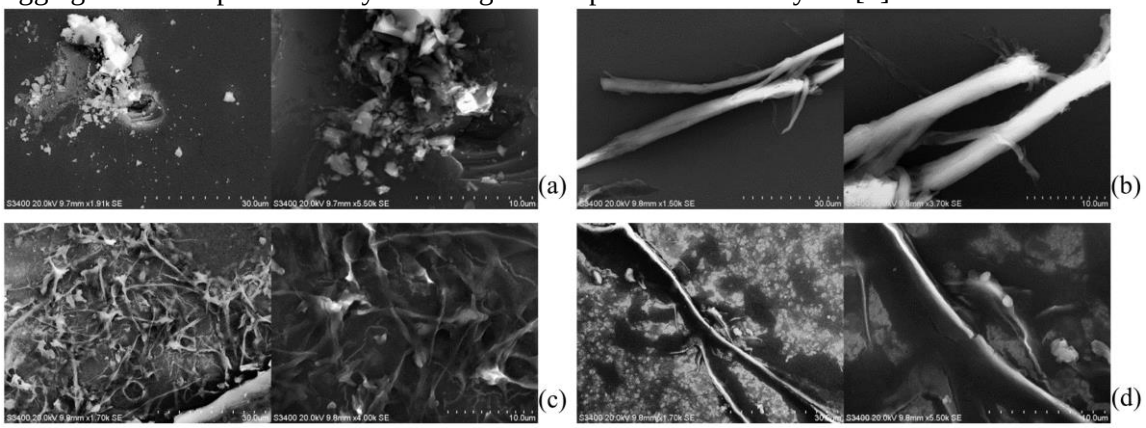


**Fig. 1** SEM images at low and high magnifications of: Aβ(1-42) on Si covered by C60 layer L-B (a); Aβ(1-42) + Ch on Si covered by C60 layer L-B (b); Aβ(1-42) on Si covered by C60 layer DC (c); Aβ(1-42) + Ch on Si covered by C60 layer DC (d) [1].

The particularities characterizing the aggregation of amyloid molecules and the effect of C60 layer on this process, in the presence or absence of Ch, were investigated by the correlation of SEM (Fig.1), EDX (Fig.2) with FTIR, Raman and AFM analysis [1]. SEM images (Fig.1) confirmed that the aggregation and secondary structures development in peptides films deposited on C60 layer in the presence of Ch is affected by the deposition method: L-B or DC. Thus, Ch favored the development

of the fibril secondary structure in the layer of Aβ(1-42) deposited by DC on Si covered by C60 layer. The fibrillization process in the film of Aβ(1-42) deposited by L-B on Si covered by C60 layer has been inhibited by Ch [1]. Thus, there have been identified the factors favoring and those inhibiting the appearance of the structural forms of Aβ(1-42) which could be associated either with different charge carrier transport mechanisms and electrical properties, important for electronic applications, or different neurotoxicity, with medical relevance [1].

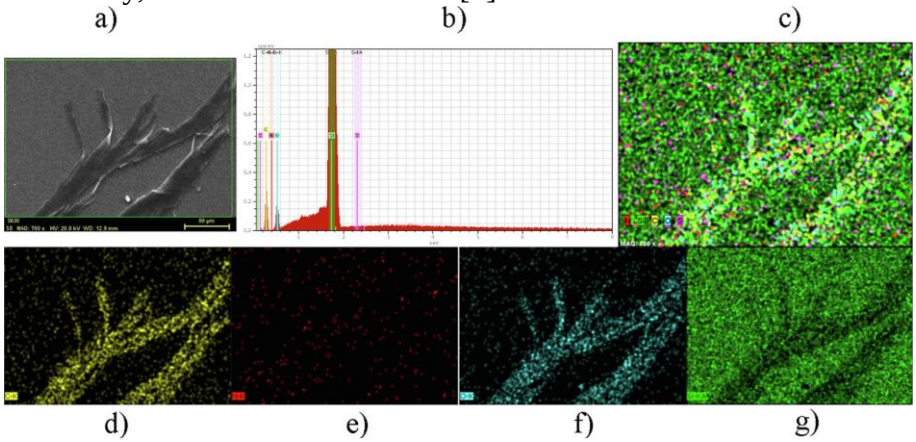


**Fig. 2** Example of EDX analysis for Aβ(1-42)+Ch film deposited by DC on Si covered by C60 layer: SEM image (a); EDX spectrum; (b); EDX mapping for all elements(c); EDX mapping for each element: C-(d), N-(e), O-(f), Si-(g).

The effect of the surface 2D patterning on the structural, morphological, optical and electrical properties of the heterostructures realized with materials with biological significance such as nucleic acid bases, has been investigated.

Thus, we realized a comparative study between two methods which could be used to develop nanostructures on a rigid substrate, for example silicon [2]. Electron Beam Lithography (EBL) and UV Nanoimprint Lithography (UV-NIL) were used to design and manufacture metasurface lenses, consisting in a periodic network of rectangular nanostructures, optimized for focusing wavelength with 1.55 μm (Fig.3). It was revealed that the geometrical rectangular shape of the nanostructures is affected by rounding during the pattern transfer processes from the resistance to silicon due to the presence of a thicker residual layer in the UV-NIL process, affecting the lens' efficiency [2].

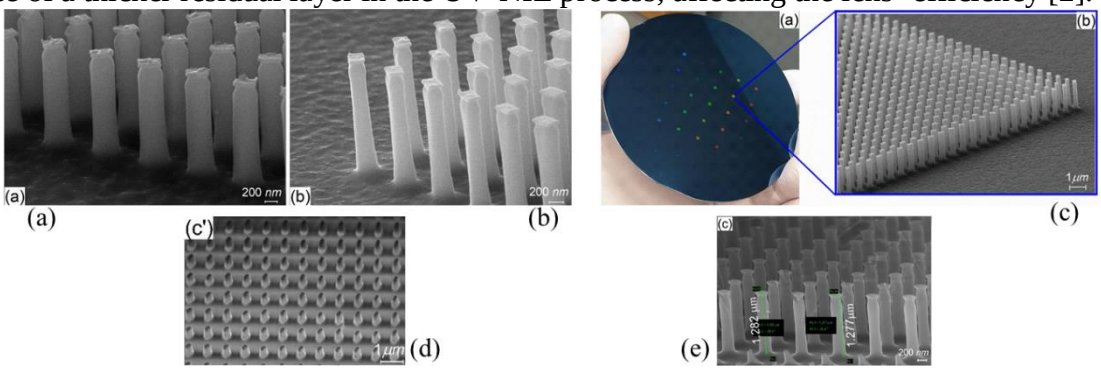


**Fig. 3** EBL rectangular nanostructures patterned in Al (a) and Ti (b) films. Si wafer with EBL nanopatterned metasurfaces (c). SEM micrographs of the UV-NIL nanostructures (metalens): resist (d) and Si (e) [2].

Considering the simple technology involved and the significant advantages (high throughput and low cost) UV-NIL was selected to develop the 2D array of nanostructures in a polymeric layer on glass substrate and the ITO electrode was deposited on both nanostructured and flat substrate [3]. The preservation of the 2D array of nanostructures after the deposition of ITO (Fig.4a,b) and nucleobases thin films (Fig.5) has been revealed by the SEM images, the particularities of each base determining the molecular arrangement in the organic layers [3].

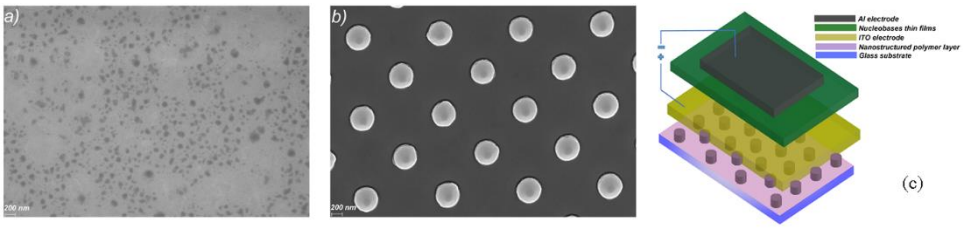


**Fig. 4** SEM images of the ITO films deposited on flat (a) and nano-patterned substrate (b). Schematic representation of the investigated heterostructures on nano-patterned ITO electrode (c) [3].

The films deposited on nano-patterned ITO showed an increase in absorption due to the decrease of the incident photons loss by multiple reflections, compared to the films deposited on flat ITO [3]. The emission properties of the bio-organic films deposited on nanostructured ITO electrodes are affected by the reflections on the walls of the cavities, deliniated by the pillars of the nanostructure and filled with nucleobase molecules, and re-absorption of the emitted radiation [3].

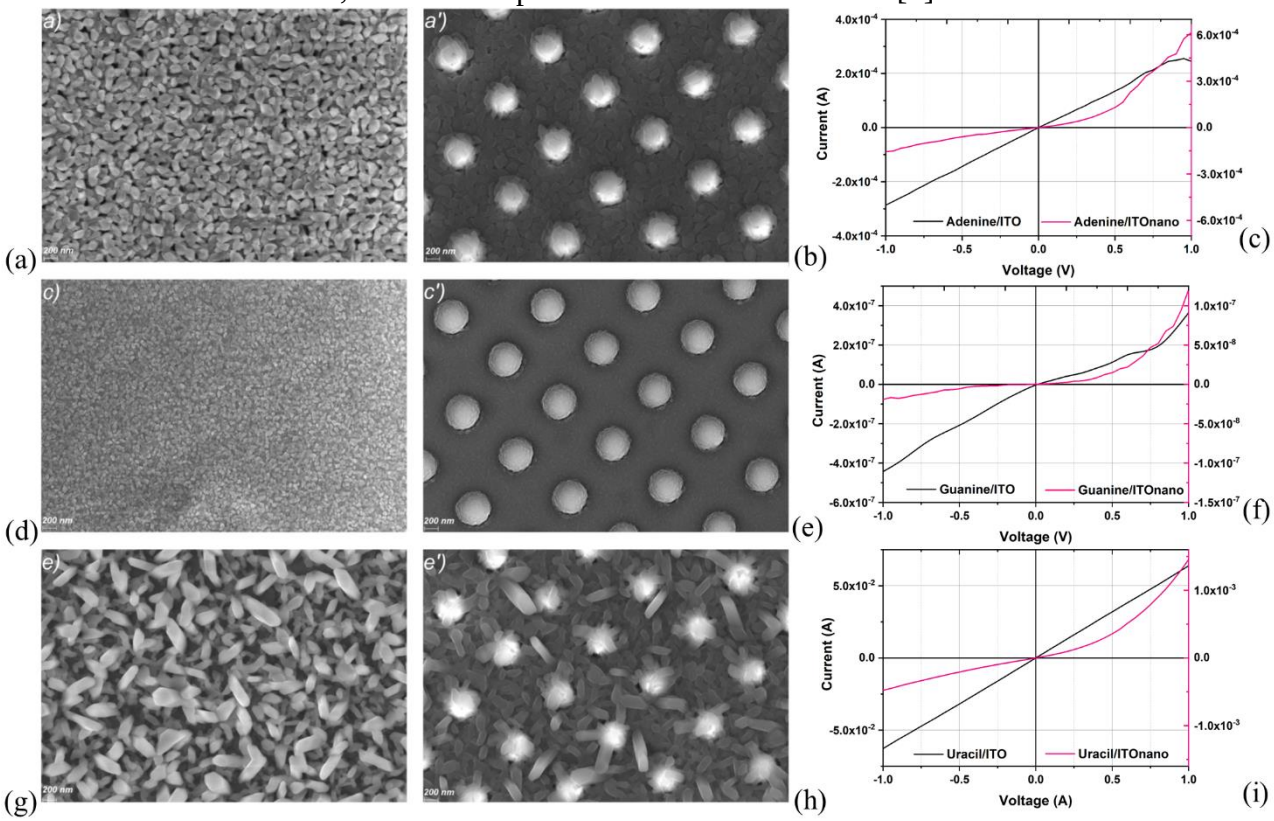


**Fig. 5** SEM images of the adenine, guanine and uracil deposited on flat glass/ITO (a,d,g) and nano-patterned glass/ITO (b,e,h) and I-V characteristics of the heterostructures (Fig.4c) based on: adenine (c), guanine (f), uracil (i) [3].

The I-V characteristics in dark (Fig.5) of the heterostructures with adenine, guanine and uracil film on nano-patterned ITO showed a behavior close to rectifying diode as a result of energetic criteria, large collection area of the electrode, pathway of the charge carriers and film's morphology [3].

*References*

1. C. Breazu, O. Rasoga, M. Socol, P. Ganea, F. Stanculescu, T. Tite, E. Matei, A. Stanculescu, "The effect of fullerene layer on the aggregates formation in amyloid beta Langmuir-Blodgett films", Appl. Surf. Sci. 537, 147800 (2021).
2. A. M. Baracu, M. A. Avram, C. Breazu, M. C. Bunea, M. Socol, A. Stanculescu, E. Matei, P. C. V. Thrane, C. A. Dirdal, A. Dinescu, O. Rasoga, " Silicon metalens fabrication from Electron Beam to UV-nanoimprint Lithography", Nanomaterials 11(9) 2329 (2021).
3. C. Breazu, M. Socol, N. Preda, O. Rasoga, A. Costas, G. Socol, G. Petre, A. Stanculescu, " Nucleobases thin films deposited on nanostructured transparent conductive electrodes for optoelectronic applications", Sci. Rep. 11(1), 7551 (2021).

# New perspectives and developments for rare-earth doped sol-gel derived nano-glass ceramics

**M. Secu, C.E. Secu and C. Bartha**
National Institute of Materials Physics, Atomistilor Str 405A, 077125 Magurele, ROMANIA

Glass-ceramics technology is based on the controlled nucleation and crystallisation of the precursor glass, thermally converted into a glass-ceramic formed by one or more crystalline phases evenly distributed within the glass phase [1]. The improved functionalities of the dispersed crystals make the transparent oxyfluoride glass-ceramic a new generation of tailorable optical materials with high potential for optical related applications such as optical amplifiers, optical waveguides, white LEDs. Their key features are related to the high transparency given by the fluoride nanocrystals smallness (i.e. nanometers size) and luminescence properties, while keeping the advantages of oxide glasses.
Sol-gel chemistry offers a flexible synthesis approach to prepare various materials such as glass, ceramics, and organic-inorganic hybrids by using colloidal solutions (sol) as starting materials [3]. The glass ceramics' synthesis by using the sol-gel method has several advantages such as lower processing temperature, the ability to control the purity and homogeneity of the final materials on a molecular level, and the large compositional flexibility that is difficult to obtain via the melt-quenching technique.
The synthesis sol-gel derived oxyfluoride glass ceramics are based and limited to the synthesis initially developed by Fujihara et al. [4,5], using TMOS and/or TEOS as the $SiO_2$ precursor and TFA as the fluorine source. The synthesis is performed in two steps: (i) preparation of a silica sol gel by using classic route with metal alkoxides (ii) followed by mixing with a second rare-earth trifluoroacetates solution. The liquid mixture is dried and aged at room temperature under sealed containers for several days or weeks. The nanocrystalline phase precipitation is obtained during subsequent calcination of dried xerogel above the thermal decomposition temperature of trifluoracetates at around 300 °C. Since then, the number of the publications on that topic has increased steadily and many compositions and crystalline phases have been studied using different $Ln^{3+}$ ions as dopants to obtain enhanced linear and nonlinear optical processes for a wide application range. Most of the research efforts were dedicated to oxyfluoride glass ceramics with a simple composition according to the formula: $(100 - x)\ SiO_2\text{-}xM1F_2/M2F_3/M1M2F_4$, where M1 and M2 are alkaline, alkaline-earth metals, or lanthanide elements, respectively [6]. The research efforts were focused primarily on optical (luminescence) properties of the RE-doped nanocrystals.
As the sol-gel method shows a large compositional flexibility and a high control of final material, future research efforts are expected to be dedicated to the discovery of new glass ceramic materials with multifunctional properties (optical, electric, and magnetic) for new and improved applications ([7] and references therein). Several steps in this direction have been made (see below) ([7] and references therein) but there is still much to do: new compositions and new applications or improvement of present ones.
(i) The sol-gel route has been used to obtain new oxyfluoride glass-ceramics compositions comprising thernary fluoride nanocrystalline Me1Me2F4 phases embedded in silica matrix, with Me1=Na,K, Me2=Y,La,Gd) [8-14] and their optical properties related to the rare-earth ions dopants have been investigated. In these cases, the crystallization mechanism seems to be more complicated and the decomposition of metal trifluoroacetates is likely to be accompanied by some chemical reaction between metal and fluorine partners, followed by nanocrystalline phase precipitation within the glassy matrix. It was observed that the nature of the final precipitate crystalline phase is strongly dependent on the molar ratio between trivalent ion (Y, Gd, La) and alkali metals ions (Li, Na or K), and in general, mixtures of fluorides were obtained [9,13,14] or different phase mixtures of the same compound (cubic and/or hexagonal nanocrystals [10,11]. Hence, a deeper investigation of the crystallization mechanism and optimization of the initial composition and processing parameters (time and temperature) is required to obtain and to control the precipitation of the desired crystalline phase.

(ii) Transparent ***glass ceramic waveguides*** offer specific characteristics of capital importance for photonics related applications and the sol-gel approach has proved to be a very convenient and flexible way to deposit glass ceramic thin films on a variety of substrates for different applications, such as planar waveguides or integrated optics. New glass ceramic thin films comprising RE-doped oxide semiconducting nanocrystals such as $SnO_2$, $ZrO_2$, $CeO_2$, $HfO_2$ have been already obtained and optical properties studied [82-84]. The investigations of optical and electric properties would be interesting for basic and applied research.

(iii) New developments of the glass ceramic films can include ***patterned glass ceramic thin films*** that can be produced by using laser-induced crystallization [18] allowing the development of active integrated optical circuits. Moreover, a higher crystallized fraction of the nominal active fluoride crystalline phase is expected to improve the optical properties. Recent studies have shown that crack-free $SiO_2$-$LaF_3$ glass ceramic films with a crystalline $LaF_3$ crystalline fraction of 18 wt% can be obtained.

(iv) The investigations of glass ceramics with $Gd^{3+}$-based fluorides nanocrystals embedded in the glass matrix were limited to the analysis of luminescence properties of the co-dopant RE-ions [19,20]. The magnetic properties related to $Gd^{3+}$ ions and the influence of the magnetic field on optical properties, in particular on the energy transfer processes, have been overlooked/missed. Such novel, multifunctional *magneto-optical materials* allow the intertwining between the magnetism and photonics and might offer new opportunities for magneto-optical devices [21].

(v) Sol–gel synthesis has been used to obtain not only thin films but also monolithic silica and glass ceramics [22] giving the opportunity to produce *monolithic scintillating glass ceramics* based on $BaF_2$, $CaF_2$, $CeF_3$ and $BaCl_2$. Proper co-doping with broad blue absorbing sensitizer ions ($Bi^{3+}$, $Sn^{3+}$, etc.) capable to transfer their excitation energy to neighboring *activator* ions might be useful as spectral down-converter for solar cells applications.

(vi) The optical properties investigations of oxyfluoride glass ceramics were focused only on trivalent ions related ones and divalent $Eu^{2+}$ and $Sm^{2+}$ ions were omitted. Previous investigations [23] have shown the incorporation of the reduced $Eu^{2+}$ and $Sm^{2+}$ ions in sol-gel glasses (not ceramic ones) under moderate conditions of temperature and atmosphere in two steps, glass-formation, and their reduction to the bivalent state by calcination in reducing atmosphere. $Eu^{2+}$ and $Sm^{2+}$ ions have attracted significant attention because they have a great potential for various *photonics-related applications or radiation detection*. The $Sm^{2+}$ ion shows persistent spectral hole burning (PSHB) and potential application for high density *optical memories* [24]. On the other hand, $Eu^{2+}$ doping is crucial for scintillator detectors or X-ray storage phosphor for digital imaging applications. However, the incorporation of such bivalent ions into the precipitated nanocrystals from the glass ceramics still remains an open problem.

(vi) A new approach for sol-gel glass ceramics was recently proposed by Cruz M.E. et al. (2020) [25], where dispersed nanocrystals were incorporated in the silica glass matrix. This approach allows the incorporation in the silica glass matrix of a broader range of nanocrystalline phosphors such as $Eu^{2+}$-doped persistent phosphors [26] or $Sm^{3+}$-doped BaFCl for optical data storage applications [24].

In conclusion, sol-gel derived glass ceramic materials based on stabilized rare-earth doped nanoparticles embedded in a glass matrix were demonstrated to be attractive materials for *photonics-related applications*. Moreover, they are showing promising materials *magneto-optical applications* allowing the intertwining between the magnetism and photonics or as *phosphors for radiation detection.* However, the advantages of sol-gel chemistry and thin films' deposition ability have not been fully exploited for advances in both basic and applied research. Therefore, the development of new glass ceramic materials with multifunctional properties for new and improved applications is highly desirable.

*References*


1. J. Deubener et al., "Updated definition of glass-ceramics", J. Non-Cryst. Solids 501, 3–10 (2018)
2. A. Pablos-Martin et al., "Nanocrystallisation in oxyfluoride systems: Mechanisms of crystallization and photonic properties", Int. Mater. Rev. 57, 165–186 (2012)
1. Brinker, C.J.; Scherer, G. Sol-Gel Science: The Physics and Chemistry of Sol-Gel Processing, 1st ed.; Academic Press Inc. New York, NY, USA, 1990; Levy, D.; Zayat, M. The Sol-Gel Handbook: Synthesis, Characterization and Applications; Wiley-VCH: Weinheim, Germany, 2015.
2. S. Fujihara et al., "Formation of $LaF_3$ microcrystals in sol-gel silica", J. Non-Cryst. Solids 244, 267–274 (1999)
3. S. Fujihara et al., "Influence of solution composition on the formation of $SiO_2$/$LaF_3$ composites in the sol gel process" J. Mater. Sci. 35, 2763–2767 (2000)
4. G. Gorni et al., "Transparent Glass-Ceramics Produced by Sol-Gel: A Suitable Alternative for Photonic Materials, Materials 11, 212 (2018)
5. M. Secu et al., "Optical Properties of Transparent Rare-Earth Doped Sol-Gel Derived Nano-Glass Ceramics", Materials 14, 6871 (review) (2021)
6. A. Santana-Alonso et al., "Sol–gel transparent nano-glass ceramics containing $Eu^{3+}$-doped $NaYF_4$ nanocrystals" J. Non-Cryst. Solids 356, 933–936 (2010)
7. M.E. Cruz et al., "Process and Site-Selective Excitation of $Nd^{3+}$ in $LaF_3$/$NaLaF_4$ Sol–Gel-Synthesized Transparent Glass- Ceramics" Crystals 11, 464 (2021)
8. 10. J.J. Velázquez et al., "Novel sol-gel $SiO_2$-$NaGdF_4$ transparent nano-glass- ceramics, J. Non-Cryst. Solids 520, 119447 (2019)
9. M.E. Cruz et al., "$Nd^{3+}$doped- $SiO_2$–$KLaF_4$ oxyfluoride glass-ceramics prepared by sol-gel", J. Lumin. 235, 118035 (2021)
10. A.C. Yanes et al., "Enhanced emission via energy transfer in RE co-doped $SiO_2$-$KYF_4$ nano-glass-ceramics for white LEDs", J. Alloys Compd. 658, 170–176 (2016)
11. G. Kawamura et al., "A unique approach to characterization of sol–gel-derived rare-earth-doped oxyfluoride glass-ceramics", J. Am. Ceram. Soc. 96, 476-480 (2013)
12. M. Secu et al., "Up-conversion luminescence of $Er^{3+}$/$Yb^{3+}$ co-doped $LiYF_4$ nanocrystals in sol–gel derived oxyfluoride glass- Ceramics", J. Non-Cryst. Solids 426, 78–82 (2015)
13. J. del-Castillo et al., "Luminescent properties of transparent nanostructured $Eu^{3+}$ doped $SnO_2$–$SiO_2$ glass-ceramics prepared by the sol-gel method", Nanotechnology 16, S300–S303 (2005)
14. T.T. Van Tran et al., Environment segregation of $Er^{3+}$ emission in bulk sol-gel-derived $SiO_2$-$SnO_2$ glass ceramics. J. Mater. Sci. 2014, 49, 8226–8233.
15. R.R. Gonçalves et al., "Erbium-activated silica-zirconia planar waveguides prepared by sol-gel route", Thin Solid Films 516, 3094–3097 (2008)
16. G.H. Beall et al., "Laser-Induced Crystallization of Transparent Glass-Ceramics" US Patent No. 6928224, 9 August 2005
17. J.J. Velázquez et al., "Transparent $SiO_2$-$GdF_3$ sol–gel nano-glass ceramics for optical applications", J. Sol-Gel Sci. Technol. 89, 322–332 (2019)
18. N. Pawlik et al., "Photoluminescence and energy transfer in transparent glass-ceramics based on $GdF_3$:$RE^{3+}$ (RE = Tb, Eu) nanocrystals", J. Rare Earths 37, 1137–1144 (2019)
19. C.E. Secu et al., "$Gd^{3+}$ co-doping influence on the morphological, up conversion luminescence and magnetic properties of $LiYF_4$:$Yb^{3+}$/$Er^{3+}$ nanocrystals", J. Phys. Chem. Solids 130, 236-241 (2019)
20. Kajihara, K., "Recent advances in sol–gel synthesis of monolithic silica and silica-based glasses", J. Asian Ceram. Soc., 1, 121–133 (2013)
21. M. Nogami et al., "Enhanced emission from $Eu^{2+}$ ions in sol-gel derived $Al_2O_3$–$SiO_2$ glasses", Appl. Phys. Lett. 69, 3776–3778 (1996)
22. N. Riesen et al., "Towards rewritable multilevel optical data storage in single nanocrystals", Opt. Express 26, 12266–12276 (2018)
23. M.E. Cruz et al., "A new sol–gel route towards $Nd^{3+}$-doped $SiO_2$–$LaF_3$ glass-ceramics for photonic applications", Mater. Adv. 1, 3589–3596 (2020)
24. Y Li et al., "Long persistent phosphors-from fundamentals to applications", Chem. Soc. Rev. 45, 2090–2136 (2016)

# Structural and morphological peculiarities of $NiO/NiWO_4/WO_3$ nanowire heterostructures for gas sensing

**Valentin-Adrian Maraloiu,[a] Navpreet Kaur,[b] Dario Zappa,[b] Elisabetta Comini [b]**
[a]National Institute of Materials Physics, 405A Atomistilor Str., Magurele, Romania, 077125
[b]SENSOR Laboratory, Department of Information Engineering, University of Brescia, Via D. Valotti 9, Brescia, Italy, 25133

Volatile organic compounds (VOCs) are among the most common and highly harmful for human life air pollutants (Threshold Limit Value = 250 ppm) [1–5]. Also, the amount of acetone exhaled in the human breath is used for the detection of diseases such as diabetes [6]. Nitrogen dioxide ($NO_2$), another highly toxic and harmful volatile inorganic compound, comes from the combustion of fossil fuels and the exhaust of motor engines. The Occupational Safety and Health Administration (US) [4] set that the maximum permissible exposure for general industries is 5 ppm, reduced to 1 ppm for short-term exposure. Thus, highly sensitive sensors are needed for the detection of $NO_2$ and acetone at such low threshold values.

Nowadays, the research in the chemical/gas sensor technology is mainly focused on the improvement of selectivity, sensitivity and fast reactivity [7–8]. There are several ways to improve the selectivity of metal oxide-based gas sensors: functionalization, doping/addition or building a junction between two similar or dissimilar materials [9–11]. Another approach is to build sensor arrays consisting of various metal-oxide sensing elements combined with pattern recognition algorithms [12, 13]. Particularly, nano-heterostructure devices based on metal oxides received significant attention due to their superior sensing performances as compared to individual nano-materials [14]. The interface between two nanostructured materials modifies the charge carrier transport and increases the surface area for reaction with gas analyte by bringing both nanostructured materials on single sensing platform.

In this work [15], the design of the metal oxide-based 3D nanostructure system based on $NiO/NiWO_4/WO_3$ heterostructure directly synthetized on the active transducers and their integration into a single sensing platform is presented.

For structural analysis of intermediate $NiWO_4$, the heterostructure samples were investigated by Transmission Electron Microscopy (TEM). Firstly, the diameter of the branches of $WO_3$ formed on the NiO core ranges between 6 and 11 nm, as presented in the Conventional TEM (CTEM) images (Figure 1). The average diameter of the small nanowires was calculated around 8.6 nm. Figure 2b,c demonstrates the formation of a nucleation site on the NiO nanowire, from which a small branch initiates. This kind of nucleation can be explained using a vapor-solid (VS) mechanism related to the vapor phase growth method. In VS growth, the source materials ($WO_3$) are vaporized at high temperature and directly condensed on the target surface (NiO NWs). Once the condensation process starts, the initially condensed molecules create a seed crystal that serve as nucleation sites for the further growth of nanostructures.

Selected Area Electron Diffraction (SAED) pattern (figure 2b) of the heterostructures taken from the nanostructures presented in figure 2a clearly show the superposition of different lattices due to the materials composing the heterostructure. Here, [110] and [112] reflections were related to $WO_3$, while for $NiWO_4$ [111] and [221] reflections were observed.

Moreover, High-Resolution TEM image (Figure 2c) clearly shows the interface between two phases related to $WO_3$ and $NiWO_4$. In figure 2a, c, the formation of a $NiWO_4$ seed is clearly visible. The $NiWO_4$ intermediate phase between core of NiO and $WO_3$ was found highly crystalline with orientation of (110) corresponding to a monoclinic crystalline phase of nickel tungstate.

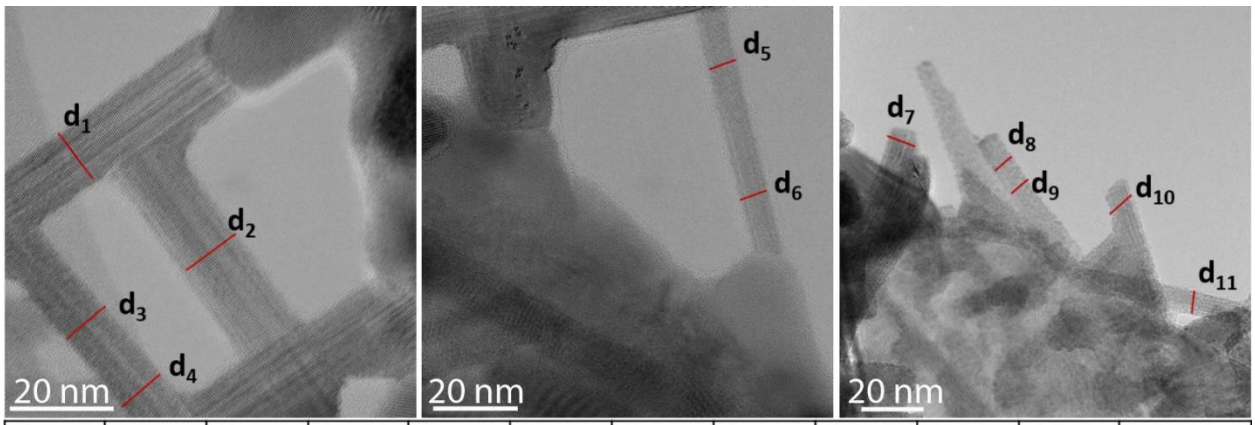


| $d_1$ | $d_2$ | $d_3$ | $d_4$ | $d_5$ | $d_6$ | $d_7$ | $d_8$ | $d_9$ | $d_{10}$ | $d_{11}$ | *Average* |
|---|---|---|---|---|---|---|---|---|---|---|---|
| 11 nm | 12.5 nm | 9.35 nm | 9.4 nm | 6.75 nm | 6.47 nm | 8.74 nm | 7.37 nm | 7.25 nm | 8.44 nm | 7.6 nm | 8.64 nm |

**Fig. 1** TEM images of heterostructure sample including a table form of calculated diameters for the WO3 nanowires.

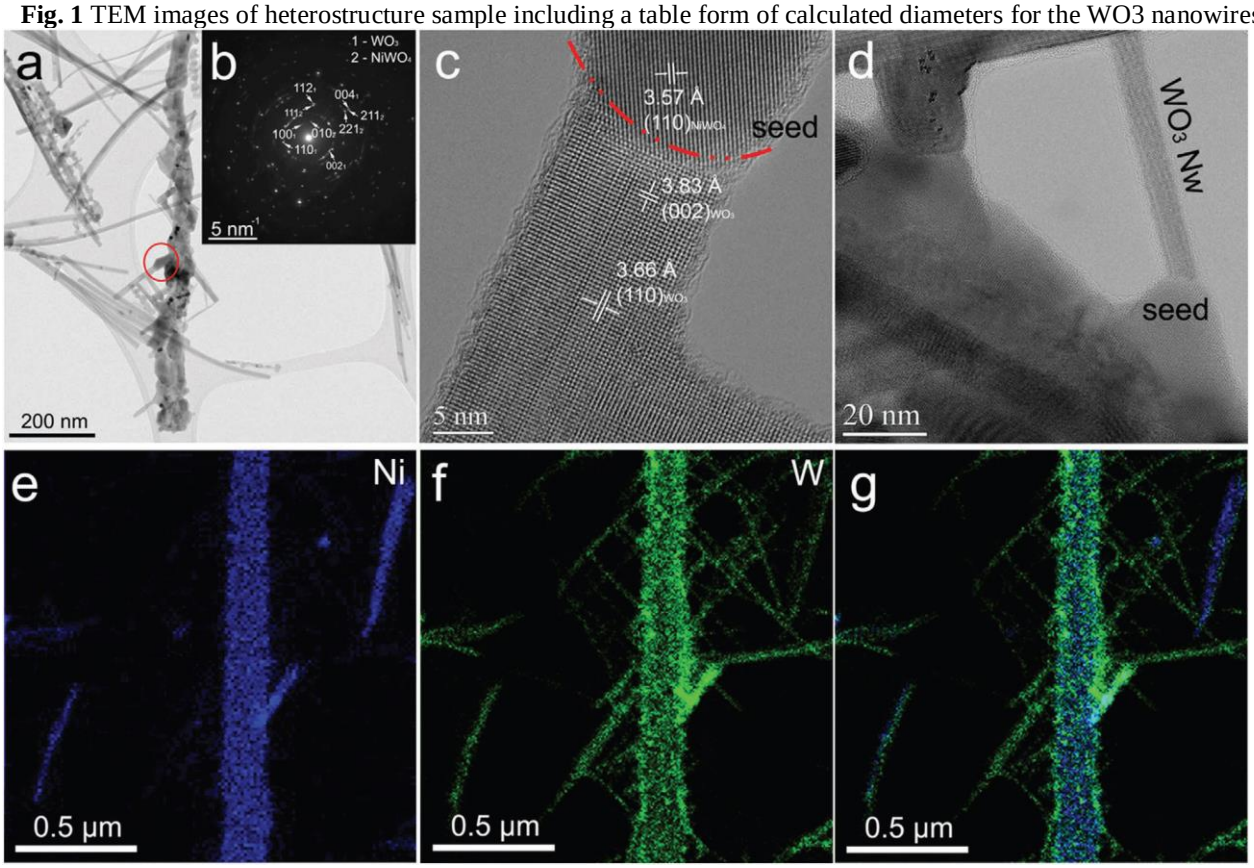


**Fig. 2** (a) CTEM image of NWO heterostructures; (b) SAED pattern of the area marked by red circle in (a); (c), (d) HRTEM images of the interface between seed of NiWO4 and WO3 nanowire; (e) EDX elemental map of Ni; (f) EDX elemental map of W; (g) overlay of Ni and W elemental maps.

Furthermore, EDX maps of the selected chemical elements (Figure 2e-g) show a well identified thick core of NiO with scattered branches of $WO_3$.

A novel and complex heterostructure of $NiO/NiWO_4/WO_3$ has been successfully synthesized by single vapor-phase growth technique on alumina substrates. As synthesized host NiO nanowires show dense and long nanowire morphology with the diameter in the range of 20–60 nm. Structural studies reveal that small $WO_3$ nanowires (diameter 6–11 nm) grew effectively on NiO nanowires surface first by creating a seed of a ternary material NiWO4, which acts as a nucleation site for the $WO_3$ nanowires. Furthermore, the NWO heterostructured sensor shows the superior sensing performances compared to the ones of NiO and $WO_3$ nanowires. In particular, the heterostructured sensors show higher response toward VOCs at temperature of 400 °C and toward $NO_2$ at 300 °C. Based on the

observations and in-depth analysis, the fundamental reason behind their superior performances is the formation of an interface between three nanostructured oxides with tunable and distinctive electrical properties. By controlling the charge carrier's density and their flow within the heterostructure with temperature, the sensors respond selectively toward both oxidizing and reducing gas analytes. Specifically, at 300 °C free electrons in the conduction band of $WO_3$ exist in the heterostructure, which makes them more selectively reactive toward $NO_2$ (oxidizing gas) with a response of 195 toward 5 ppm of $NO_2$. At the same time, at 400 °C, a significant electron-hole recombination consumes the free electrons and large number of holes existing in heterostructures, which makes them more selective toward the electron donating gases. Due to this, at 400 °C sensor showed selectivity toward the VOCs (reducing gases) with a response of 35 and 48 toward 50 ppm of ethanol and acetone respectively. Overall, we are convinced that the proposed novel heterostructure sensors would pave a way to build highly sensitive devices in the application of 1D heterostructure gas sensors and to develop a sensor array for interesting future gas sensing technology.

*References*


1. J. Shuai et al., "Health risk assessment of volatile organic compounds exposure near Daegu dyeing industrial complex in South Korea," BMC Public Health 18, 528 (2018).
2. M. Hodgson et al., "Volatile organic compounds and indoor air," J. Allergy Clin. Immunol. 94, 296 (1994).
3. A. Mirzaei et al., "Detection of hazardous volatile organic compounds (VOCs) by metal oxide nanostructures-based gas sensors: A review," Ceram. Int. 42, 15119 (2016).
4. OSHA Annotated PELs, Occupational Safety and Health Administration.
5. R. R. Shah and N. L. Abbott, "Principles for Measurement of Chemical Exposure Based on Recognition-Driven Anchoring Transitions in Liquid Crystals," Science 293, 1296 (2001).
6. V. Ruzsányi and M. P. Kalapos, "Breath acetone as a potential marker in clinical practice," J. Breath Res. 11, 024002 (2017).
7. A. Dey, "Semiconductor metal oxide gas sensors: A review'" Mater. Sci. Eng. B 229, 206 (2018).
8. T. Li et al., "Quasi-one-dimensional metal-oxide-based heterostructural gas-sensing materials: A review," Sens. Actuators B 221, 1570 (2015).
9. Q. Kuang et al., "Enhancing the Photon- and Gas-Sensing Properties of a Single $SnO_2$ Nanowire Based Nanodevice by Nanoparticle Surface Functionalization," J. Phys. Chem. C 112, 11539 (2008).
10. S. Park et al., "$H_2S$ gas sensing properties of CuO-functionalized $WO_3$ nanowires," Ceram. Int. 40, 11051 (2014).
11. S. Park et al., "Enhanced CO gas sensing properties of Pt-functionalized $WO_3$ nanorods," Thermochim. Acta 542, 69 (2012).
12. C. Durán et al., "Response Optimization of a Chemical Gas Sensor Array using Temperature Modulation," Electronics 7, 54 (2018).
13. H. S. Hassan et al., "Development of polypyrrole coated copper nanowires for gas sensor application," Sens. Bio-Sens. Res. 1, 34 (2014).
14. N. Kaur et al., "Branch-like NiO/ZnO heterostructures for VOC sensing," Sens. Actuators B 262, 477 (2018).
15. N. Kaur, D. Zappa, V.A. Maraloiu, E. Comini, "Novel Christmas Branched Like NiO/$NiWO_4$/$WO_3$ (p–p–n) Nanowire Heterostructures for Chemical Sensing," Adv. Funct. Mater. 31, 2104416 (2021)

# Ferroelectric $HfO_2$ phase formation by self-control of Ge-doping and strain in $HfO_2$/Ge-$HfO_2$/$HfO_2$ 3-layer structures

**C. Palade,[a] A.M. Lepadatu,[a,*] A. Slav,[a] O. Cojocaru,[a] A. Iuga,[a] V.A. Maraloiu,[a] A. Moldovan,[b] M. Dinescu,[b] V.S. Teodorescu,[a] T. Stoica,[a,*] M.L. Ciurea[a,*]**

[a]National Institute of Materials Physics, 405A Atomistilor Street, 077125 Magurele, Romania

[b]National Institute for Laser, Plasma and Radiation Physics, 409 Atomistilor Street, 077125 Magurele, Romania

In the last decade, the recent discovery of ferroelectricity in very thin $HfO_2$ films has opened up a new prospect for ferroelectric memory applications, offering a better alternative to perovskites thanks to its compatibility with CMOS processes. $HfO_2$-based ferroelectricity is obtained at only a few nanometers thickness allowing high-density FeFET integration. There is a consensus in explaining the ferroelectricity in $HfO_2$ by the stabilization of orthorhombic non-centrosymmetric phase. Ferroelectric phase was obtained by various deposition methods of undoped (oxygen vacancies) $HfO_2$ and doped (Si, Ge, Al etc.) $HfO_2$ films, as well as of $Hf_{1-x}Zr_xO_2$ solid-solution system and $ZrO_2$/$HfO_2$ bilayer. Few papers approached $HfO_2$ ferroelectric orthorhombic phase formation by Ge-doping, and only for low Ge doping. Beside doping, substrate interface and cladding layers also have a strong influence on crystallization and ferroelectric properties of thin $HfO_2$ layers.

We present here highlights of advanced studies on formation of ferroelectric orthorhombic $HfO_2$ phase by annealing of 3-layers structures consisting in Ge-rich $HfO_2$ intermediate layer cladded by top and bottom $HfO_2$ layers deposited by magnetron sputtering on Si [1]. The optimal self-controlled Ge-doping of $HfO_2$ crystallites is obtained by segregation and diffusion during rapid thermal annealing (RTA) of 3-layer memory structures of *20-60nm top $HfO_2$/10-20nm Ge-rich intermediate Ge-$HfO_2$* ~79 at% Ge/ *~10nm bottom $HfO_2$* stack of layers on p-Si wafers (Fig. 1a).

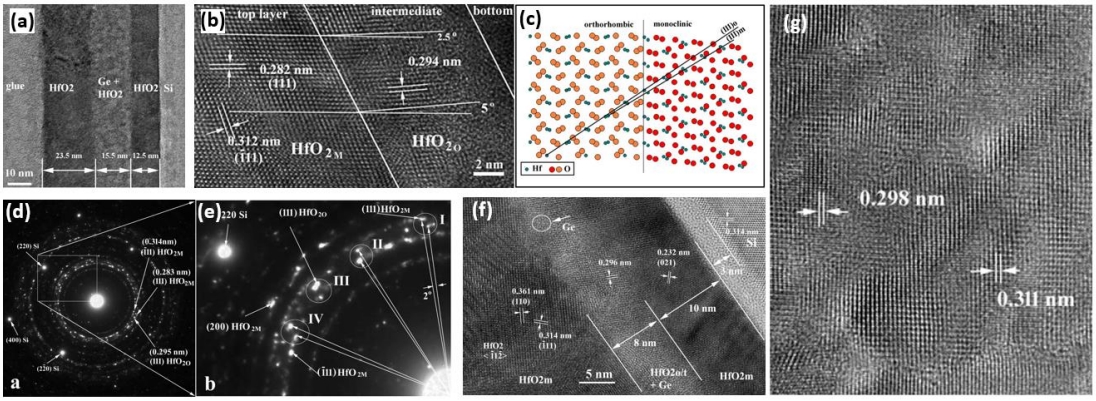


**Fig. 1** HRTEM results on $HfO_2$/Ge-$HfO_2$/$HfO_2$ on Si after RTA at 550 – 600 $^oC$: XTEM revealing the 3-layer structure (a); continuous martensitic transition at top $HfO_2$/Ge-$HfO_2$ interface from M to O structure in a single $HfO_2$ crystallite (b) and schematic simulation (c); SAED pattern (d) and an enlarged detail view (e) showing spots of monoclinic and orthorhombic $HfO_2$ crystallites with angular distance of about $2^o$ or $3^o$ like in (b); orthorhombic $HfO_2$ and amorphous Ge NPs in the Ge-$HfO_2$ layer (f); HRTEM plan view image with (121) zone axis, showing stressed lattice of correlated orthorhombic and monoclinic $HfO_2$ nanodomains (g) [1].

Top $HfO_2$ capping layer plays an important role in the strain induced into intermediate Ge-$HfO_2$ layer, that stabilizes together with the Ge-doping the metastable orthorhombic phase. We developed the mechanism of Ge-induced $HfO_2$ orthorhombic phase formation by detailed structural investigations using HRTEM, HAADF-STEM and grazing incidence GI-XRD. The stability of $HfO_2$ orthorhombic phase induced by Ge doping was also proved by DFT computation of the formation energy of different crystalline phases. The remanent polarization of structures was assessed by measurements of polarization – voltage ($P$ – $V$) hysteresis loops and PFM.

Crystal lattice growth continuity from top and bottom $HfO_2$ layers into intermediate Ge-doped layer with a spatial transition from monoclinic (M) to orthorhombic (O) was observed and exemplified in Fig. 1b by HRTEM image acquired from a region of interface between the top and intermediate $HfO_2$ layers. The transition from M to O takes place by continuous transition at atomic scale of {111} lattice

planes in a single crystallite, with angular distance changes of about 2° or 3° as from experiments and schematic simulation in Fig. 1c. Same results are revealed by SAED pattern in Fig. 1d,e with correlated spots of M and O phases. These findings support the mechanism of O phase formation during annealing by martensitic-like transformation of initially grown tetragonal (T) crystallites into M and O phases in the top $HfO_2$ and intermediate Ge-$HfO_2$ layers, respectively. The ferroelectricity is enhanced by the strain induced in O regions by $HfO_2$ capping as well as due to the M to O spatial transition. Ge segregation into amorphous nanoparticles (Fig. 1f) can also have a contribution to the induced strain. By martensitic-like transformation and strain fluctuations, the area of initially formed crystallites becomes an organized mosaic of coherent domains as shown in Fig. 1g. The HRTEM valuable results are in very good agreement with theoretical simulation and GI-XRD experiments.
The stability of Ge-doped $HfO_2$ orthorhombic phase was also demonstrated by DFT atomistic computation (Quantum Espresso software) of total energy per formula unit. For M, O and T phases, a variable cell approach was used for the unit cell corresponding to pure $HfO_2$ without Ge and also appropriately sized supercells for different Ge-doping and supercell versions. For both versions V1 and V2 of supercell and Ge-doping of 0%, 6.25% and 12.5 at .%, the crystalline formation energy for O phase is significantly reduced by Ge doping reaching a value close or even smaller than that of the more stable M phase (Fig. 2a). This means that O phase stability is energetically favorable in respect to T phase and is close to the M phase for Ge doping higher than 6%, explaining the coexistence of O and M phases in our 3-layer structures.

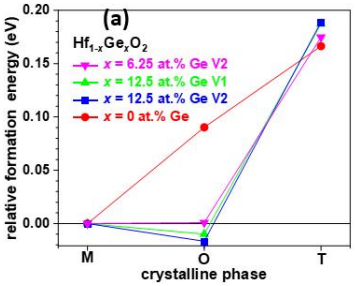


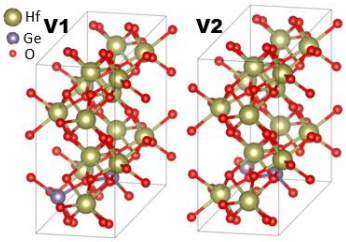


(b) The investigated samples with thicknesses of component layers

| Sample | p-Si substrate resistivity [Ω cm] | Designed/ $T_{RTA}$ [°C] | Label | $d_{top}$ [nm] | $d_{int}$ [nm] | $d_{bot}$ [nm] | $d_{int}/d_{top}$ [%] |
|---|---|---|---|---|---|---|---|
| S1 | 7–14 | Designed | S1 | 60 | 10 | 10 | 16.7 |
| | | 550 | S1-550 | 57 | 10 | 11 | 17.5 |
| | | 600 | S1-600 | 57 | 8 | 11 | 14.0 |
| S2 | 7–14 | Designed | S2 | 60 | 20 | 10 | 33.3 |
| | | 550 | S2-550 | 57 | 22 | 13 | 38.6 |
| | | 600 | S2-600 | 65 | 19 | 13 | 29.2 |
| S3 | 7–14 | Designed | S3 | 24 | 7.5 | 10 | 31.3 |
| | | 600 | S3-600 | 25 | 6.5 | 9.5 | 26.0 |
| S4 | 0.2–2.0 | Designed | S4 | 30 | 15 | 10 | 50.0 |
| | | 600 | S4-600 | 23.5 | 15.5 | 12.5 | 66.0 |

**Fig. 2** (a)- atomistic simulation of the formation energy for M, O and T phases of $Hf_{1-x}Ge_xO_2$ relative to M phase of $HfO_2$ crystals using supercells exemplified by 3D schematics of V1 and V2 versions for 12.5% Ge;
(b)- table of investigated samples for different RTA temperatures and layer thicknesses [1].

Different investigated samples obtained by varying component layers thicknesses and RTA temperature are presented in the table from Fig. 2b. GI-XRD diffractograms measured at incident angle $\omega$ of 2° on samples S1–S4 annealed by RTA at 600 °C are shown in Fig. 3a, and they reveal a mixture of M and O $HfO_2$ phases as also clearly evidenced by HRTEM investigations. In fact, the interplanar distances for O and T phases are very similar, and therefore it is experimentally difficult to distinguish between them. Additionally, the existing strain can shift the peak positions from the calibrated bulk values. Moreover, atomistic simulation shows O phase much more energetically favorable than T phase. Thus, the O/T peaks are attributed only to O phase. Diffractograms in the 2θ range of main peaks of monoclinic M(-111), M(111) and orthorhombic O(111) are shown in Fig. 3b. The evolution with GI-XRD angle of the areas of main peaks is shown in Fig. 3c for two RTA temperatures, being in very good agreement with the depth distribution revealed by HRTEM with M and O phases mainly in the upper and bottom parts of the 3-layer structure, respectively. The ratio $R_M$ = M/(M+O) of XRD peak areas reflecting the M non-ferroelectric phase composition in film is correlated with the thickness ratio $d_{int}/d_{top}$ in Fig. 3d. It is known from literature that smaller $R_M$ values correspond to better ferroelectric behavior due to higher content of O phase. This is also valid in our case, sample S4 with smaller $R_M$ of ~13% shows the highest remanent polarization.

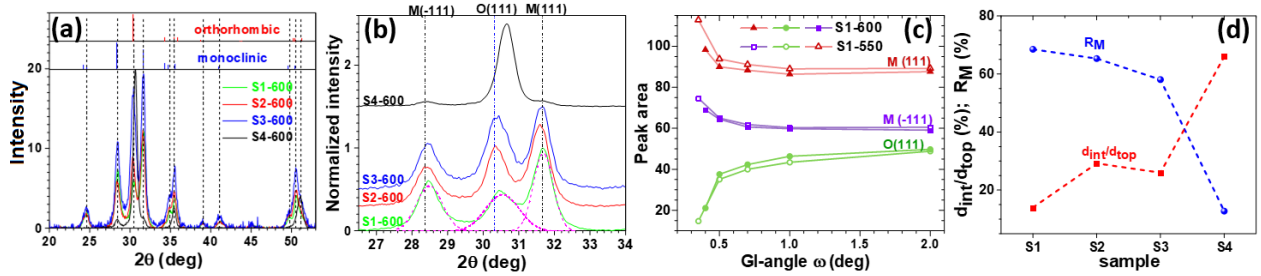


**Fig. 3** GI-XRD results: (a)- large 2θ-range diffractogram measured for GI angle $\omega = 2^o$ for different samples compared with literature diffraction lines positions for O and M phases of $HfO_2$; (b)- normalized diffractograms in the region of main diffraction peaks M(111), O(111) and M(-111), shifted on vertical, including an example of peaks deconvolution; (c)- GI-angle dependence of peaks intensity areas; (d)- monoclinic fraction $R_M$ for $\omega = 2^o$ correlated with the ratio of thicknesses of top $HfO_2$ and intermediary Ge-$HfO_2$ layers for samples S1-S4 [1].

The procedure for measuring remanent polarization loops by subtraction of a second non-switching from a first switching polarization hysteresis is exemplified in Fig. 4a. The resulted remanent polarization curves for different maximum polarization voltage within 7 – 8 V range are shown in Fig. 4b. The switching from up to down of the polarization direction was also demonstrated by changing the phase of PFM signal for ±10V poling.

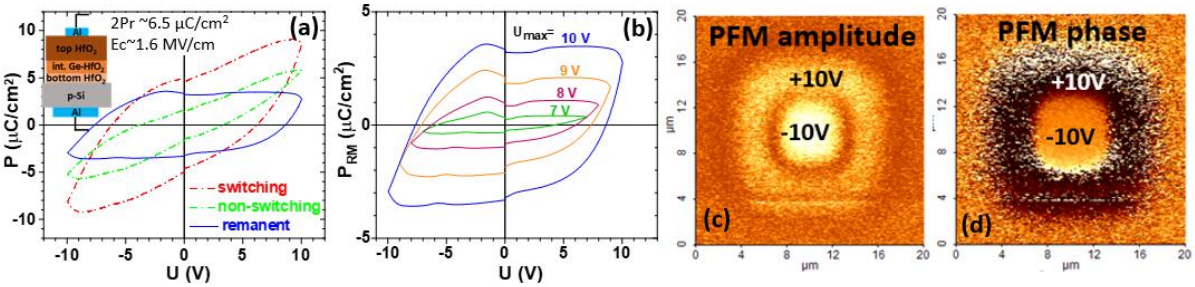


**Fig. 4** Ferroelectric induced polarization in sample S4-600: (a) example of remanent polarization hysteresis (blue) obtained by subtracting from a first switching pulse hysteresis (red) the second non-switching one (green), the inset schematically shows the sandwich structure; (b) remanent polarization hysteresis for different maximum voltage values; (c) amplitude and (d) phase images of out-of-plane PFM measurements after substrate +10 V bias poling on 10×10 μm² followed by -10 V poling on 5×5 μm² [1].

Finally, it is worth mentioning that, in addition to helping to understand the O phase formation in $HfO_2$ doped with Ge, the investigated 3-layer $HfO_2$ structure offers an advantage of using it as a floating gate memory that combines the ferroelectric and charge injection effects.

*References*

1. C. Palade, A.M. Lepadatu, A. Slav, O. Cojocaru, A. Iuga, V.A. Maraloiu, A. Moldovan, M. Dinescu, V.S. Teodorescu, T. Stoica, M.L. Ciurea, "A nanoscale continuous transition from the monoclinic to ferroelectric orthorhombic phase inside $HfO_2$ nanocrystals stabilized by $HfO_2$ capping and self-controlled Ge doping", J. Mater. Chem. C 9(36), 12353-12366 (2021).

# HRTEM structural refinement on biomineralized iron oxide in magnetotactic bacteria

**Corneliu Ghica,[a] Walid Baaziz,[b] Jefferson Cypriano,[c] Fernanda Abreu,[c] Karine Anselme,[d] Ovidiu Ersen,[b] Marcos Farina,[e] JacquesWerckmann,[e, f]**

[a]National Institute of Materials Physics, 405A, Atomistilor Street, Magurele, Romania, 077125
[b]Institut de Physique et Chimie des Matériaux de Strasbourg, University of Strasbourg, 23 rue du Loess, Strasbourg, France, 67034
[c]Instituto de Microbiologia Paulo de Góes, Universidade Federal do Rio de Janeiro, Avenida Carlos Chagas Filho, 373, Rio de Janeiro, Brazil, 21941-902
[d]Institut de Science des Matériaux de Mulhouse, University of Haute Alsace, Mulhouse, France, 68057
[e]Instituto de Ciências Biomédicas, Universidade Federal do Rio de Janeiro, Rio de Janeiro, Brazil, 21941-902
[f]Centro Brasiliero de Pesquisas Fisicas, LABNANO, Rio de Janeiro, Brazil, 22290-180

Magnetotactic bacteria (MTB) are widespread microorganisms observed in aquatic environments [1]. MTBs synthesize chains of nano-sized, iron-rich magnetic mineral crystals composed of magnetite ($Fe_3O_4$) or greigite ($Fe_3S_4$) named magnetosomes (MS) [2-4]. The great interest in studying MTBs aims at understanding their structure and properties induced by magnetic nanoparticles biomineralized inside the cell body and the mechanism of biomineralization, for possible applications in biomedicine and paleomagnetism. Our study [5] focuses on the analysis of whole mounts of *Magnetospirillum magneticum* strain AMB-1 coccus-type bacterium. The sediments were collected on the lagoon beach. After filtration, they were stored in a 1 L bottle for 1 month in natural light. The collected MTBs were magnetically enriched by attaching a permanent magnet to the outside of the bottle. The whole cells were directly deposited on 300-mesh gold-coper lacey carbon grids and observed after drying. The atomic structure of the magnetosomes was analyzed by HRTEM using a JEM ARM 200F instrument operating at 200 kV and the MacTempas software for image and electron diffraction pattern simulations.

Although it is widely accepted that the crystal structure of the iron-based magnetosomes is that of magnetite ($Fe_3O_4$, spinel structure), our investigations raised suspicions about the unicity of the synthesized phase. An in-depth HRTEM study was performed to check whether other types of iron oxides may result through the biomineralization process, maghemite ($\gamma Fe_2O_3$) being one of the main candidates.

The iron based magnetosomes in our samples typically consist in ensembles of faceted elongated grains with a size of up to 120 nm, often lined up in short chains along their long axis (Fig. 1). HRTEM micrographs have been recorded from different magnetosomes observed inside the same or different bacteria. The atomic-resolution patterns of the zone-axis oriented magnetosomes and the associated FFT patterns have been used for the identification of their crystal structure.

The nanograin denoted by "1" in Fig. 1 is analysed in Fig. 2 where the HRTEM micrograph and the associated FFT pattern are pictured. The attempt of indexing the FFT pattern in Fig. 2c according to the magnetite crystal structure fails due to the presence of intensity spots in forbidden positions (marked with white arrowheads) which suggests possible structural/stoichiometry defects. The presence of vacancies could induce the imbalance of the magnetite structure factor, pointing to the formation of the related maghemite structure. The way in which the Fe vacancies may be distributed among the octahedral positions generates three variants of maghemite with three different symmetries. In the case of random distribution of the Fe vacancies over the octahedral positions, a maghemite ($Fe_2O_3$) structure is obtained, with the Fd-3m symmetry, as for the vacancy-free spinel structure of magnetite ($Fe_3O_4$).

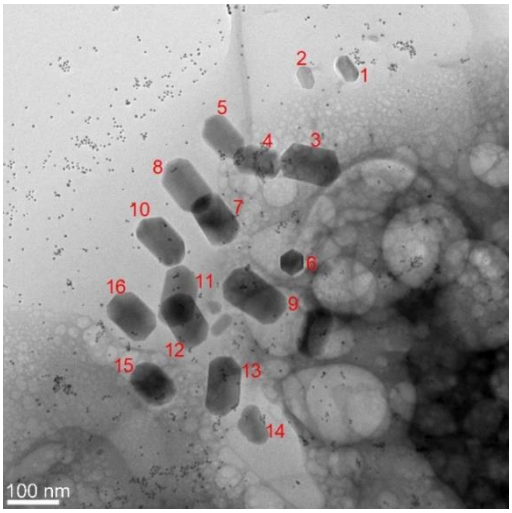


**Fig. 1** Low-magnification TEM image of a typical collection of magnetosomes mineralized inside a magnetotactic bacterium.

Two different symmetries can be generated by Fe vacancies ordering on the octahedral positions: a cubic primitive (S.G. $P4_132$) lattice, with the same lattice parameter ($a$=0.833 nm) or a tetragonal one (S.G. $P4_32_12$). The tetragonal unit cell has the $c$ lattice parameter three times as the one of spinel ($a$=$b$=0.8330 nm, $c$=2.4990 nm), and ordered Fe vacancies placed in the 5/8 3/8 2/24 octahedral positions (8b Wyckoff position).

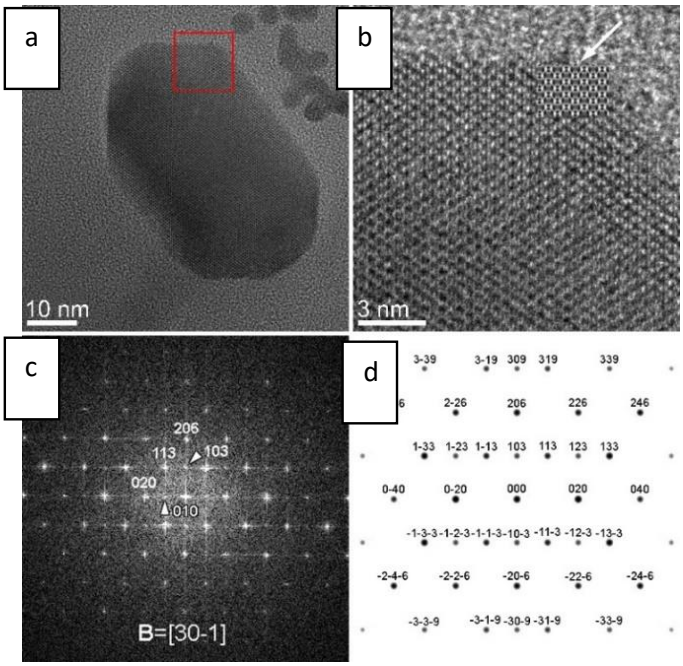


**Fig. 2** (a) HRTEM micrograph of the nanograin denoted "1" in Fig. 1; (b) enlarged image of the upper right corner of the nanograin showing the detailed HRTEM pattern; (c) FFT micrograph corresponding to the area delimited by the red square in A; (d) simulated SAED pattern considering the tetragonal unit cell of maghemite (cif no. 9006318).

Some of the analysed diffraction patterns could only be explained by using the tetragonal unit cell. The graphical representation of the tetragonal unit cell is depicted in Fig. 3b where the vacancy containing cell (right-hand side) is shown along the [1-10] direction next to a fully populated one (3 magnetite cells piled up), so that the Fe vacancies can be clearly noticed.

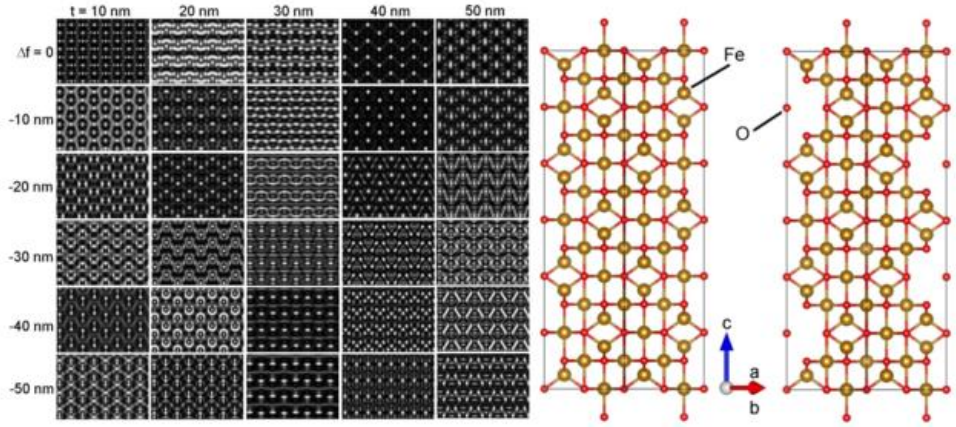


(a)

(b)

**Fig. 3** (a) Matrix of simulated HRTEM patterns based on the tetragonal unit cell of maghemite in B=[30-1] orientation; (b) Structural model of the tetragonal unit cell of maghemite (right-hand side) viewed along the [1-10] crystallographic direction revealing the vacant octahedral Fe positions with respect to the same structure with fully occupied atomic positions (magnetite).

The simulated HRTEM pattern obtained with the MacTempas simulation program for the specimen thickness of 10 nm and objective lens defocus of -20 nm fits very well the experimental image in the thinnest regions of the grain. For a better comparison, the mentioned simulated HRTEM pattern has been inserted in the upper-right corner of the grain in Fig. 3b.

Moreover, the simulated SAED pattern represented in Fig. 2d, perfectly fits the FFT distribution in Fig. 2c, as the 103 spot is now allowed by the symmetry conditions ruling the vacancies-containing tetragonal structure. The same tetragonal structure was applied for the successful interpretation of other HRTEM images and associated FFT patterns (e.g. grains 2, 4 or 5 in Fig. 1). In some other cases, the grain orientation did not allow us to come to a clear conclusion as to their crystal structure, since the observed lattice fringes and the associated FFT patterns could be indexed either as magnetite or maghemite.

Our HRTEM investigations have demonstrated that along with magnetite, maghemite is also present inside the cell body, paving the way for new interpretations on the nucleation and growth mechanisms of biogenic iron oxides within MTBs.

*References*

1. C. T. Lefèvre et al., “Ecology, Diversity, and Evolution of Magnetotactic Bacteria,” Microbiol. Mol. Biol. Rev. 77, 497–526 (2013).
2. D. L. Alkwill et al., “Ultrastructure of a magnetotactic spirillum”, J. Bacteriol. 141, 1399-1408 (1980).
3. E. F. DeLong et al., “Multiple Evolutionary Origins of Magnetotaxis in Bacteria,” Science 259, 803-806 (1993)
4. F. Abreu et al., “Common ancestry of iron oxide- and iron-sulfide-based biomineralization in magnetotactic bacteria,” ISME J. 5, 1634–1640 (2011).
5. W. Baaziz, C. Ghica, et al., “New phenotype and mineralization of biogenic iron oxide in magnetotactic bacteria species,” Nanomaterials 11, 03189 (2021).

# HRTEM evidence of strain-tailored functional properties of $ZrO_2$ thin films

**Raluca F. Negrea,[a] Marian C. Istrate,[a] Corneliu Ghica,[a] José P. B. Silva,[b] Koppole C. Sekhar,[c] Sangita Dutta,[d] Hugo Aramberri,[d] Jorge Íñiguez,[d] Fábio G. Figueiras,[e] Andrei L. Kholkin[f]**

[a]National Institute of Materials Physics, Magurele 077125, Romania

[b]Centre of Physics of Minho and Porto Universities (CF-UM-UP), Braga 4710-057, Portugal

[c]Department of Physics, School of Basic and Applied Science, Central University of Tamil Nadu, Thiruvarur 610 101, India

[d]Luxembourg Institute of Science and Technology (LIST), Esch/Alzette L-4362, Luxemburg

[e]IFIMUP & Department of Physics and Astronomy, Sciences Faculty, University of Porto, Porto 4169-007, Portugal

[f]Department of Physics, CICECO-Aveiro, Institute of Materials, University of Aveiro, Aveiro 3810-193, Portugal

Since the discovery of ferroelectricity in doped $HfO_2$ [1], a crucial interest for this material was developed, because ferroelectricity at nanoscale is very important for the next generation of memories and electronic devices. It was recently demonstrated that the thickness range for the feasible ferroelectric performance was decreased to approximately 1 nm [2]. The recent studies established that a high-pressure orthorhombic phase with noncentrosymmetric space group $Pca2_1$, induced in a constrained environment, is at the origin of ferroelectricity. Various factors, such as surface energy, stress, and dopant level have been proposed to be responsible for ferroelectricity in $HfO_2$ and $Hf_{0.5}Zr_{0.5}O_2$ (HZO) thin films. These HZO-based materials attracted great attention for their many advantages, such as large polarization density in ultra-thin film, large band gap energy (>5 eV), and compatibility with CMOS (complementary metal-oxide-semiconductor) processing. However, to induce ferroelectricity in orthorhombic HZO films, researchers usually employ an initial wake-up pre-cycling, which is technologically inconvenient and causes serious problems in device operation [3]. The wake-up effect consists in the migration of defects or the transition from a non-ferroelectric phase to a ferroelectric phase. In 2018, Wei et al. reported an unprecedented rhombohedral ferroelectric phase in epitaxially strained HZO thin film deposited on (001)-oriented LSMO/STO substrates, suggesting that the ferroelectric rhombohedral phase could have either R3m or R3 symmetry group and that is probably stabilized by a combination of the internal pressure inside the nanoparticles and the substrate-imposed compressive strain [4].

In this work a 8 nm $ZrO_2$ thin film was deposited on a (111)-oriented $Nb:SrTiO_3$ substrate in order to induce the (111) orientation in the thin film and to eliminate the need for the $La_{0.7}Sr_{0.3}MnO_3$ bottom electrode [5].

Transmission electron microscopy is a very powerful technique which allows us to determine the local crystalline phase of the $ZrO_2$ thin film. Combining atomic-resolution TEM observations and DFT calculations, the existence and stability of the R3m phase in our $ZrO_2$ films is demonstrated. $ZrO_2$ thin films have been deposited by ion-beam sputtering technique on a (111)-oriented $Nb:SrTiO_3$ substrate, at a temperature of 330 $^oC$, followed by rapid thermal annealing (RTA) in $N_2$ (6 mbar) at 700 $^oC$ for 60 s.

Annular bright-field (ABF) STEM imaging combined with high-resolution transmission electron microscopy (HRTEM) can provide an in-depth characterization of the local crystalline structure of $ZrO_2$ thin film. Using Fast Fourier Transform (FFT) performed on the HRTEM micrographs and atomic structural models of $ZrO_2$ in the [-110] zone axis obtained with the VESTA software, the crystalline phase of the $ZrO_2$ thin film was determined to be rhombohedral with R3m space group.

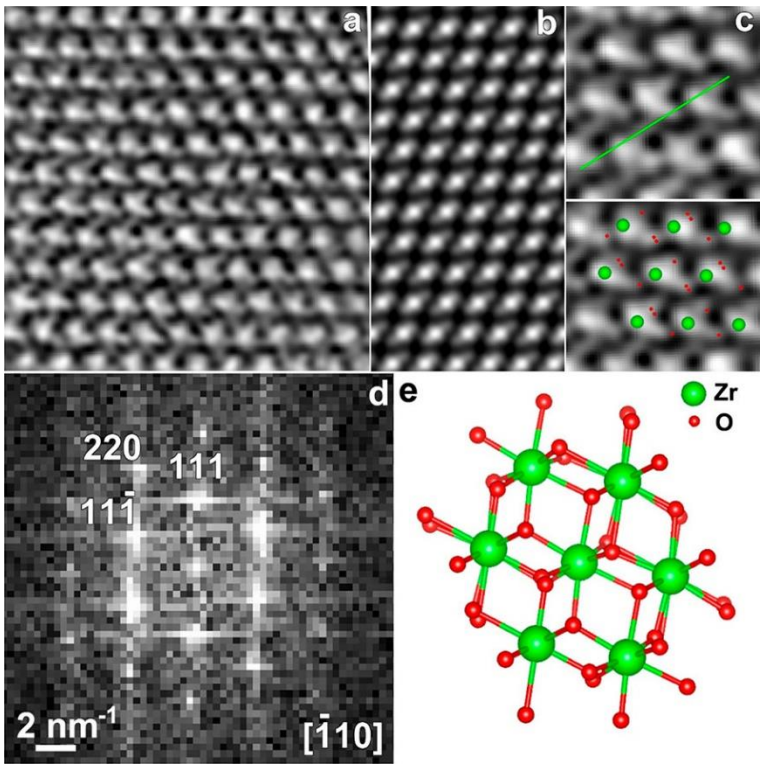


**Fig. 1** (a) ABF-STEM image of the $ZrO_2$ structure; (b) STEM image simulation of a $ZrO_2$ crystal; (c) details extracted from the ABF-STEM image in (a) showing the atomic arrangement of zirconium and oxygen and the collinearity of the oxygen atoms. The green line is a guide to the eye showing that the O−Zr−O//O− Zr−O columns are collinear. (d) FFT pattern corresponding to the ABF-STEM image a in [−110] orientation; (e) Atomic model of $ZrO_2$ in the R3m space group in a trigonal system with [−110] orientation.

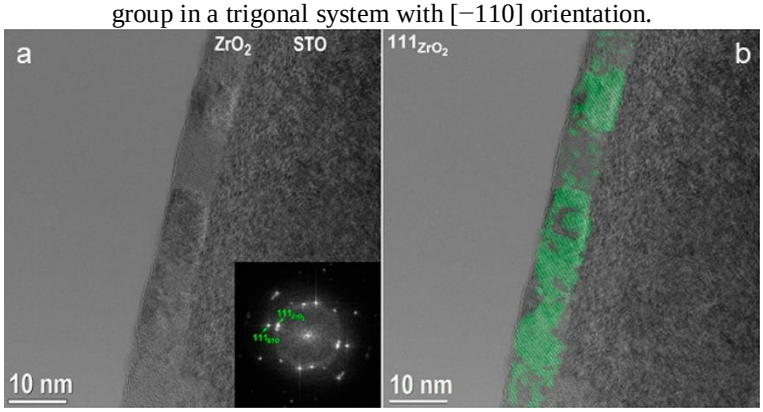


**Fig. 2** (a) HRTEM image of the $ZrO_2$ layer deposited on STO (111) substrate and the corresponding FFT pattern (inset); (b) filtered image of $111_{ZrO2}$ spot overlapped on HRTEM image (a).

ABF-STEM imaging has been used for the direct visualization of the oxygen atoms around the zirconium atoms. The contrast in the experimental and simulated ABF images was inverted for a better visibility of oxygen atoms. The ABF image of an area inside of the $ZrO_2$ thin film is presented in Fig. 1c. ABF image of $ZrO_2$ layer was compared with our DFT-calculated structural model (Fig. 1e) of the R3m phase (inset in Fig. 1c) with hexagonal lattice parameters a = b = 7.197 Å, c =8.822 Å, $\alpha = \beta = 90°$, and $\gamma = 120°$ (corresponding to $d_{111}$ =2.94 Å in the trigonal description). Also, the ABF image simulation (Fig. 1b) was performed to validate the contrast in the experimental ABF image. Along the [-110] zone axis of the $ZrO_2$ layer, the oxygen columns are situated around the Zr columns as in the atomic model (Fig. 1e) and can be better observed in the zoomed area in Fig. 1c. In addition, the O−Zr−O//O−Zr−O columns are collinear (green line in Fig. 1c), which rules out the possible existence of the R3 phase, where the loss of mirror symmetry would result in the loss of this collinearity [6]. This result represents the first experimental evidence of the R3m phase in $ZrO_2$ films. To reveal the rhombohedral R3m phase distribution in a large film area, fast FFT (inset of Fig. 2a)

was performed on the HRTEM image shown in Fig. 2a and the spots assigned to $111_{ZrO2}$ of the rhombohedral phase were identified. In Fig. 2b, the filtered image corresponding to the $111_{ZrO2}$ spots was overlapped (green areas) on the HRTEM image shown in Fig. 2a, which can be considered as a structural map of the rhombohedral crystalline phase. From the TEM measurements combined with DFT calculations, one can conclude that a significant fraction of the film has the desired rhombohedral crystal structure. Usually, it is observed that the rhombohedral R3m phase is stabilized by a combination of the large surface energy induced internal pressure of the nanoparticles and the substrate imposed compressive strain. In the presented case, the growing crystallites are subjected to a large epitaxial compressive strain that elongates the cubic unit cell along the out-of-plane [111] direction, inducing a rhombohedral symmetry with a polar unit cell [4]. Therefore, the Nb:STO (111)-oriented substrate provides a suitable template for the growth of the rhombohedral R3m phase of $ZrO_2$, without the formation of an in-plane tensile-strained tetragonal phase, as observed when HZO films are deposited on (001)-oriented $La_{0.7}Sr_{0.3}MnO_3/SrTiO_3$ substrates [4]. In addition, by using the Nb:STO (111)-oriented substrate as template, we remove the need to deposit a bottom $La_{0.7}Sr_{0.3}MnO_3$ electrode, which simplifies the growth process. The IBSD technique was combined with RTA, which allows the growth of rhombohedral R3m phase $ZrO_2$ at lower temperatures, when compared to the conditions used to grow rhombohedral R3m phase HZO films [4].

The lower temperatures used in this work are also very advantageous from the technological point of view and responsible for the existence of amorphous $ZrO_2$ regions between the crystalline ones. Further studies on the effect of RTA conditions, e.g., annealing time and temperature, to eliminate / reduce the existence of the amorphous $ZrO_2$ regions will be performed. As the rhombohedral R3m phase is polar, it is worth investigating the ferroelectric properties of the $ZrO_2$ films. These properties will be investigated in the sequel through PFM, P−E loops, and time-dependent polarization reversal characteristics.

*References*


1. J. Müller et al., "Ferroelectricity in Yttrium-doped Hafnium Oxide," J. Appl. Phys. 110, 114113 (2011).
2. S. Cheema et al., "Enhanced Ferroelectricity in Ultrathin Films Grown Directly on Silicon," Nature 580, 478-482 (2020).
3. A. Chouprik et al., "Wake-Up in a $Hf_{0.5}Zr_{0.5}O_2$ film: A Cycle-by-cycle Emergence of the Remnant Polarization via the Domain Depinning and the Vanishing of the Anomalous Polarization Switching," ACS Appl. Electron. Mater. 1, 275-287 (2019).
4. Y. Wei et al., "A Rhombohedral Ferroelectric Phase in Epitaxially Strained $Hf_{0.5}Zr_{0.5}O_2$ Thin Films," Nat. Mater. 17, 1095-1100 (2018).
5. J. Silva, R. Negrea, M. Istrate, et al, "Wake-up free ferroelectric rhombohedral phase in epitaxially strained $ZrO_2$ thin films" ACS Applied Materials & Interfaces 13, 51383-51392 (2021).
6. L. Begon-Lours et al., "Stabilization of Phase-pure Rhombohedral $HfZrO_4$ in Pulsed Laser Deposited Thin Films", Phys. Rev. Materials 4, 043401 (2020).

# Towards applications

# Electrochemical biosensors with proteins and DNA

**V.C. Diculescu[a,*], M.M. Barsan[a], T.A. Enache[a], E. Matei[a], M. Enculescu[a], I. Enculescu[a], A. Evanghelidis[a], C.G. Sanz[a], M.C. Bunea[a], R.J.B. Leote[a,b], A. Aldea[a], M. Onea[a,b]**

[a]National Institute of Materials Physics, Str. Atomistilor 405A, 077125, Măgurele, Romania

[b]Faculty of Physics, University of Bucharest, Str. Atomistilor 405, 077125, Măgurele, Romania

Oxidative stress leads to the release of reactive oxygen species (ROS), which are neutralized by the body antioxidant defense system to protect cells. However, ROS can in some cases defeat the antioxidant system by exposure to toxic agents and their harmful effect on cells is localized at the level of nucleic acids, proteins and lipids, which change their natural structures and conformations as a result of oxidation, consequently losing their normal function.

In this context, we report the development and application of electrochemical assays for the detection and quantification of molecules released as a result of oxidative stress, detection of toxic drugs as well as their interaction mechanisms with proteins and DNA. Electrochemical assays for the detection of biomarkers of the biological regulation mechanisms that maintain an equilibrium between functional proteins and those exposed to damaging factors (*protein turnover*) will also be discussed.

Hyperglycemia can promote oxidative stress through *de novo* free radical generation and simultaneous suppression of the body antioxidant defense systems. As a result, diabetic persons tend to have more oxidative cell damage compared to healthy individuals [1]. As such, glucose monitoring is crucial in maintaining the balance between ROS and the antioxidant system. Electrochemical flexible glucose biosensors were constructed by using electrospun fiber of poly(methyl methacrylate) coated with gold and the enzyme glucose oxidase which enables the selective detection of glucose in biological fluids. Biosensor morphology investigated by scanning electron microscopy revealed multi-layers of random oriented fibers of approx. 400 nm diameter. The electrochemical characterization of the flexible electrodes proved their superior electroactive area and electron transfer kinetics when compared to planar gold electrodes obtained on silicon wafers. Glucose detection on the flexible fiver biosensor was performed in neutral aqueous solutions by fixed potential amperometry at -0.4 V vs. Ag/AgCl, the sensor exhibiting a sensitivity of 3.10 $\mu A\ cm^{-2}mM^{-1}$, and a detection limit of 0.33 mM. The biosensor was successfully applied for glucose detection in body fluids, such as artificial sweat and serum samples[2].

The effect of the immunosuppressive drug azathioprine (AZA) interaction with deoxyribonucleic acid (DNA) was investigated electrochemically, using mass spectrometry (MS), and scanning electron microscopy (SEM). The AZA redox mechanism, investigated by voltammetric techniques, revealed that the electroactive center of AZA is the nitro group. An electrochemical DNA biosensor was developed by immobilizing a DNA film on a GCE surface to study the interactions between AZA and DNA. For this, different concentrations, incubation times, and applied potential values were used in the study. The obtained results indicated that electrochemically reduced AZA molecules bound to the DNA and induce structural changes seen in SEM recorded at DNA films before and after interaction with AZA. The oxidative damage of AA on DMA is recognized through the occurrence of the 8-oxo-deoxyguanosine oxidation peak. Mass spectrometry investigation of the DNA films before and after interaction with AZA points as well to the formation of AZA adducts with purine bases (Fig. 1) [3].

One of the results of the oxidative stress on cells are the oxidized, misfolded proteins, which are no longer able to perform their normal function. The enzyme proteasome degrades misfolded, damaged or unfolded proteins, which are linked to processes like inflammation, autoimmunity, neurodegenerative disorders and cancer. It has been reported that, when found in body fluids, such as blood serum or plasma (circulating-proteasome), it may pose as a novel biomarker (circulating-proteasome), thus signaling the development of such medical conditions.

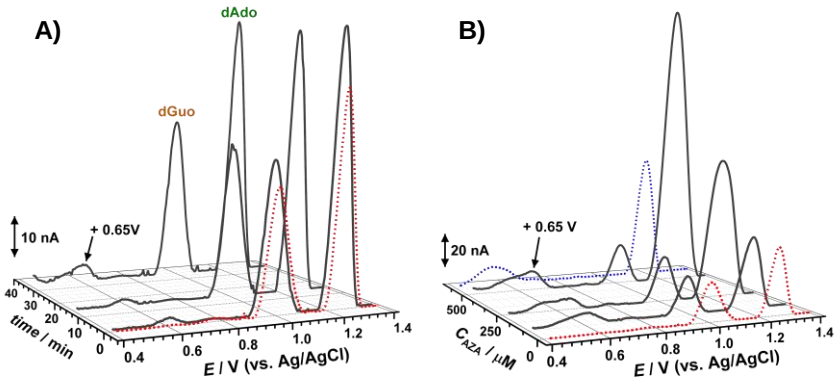


**Fig. 1**. DP voltammograms in acetate buffer 0.1 M pH 4.5 with the dsDNA biosensor after incubation at -0.60 V: **A)** in 100 µM AZA during 1, 5 and 35 min, and **B)** during 10 min in 100, 250 and 500 µM AZA; the red dotted curve is the DP voltammogram with the dsDNA biosensor after incubation at -0.60 V in buffer; the blue dotted curve is the DP voltammogram in AZA after applying -0.60 V. Adapted from [3] , with permission.

First, a 20S proteasome electrochemical biosensor was developed for investigating the 20S proteasome activity and its inhibition by drugs. For this, the 20S proteasome is immobilized at the electrode surface through bio-affinity interactions with three different antibodies that target different subunits on the 20S proteasome, enabling the investigation of the effect of an enzyme's orientation on biosensor response. The enzymatic activity of preoteasome is then analyzed electrochemically by using a peptide marked with an electroactive group 7-amino-4-methylcoumarin (AMC). The detection principle involves the oxidation of AMC released from the enzyme's substrates upon proteolysis, which is carried out by fixed potential amperometry at +0.8 V vs. Ag/AgCl. The biosensor was able to distinguish between the 20S multicatalytic activity, i.e. the caspase-, trypsin- and chymotrypsin-like activity, by exhibiting different sensitivities towards substrates targeting different proteolytic action. The highest sensitivity was recorded for the substrates of chymotrypsin-like activity, Suc-LLVY-AMC being of 24 µA $cm^{-2}$ $mM^{-1}$, with a corresponding detection limit of 0.4 µM. The developed biosensor can be successfully applied for the detection of drugs with inhibitory effect on 20S, demonstrated in the study by the use of two 20S inhibitors, epoxomicin and bortezomib [4].

Secondly, an electrochemical method for proteasome 20S detection is developed, based on a sandwich-type electrochemical immunosensor, containing the capture monoclonal antibody Abβ and the detection polyclonal antibody $Ab_{core}$, which was labeled with the enzyme alkaline phosphatase (AlkP) (see Scheme 1).

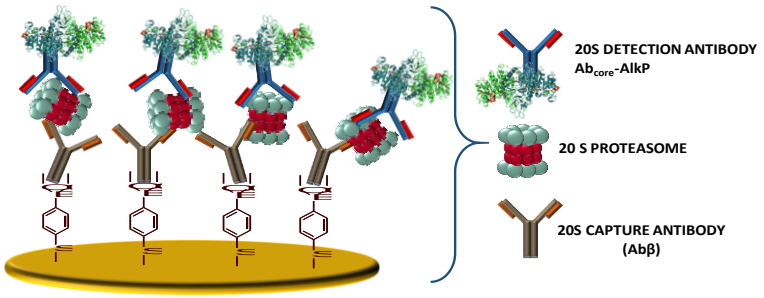


**Scheme 1.** 20S immunosensor Au/4-MPBA/Abβ/20S/$Ab_{core}$-AlkP architecture. Adapted from [5], with permission.

The enzyme AlkP is used for the indirect electrochemical detection of 20S, generating the electroactive aminophenol form aminophenylphosphate. In order to efficiently immobilize the capture antibody, the Au electrode was previously modified with a chemically adsorbed monolayer of via 4-mercaptophenilboronic acid (4-MPBA). Further, the proteasome 20S interacts with the immobilized antibody via bioaffinity interactions, which eventually lead to 20S adsorption. The last step was the adsorption of the detection antibody $Ab_{core}$-AlkP, which allowed the detection of 20S at +0.2 V in a concentration range appropriate for clinical studies in patients with abnormal 20S levels.

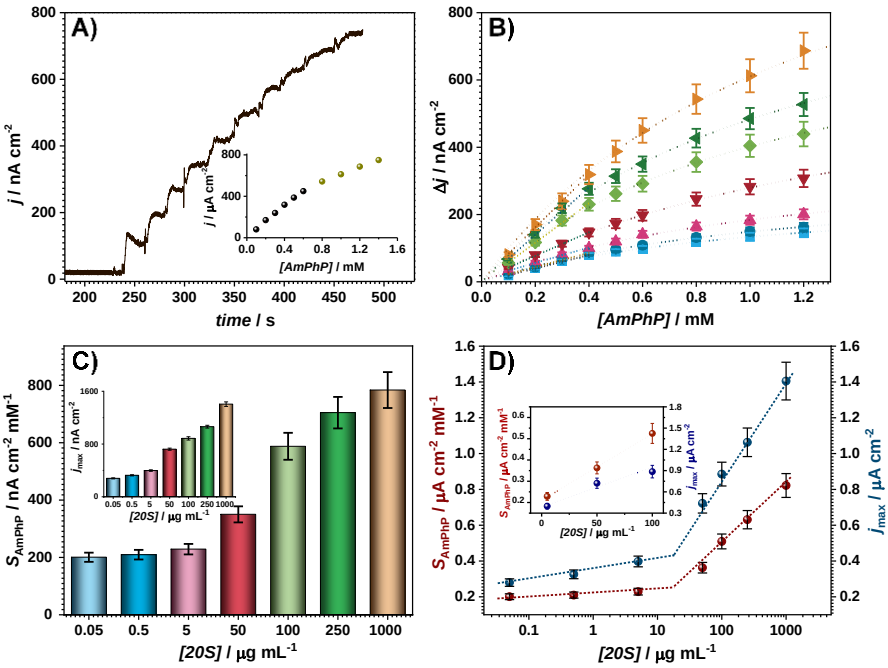


**Fig 2. A)** CA response recorded at Au/4-MPBA/Abβ/20S/$Ab_{core}$-AlkP (with 1000 µg $mL^{-1}$ 20S), at +0.20 V upon successive injections of AmPhP; the inset is the corresponding calibration curve. **B)** Calibration curves for different 20S concentrations, and non-linear fitting with the Michaelis Menten model. **C)** $S_{AmPhP}$ values for different 20S concentrations (the inset represents $j_{max}$ values for different 20S concentration). **D)** Dependence of both $S_{AmPhP}$ and $j_{max}$ on log[20S]; inset represents the linear dependence of $S_{AmPhP}$ and $j_{max}$ with [20S] between 5 and 100 µg $mL^{-1}$. Adapted from [5], with permission.

The biosensor based on the capture antibody and proteasome detected 20S in the concentration range 5-100 µg $mL^{-1}$, with a sensitivity of 0.45 nA $cm^{-2}$ $mM^{-1}$ (µg $mL^{-1}$) and a detection limit of 1.43 µg $mL^{-1}$ 20S (Fig. 2). The use of the detection antibody labeled with AlkP decrease the operating potential from +0.8 down to +0.2 V, lowering the matrix effect, and increased the sensitivity to 3.1 nA $cm^{-2}$ $mM^{-1}$ (ug $mL^{-1}$)$^{-1}$, lowering as well the detection limit to 0.16 µg $mL^{-1}$ [5].

*References*


1. O.M. Ighodaro, Molecular pathways associated with oxidative stress in diabetes mellitus, Biomed. Pharmacother. 108 656–662 (2018). https://doi.org/10.1016/J.BIOPHA.2018.09.058
2. A. Aldea, R.J.B. Leote, E. Matei, A. Evanghelidis, I. Enculescu, V.C. Diculescu, Gold coated electrospun polymeric fibres as new electrode platform for glucose oxidase immobilization, Microchem. J. 165 106108 (2021). https://doi.org/10.1016/j.microc.2021.106108.
3. M.C. Bunea, V.C. Diculescu, M. Enculescu, H. Iovu, T.A. Enache, Redox Mechanism of Azathioprine and Its Interaction with DNA, Int. J. Mol. Sci. 22 (2021) https://doi.org/10.3390/IJMS22136805.
4. M.M. Barsan, V.C. Diculescu, An antibody-based amperometric biosensor for 20S proteasome activity and inhibitor screening, Analyst. 146 3216–3224 (2021). https://doi.org/10.1039/D0AN02426K.
5. M.M. Barsan, C.G. Sanz, M. Onea, V.C. Diculescu, Immobilized Antibodies on Mercaptophenylboronic Acid Monolayers for Dual-Strategy Detection of 20S Proteasome, Sensors, 21, 2702 (2021) https://doi.org/10.3390/S21082702.

# Tailoring the interfacial adhesion of basalt fibers/epoxy resin composites by ZnO electroless deposition

**N. Preda,[a] A. Costas,[a] M. Lilli,[b] F. Sbardella,[b] C. Scheffler,[c] J. Tirillo,[b] F. Sarasini,[b]**

[a]National Institute of Materials Physics, Atomistilor 405A, Magurele, Romania, 077125

[b] Department of Chemical Engineering Materials Environment, Sapienza-Università di Roma & UdR INSTM, Via Eudossiana 18, 00184 Roma, Italy

[c] Leibniz-Institut für Polymerforschung Dresden e.V. (IPF), Hohe Strasse 6, 01069 Dresden, Germany

ZnO electroless deposition is a versatile functionalization method with the following advantages: simplicity of the required equipment, low process temperature, ambient pressure processing, high yields of pure products at low-fabrication cost and scalability. This solution-based approach is suitable for functionalization of complex shape featured by a non-conductive surface-like fabrics with large-area ZnO uniform layers, the deposited metal oxide nanostructures having a good adhesion to the substrates. Moreover, the fibers are ideal substrates for deploying nanostructures featured by a large surface area characteristic for a given weight or volume of fabric.

In our study [1], basalt fibers were functionalized by ZnO electroless deposition in order to develop a ZnO nanostructured interphase that can improve the fiber/matrix interfacial adhesion in the polymer composites based on basalt fibers and epoxy resin. It is well known that the mechanical properties of the composites are strongly related to the performance of the interphase, this being responsible for the load transfer between the fibers and the polymer matrix. The morphological and structural properties of the ZnO-coated basalt fibers were evaluated by X-ray diffraction (XRD) and field emission scanning electron microscopy (FESEM).

The XRD patterns (Fig. 1) reveal a broad bump related to the amorphous silica in the basalt fibers and sharp, narrow and intense diffraction peaks assigned to ZnO hexagonal wurtzite phase, which confirm the deposition of ZnO crystallites on the surface of the basalt fibers.

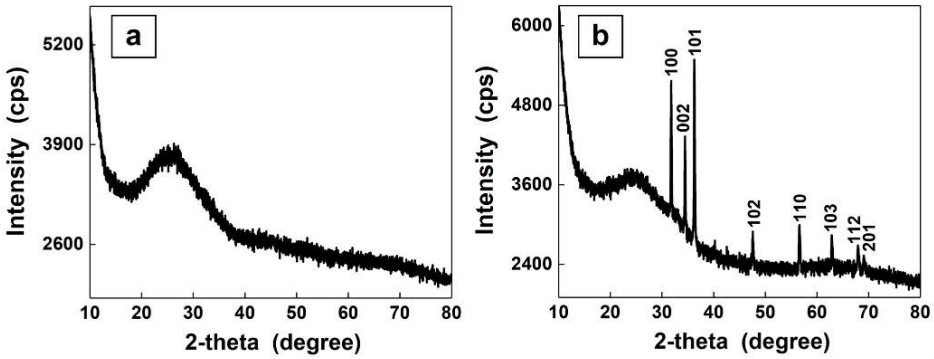


**Fig. 1** XRD patterns of basalt fibers (a) and ZnO-coated basalt fibers (b).

The FESEM images of the basalt fibers before and after functionalization (Fig. 2) emphasize that ZnO electroless deposition allows the functionalization of non-conductive and non-planar basalt fibers providing a relatively uniform coating on large areas. Basalt fibers as fabrics or yarns were involved in the ZnO electroless deposition for evaluating the effects induced by the sample geometry (fabric or yarn) on the growth mechanism of ZnO nanostructures (Fig. 3 and Fig. 4). After ZnO electroless deposition, the smooth surface of the basalt fibers are covered with ZnO nanostructures, their shape and size being strongly related to the sample geometry (fabric or yarn).

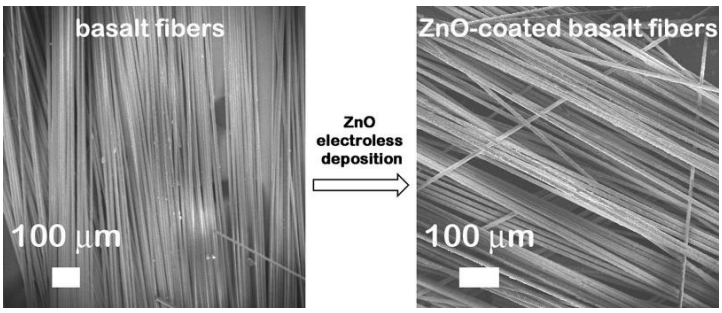


**Fig. 2** FESEM images of basalt fibers and ZnO-coated basalt fibers as fabrics.

Hence, the basalt fibers as fabrics are covered by well faceted twin hexagonal prisms, oriented and connected along the *c*-axis of the growing crystallites (base diameter of 500 nm and height of 1 μm), the typical shape of ZnO synthesized by electroless deposition. In comparison, the basalt fibers as yarns reveal tightly packed twin hexagonal prisms having smaller sizes (base diameter of 300 nm and height of 100 nm), which are oriented with the "flat face" of the hexagon perpendicular to the surface of the basalt fiber, this particular arrangement favoring a completely and more uniform coverage of the substrate.

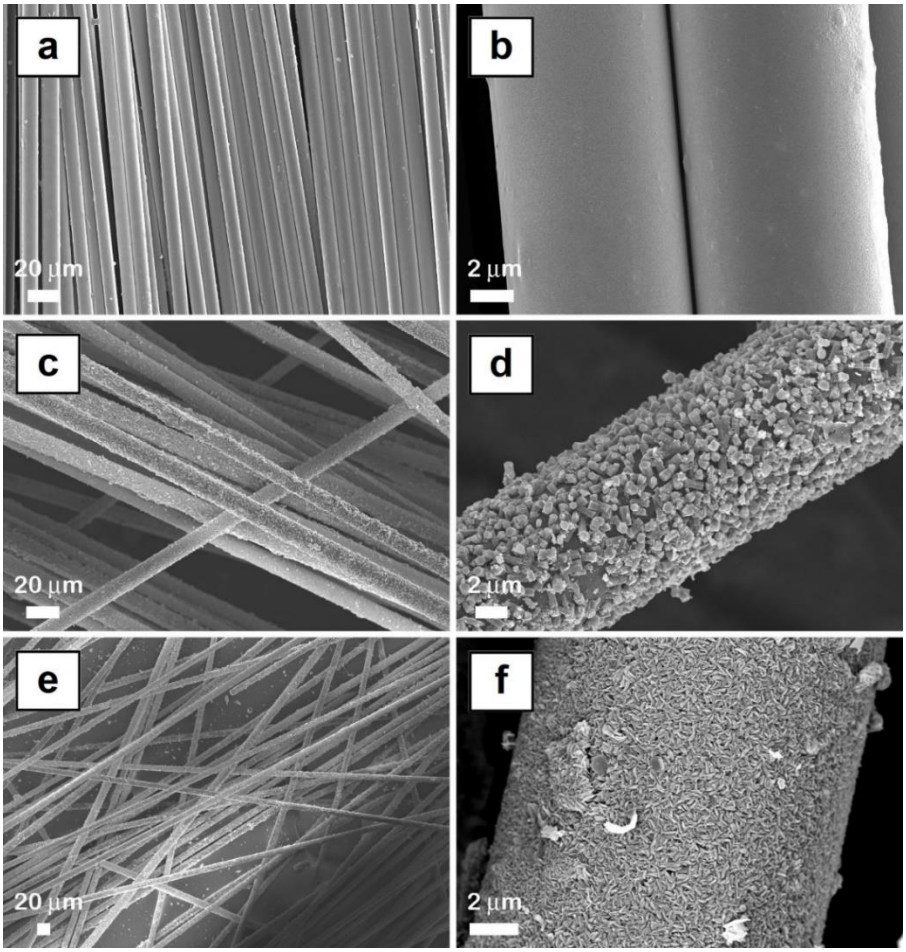


**Fig. 3** FESEM images at two magnifications of basalt fiber fabrics (a, b), ZnO-coated basalt fiber fabrics (c, d) and ZnO-coated basalt fiber yarns (e, f).

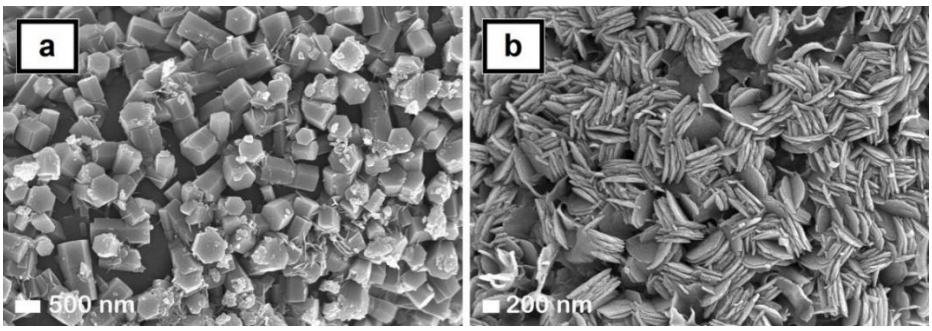


**Fig. 4** FESEM images at higher magnifications of ZnO-coated basalt fibers as fabrics (a) and yarns (b).

The result can be explained taking into account that during the immersion into the three aqueous solutions (sensitization – $SnCl_2$, activation – $PdCl_2$ and deposition – $Zn(NO_3)_2$ and $(CH_3)_2NHBH_3$) used in the ZnO electroless deposition, the basalt yarn end "opens" like a hand fan into numerous fibers providing a larger metal-catalyzed surface area than that of the basalt fabric. Thus, when the yarn containing palladium colloids on its surface is immersed in the ZnO deposition bath, a larger number of ZnO nuclei are rapidly formed comparing with those generated when the fabric is used as substrate. Considering that the ZnO nuclei are growth sites and the fact that that growth process is triggered by the increase of the pH only in the vicinity of the metal-catalyzed surface, the number of nuclei can be directly linked to the size of the twin prisms: smaller number leads to prisms with larger dimensions while a larger number resulting in prisms with smaller dimensions.

The contact angle investigations reveal that the ZnO prisms deposited on the surface of the fibers change the hydrophilic basalt fabric into a hydrophobic one (~130°).

The single fiber pull-out test confirms that the presence of the ZnO nanostructures on the surface of the basalt fibers leads to an important improvement of the apparent interfacial shear strength (~42%) with a limited degradation of the pristine basalt fibers tensile strength (a reduction of ~17%). Thus, ZnO electroless deposition can be regarded as an effective functionalization path to improve the mechanical performance of basalt/epoxy composites.

The functionalization of basalt fibers by ZnO electroless deposition opens new insights in designing ZnO nanostructured interphase for enhancing the surface area for bonding and the mechanical interlocking with the epoxy matrix in order to increase the stress transfer. Hence, by introducing ZnO nanostructured interphase, the interfacial properties of the fiber reinforced composite can be tailored to meet a wide range of requirements necessary for expanding their potential range of applications. In addition, using easily accessible raw materials and inexpensive equipment, ZnO electroless deposition presents a good potential for scale-up.

*References*

1. N. Preda et al., "Functionalization of basalt fibers with ZnO nanostructures by electroless deposition for improving the interfacial adhesion of basalt fibers/epoxy resin composites", Compos. A – Appl. Sci. Manuf. 149, 106488 (2021).

# Semiconductor Nanotubes with Photocatalytic Properties Fabricated by Electrospinning

**Monica Enculescu[a], Andreea Costas[a], Mihaela Beregoi[a], Alexandru Evanghelidis[a], Ionut Enculescu[a]**

[a]National Institute of Materials Physics, Laboratory of Functional Nanostructures, Atomistilor 405 A, Magurele, Romania, 077125

Nanostructures obtained via the electrospinning technique can be used for various domains, from biomedical applications to photocatalytic applications. Functionalization of polymer nanofibers obtained by electrospinning was recently made by electrochemical deposition [1], incorporation of the nanostructures in the electrospun solution [2] or sol-gel deposition [3]. In this study [3] we report the fabrication of semiconducting nanotubes for photocatalytic applications via the electrospinning process.

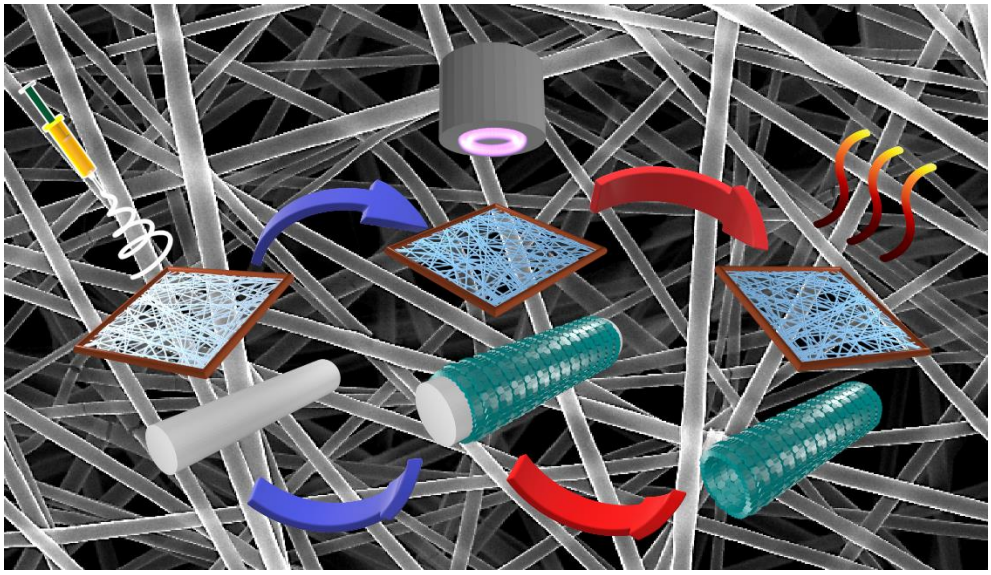

**Fig. 1** Illustration of the three-steps semiconductor nanotubes' fabrication process.

Semiconductor nanotubes were fabricated by a three-steps process (Figure 1). In the first step, the electrospinning method was used to obtain polymethyl methacrylate (PMMA) fiber mats collected on metallic frames. Secondly, the polymer fibers were coated uniformly with thin layers of semiconductor materials (ZnO or $TiO_2$) by using radio-frequency magnetron sputtering. In the third step, the polymer core was removed by calcination and thus ZnO nanotubes and $TiO_2$ nanotubes were obtained.

The morphology of semiconductor nanotubes was evaluated using field emission scanning electron microscopy (FESEM) confirming that the fibers templates were replicated on a large scale (Figure 2a and b) and that the semiconductor material was deposited uniformly on the surface of the electrospun fibers (Figure 2 c and d). The ZnO nanotubes have wall thicknesses of ~50 nm, whereas the $TiO_2$ nanotubes have wall thicknesses of ~35 nm (or less).

XRD measurements confirmed that the ZnO nanotubes were crystalline with hexagonal wurtzite structure and the $TiO_2$ nanotubes are of single crystalline phase with anatase structure. Reflectance measurements were used in order to calculate the band gap. The nanotubes show values of $E_g$ of about 3.04 eV for ZnO and 3.16 eV for $TiO_2$.

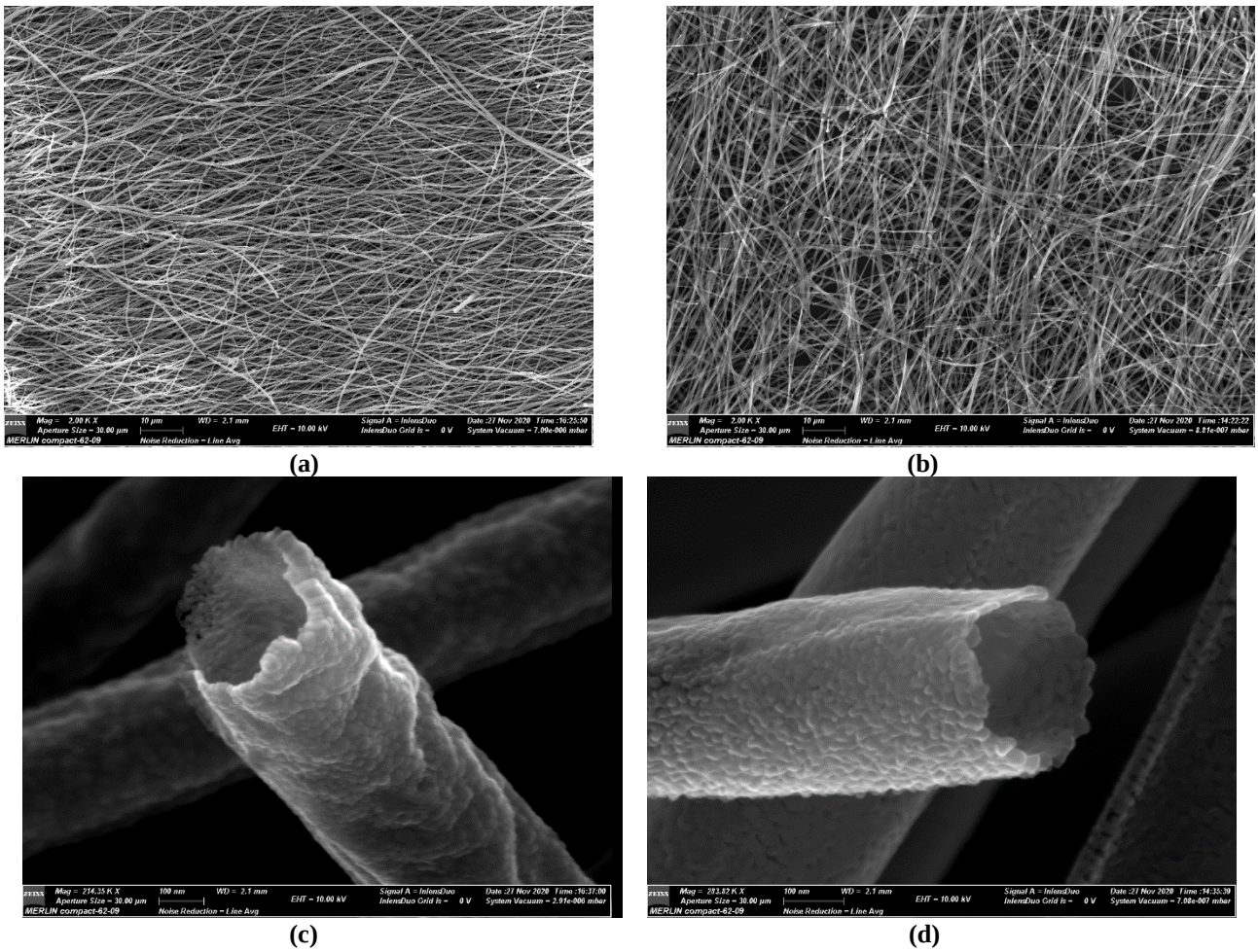

**Fig. 2** FESEM images at different magnifications of ZnO nanotubes (a and c) and $TiO_2$ nanotubes (b and d).

The photocatalytic properties of ZnO and $TiO_2$ nanotubes were evaluated by monitoring the photodegradation of the Rhodamine B (Rh B) during the irradiation with solar light. Thus, ~0.5 mg of nanotubes deposited on Si substrates were immersed in approximately 10 mL of Rh B aqueous solution ($10^{-5}$ M). Irradiation with white light from a solar simulator was performed for 600 min. During the irradiation, at different time intervals, the optical absorbance spectra of the samples at $\lambda$ = 400–700 nm were measured, the characteristic absorption band of RhB (peak at ~554 nm) was monitored, and its photodegradation was evaluated.

The degradation efficiencies were calculated for ZnO nanotubes (Figure 3a) and for $TiO_2$ nanotubes (Figure 3b) from the absorption spectra registered at different times (Figure 3, insets). It was determined that the photocatalytic degradation of ZnO nanotubes had an efficiency of ~55% whereas the degradation efficiency for the $TiO_2$ nanotubes was above 95%.

The high degradation efficiency is demonstrated by the complete bleaching of the Rh B solution as presented in Figure 4a. The photocatalytic degradation is schematically illustrated in Figure 4b.

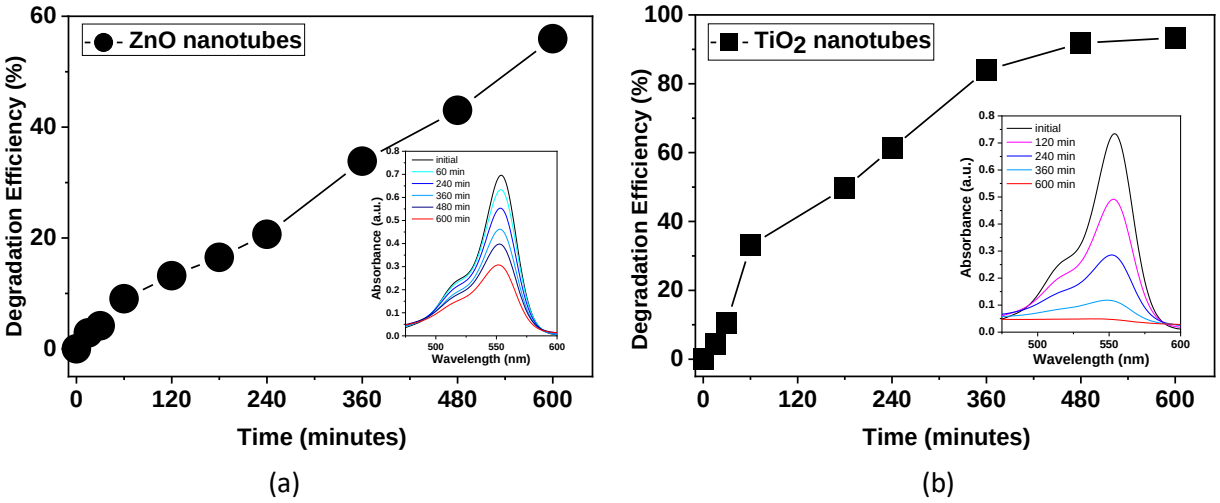


(a) (b)

**Fig. 3** Degradation efficiency and absorption spectra (insets) of RhB solutions after irradiation with white-light for: (a) ZnO nanotubes and (b) $TiO_2$ nanotubes.

In the photocatalytic process, a photon with an energy higher than the energy of the semiconductor's band gap activates the electron in the valence band to make the band-to-band transition, producing an electron–hole pair. The charge carriers from the surface of the nanotubes interact with the chemicals in the aqueous solution, degrading them and forming the reaction products.

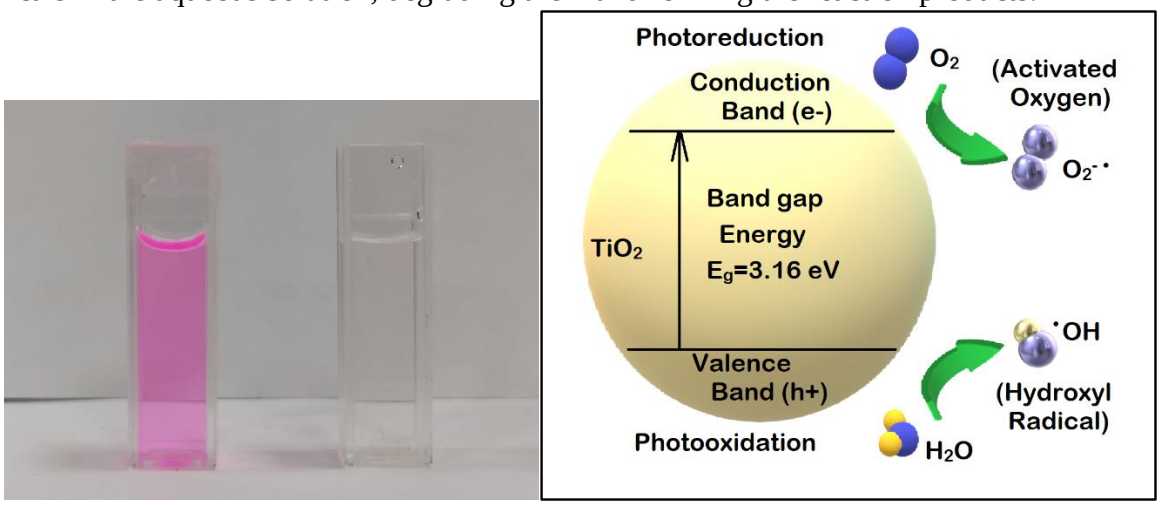


(a) (b)

**Fig. 4 (a)** Solution of RhB, initial (left) and after 600 minutes degradation with solar light in the presence of the $TiO_2$ nanotubes**. (b)** Mechanism of photocatalysis and degradation of RhB solution using $TiO_2$ nanotubes.

*References*

1. E Matei, C Busuioc, A Evanghelidis, I Zgura, M Enculescu, M Beregoi, "Hierarchical functionalization of electrospun fibers by electrodeposition of zinc oxide nanostructures", Applied Surface Science 458, 555-563N (2018).
2. SI Jinga, AI Zamfirescu, G Voicu, M Enculescu, A Evanghelidis, C Busuioc, "PCL-ZnO/TiO2/HAp electrospun composite fibers with applications in tissue engineering", Polymers, 11 (11), 1793 (2019).
3. M Beregoi, N Preda, A Costas, M Enculescu, RF Negrea, H Iovu, "Synthesis of core–double shell nylon-ZnO/polypyrrole electrospun nanofibers", Nanomaterials 10 (11), 2241 (2020).
4. M Enculescu, A Costas, A Evanghelidis, I Enculescu, "Fabrication of ZnO and TiO2 nanotubes via flexible electro-spun nanofibers for photocatalytic applications", Nanomaterials, 11 (5), 1305 (2021).

# Magnetic nanoparticles and nanocomposites for bio-medical applications

**V. Kuncser[a], P. Palade[a], N. Iacob[a], V. Mihalache[a], A. Kuncser[a], C. Comanescu[a], G. Schinteie[a], A. Stanciu[a], C. Negrila[a], I. Mercioniu[a], I. Craciunescu[b], G. M. Ispas[b], R. Turcu[b]**

[a]National Institute of Materials Physics, Atomistilor 405A, 077125 Magurele, Ilfov, Romania

[a]National Institute of Isotopic and Molecuilar Technologies, Cluj-Napoca, 400293, Romania

Magnetite ($Fe_3O_4$) and ferrite ($MFe_2O_4$, M—Mn, Zn) hydrophobic magnetic nanoparticles with various shapes and sizes were synthesized by high temperature reaction of organic precursor solutions by varying the precursor salt concentrations and the oleic acid / oleylamine surfactant ratio. Spherical, cubic, hexagonal and octahedral shapes and sizes ranging from 10 to 100 nm were obtained (fig. 1). It has been proven that the reported high capability of tailoring the shape and the size of the surface-coated nanoparticles allows controlling a variety of properties that are relevant to many potential applications.

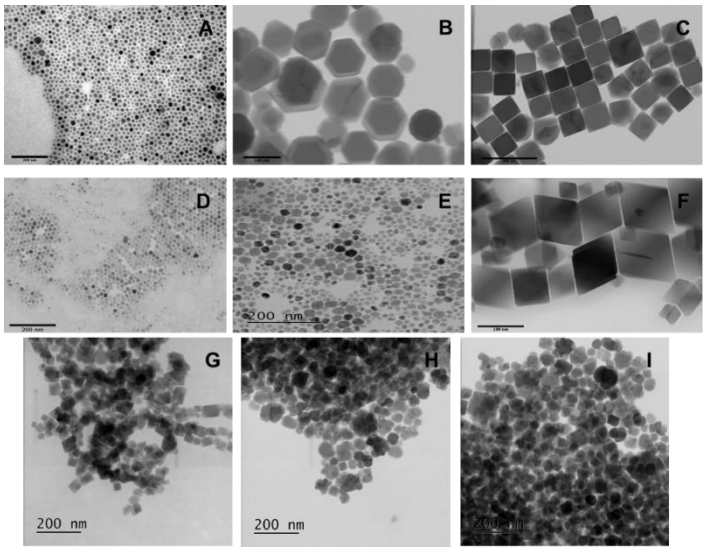


**Fig. 1** The morphology of hydrophobic MNPs: (A) 10 nm round shape $Fe_3O_4$, (B) 50 nm polyhedral shape $Fe_3O_4$, (C) 100 nm cubic shape $Fe_3O_4$, (D) 10 nm round shape $MnFe_2O_4$, (E) 50 nm polyhedral shape $MnFe_2O_4$, (F) 100 nm cubic/polyhedral shape $MnFe_2O_4$, (G) (H) (I) 50-70 nm polyhedral shape $ZnFe_2O_4$.

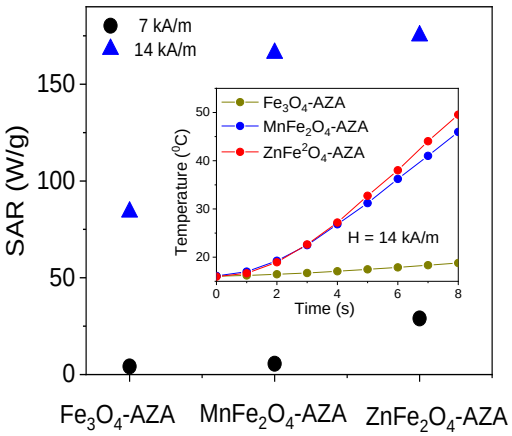


**Fig.2** SAR values for the analyzed hydrophilic MNPs measured in AC magnetic field of 7 kA/m and 14 kA/m. Heating curves are illustrated in the inset.

The hydrophobic oleic acid shell was successfully transformed by a simple and environmentally friendly oxidative scission method into azelaic acid using sodium metaperiodate ($NaIO_4$). This oxidative scission of oleic acid does not induce aggregation, obtaining therefore a very narrow dimensional distribution of the hydrophilic coated magnetic nanoparticles. The resulting hydrophilic surfactant outer layer is very thin and allows a convenient control of the site occupation in the spinel structure in order to provide high saturation magnetization at low temperature for the obtained hydrophilic MNPs (e.g., $\sigma^* = 100$ emu/g for $Fe_3O_4$-AZA, $\sigma^* = 95$ emu/g for $MnFe_2O_4$-AZA and $\sigma^* = 90$ emu/g for $ZnFe_2O_4$-AZA). The morpho-structural characteristics, size distributions, chemical composition and magnetic properties of the resulting hydrophilic nanoparticles were investigated by TEM, XRD, FTIR, XPS, Mössbauer spectroscopy and magnetometry. Magnetic hyperthermia measurements have been performed in a specially designed sample holder placed in an inductor with copper windings assuring alternating magnetic field. The dominant heat transfer mechanism is due to hysteresis losses which are again different for the magnetite as compared to Mn and Zn ferrite MNPs. Among all samples, the highest specific absorption rate (SAR) in alternate magnetic fields of up to 200 Oe was found for the $ZnFe_2O_4$ MNPs (SAR = 175 W/g for 14 kA/m amplitude of the AC field, being more than 5 times higher than for 7 kA/m amplitude of the AC field) (fig. 2). They have a soft magnetic behaviour ($KV = 0.733 \times 10^{-20}$ J) and the highest susceptibility in magnetic field intensities

of 100—200 Oe. At higher intensities of the excitation field, the role of the saturation magnetization and of the coercive field becomes more important and manganese ferrite MNPs can also have a consistent heating effect (SAR = 165 W/g for 14 kA/m of the AC field), being more than 16 times higher than for 7 kA/m of the AC field. It seems that the multi-domain configuration of the 100 nm magnetite MNPs, is less effective for an efficient heat transfer in hyperthermia applications compared to the single domain configuration specific the 50 nm $ZnFe_2O_4$ and 100 nm $MnFe_2O_4$ MNPs. A surfactant-assisted synthetic route was employed to synthesize cobalt ferrite MNPs over a wide pH range (3-13). Pure cobalt ferrite phase formation has been confirmed to occur at pH greater than 7. Both XRD and Mössbauer spectroscopy proved that lower pH values led to formation of hematite (α-

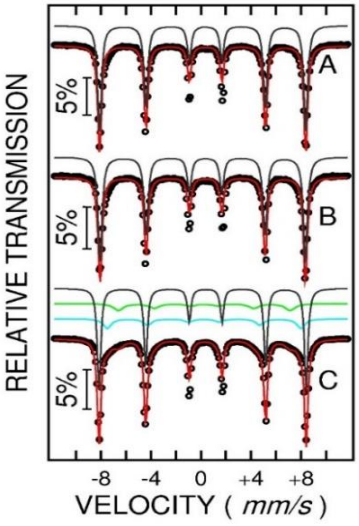


**Fig. 3** The room temperature Mössbauer spectra collected from Co-Fe-O NPs synthesized at pH = 3 (A), pH = 5 (B), pH = 7 (C).

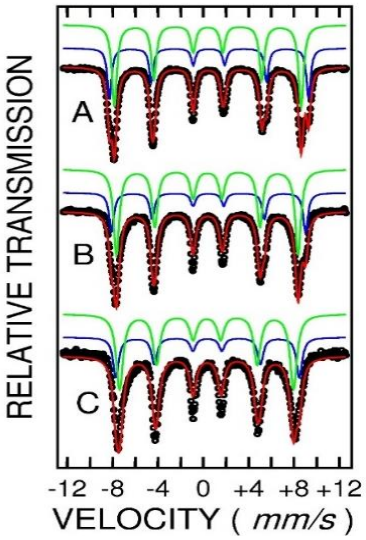


**Fig. 4** Mössbauer spectra collected at different temperatures (8 K (A), 200 K (B), 300 K (C)) for Co-Fe-O NPs synthesized at pH = 8.

$Fe_2O_3$) as main parasite phase (pH 3-5), or a mixture of hematite-cobalt ferrite (pH 5-7). The calcination step (550 °C) did not generate a significant increase of the crystallite size. The crystallite size varied between 5-20 nm. Mössbauer investigation (fig. 3, fig. 4) provided the hyperfine interaction parameters, in good agreement to those recently reported for cobalt ferrite MNPs and in addition, allowed the deeper investigation of the phase composition, inversion degree and magnetic relaxation effects in such systems. The porosity of the obtained materials is high, making them suitable for controlled targeted drug delivery purposes.

Zn-Fe-O nanoparticle systems (Z3F, Z20F and Z60F) were produced by changing the Zn:Fe ratio (0.97:0.03, 0.8:0.2 and 0.4:0.6 in at.%, respectively) in Zn(II)-Fe(III)-carboxylate precursors [2]. According to X-ray diffraction, Z60F is nearly single-phase $ZnFe_2O_4$ (5.9 nm crystallite size), Z20F is a $ZnO/ZnFe_2O_4$ nanocomposite consisting of 48.8% $ZnFe_2O_4$ (4.7 nm crystallite size), and Z3F is apparently pure ZnO (9.5 nm). We found evidence for a $ZnFe_2O_4$ spinel of high inversion degree (80-100%) and with superparamagnetic (SPM) behaviour at room temperature in all three samples. The large magnetocrystalline anisotropy constant, $10^6$-$10^7$ erg/cm$^3$, of the $ZnFe_2O_4$ nanoparticles and the concentration dependence of their magnetic energy barrier are explained in terms of (dipole-like) interparticle interactions interlinked with finite size effects and high inversion degree; these factors also control the other parameters of importance for applications, including the blocking temperature $T_B$ (13–111 K), saturation magnetization $M_s$ (1.08-17.7 emu/g at 300 K, 4.6-44.8 emu/g at 5 K) and coercivity $H_c$ (85.4-491 Oe at 5 K). Magnetic dynamic results, particularly modelled by the Néel-Brown and Vogel-Fulcher relaxation laws (Fig. 5), yield for $\Phi$, $\tau_0$, $T_0$ and $\eta$ specific values that

validate the presence of interaction between $ZnFe_2O_4$ nanoparticles, strongly depending on the concentration of Fe (or zinc ferrite nanoparticles).
Niobia-based magnetic nanocomposites were prepared by covering $Fe_3O_4$ NPs cores with either $Nb_2O_5$ or $Nb_2O_5$@SiO2 shells by using a synthetic procedure in two steps. In the first step NPs were prepared by coprecipitation. The second step involved their coverage with either $Nb_2O_5$ shells (via precipitation), or with $Nb_2O_5$@$SiO_2$ shells, using a sol-gel method followed by subsequent precipitation with addition of CTAB surfactant. They proved to be highly selective catalysts for glucose dehydration to HMF (5-hydroxymethylfurfural). The produced yields to HMF using these catalysts were higher (32.9 %) than those reported in literature (20 % for bulk $Nb_2O_5$ or $Nb_2O_5$/carbon) Moreover, the new synthesized catalysts are hydrothermally stable and easily removable from the reaction mixture by magnetic separation.

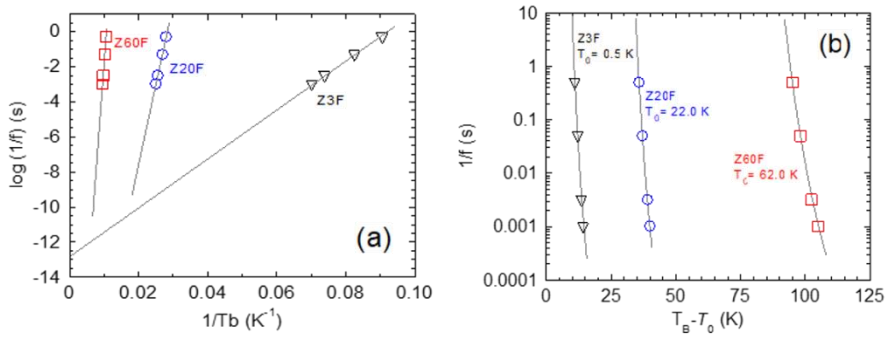


**Fig. 5** Thermal variation of the relaxation time $1/f$ (a) and the fit with Vogel–Fulcher law for ZF samples (b).

*References*


1. I. Craciunescu, P. Palade, N. Iacob, G. M. Ispas, A. E. Stanciu, V. Kuncser, R. P. Turcu, "High-performance functionalized magnetic nanoparticles with tailored sizes and shapes for localized hyperthermia applications", J. Phys. Chem. C 125(20), 11132-11146 (2021).
2. V. Mihalache, C. Negrila, I. Mercioniu, N. Iacob and V. Kuncser Phys. Chem. Chem. Phys., 2021,23, 16107-16127
3. A. Tirsoaga, V. Kuncser, V.-I. Parvulescu, S. M. Coman, "Niobia-based magnetic nanocomposites: Design and application in direct glucose dehydration to HMF", Catal. Today 366, 48-56 (2021).
4. C. Comanescu, P. Palade, V. Kuncser, "Mössbauer spectroscopy investigation of Fe oxide nanoparticles synthesized by a novel hydrothermal process over a wide pH range (3-13)", Hyperfine Interac. 242(1), 42 (2021).

# New directions of $MgB_2$ – based materials application: biomedical, ecology, and heritage

**P. Badica,[a] M. A. Grigoroscuta,[a] M. Burdusel,[a] G. V. Aldica,[a] I. Pasuk,[a] A. Kuncser,[a] M. Enculescu,[a] D. Radu,[a] I. Gheorghe,[b] V. M. Corbu, [b] L. G. Marutescu, [b] M. Popa, [b] I. Balotescu, [b] A. S. Dumbrava, [b] O. E. Zetu, V. Lazar, [b] L. M. Ditu, [b] M. C. Chifiriuc, [b] I. Avram,[b] D. Zaharia,[b] G. Gradisteanu Pircalabioru,[b] O. Thamer,[b] I. Blajan,[c] V. Mateescu,[c] I. Pecete,[d] V. C. Cristea,[d] N. D. Batalu,[e] A. D. Datcu,[f] N. Ianovici,[f] C. Bleotu,[g] B. G. Dumitriu,[h] L. Olariu,[h] A. Bicu,[h] B. Purcareanu,[h] L. Operti,[i] V. Bonino,[i] A. Agostino,[i] M. Truccato,[i] S. K. Padhi,[i] N. Baglieri,[i]**

[a] National Institute of Materials Physics, Street Atomistilor 405A, 077125, Magurele, Romania
[b] University of Bucharest, Şoseaua Panduri, nr. 90, 050663, Bucharest, Romania
[c] Romanian Peasant Museum, Şoseaua Pavel D. Kiseleff 3, Bucharest, Romania
[d] Central Reference Synevo-Medicover Laboratory, B-dul Pache Protopopescu, Nr. 81, 021408, Bucharest, Romania
[e] University Politehnica of Bucharest, Splaiul Independenței 313, 060042, Bucharest, Romania
[f] West University of Timisoara, Bulevardul Vasile Pârvan 4, 300223, Timisoara, Romania
[g] Ştefan S Nicolau Institute of Virology, Romanian Academy, Bd. 285 Mihai Bravu, 030304, Bucharest, Romania
[h] Biotehnos S.A., Strada Gorunului, 3-5, 075100, Otopeni, Ilfov, Romania
[i] University of Turin, Physics and Chemistry Departments, Via P. Giuria 1-7 10125, Turin, Italy

$MgB_2$ is usually prized for being a light-weight material with superconducting properties. Recently, this material was shown to be useful for other applications, beyond superconductivity.

Microbial infections remain one of the primary causes of morbidity and mortality globally. High antibiotics use from the last years raise the concerns of the emergence of new multidrugresistant microbial strains posing a significant health threat and urges the development of new and effective antimicrobial nanomaterials as an alternative viable solution. In particular, formation of biofilms is dangerous since they are highly resistant when compared to the same microbes in the plaktonic state. Microbes are important not only in health and medicine, but also in other fields such as heritage and ecology where they are among the factors involved in deterioration processes.

Our work focused on development and evaluation of $MgB_2$-based materials from the viewpoint of bioactivity. Materials were in the form of powders [1, 2, 4], coatings [3], and bulks [5] (Fig. 1).

Commercially available $MgB_2$ powders and laboratory made biodegradable $MgB_2$ powders [1, 2, 5] were tested for antimicrobial properties. The laboratory-produced powders were found to be more active against different bacterial and fungi strains than the comercial ones. The efficiency of the $MgB_2$ powders was often similar or, in some cases, even higher against biofilms than on microbes in the planktonic state. In our assessment we used standard microbes cultivated in the lab. We also used fungi collected from heritage objects (Fig. 2). The tested powders proved to be ecofriendly at the active antifungal concentrations. Experiments confirmed the antimicrobial efficiency of $MgB_2$ in the *in vitro* tests against 29 methicillin resistant clinical S. aureus isolates and 33 vancomycin resistant E. faecium/faecalis strains. Treatment of infected mice led to a significant decrease of E. coli colonization in liver, spleen and peritoneal liquid and it also caused changes in the intestinal microbiota (Fig. 3). Changes in microbiota and *in vitro* tests against tumor cell lines pointed on $MgB_2$ as a candidate to fight cancer.

The composite coatings of PVP-$MgB_2$ fabricated by dip-coating were tested at diferent times of incubation against the bacterial growth of Staphylococcus aureus ATCC 25923, Enterococcus faecium DMS 13590, Escherichia coli ATCC 25922, Pseudomonas aeruginosa ATCC 27853. The coatings were applied on flexible plastic foils cut from a reservoir of a commercial urinary catheter. The coatings were efficient both against planktonic microbes and microbial biofilms [3].

In the case of: (i)- $MgB_2$-bulks fabricated by spark-plasma-sintering and added with hexagonal BN as an ingredient to ensure machinability by chipping of the composite and of (ii)- 3D-printed PLA-$MgB_2$ materials, the antimicrobial effects were found to depend on the tested samples and microbes, with E. faecium being the most resistant and E. coli the most susceptible [5].

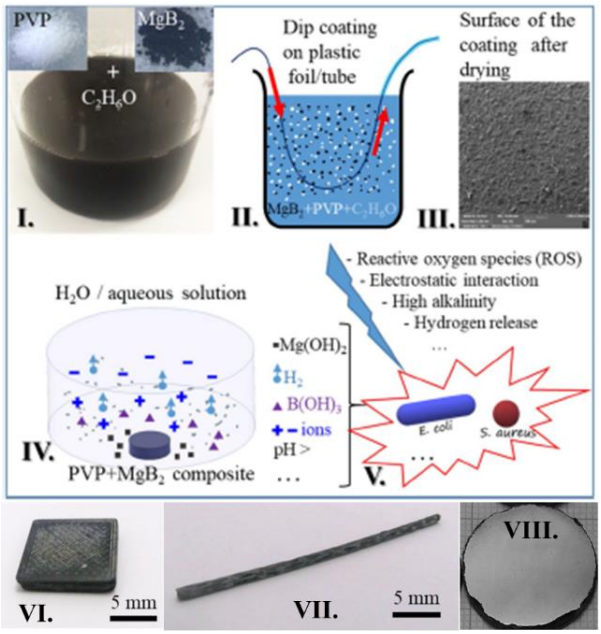


**Fig. 1** Preparation of composite $MgB_2$-PVP coatings (I–III), release of active $MgB_2$ from the composite coating and its decomposition in the presence of water/aqueous solution (IV), and the antimicrobial effect through possible mechanisms on different microbes (V). SEM image from III is taken on a PVP-$MgB_2$ coated on a plastic foil cut from the reservoir of a commercial urinary catheter; The 3D-printed PLA-$MgB_2$ sample (VI), the filament of PLA with embedded $MgB_2$ particles (VII) used to print sample from VI, and bulk $MgB_2$ sintered disc, metallographically polished (VIII).

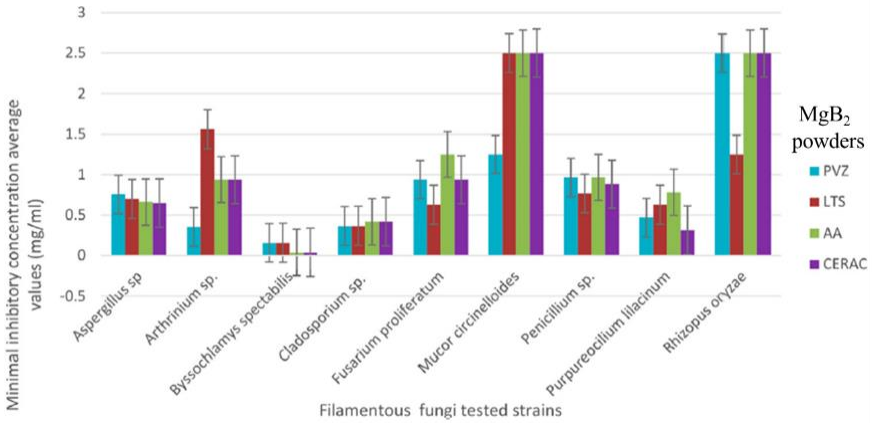


**Fig. 2** Minimal inhibitory concentrations (average values) obtained for the fungal strains belonging to different genera. In vitro tests were performed on 4 commercial powders named PVZ, LTS, AA, CERAC. Indicated powders contain a different amount of $MgB_2$ phase (80-97 wt. %).

The obtained results evidence the promising potential of $MgB_2$ to inhibit the biodeterioration by fungi growth, while it proved to be ecofriendly to the antifungal concentrations. This result may enable and impact conservation/restoration solutions for safeguarding the heritage objects and monuments. Results are also promising and recommend $MgB_2$ for designing efficient anti-infective and anti-tumor solutions. This work opens new directions of study and applications of $MgB_2$ for various biomedical devices, instruments, infrastructure, and systems. Taking advantage of its biocompatibility, biodegradation, and antimicrobial activity other possible applications could be found in the packaging industry, e.g. for food transportation, preservation, and enhancement of the shelf life. $MgB_2$ can be also useful in industries where free surfaces of biological materials are necessary. We mention the management of potable water, but other biofouling applications are also expected to emerge.

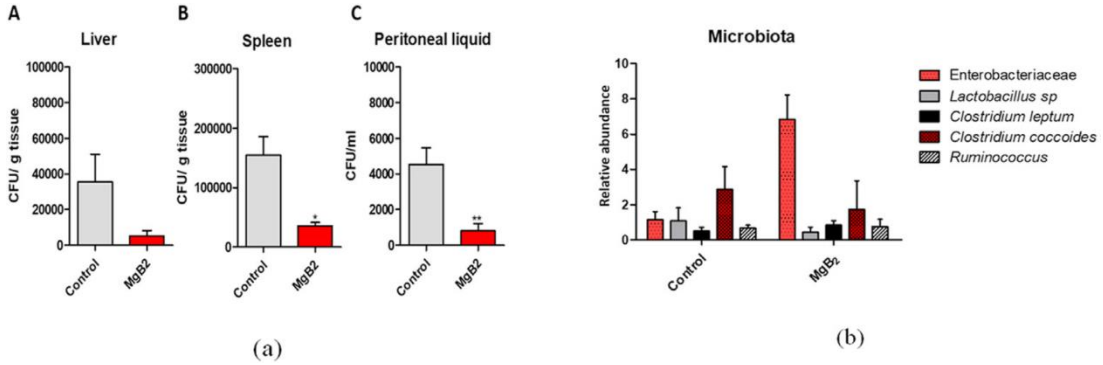


**Fig. 3** (a) The average abundance of the colony forming units (CFU/g) of E. coli in the liver (A), spleen (B), and peritoneal fluid (C) in nude CD-1 mice infected with E. coli (Control) and infected with E. coli and treated with $MgB_2$; (b) The relative abundance of different bacteria in the intestinal microbiota in healthy mice (Control) and in mice treated with $MgB_2$.

*References*


1. Irina Gheorghe, Ionela Avram, Viorica Maria Corbu, Luminita Marutescu, Marcela Popa, Irina Balotescu, Ion Blajan, Venus Mateescu, Daniela Zaharia, Andreea Stefania Dumbrava, Octavia Emilia Zetu, Ionut Pecete, Violeta Corina Cristea, Dan Batalu, Mihai Alexandru Grigoroscuta, Mihail Burdusel, Gheorghe Virgil Aldica, Petre Badica, Adina Daniela Datcu, Nicoleta Ianovici, Coralia Bleotu, Veronica Lazar, Lia Mara Ditu, and Mariana Carmen Chifiriuc, In Vitro Evaluation of $MgB_2$ Powders as Novel Tools to Fight Fungal Biodeterioration of Heritage Buildings and Objects (2021) Frontiers in Materials 7, 01059. https://doi.org/10.3389/fmats.2020.601059
2. P. Badica, N. D. Batalu, M. C. Chifiriuc, M. Burdusel, M. A. Grigoroscuta, G. Aldica, I. Pasuk, A. Kuncser, M. Enculescu, M. Popa, L. G. Marutescu, I. Gheorghe, O. Thamer, C. Bleotu, G. Gradisteanu Pircalabioru, L. Operti, V. Bonino, A. Agostino, M. Truccato, $MgB_2$ powders and bioevaluation of their interaction with planktonic microbes, biofilms, and tumor cells, (2021) Journal of Materials Research and Technology 12, 2168-2184P. Badica, N.D. Batalu, M. Burdusel, M.A. Grigoroscuta, G. Aldica, M. Enculescu, G. Gradisteanu Pircalabioru, M. Popa, L.G. Marutescu, B.G. Dumitriu, L. Olariu, A. Bicu, B. Purcareanu, L. Operti, V. Bonino, A. Agostino, M. Truccato, and M.C. Chifiriuc, Antibacterial composite coatings of $MgB_2$ powders embedded in PVP matrix, (2021) Scientific Reports 11, 9591. https://doi.org/10.1016/j.jmrt.2021.04.003.
3. S.K. Padhi, N. Baglieri, V. Bonino, A. Agostino, L. Operti, N.D. Batalu, M.C. Chifiriuc, M. Popa, M. Burdusel, M.A. Grigoroscuta, G.V. Aldica, D. Radu, P. Badica, M. Truccato, Antimicrobial activity of $MgB_2$ powders produced via reative liquid infiltration method, (2021) Molecules 26, 4966. https://doi.org/10.1038/s41598-021-88885-2.
4. P. Badica, N.D. Batalu, M.C. Chifiriuc, M. Burdusel, M.A. Grigoroscuta, G.V. Aldica, I. Pasuk, A. Kuncser, M. Popa, A. Agostino, L. Operti, S.K. Padhi, V. Bonino, M. Trucatto, Sintered and 3D-printed bulks of $MgB_2$-based materials with antimicrobial properties, (2021) Molecules 26, 6045 . https://doi.org/10.3390/molecules26164966
5. P. Badica, N.D. Batalu, M.C. Chifiriuc, M. Burdusel, M.A. Grigoroscuta, G.V. Aldica, I. Pasuk, A. Kuncser, M. Popa, A. Agostino, L. Operti, S.K. Padhi, V. Bonino, M. Trucatto, Sintered and 3D-printed bulks of $MgB_2$-based materials with antimicrobial properties, (2021) Molecules 26, 6045.

# New superconductor/ferromagnet heterostructures with giant magnetoresistance for applications in superconducting digital and quantum circuits.

**I Ivan[a,*], I Pasuk[a], A Crisan[a],V Sandu[a], M Onea[a] ,A M Ionescu[a], M Burdusel[a] and A Leca[a]**
[a]National Institute for Materials Physics, PO Box MG-7, Magurele, Romania, 077125

Epitaxial bilayers of $Y_1Ba_2Cu_3O_{7-x}$ (YBCO) and $CaRuO_3$ (CRO) was grown using a 248 nm KrF excimer laser from solid targets with stoichiometric compositions. As substrate, 5×5 $mm^2$ STO (001) single crystal is used. YBCO (380 nm) was first grown as bottom layer and the CRO (130 nm) was grown on top. The layers were deposited at 780 °C and 700 °C respectively. The deposition parameters were similar for both layers: energy density 1.7 J/$cm^2$, pulse frequency 2.0 Hz, $O_2$ partial pressure 0.25 mbar. After growth, these films were annealed in a 680 mbar oxygen atmosphere at 550 °C for two hours, to achieve the oxygenation for the YBCO layer, followed by slow cooling down to the room temperature.

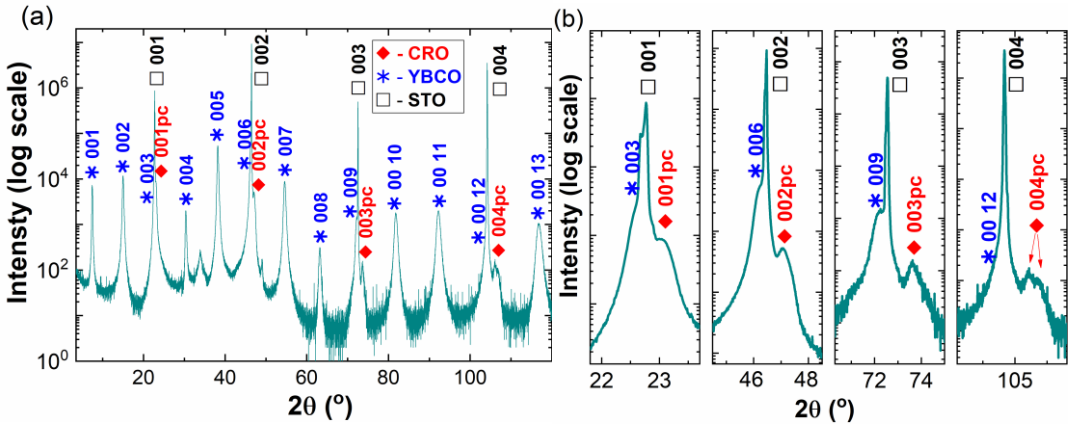


**Fig. 1** XRD data and their interpretation. (a) 2θ-ω scan; (b) zoomed views of the 2θ-ω scan around the substrate peaks;

| Film | In-plane | | Out-of-plane |
|---|---|---|---|
| | a (Å)<br>strain | b (Å)<br>strain | c (Å)<br>strain |
| **CRO**<br>Bulk pc<br>a=3.840 Å | 3.83<br>- 0.16 % | 3.905<br>+ 1.66 % | 3.855<br>+ 0.39 % |
| **YBCO**<br>Bulk<br>a=3.817 Å<br>b=3.883 Å<br>c=11.682 | 3.83<br>+ 0.45 % | 3.905<br>+ 0.57 % | 11.760<br>+ 0.67 % |

**Table 1**. The measured lattice constants.

The XRD analysis from above shows that the in-plane tensile strain of about 1.7%. substantially alter the magnetic properties of $CaRuO_3$(CRO) layer deposited on epitaxial YBCO film, making CRO a suitable candidate not only for the realization of superconductor straintronic devices but also for the fabrications of S/F heterostructures based on high-$T_c$ for which a small number of ferromagnetic materials exist.

The secondary electrons microscopy (SEM) image of the YBCO/CRO heterostructure presented in Fig. 2(a) shows a good uniformity of the $CaRuO_3$ film with a specific number of holes and droplets related to the PLD process. The layer thicknesses obtained from cross-sectional SEM images were $d_{YBCO}$ ~ 380 nm and $d_{CaRuO}$ ~ 130 nm.

Energy dispersive X-ray microanalysis (EDX) was performed in order to obtain the chemical composition at the interface. In the spectrum presented in Fig. 2(b) one can observe the presence of the Ca and Ru atoms from the ferromagnetic layer with a good transition.

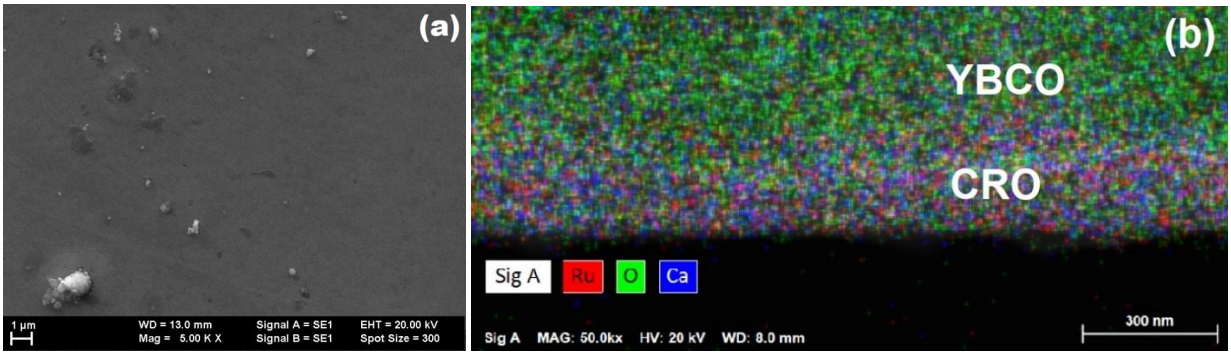


**Fig. 2**. ***(a)*** SEM image of the surface of $CaRuO_3$ layer grown onto $Y_1Ba_2Cu_3O_{7-x}$ thin film. ***(b)*** Cross-sectional elemental mapping obtained by EDX. The estimated thickness of the $CaRuO_3$ layer is ~130 nm.

Magnetization versus magnetic field isotherms were collected at $T$ = 300 K for both CRO-single film and YBCO/CRO heterostructure as can be seen in Fig. 3. The CRO ferromagnetic layer has identical remanence (6.15 emu/cc). However, the saturation of the macroscopic magnetization in the case of CRO- single film is attained at a slightly higher $H$ due to an increased tensile strain, as was discussed.

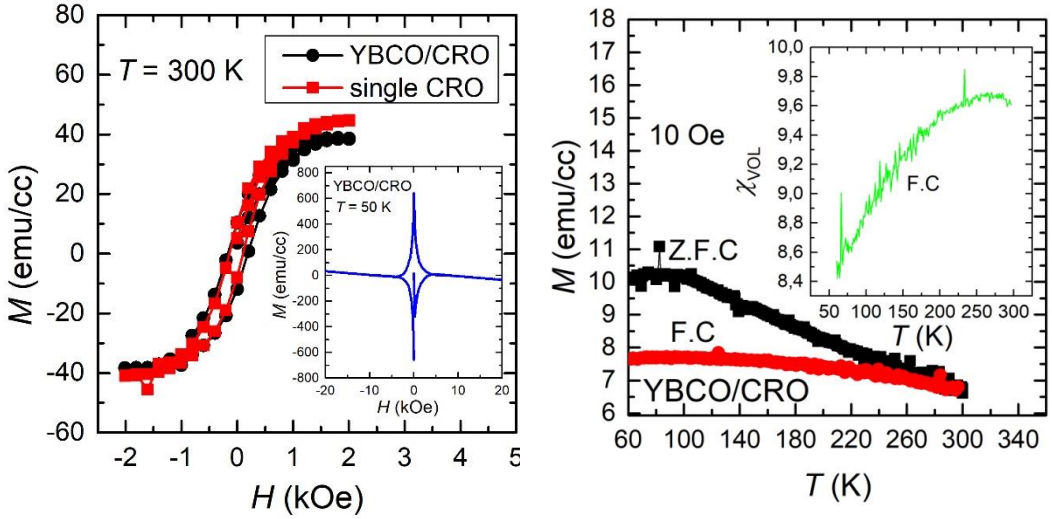


(a) (b)

**Fig. 3**. (a)Magnetization hysteresis loops at $T$ = 300 K for the YBCO/CRO heterostructure and single $CaRuO_3$ thin film grown on STO substrate using identical deposition condition. Inset: $M(H)$ hysteresis loop at $T$ = 50 K for YBCO/ CRO heterostructure.(b) Zero-field-cooled (Z.F.C) and field-cooled (F.C) magnetization $M$ vs temperature $T$ plots for $T > T_c$ with $H$ perpendicular to the sample plane. Inset: $T$ dependence of the magnetic susceptibility $\chi_{VOL}$.

The temperature dependence of magnetic susceptibility $\chi_{VOL}$ (see the inset of Fig. 3(b)) shows a plateau around $T$ = 260 K from which $\chi_{VOL}$ begins to drop. According to the well known Curie-Weiss law, we can roughly estimate the value of the Curie temperature $T_{Curie}$ as being 340 K. The same value can be deduced by extrapolating the $M(T)$ data presented in the main panel of Fig.3.

The magnetoresistance of the heterostructure was measured using the standard four-probe technique with contacts made directly to the CRO layer using silver paste. The magnetic field was applied perpendicular to the sample plane and it's intensity was swept between 0 and 500 Oe at temperatures fixed along the superconducting resistive transition, as can be seen in Fig. 4.

Large magnetoresistance dips are observed with relative height decrease when the temperature is increased. The possible mechanism related to this effect can be due to a lowered average exchange field seen by the Cooper pairs when different directions of the ferromagnet's exchange field $h_{ex}$ are occurring during the applied magnetic field swiping.

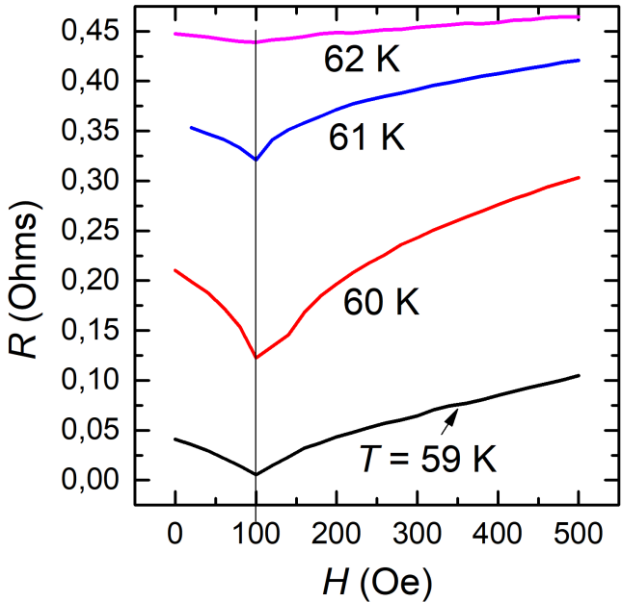


**Fig. 4**. Resistance as a function of magnetic field, *R*(*H*), for YBCO/CRO heterostructure, measured along the superconductivity tranzition at *T* between 59 K - 62 K.

*References*

1. I Ivan, I Pasuk, A Crisan, V Sandu, M Onea, A Leca, C Cosar and M Burdusel," New superconductor/ferromagnet heterostructure formed by YBa2Cu3O7−x and CaRuO3", Superconductor Science and Technology 34(11), 115009 (2021).

# Chalcogenide materials engineering for emerging memory applications

**C. Mihai,[a] F. Sava,[a] I.D. Simandan,[a] A.T Buruiana,[a] A.C. Galca,[a] A. Velea[a,*]**
[a]National Institute of Materials Physics, 405A Atomistilor Street, Magurele, Romania, 077125

Emerging chalcogenide memories, such as resistive random access memories (RRAMs) and phase change memories (PCMs), can store information as different resistivity states when subjected to an external electrical or optical signal. PCMs exhibit a reversible structural phase change between an amorphous (high resistivity or low reflectivity) state and a crystalline (high conductivity or high reflectivity) state. RRAMs on the other hand are based on metal cations (such as $Cu^+$ or $Ag^+$) migration in a solid electrolyte and the formation of metallic filaments that connect the electrodes. Moreover, PCMs can store multiple bits of information per memory cell, known as multi-level cell, which paves the way for ultra-dense memories. To create high-speed, ultra-dense memories with low energy consumption, new chalcogenide materials with specific memory properties, thermally stable and with controllable crystallization are needed.

A combinatorial approach through magnetron co-sputtering for materials' library synthesis can be employed to successfully search for new memory materials [1]. The compositional space of the Si–Ge–Te system, beyond the known glass formation domain of bulk glasses (GFD), was explored. The magnetron sputtering system used for the deposition of the Si-Ge-Te library is schematically represented in Figure 1a. The final library has the following compositional spread by element: [8.1 ÷ 45.6] at.% for Si, [16 ÷ 62.5] at.% for Ge and [15 ÷ 69.8] at% for Te. In comparison with other studies of the Si–Ge–Te system, the new compositional domain is at least 5 times larger.

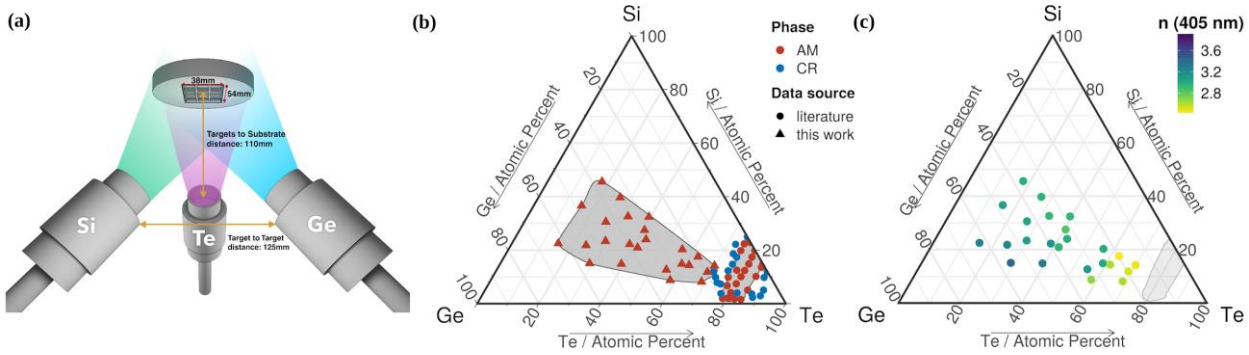


**Fig. 1** Combinatorial Si–Ge–Te library: (a) schematic diagram of the experimental deposition setup, (b) as-deposited library structure (AM = amorphous, CR = crystalline) and GFD and (c) library refractive index at 405 nm.

The chemical composition and structure of the samples in the library, together with the GFD known from literature, are shown in the ternary diagram from Figure 1b. The X-ray diffraction measurements revealed that all the as-deposited samples have amorphous structure, thus significantly extending the compositional space of potential PCM candidates. Further, their optical properties were explored. For example, the refractive indices at 405 nm (the wavelength used for Blu-ray Discs) obtained by spectroscopic ellipsometry, are shown in Figure 1c. The Te percent has a large influence on the refractive index. At this wavelength, the refractive index has a minimum close to the GFD.

$Ge_2Sb_2Te_5$ is a ternary chalcogenide material intensely studied and used for optical and electrical memory applications due to its fast and reversible crystalline to amorphous phase transition that leads to a remarkable change in reflectivity and resistivity, respectively. However, phase change materials are known to exhibit deposition-dependent optical and structural properties, such as mass density, optical bandgap and refractive index. Thus, a comparison of the structural and optical properties of $Ge_2Sb_2Te_5$ films obtained by magnetron sputtering (MS), pulsed laser deposition (PLD) and a deposition technique combining both methods (MSPLD) is presented [2]. The optical properties of the as-deposited (amorphous) and annealed (crystallized) films are shown in Figure 2a-c.

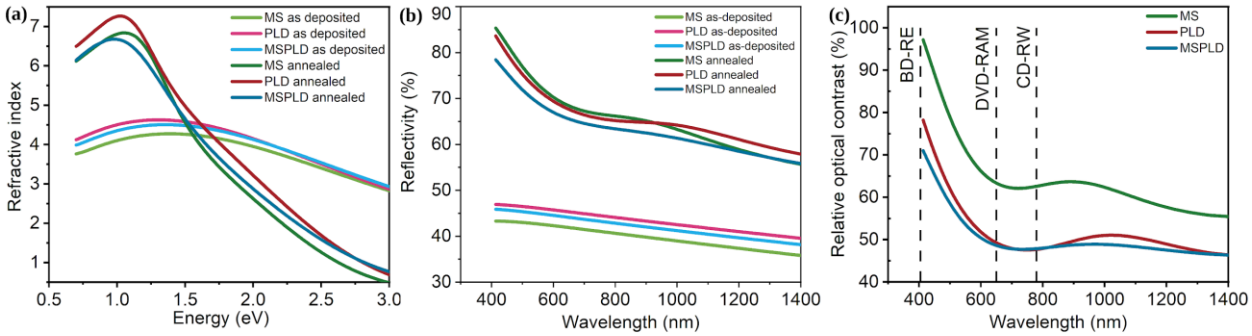


**Fig. 2** Optical properties of GST-225 films deposited by different deposition techniques: (a) refractive index, (b) optical reflectivity and (c) relative optical contrast.

Films obtained by PLD and annealed have the highest refractive index (Figure 2a). The reflectivity of the films in the as-deposited state is between 36 and 47%, whereas after annealing, the reflectivity is between 55 and 85% in the measured wavelength range (Figure 2b). The highest relative optical contrast is observed for magnetron sputtering (Figure 2c). The main reason is the single-phase crystallization of MS films as compared with PLD and MSPLD films, which contain a minor $GeSb_4Te_4$ phase. In conclusion, disorder vacancies in the crystalline phase and mixed crystalline phases have a significant influence on the reflectivity. For electrical and optical PCMs, MS is the best suited deposition method.

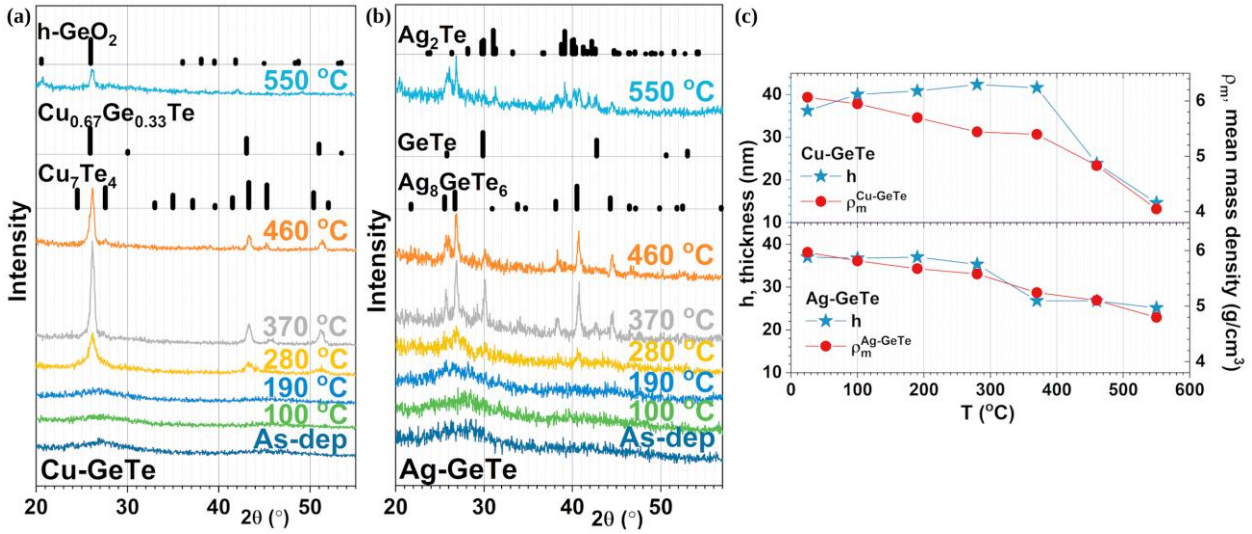


**Fig. 3** Thermal stability of metal chalcogenides: GIXRD diagrams of (a) Cu-GeTe and (b) Ag-GeTe thin films, (c) thickness and mean mass density for Cu-GeTe and Ag-GeTe thin films after annealing at different temperatures.

In order to test the thermal stability of chalcogenide RRAMs, such as Cu-GeTe and Ag-GeTe alloys, these ion-conducting amorphous chalcogenides were subjected to incremental annealing [3]. Cations migration which governs the performance of resistive memory devices is affected by the binary and ternary polycrystalline phases formed during annealing within the solid amorphous electrolytes. Thus, the formation of these phases and their fractions was determined. The changes in structure, thickness and mass density of the films are shown in Figure 3a-c. Both materials remain fully amorphous even after annealing at 190 ˚C (Figure 3a and 3b). However, above this temperature different polycrystalline phases are formed. Also, in the case of the Ag-GeTe film, Te evaporation is evidenced starting from 370 ˚C. The film thickness and mass density variation is correlated with the structural changes (Figure 3c). Cu-GeTe and Ag-GeTe films are thermally stable up to a temperature of 190 ˚C, which is enough for device setup.

Further, chalcogenide memories were built [4]. In order to obtain intermediary resistive states in lateral GeTe devices (Figure 4a), DC sweeps were applied, the start value being 0 V, while the stop value ranges between 3 and 9.5 V. After each sweep, the current was read at 0.1 V for several seconds.

Various intermediate resistance states were obtained (Figure 4b). The change in resistance is due to a progressive crystallization of the amorphous region between the electrodes after applying the increasing voltage sweeps. In the forming step, pristine devices are subjected to a thermal treatment in order to produce small size crystalline nuclei which are the seeds that will grow and connect to form metallic filaments that span between electrodes during device switching.

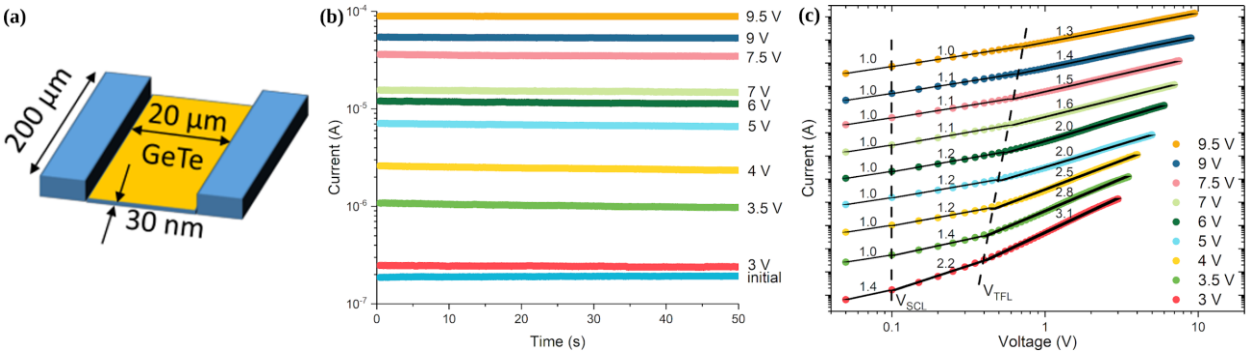


**Fig. 4** Multiple resistance levels obtained in GeTe devices by using voltage sweeps: (a) schematic illustration of a device, (b) the current at 0.1 V in the initial state and after applying voltage sweeps and (c) I–V characteristics in different resistance states after applying DC sweeps modeled by trap-controlled SCLC.

The subthreshold conduction in GeTe devices was modeled using the trap-controlled space charge limited conduction (SCLC) theory. The double-logarithmic I–V plots of the GeTe memristor (Figure 4c) show three clearly delimited regions in the high resistive state: (i) an ohmic region at very low voltages ($I \propto V$); (ii) a SCLC region at higher voltages ($I \propto V^2$), and (iii) a stronger field dependence near the threshold field ($I \propto V^3$). By approaching the low resistivity states, all the regions merge in a single linear ohmic region. The multiple resistance states can act as synaptic weights modulated by electrical pulses, thus the devices could be used in neuromorphic computing.

*References*


1. C. Mihai, F. Sava, I.D. Simandan, A.C. Galca, I. Burducea, N. Becherescu, A. Velea, "Structural and optical properties of amorphous Si–Ge–Te thin films prepared by combinatorial sputtering", Sci. Rep. 11, 11755 (2021)
2. I.D. Simandan, F. Sava, A.T. Buruiana, A.C. Galca, N. Becherescu, I. Burducea, C. Mihai, A. Velea, "Influence of Deposition Method on the Structural and Optical Properties of $Ge_2Sb_2Te_5$", Materials 14, 3663 (2021).
3. F. Sava, I.D. Simandan, I. Stavarache, C. Porosnicu, C. Mihai, A. Velea, "Thermal stability of amorphous metal chalcogenide thin films", J. Non-Cryst. Solids 559, 120663 (2021).
4. A. Velea, V. Dumitru, F. Sava, A.C. Galca, C. Mihai, "Multilevel Memristive GeTe Devices", Phys. Status Solidi RRL 15, 2000475 (2021).

# Insights about CO sensing mechanism with NiO based gas sensors – the influence of humidity

**Cristian E. Simion,[a] Corneliu Ghica,[a] Catalina G. Mihalcea,[a,c] Daniela Ghica,[a] Ionel Mercioniu,[a] Simona Somacescu,[b] Ovidiu G. Florea,[a] Adelina Stanoiu[a,*]**

[a]National Institute of Materials Physics, Atomistilor 405A, Magurele, Romania, 077125

[b]"Ilie Murgulescu" Institute of Physical Chemistry, Romanian Academy, Spl. Independentei 202, Bucharest, Romania, 060021

[c]University of Bucharest, Faculty of Physics, Atomistilor 405, Magurele, Romania, 077125

In this report, polycrystalline NiO based materials have been prepared via a hydrothermal method using Ethylene glycol (EG) as template and Ethylenediaminetetraacetic acid (EDTA) as complexing agent, further deposited onto commercial $Al_2O_3$ substrates provided with Pt electrodes and heater [1]. The SEM image in Figure 1a reveals the growth morphology as quasispherical formations, having dimensions of ~1 μm.

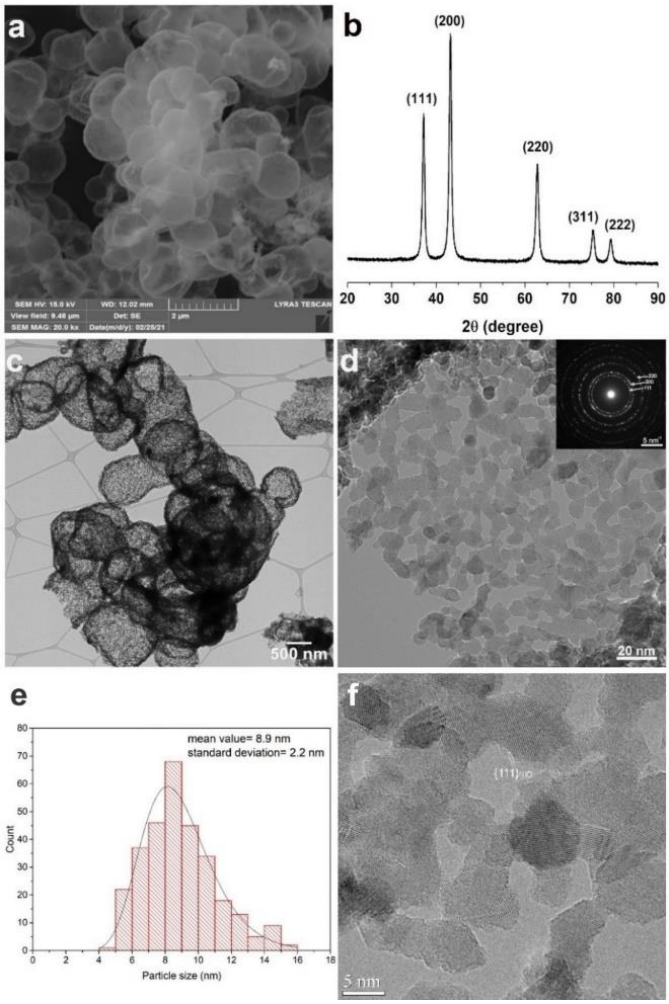


**Fig. 1** SEM image revealing the growth morphology as micrometric quasi-spherical formations (a); XRD pattern proving the synthesis of single-phase cubic NiO (b); low-magnification TEM image (c); high-magnification TEM image and inserted SAED pattern showing the nanostructure of the quasi-spherical formations (d); nano-particles size distribution from TEM imaging on the NiO sample (e); HRTEM image of the NiO nanoparticles (f).

The XRD pattern in Figure 1b has been recorded in a wide 2θ range and indexed ac-cording to cubic NiO as unique phase, space group Fm-3m (225), ICDD - 01-071-1179, with the lattice parameter α = 0.4178 nm.

The low-magnification TEM image in Figure 1c confirms the quasi-spherical micrometrical formations observed by SEM and also their empty ball-like morphology.

Even at low magnification one can notice that the membrane shaping these globular bodies is not continuous, but exhibits a certain nanoscale structure.
The high-magnification TEM image in Figure 1d has been recorded from a broken globular micro-object showing that the membrane consists of self-assembled nanoparticles.
The crystalline structure was analyzed by selected area electron diffraction (SAED) confirming the formation of face-centered cubic NiO as unique phase, as was determined by XRD.
TEM images from which we determined an average size of 9±2 nm (Figure 1e). A typical HRTEM image shows the absence of extended structural defects inside the nanoparticles (Figure 1f).
Furthermore, the CO sensor signal was evaluated as the ratio of electrical resistance: $S = R_{CO}/R_{Air}$.
Since the maximum sensor signal was attained at 250°C, we evaluate the sensor signal dependence with respect to the CO concentrations.

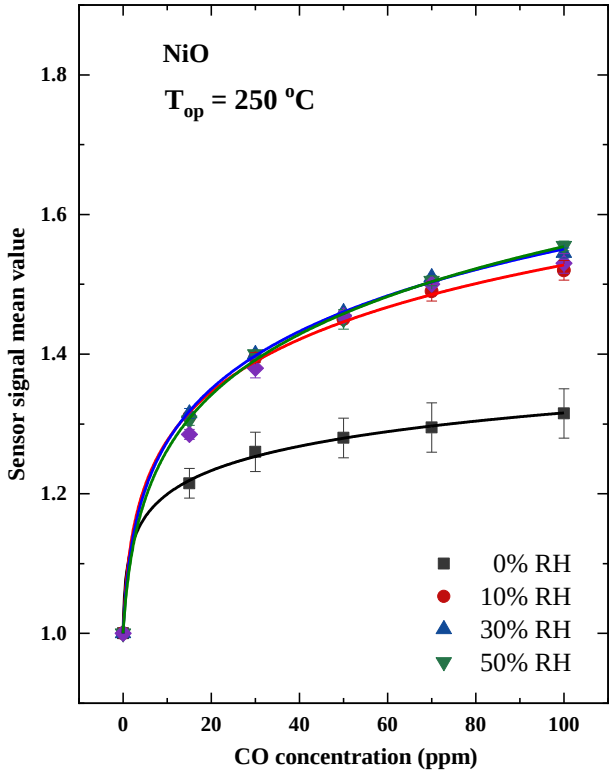


**Fig. 2** Sensor signal dependence as a function of CO concentration under dry and humid conditions.

In Figure 2 one can observe that the sensor signal with respect to CO concentration is higher in the presence of humidity being independent on the RH level without reaching saturation.
Only from basic DC measurements one cannot decouple between surface ionosorption and localized physisorption, therefore it's important to involve complementary phenomenological investigations (simultaneous electrical resistance - R and contact potential changes - CPD) in order to understand the fundamental aspects of the gas-surface interactions [2,3].
In terms of potential changes, the quantitative analysis (ΔΦ; qΔVs and Δχ) as depicted in Figure 3 a,b, gives clear evidence that the CO exposure induces a decrease of both ΔΦ and qΔVs slightly pronounced under humid conditions, while the electron affinity Δχ remains almost unchanged within the measurement error.
Such aspect reveals the fact that the reaction yield between CO takes place either with the pre-adsorbed oxygen species as it is depicted by the following quasi-chemical equation:

$$Ni + O^-_{ads} + CO^{gas} + H_2O^{gas} \rightarrow CO_2^{gas} + H_2O^{phys} + Ni + e^- \quad (1)$$

or with the lattice oxygen, leading to surface oxygen vacancies as it is revealed by the next quasi-chemical equation:

$$Ni + O_{latt} + CO^{gas} + H_2O^{gas} \rightarrow CO_2^{gas} + H_2O^{phys} + Ni + V_o^{+} + e^{-} \quad (2)$$

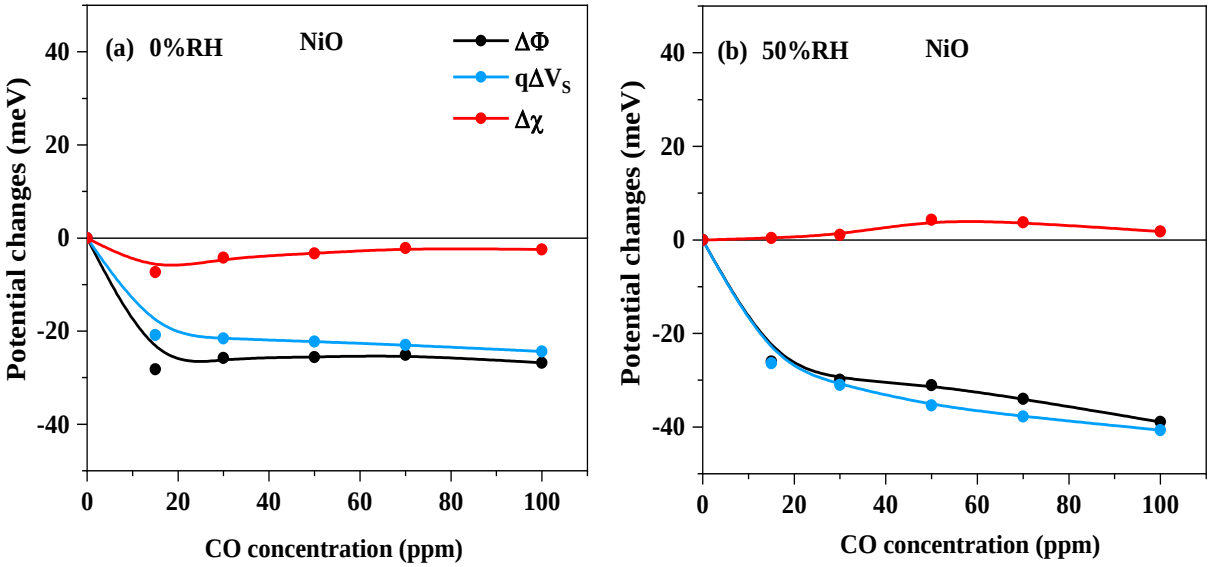


**Fig. 3** Dependence of the potential changes with respect to CO concentration for NiO based gas sensor operated at 250°C and different background humidity: 0%RH (a) and 50%RH (b).

The aforementioned results have revealed new reaction routes for CO detection under in-field conditions with NiO based gas sensors [4].

*References*


1. H-R. Kim et al., "The role of NiO doping in reducing the impact of humidity on the performance of SnO2-based gas sensors: synthesis strategies, and phenomenological and spectroscopic studies," Adv. Func. Mat. 21, 4456-4463 (2011).
2. M. Hübner et al., "Influence of humidity on CO sensing with p-type CuO thick film gas sensors," Sens. Actuators B: Chem. 153, 347-353 (2011).
3. N. Barsan et al., "Understanding the fundamental principles of metal oxide based gas sensors; the example of CO sensing with $SnO_2$ sensors in the presence of humidity," J. Phys.: Condens. Matter 15, R813 (2003).
4. C. E. Simion et al., "Insights about CO gas sensing mechanism with NiO based gas sensors – the influence of humidity," Chemosensors 9(9), 244 (2021).

# Enhancing performance of $Al_2O_3$ based floating gate memories by formation of Ge-related storage centres in addition to Ge-rich nanocrystals

**Ionel Stavarache[a,*], Ovidiu Cojocaru[a,b], Valentin Adrian Maraloiu[a], Valentin Serban Teodorescu[a], Toma Stoica[a], Magdalena Lidia Ciurea[a*]**

[a] National Institute of Materials Physics, 405A Atomistilor Street, PO Box MG-7, Magurele 077125, Ilfov, Romania
[b] Faculty of Physics, University of Bucharest, 077125 Magurele, Romania

The development of memory devices with conventional $SiO_2$ has reached its fundamental limit mainly due to high leakage currents leading to short channel effects. This problem can be solved by replacing $SiO_2$ with high-κ dielectrics. Among the high-κ dielectrics, $Al_2O_3$ presents superior characteristics compared with $SiO_2$, i.e. higher dielectric constant, good mechanical properties, high-temperatures resistance. We prepared a memory structure *$Al_2O_3$(10 nm)/ Ge(15 nm)/ [$Al_2O_3$ (4 nm)/ thermal $SiO_2$(3 nm)] /p-Si substrate* by magnetron sputtering. The tunnel region consists of *$Al_2O_3$ /$SiO_2$* on Si wafer, which is covered by a *Ge* intermediate layer and a gate *$Al_2O_3$*. The samples were annealed by RTA (500 – 900 °C, 1 min, $N_2$ flow). Top and bottom Al electrodes (1×1 $mm^2$) in planar geometry were deposited using shadow masks. Films were studied by Transmission Electron Microscopy (TEM) and electrical characterization (*C – V*). Fig.1 presents a comparative cross section TEM (XTEM) of the as-deposited sample (Fig.1a) and the 600 °C RTA sample (Fig.1b). Both samples are amorphous and differences appear at the interface of Ge layer with $Al_2O_3$ as revealed by XTEM and EDX (Fig.1b inset). In Fig.1(c) and (d) are shown High-Angle Annular Dark-Field (HAADF) and XTEM images respectively, together with EDX scan lines on 650 °C sample. The EDX scan line in the HAADF cross section evidences the principal maximum of Ge and two shoulders inside lateral $Al_2O_3$ layers (Ge diffusion) where the density of the Ge layer in the middle zone becomes lower (by voids or local low density zones).

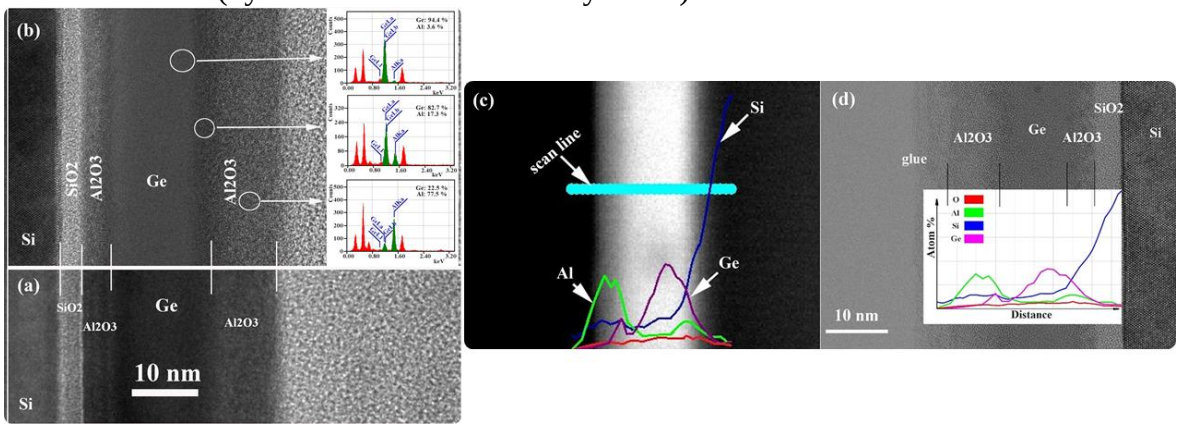


**Fig. 1** XTEM of the as deposited structure (a), and the 600 °C RTA structure (b), with EDX results as inset. EDX scan line in the HAADF cross section image (c) and EDX line scan superposed on the XTEM high-resolution image for 650 °C RTA structures (d).

In Fig.2a-d, structure details for 700 °C RTA film are presented. In the HAADF image (Fig.2b) we observe small white spots (small arrows) that represent Ge accumulation. These amorphous particles appear in the $Al_2O_3$ tunnel. Also, in the Ge layer there are some crystallized areas (big arrows-Fig.2a) that are evidenced in the high-resolution details in Fig.2(c) and (d) showing (111) Ge lattice fringes (0.326 nm) corresponding to Ge NCs (~ 2-3 nm). Therefore, after 700 °C RTA, the Ge lateral diffusion is stronger and voids or low density amorphous zones are observed in the Ge layer (Fig.2c). The structure of 800°C RTA are shown in Fig.2e-g. Two types of Ge-rich NCs appear, i.e. NCs of 4 – 5 nm size (~0.34 nm fringes), located in the Ge layer near the interface with the tunnel layer, and small NPs (~2 nm) located in the $Al_2O_3$ tunnel layer (e.g.~0.233 nm fringes) with unknown crystalline structure. We suggest that these crystallites showing 0.34 nm lattice fringes are formed by a mixed oxide of Al and Ge ($Al_2GeO_5$ and $Al_2Ge_2O_7$). Annealing at 600–650 °C induces a strong Ge diffusion

in $Al_2O_3$ layer, while the whole structure remains amorphous. After the 700 °C RTA, Ge NCs and voids are formed in the Ge layer, but the majority of Ge aggregates at the interface and inside the $Al_2O_3$ form amorphous mixed oxide Ge-rich NPs. For 800 °C RTA, Ge aggregates are present in $Al_2O_3$, forming Ge-rich mixed GeAl oxide. They are amorphous or crystalline with lattice fringes (0.34 nm; 0.23 nm) that do not correspond to the cubic Ge.

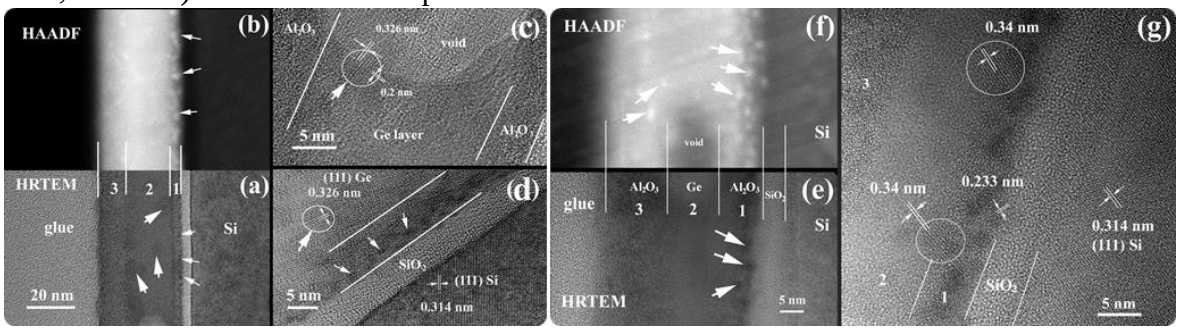


**Fig. 2** Structure of 700 °C RTA: (a) HRTEM image; (b) HAADF; (c) and (d) high resolution showing Ge NCs in the Ge layer (big arrows). Small arrows - amorphous NPs in $Al_2O_3$ tunnel layer ((a),(b) and (d)). Structure of 800 °C RTA: (e) cross section HRTEM; (f) HAADF image. Arrows indicated Ge-rich NPs formed in the tunnel or $Al_2O_3$ gate. Voids are evident in the Ge layer (f); (g) detail of the Ge NPs in the $Al_2O_3$ tunnel (1).

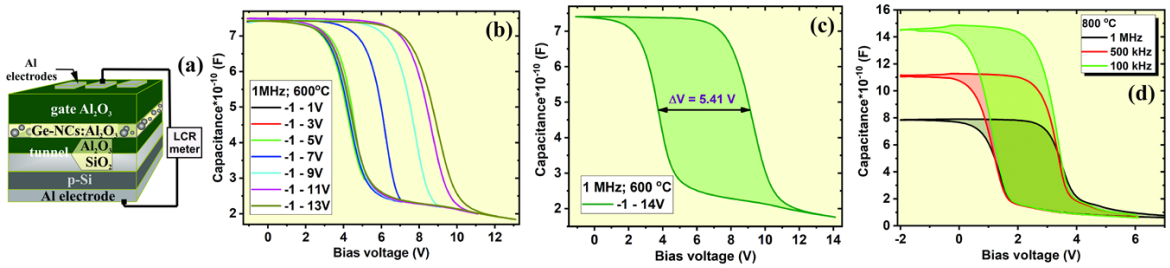


**Fig. 3** (a) measurement sketch; (b) *C – V* curves taken at 1 MHz on 600 °C RTA sample; (c) modification of hysteresis loop with the sweeping bias; (d) *C – V* curve measured at different frequencies on 800 °C RTA structures.

Measurement set-up (Fig.3a). Fig.3 b-d present the results obtained on two samples that show by XTEM the structural transformation by annealing: i) 600 °C RTA have Ge at the nanocrystallization limit but still amorphous; ii) 800 °C RTA in which oxidized Ge-rich GeAl NCs are formed (Fig.3d). The *C – V* curves on 600 °C RTA sample (Fig.3b, c) have the maximum memory window ($\Delta V_{fb}$). The $\Delta V_{fb}$ width expands with the increase of sweeping voltage range towards the saturation value of 5.4 V (Fig.3c) for -1 ÷ 14 V range. Generally, the memory effect appears by electron and hole injection from Si substrate for positive and negative writing voltage, respectively, and *C – V* curve is symmetric in respect to 0 V. Our *C – V* curves show that the memory loops are mainly changed by the electron injection from Si at positive writing voltage, meaning that the energy barrier for holes is higher than for electrons. The *C – V* curves on 800 °C RTA at 100 kHz, 500 kHz and 1 MHz are shown in Fig. 3d. $\Delta V_{fb}$ does not significantly modify with frequency, meaning that the main contribution to the memory effect ($\Delta V_{fb}$ = 2.3 V) comes from AlGeO NCs rich in Ge not from interface states. The normalized *C – V* curves (1MHz) measured on as deposited samples as well as on the other samples annealed up to 900 °C, are shown in Fig.4a. Fig. 4b shown $\Delta V_{fb}$ versus annealing temperature. So, for as deposited sample $\Delta V_{fb}$ is 1.9 V, then it increases to 5.4 V for 600 °C RTA sample, afterwards it decreases down to $\Delta V_{fb}$= 1.5V for 900 °C RTA. The memory effect of all amorphous samples, i.e. the as deposited sample and the ones annealed at 550-650 °C is due to deep electronic levels present in the whole amorphous structure, together with those located at the interface of tunnel layer with Si. As the temperature increases to 700 °C, some Ge NCs are formed contributing to the memory effect, but the $\Delta V_{fb}$ diminishes by decreasing the density of states acting as storage centers. With further increase of the annealing temperature to 800 °C, $\Delta V_{fb}$ decreases in spite of formation of Ge-rich NCs (AlGeO rich in Ge) (Fig. 2e-g). This shows that a part of the electronic states responsible for memory effect in low RTA temperature samples are in fact Ge related states

(deep energy levels) present in the Ge amorphous clusters or Ge NCs. When Ge segregates and forms Ge rich mixed GeAl oxide NCs, the density of Ge related states strongly decreases, so that the density of the total contributors (NCs and Ge related states) to the memory effect is smaller than in amorphous samples. When the temperature increases to 900 °C, Ge diffusion is strong so that Ge NCs are no longer formed and an important part of electronic states heals, i.e. the density of charge storage centers strongly decreases together with $\Delta V_{fb}$. We calculate stored carriers density and the results are plotted in Fig.4b for each annealing temperature.

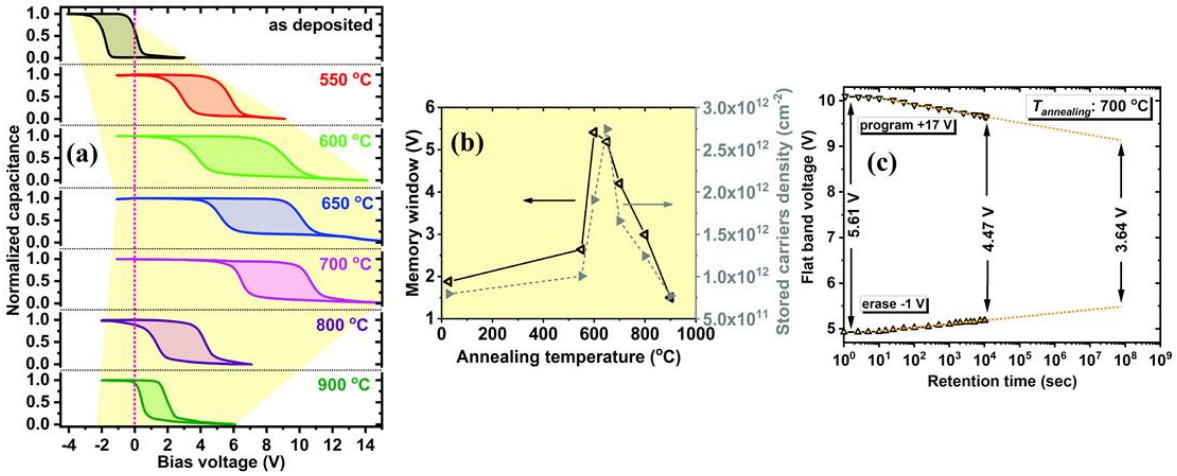


**Fig. 4** *C – V* curves (1MHz) on as deposited sample and annealed up to 900 °C (a). The *C – V* loops shift with RTA temperature. $\Delta V_{fb}$ (left axis) and stored carriers density (right axis) versus temperature (b). Retention on 700 °C RTA structure for $10^4$ s shows a decrease of charge loss ratio of 4.2% and 5.08% for program and erase states, respectively.

The retention characteristic of the trilayer structures annealed at 700 °C has been recorded for $10^4$ s and extrapolated to 10 years (Fig. 4c). For this, the ON (OFF) state retention was measured by monitoring the flat band voltage after programing (erasing) gate voltage of +17 V (-1 V) applied for 600 s. We calculate charge loss by:

$$Charge\ loss(\%) = \frac{V_{fb}(t=0) - V_{fb}(t)}{V_{fb}(t=0)}, \quad (1)$$

After $10^4$ s, the charge loss ratio is 5.1% and 4.2%, respectively. For extrapolated characteristics to 10 years, the charge loss is of 11% and 9.8% for the ON and OFF states, respectively. We have prepared Ge-based structures with high memory performances, by using magnetron sputtering followed by RTA and demonstrated that the memory properties are controlled by Ge rich NCs or Ge NCs located in the intermediate layer (700 and 800 °C), and also by Ge related local states positioned in adjacent tunnel and gate $Al_2O_3$ layers (>650 °C).

*References*

1. I. Stavarache et al., "Effects of Ge-related storage centers formation in $Al_2O_3$ enhancing the performance of floating gate memories", Appl. Surf. Sci. 542, 148702 (2021)

# Ge-rich SiGe nanocrystals in nanocrystallized $HfO_2$ for VIS-SWIR photosensitivity

**A.M. Lepadatu,[a,*] C. Palade,[a] A. Slav,[a] O. Cojocaru,[a] V.S. Teodorescu,[a] T. Stoica,[a,*] M.L. Ciurea,[a,*] D. Ursutiu,[b,c] C. Samoila,[d,e] G.A. Nemnes[f]**

[a]National Institute of Materials Physics, 405A Atomistilor Street, 077125 Magurele, Romania
[b]Transylvania Univ. of Brasov, Electronics and Computer Science Department, 29 Eroilor, 500036 Brasov, Romania
[c]Academy of Romanian Scientists, 54 Splaiul Independentei, 050094 Bucharest, Romania
[d]Transylvania University of Brasov, Department of Materials Science, 29 Eroilor, 500036 Brasov, Romania
[e]Romanian Technical Science Academy, 26 Dacia, 010413 Bucharest, Romania
[f] University of Bucharest, Faculty of Physics, 405 Atomistilor Street, 077125 Magurele, Romania

Research tackled VIS-NIR-SWIR photosensitivity of Ge-rich SiGe nanocrystals (NCs) embedded in nanocrystallized $HfO_2$ matrix (Figs. 1,2). Remarkable results of SWIR-extended cut-off wavelength of about 2 μm in the spectral photocurrent (broad 600–2000 nm response) exceeding the sensitivity limit for Ge were obtained by employing different tools, i.e. alloying Ge with little Si for increased NCs stability, inducing strain in NCs for reducing bandgap and ensuring high quality NC/matrix interface [1]. For this, magnetron sputtering was used for deposition of 3-layers stacks of cap $HfO_2$/SiGeHf$O_2$ active layer/buffer $HfO_2$/ on Si with very thin cap and buffer cladding $HfO_2$ layers employed for hampering fast Ge diffusion from the active layer. After deposition, rapid thermal annealing at 600 °C for nanostructuring was performed.

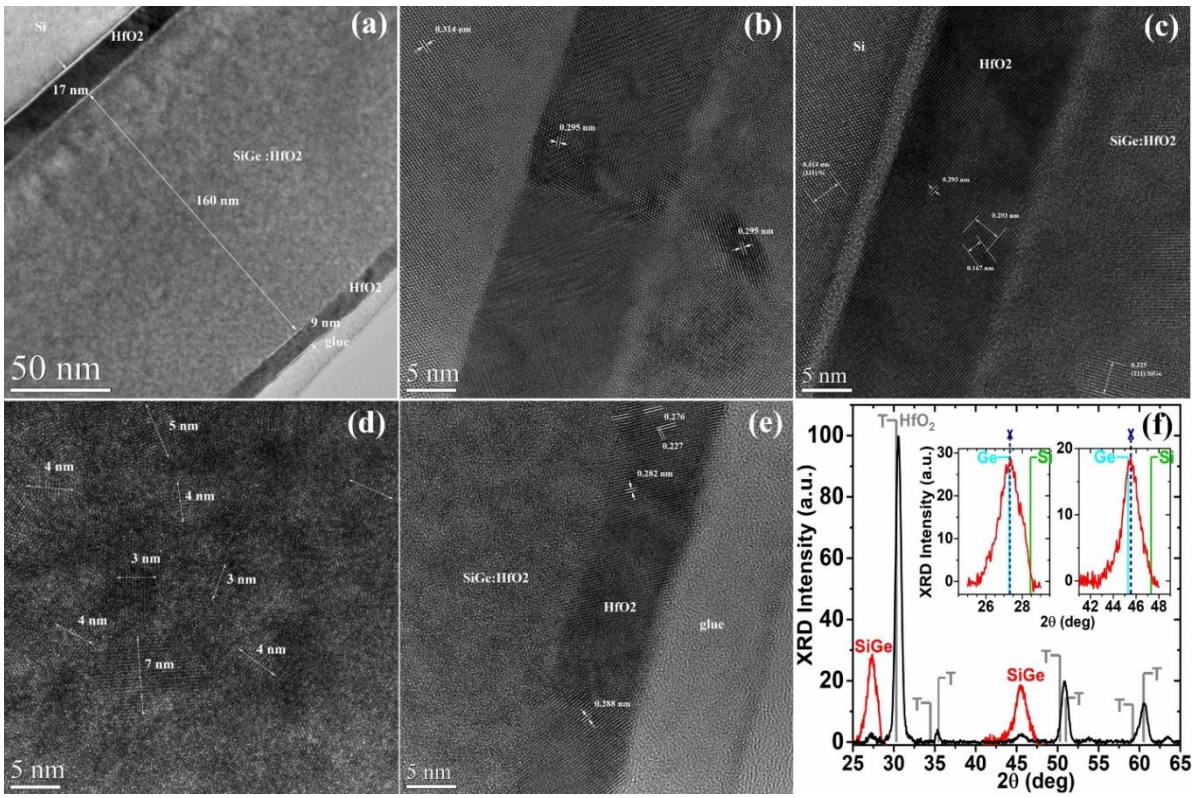


**Fig. 1** Crystalline structure and morphology of cap $HfO_2$/SiGe NCs-$HfO_2$ active layer/buffer $HfO_2$/Si structures: **(a-e)** XTEM analysis showing **a-** general view of 3-layer stack, **b,c-** HRTEM images from structures bottom evidencing lattice fringes of 0.293–0.295 nm for tetragonal/orthorhombic $HfO_2$ and (111) 0.325 nm for cubic SiGe, **d-** HRTEM image with indicated 3 to 7 nm sizes for SiGe and $HfO_2$ NCs, **e-** monoclinic top $HfO_2$ layer; **(f)** XRD full diffraction curve together with long-time scans around SiGe 111 and 220 diamond lines [1].

Photoactive layer consists in Ge-rich SiGe NCs with 3–7 nm diameter and diamond structure, being embedded in nanocrystallized matrix of $HfO_2$ with tetragonal/orthorhombic structure (Fig. 1b–e). Ge content of NCs determined from HRTEM lattice fringes is 87% in agreement with values from XRD (111) and (220) peaks of 95% and 88%, respectively. Top/cap $HfO_2$ layer has monoclinic structure (Fig. 1e), while bottom $HfO_2$ layer is tetragonal/orthorhombic (Fig. 1b,c). Raman spectroscopy also

evidences Ge-rich SiGe NCs formation by the corresponding peak (no. 2 in Fig. 2a) due to quantum confinement effect and with position also affected by 0.6% evaluated strain.

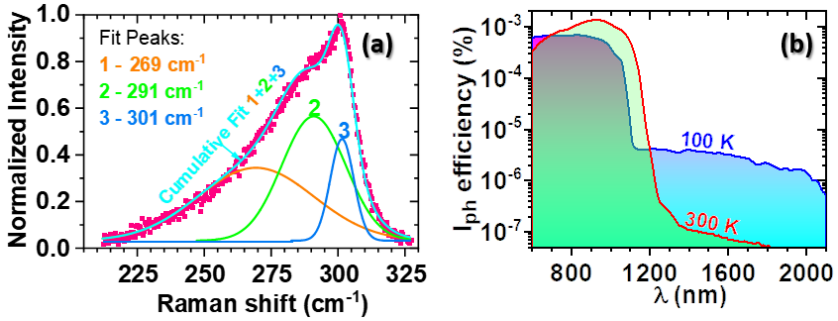


**Fig. 2 (a)** Normalized Raman spectrum with Gauss peaks deconvolution in 210–330 $cm^{-1}$ range corresponding to Ge-Ge vibrations in Ge-rich SiGe NCs (Peak 2) and in SiGe disordered component (Peak 1) and to 2TA mode of Si wafer (Peak 3). **(b)** Spectral photocurrent efficiency at 100 and 300 K (photovoltaic regime) [1].

Structures cooled at 100 K present high efficiency of photocurrent in broad 600–2000 nm spectral curves with remarkable SWIR-extended cut-off wavelength at 2 μm explained by the strain in Ge-rich SiGe NCs (reducing NC bandgap) and their high-quality interface with $HfO_2$ matrix (Fig. 2b). At 300 K, SWIR-extended sensitivity limit is still ensured even if photocurrent efficiency is lowered, and photocurrent intensity for $\lambda > 1.8$ μm is reduced below measurement setup sensitivity. SWIR photosensitivity is due to photocarrier generation in heterojunction of embedded Ge-rich SiGe NCs and Si substrate (separated by very thin buffer $HfO_2$ layer). Results can be exploited for monitoring slippery road conditions or biomedical sensing.

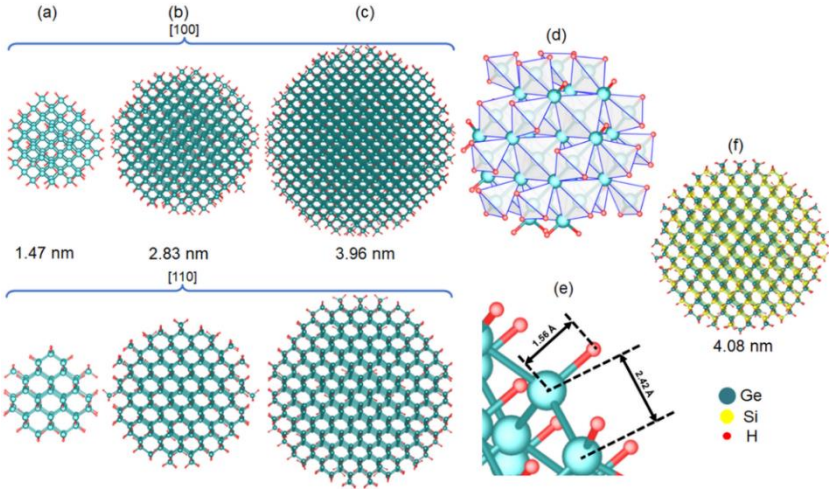


**Fig. 3 (a–e)** Relaxed Ge:H NCs: **a-** small (1.47 nm size), **b-** medium (2.83 nm), **c-** large NCs (3.96 nm) projected along [100] and [110] directions, **d-** atomic coordinates based on Ge tetrahedral symmetry, **e-** surface detail showing Ge–H bond length of 1.56 Å and Ge–Ge length of 2.42 Å. **(f)** Relaxed SiGe:H NC with 50:50 Si:Ge [2].

Other route for research is by theoretical studies to complement experimental results and achieve in-depth understanding of the relationship between structure, morphology, composition and optical, photoelectrical properties, and to serve to design and characterize Ge-rich SiGe NCs based optical sensors. So, for the first-time bandgap atomistic calculations in the frame of DFT-LDA (SIESTA) on spherical H-passivated Ge-rich $Si_{1-x}Ge_x$ NCs, with Ge atomic concentrations $x$ = 50%, 75%, 90% and 95% were conducted for 1–4 nm diameters [1]. Construction of SiGe NCs and Ge NCs (as reference) in the frame of an in-house developed code was made by considering tetrahedral symmetry (Fd-3m space group). NCs were built (VESTA models in Fig. 3) by filling the spheres with Ge and Si atoms in cubic coordination, then NCs surface was passivated with H atoms and finally lattice relaxation was performed. NC energy gaps were obtained by using computed DOS. Ge NCs energy gap dependence on diameter $E_g(d) = E_g^{bulk} + Ad^{-\alpha}$ with $A$ = 4.58 and $\alpha$ = 1.25 ($d$ > 2 nm) described

by a power law asymptotic to bulk Ge bandgap $E_g^{bulk}$ = 0.66 was evidenced. Our results fit well experimental literature data from various experiments (Fig. 4a). $E_g(d) = 0.66 + 4.58d^{-1.25}$ dependence overlaps with tight-binding TB results (Fig. 4b). Comparison with other DFT results is illustrated in Fig. 4c.

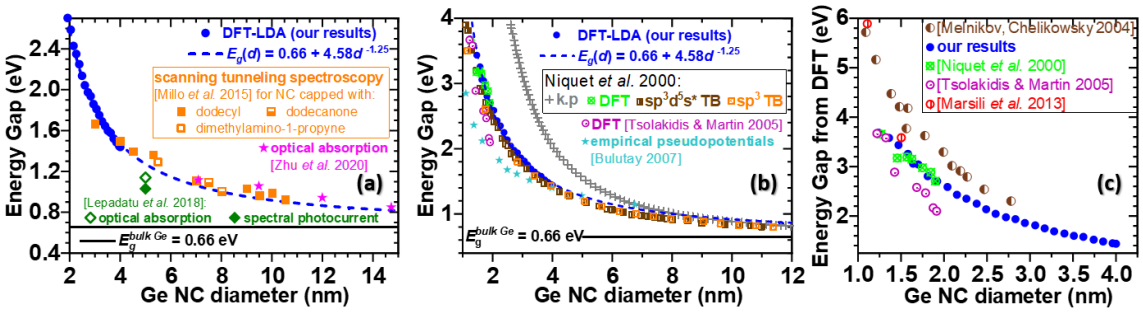


**Fig. 4** Ge NCs energy gap dependence on diameter: comparison of our results with literature data [2].

We have shown that NC bandgap energy of Ge-rich $Si_{1-x}Ge_x$ NCs strongly depends on diameter ($1/d^{1.25}$) and linearly on Ge concentration ($0.651(1–x)$) on whole investigated diameter-composition range (Fig. 5) by $E_g(d,x) = E_0^{NC} + 4.58/d^{1.25}$ with $E_0^{NC} = 0.66 + 0.651(1 - x)$ [2]. DFT results and extrapolation to bulk bandgap values of $E_g(d,x)$ fit curves are valuable for the development of optoelectronic devices based on SiGe NCs as optical sensors from VIS to SWIR also considering the lack of DFT simulation data in literature.

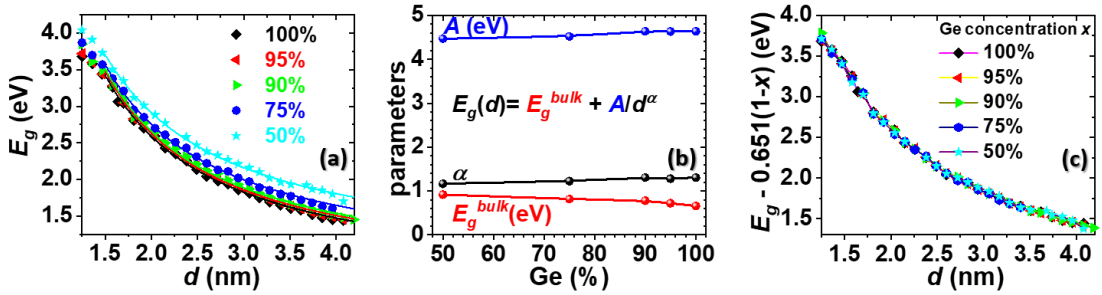


**Fig. 5** Ge-rich $Si_{1-x}Ge_x$ NCs: **(a,b)** energy gap dependence on diameter – power law with parameters $A$ and $\alpha$ and Ioffe $E_g^{bulk}$ in function of Ge content; **(c)** size dependences of computed $E_g(d)$ shifted on vertical by subtracting $0.651(1–x)$: $E_g(d,x) = E_0^{NC}(x) + A/d^{\alpha}$, $E_0^{NC} = 0.66 + 0.651(1 - x)$, $A$ = 4.58 eV, $\alpha$ = 1.25 [2].

*References*


1. C. Palade, A.M. Lepadatu, A. Slav, V.S. Teodorescu, T. Stoica, M.L. Ciurea, D. Ursutiu, C. Samoila, "Nanocrystallized Ge-rich SiGe-$HfO_2$ highly photosensitive in short-wave infrared", Materials 14(22), 7040 (2021).
2. O. Cojocaru, A.M. Lepadatu, G.A. Nemnes, T. Stoica, M.L. Ciurea, "Bandgap atomistic calculations on hydrogen-passivated GeSi nanocrystals", Sci. Rep. 11(1), 13582 (2021)

# Applications of MAX phases and MXenes as catalysts

**Iuliana M. Chirica[a,b], Anca G. Mirea[a], Stefan Neatu[a], Mihaela Florea*[a], Michel W. Barsoum*[c], Florentina Neatu*[a]**

[a]National Institute of Materials Physics, 405A Atomistilor Street, 077125 Magurele, Romania.
[b]University of Bucharest, Faculty of Physics, 405 Atomistilor Street, 077125 Magurele, Romania
[c]Department of Materials Science & Engineering, Drexel University, Philadelphia, PA19104, USA.

The MAX phases ($M_{n+1}AX_n$) and their derivatives, MXenes ($M_{n+1}X_nT_x$), (with n=1–4, M=early transition metal, A=A-group element, X=carbon or nitrogen and T=various surface terminations, such as –O, –OH and –F) are a relatively new class of materials that have been discovered in the last two decades.[1,2] These materials manage to bring together two completely different classes of materials (ceramics and metals) by combining important properties from both classes, such as high thermal and electrical conductivity, mechanical strength and low density. The unique properties of MAX phases arise from their lamellar structure, metallic/covalent bonds, and the relatively weak bonds between the M and A layers. In this review, we intend to present general aspects to be considered and to outline which are currently the most efficient catalytic systems based on these materials in: *(i)* catalytic processes centered on C–H and C–O activation, *(ii)* fine chemical reactions, *(iii)* catalytic degradation, and *(iv)* photocatalytic applications. An application road map is depicted in Scheme 1.


**Scheme 1**. Application road map of the MAX phases and their MXene derivatives.

The mind map (Scheme 2) summarizes the materials used in C–H and C–O bond activation and their corresponding catalytic reactions. Catalytic C–H activation includes the dehydrogenation reactions divided to direct dehydrogenation (DDH) and oxidative dehydrogenation (ODH) of hydrocarbons, which are important reactions in order to obtain alkene monomers, that are, in turn, key intermediates in the polymer industry.[3] The MAX phases and MXenes show activity and long-term stability in these types of reactions. MXenes can act as a catalytic support and the presence of noble metals as nanoparticles on a support such as these materials can favor the reduction of metal from MXenes and/or the removal of surface functional groups. Other theoretical studies have shown that supporting different noble metals on MXenes can facilitate the formation of single-atom catalysts (SACs) due to the fact that the defects from the supports' surface have been found to play a crucial role in stabilizing single atoms. It follows that MXenes, due to their 2D structure and defective surfaces, allow SAC formation and enhance the stability of SACs without affecting their activity or selectivity. Zhou et al.[4] carried out a theoretical study in which they studied CO oxidation on single Ti atoms anchored on $Ti_2CO_2$. The have used $Ti_2CO_2$ monolayers in order to prevent the formation of Ti clusters, and therefore to increase the intrinsic activity, efficiency and stability of the catalyst. Another theoretical study of CO oxidation was reported using MXene as a support for single Pd atoms anchored on $Mo_2CO_2$ monolayers.[5] The key point of this study was the comparison of pristine and defective $Mo_2CO_2$ monolayers with an oxygen vacancy (denoted as $O_V$–$Mo_2CO_2$). Considering the basis of first-principles calculations, different metals, such as Fe, Co, Ni, Cu, Zn, Ru, Rh, Ag, Ir, Pt, Au were decorated on defective $Mo_2CO_{2-\delta}$ monolayers and investigated as SAC candidates for a low-temperature CO oxidation reaction.[6] In order to design stable SACs, a systematic screening was performed using first principles calculations based on DFT.[7] This study concerns different metal atoms such as Sc, Ti, V, Cr, Mn, Fe, Co, Ni, Cu, Zn, that are deposited on different MXene surfaces with a $M_2C$ stoichiometry (Ti, V, Cr, Zr, Nb, Mo, Hf, Ta, W).[7]

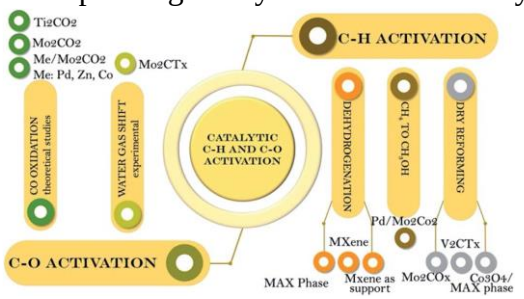


**Scheme 2**. Types of MAX phases and MXenes used in C–H and C–O activation.

Fine chemical reactions are an important class of chemical transformations, in which MXenes are starting to be explored as catalysts due to their interesting properties (Scheme 3). Zielinska et al.[8] tested $Ti_3C_2T_x$ as a catalyst for the α-pinene isomerization reaction to camphene, one of the most pervasive monoterpenes. The target point of this catalytic process is to produce camphene with high selectivity because it is of great importance in the perfumery industry, as an intermediate in organic synthesis. There are also studies[9] confirming its anticancer properties. The catalytic hydrogenation reactions are among the most important reactions concerning the industrial production of chemicals. Selective hydrogenation is difficult, particularly when it is possible to hydrogenate more than one functional group per molecule of reactant. Heterogeneous metal-based catalysts possess chameleonic properties and are good materials to be developed for selective catalytic hydrogenation toward desired reaction products.[10] In the case of nitroderivates, the selective reduction of the $–NO_2$ groups while preserving intact the other reducible groups is highly desirable, but not easy to obtain; the nitrostyrene molecule used as substrate, is considered to be the most demanding because the –C=C bond is quite sensitive and more susceptible to be reduced than $–NO_2$. Trandafir et al.[11] explored the use of MAX phases as supports for Pd nanoparticles (NPs), at remarkably low concentrations, for the chemoselective hydrogenation of a functionalized nitro-compounds. The high chemoselectivity of the Pd/MAX phase catalyst can be assigned to the synergetic effect between the Pd nanoparticle size and dispersion and also to the non-Ti containing that, preferentially activate the nitro group. Pt nanoparticles on $Ti_3C_2T_x$-based MXenes as efficient catalysts have also been investigated recently[12] for selective hydrogenation of p-chloronitrobenzene (p-CNB) to p-chloroaniline (p-CAN). It is remarkable that this catalyst can catalyse the complete conversion of p-CNB to p-CAN with 99.5% selectivity. One of the most promising molecular platforms derived from hemicelluloses is furfural, mainly considering the value added chemicals obtained by different catalytic reactions such as furfuryl alcohol. Naguib et al.[13] reported the catalytic activity of $Ti_3C_2T_x$ and $Ti_3CNT_x$ for the hydrogenation of furfural to furfuryl alcohol with the aim to understand the role of the presence of nitrogen in the support for carbonyl hydrogenation. Both catalysts had similar activities (36–42%) and selectivities (49–52%).

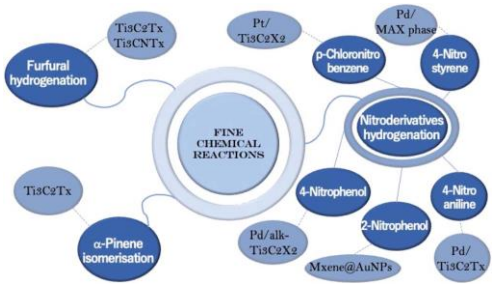


**Scheme 3**. MAX phases and MXenes used in fine chemical reactions.

Pharmaceuticals are used extensively for the treatment of humans and animal's diseases. Most of the drugs used end up in wastewater or groundwater, and their disposal or destruction becomes a very difficult task due to their low biodegradability or non-biodegradability.

Similarly, dyes pollute water systems and their disposal is a major concern. They are used in many industries, and the most commonly used are methylene blue, rhodamine B, methyl orange or congo red. Pesticides can also have a negative impact on humans and animals because of their toxicity. 2,4-dichlorophenoxyacetic acid has frequently been found in drinking water due to its high solubility and the development of methods to remove it from the environment is of great importance. It can also endanger aquatic life. MAX phases and MXene-based heterojunction materials have been shown to be effective catalysts in the degradation of organic compounds such as pharmaceuticals, dyes, pesticides and other compounds (Scheme 4). Photocatalysis can be described as the acceleration of a photoreaction in the presence of a catalyst, called a photocatalyst, which is often stable to photolytic conditions and achieves a large number of oxidative conversions per active situs without considerable degradation of its redox catalytic capacity.[14] The association of MXenes with various semiconducting photocatalysts has led to a considerable increase in photoactivity. Such phenomena are driven by the structural qualities of MXenes, including *(a)* the abundance of hydrophilic groups (-OH and -O) present on the outer surfaces that allow considerable interaction

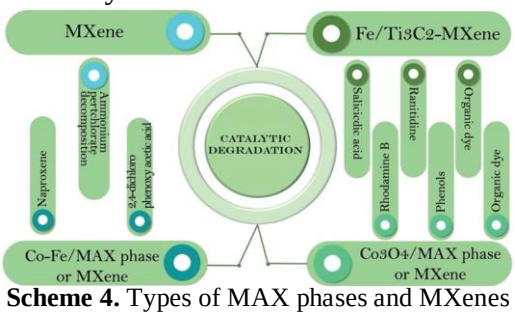


**Scheme 4.** Types of MAX phases and MXenes used in catalytic degradation reactions.

with various semiconductors to form compound heterostructured photocatalysts, *(b)* the high redox activities of surface metal sites (Ti, Nb or V) on MXene surfaces, which are higher than the redox reactivity of carbon materials[15] and *(c)* due to their metallic character, MXenes possess excellent electronic conductivity that guarantees efficient charge transport. As a representative example of MXenes, $Ti_3C_2T_x$ exhibits high electrical conductivity, surface hydrophilicity and adjustable electronic properties, making it a convenient co-catalyst in various photocatalytic uses. The application of $Ti_3C_2T_x$ in the field of photocatalysis is described in this review by the following four aspects: *(a)* the photocatalytic hydrogen evolution reaction by water splitting, *(b)* the photocatalytic carbon dioxide reduction reaction, *(c)* the photocatalytic degradation reactions of various pollutants, and *(d)* $N_2$ photofixation and other photocatalytic/photo-assisted processes (Scheme 5).[16] This study awards that MAX and MXene phases, with distinct chemical compositions, can be considered as potential catalysts as well as carriers, creating synergies with various active species. These materials show great promise in various catalytic applications; however, their surface chemistry and thermal stability are not fully understood. It has been showed that these materials are extremely resistant, or if deactivation has been observed, it has been reduced compared with standard catalysts. The deposition of different chemical species (oxides and transition metals) on MAX or MXenes can lead to new different compounds/structures that have never been reported as "classical support", leading us to believe that these materials are under-explored and represent a vast reservoir of both knowledge and potential applications.

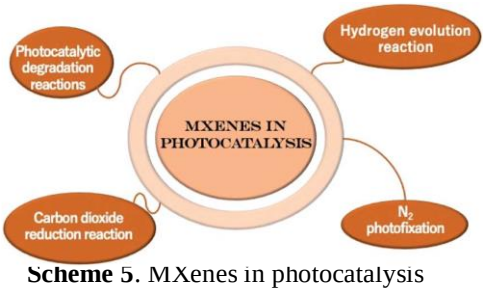


**Scheme 5**. MXenes in photocatalysis

*References*


1. Barsoum, M. W. The MN+1AXN phases: A new class of solids: Thermodynamically stable nanolaminates. Prog. Solid State Chem. 28, 201–281 (2000).
2. Naguib, M. et al. Two-dimensional nanocrystals produced by exfoliation of Ti 3AlC 2. Adv. Mater. 23, 4248–4253 (2011).
3. Gibson, M. A. & Hightower, J. W. Oxidative dehydrogenation of butenes over magnesium ferrite kinetic and mechanistic studies. J. Catal. 41, 420–430 (1976).
4. Zhang, X. et al. A Ti-anchored Ti2CO2 monolayer (MXene) as a single-atom catalyst for CO oxidation. J. Mater. Chem. A 4, 4871–4876 (2016).
5. Cheng, C. et al. Single Pd atomic catalyst on Mo2CO2 monolayer (MXene): unusual activity for CO oxidation by trimolecular Eley–Rideal mechanism. Phys. Chem. Chem. Phys. 20, 3504–3513 (2018).
6. Cheng, C., Zhang, X., Yang, Z. & Hermansson, K. Identification of High-Performance Single-Atom MXenes Catalysts for Low-Temperature CO Oxidation. Adv. Theory Simulations 2, 1900006 (2019).
7. Oschinski, H. et al. . Interaction of First Row Transition Metals with M2C (M = Ti, Zr, Hf, V, Nb, Ta, Cr, Mo, and W) MXenes: A Quest for Single-Atom Catalysts. J. Phys. Chem. C 125, 2477–2484 (2021).
8. Zielińska, B. et al. High catalytic performance of 2D Ti3C2Tx MXene in α-pinene isomerization to camphene. Appl. Catal. A Gen. 604, 117765 (2020).
9. Girola, N. et al. Camphene isolated from essential oil of Piper cernuum (Piperaceae) induces intrinsic apoptosis in melanoma cells and displays antitumor activity in vivo. Biochem. Biophys. Res. Commun. 467, 928–934 (2015).
10. Vile, G., et al. J. Advances in the Design of Nanostructured Catalysts for Selective Hydrogenation. ChemCatChem 8, 21–33 (2016).
11. Trandafir, M.-M. et al. Highly Efficient Ultra-low Loading Pd Supported on MAX Phases for Chemoselective Hydrogenation. ACS Catal. (2020) doi:10.1021/acscatal.0c00082.
12. Chen, Q., Jiang, W. & Fan, G. Pt nanoparticles on Ti3C2T: X-based MXenes as efficient catalysts for the selective hydrogenation of nitroaromatic compounds to amines. Dalt. Trans. 49, 14914–14920 (2020).
13. Naguib, M. et al. Catalytic Activity of Ti-based MXenes for the Hydrogenation of Furfural. ChemCatChem 12, 5733–5742 (2020).
14. Fox, M. A. & Dulay, M. T. Heterogeneous photocatalysis. Chem. Rev. 93, 341–357 (1993).
15. Ran, J. et al. Ti3C2 MXene co-catalyst on metal sulfide photo-absorbers for enhanced visible-light photocatalytic hydrogen production. Nat. Commun. 8, 13907 (2017).
16. Chirica, I. M. et al. Applications of MAX phases and MXenes as catalysts. J. Mater. Chem. A 9, 19589–19612 (2021).

# Development of electrocatalysts for energy production

**S. Neaţu,[a] F. Neaţu,[a] I.M. Chirica,[a] M.M. Trandafir,[a] I. Borbath,[b] E. Talas,[b] A. Tompos,[b] S. Somacescu,[c] P. Osiceanu,[c] M.A. Folgado,[d] A.M. Chaparro,[d] I. Ayyubov,[b] Z. Pászti,[b] Z. Sebestyén,[b] J. Mihály,[b] T. Szabó,[e] E. Illés,[f] A. Domján,[g] D. Radu,[a] A. Kuncser,[a] L. Navarrete,[h] J.M. Calderon-Moreno,[c] J.M. Serra,[h] M. Florea[a]**

[a]National Institute of Materials Physics, 405 A, Atomistilor Street, 077125, Bucharest, Romania

[b]Research Centre for Natural Sciences, Institute of Materials and Environmental Chemistry, Eötvös Loránd Research Network (ELKH), Magyar Tudósok körútja 2, Budapest 1117, Hungary

[c]"Ilie Murgulescu" Institute of Physical Chemistry, Romanian Academy, 060021, Bucharest, Romania

[d]Department of Energy, Centro de Investigaciones Energéticas, Medioambientales y Tecnológicas (CIEMAT), Avda. Complutense 40, 28040 Madrid, Spain

[f]Department of Physical Chemistry and Materials Science, University of Szeged, Rerrich Béla tér 1, Szeged 6720, Hungary, Department of Food Engineering, Faculty of Engineering, University of Szeged, Mars tér 7, Szeged 6724, Hungary

[g]Research Centre for Natural Sciences, Centre for Structural Science, Eötvös Loránd Research Network (ELKH), Magyar Tudósok Körútja 2, Budapest 1117, Hungary

[h]Instituto de Tecnología Química, (Universidad Politecnica de Valencia - Consejo Superior de Investigaciones Científicas),46022, Valencia, Spain

Today's energy and environmental problems require the development of new energy supply technologies using renewable energy sources. Fuel cells are a promising alternative for efficient energy generation technologies.[1] Fuel cells can be fueled either with hydrogen gas or different liquids such as alcohols or non-alcohols (formic acid, dimethyl ether, etc.), each with their own advantages and disadvantages.[2] These devices should meet the technical targets for portable power sources set by the US Department of Energy, such as; a specific power of 45-50 $W \cdot kg^{-1}$, a peak power density (PPD) of 55-70 $W \cdot L^{-1}$ and a cost of \$7-5 $W^{-1}$. These values are difficult to achieve for most direct alcohol fuel cells (DAFCs) but in terms of market implementation, direct methanol fuel cells (DMFCs) are the most developed.[3]

This paper provides a brief overview of the main advances in the field of portable PEMFCs and some details on potential electrocatalysts and their support. Regarding the current state of the art of electrocatalysts used in recent years in various fuel cells, the importance of the relationship between physicochemical properties and cell performance is decisive when designing new efficient electrocatalysts.

Among the main characteristics that electrocatalysts must fulfil in order to achieve reliable, high and constant performances are: (1) high porosity suitable for alcohol and oxygen transport, (2) sufficient electronic conductivity; (3) high chemical stability and tolerance to C and CO (ensured by well-defined chemical states that do not undergo major changes) in a reducing fuel atmosphere; (4) compatibility with other DAFC components; (5) ease of fabrication; (6) relatively low cost induced by the use of free metallic Pt or ultra-low amount of Pt.

As a novelty, in recent years various catalysts with excellent performance that exhibit unique structures and morphologies, such as nanowires, nanosheets and assembly structures have been synthesized. The portability of PEMFC and DAFC with hydrogen remains a burning issue that requires the electrode configuration to be adjusted to facilitate passive anode and cathode operation. These improvements also aim to reduce weight and volume in order to increase the energy generated by these systems. Among the fuel cell type devices, the most promising for portable applications are those operating at low temperatures fueled by hydrogen, methanol, ethanol or glycerol. The best power density (>1000 $mW \cdot cm^{-2}$) is generated by hydrogen fuel cells in conventional configuration, but is expected to decrease in real portable operation. The use of liquid fuels is also starting to show potential, developing power densities of over 200 $mW \cdot cm^{-2}$ for methanol and 100 $mW \cdot cm^{-2}$ for ethanol and glycerol. Optimisation of electrodes and fuel cell design to operate under portable energy conditions is needed for improved results.

An example of materials with special structures is NiO/Sr doped $Ce_{0.85}Pr_{0.10}Er_{0.05}O_{2-\delta}$.[4] This material shows efficient mesoarchitectures that have been successfully obtained and is cost-effective. This

material was evaluated in the $CH_4$ oxidation reaction and also electrochemically to determine its efficiency as an electrocatalyst for anodes fueled by $H_2$.

The synthesis of doped NiO/Sr involved a hydrothermal pathway process tempered by a non-ionic surfactant -Triton X100. The NiO deposition method was wet impregnation and the material was calcined in air at 900 °C to ensure a good interaction between Ni and the mesoporous matrix. The study involved the use of two concentrations of Sr (2.5 and 5 mol.% Sr), which resulted in two materials (CPS1 and CPS2, respectively). XRD and Raman spectroscopy revealed a mainly cubic fluorite phase with some traces of $Pr_2O_3$ and Sr wax (Fig. 1a). It was observed that the fluorite-type ceria-doped phase of CPS2 (the material with the higher Sr content) has a lower lattice parameter (5.394) than in CPS1 (lower Sr content) (5.404). This may be associated with a higher content of Pr actually incorporated into the Ce lattice.

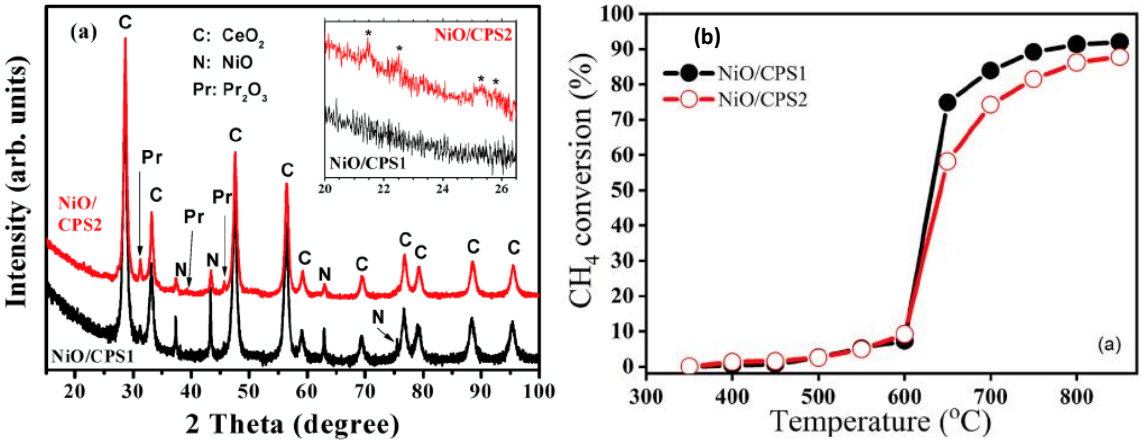


**Fig. 1 (a)** XRD patterns (for NiO/CPS1 and NiO/CPS2 and (b) Catalytic partial oxidation of methane at different temperature

Textural analysis revealed the formation of mesoporous structures at 900 °C with an average pore size in the range (20-30) nm. Oxygen vacancies were also evidenced and implied increased oxygen mobility by XPS investigation of the material surface, whereby the presence of $Er^{3+}$ and $Pr^{3+}$ in ceria containing only $Ce^{4+}$ ions was observed. It was also observed that $Ni^{2+}$ interacts strongly with the support, and SEM and TPR analyses confirmed that $Ni^{2+}$ is highly dispersed. The presence of $Sr^{2+}$ observed from XPS is responsible for the increased electronic conductivity of the material.

In the partial catalytic methane oxidation (CPOM) reaction, these materials proved to be good catalysts showing remarkable $CH_4$ conversion and CO selectivity (95%) at intermediate temperatures in the range 600-900 °C (Fig. 1b). These materials also show excellent stability in time.

To demonstrate the ability of these materials to function as electrocatalysts for fuel cells, an electrochemical cell with NiO/Sr doped $Ce_{0.85}Pr_{0.10}Er_{0.05}O_{2-\delta}$ on the anode side fed with wet $H_2$ (2.5% vol. $H_2O$) and yttrium stabilized zirconium (YSZ) as electrolyte and gadolinium-doped ceria (GDC) as buffer layer was build. The NiO/CPS1 anode showed an improvement in electrochemical properties. A lower resistance was observed with two perfectly distinct resistances at high (935 Hz) and medium (110 Hz) frequencies. This complex impedance behavior may be related to intrinsic electrocatalytic activity, a stronger activation by the desirable cations with lower valence states able to stabilize the cubic ceria.

Regarding the electrocatalyst supports, the use of hybrid materials like $TiO_2$-C (carbon) are promising. The presence of $TiO_2$ enhanced the stability of the support, while the use of new types of carbonaceous materials such as reduced graphene oxide instead of traditional active carbon provides certain benefits.[5] To explore and evaluate the particularities of such a hybrid system we compared $TiO_2$-C systems formulated with GO (TiGO) and Black Pearls (BP) carbon (TiBP). The preparation method used was solvothermal with some modifications in order to overcome some difficulties, like $TiO_2$ nuclei formation or GO delamination.

As observed from XPS and TEM, it can be concluded that, regardless of the carbon source, sintering of titania during high-temperature treatment of $TiO_2$-C composites leads to the formation of relatively large crystallites with incomplete coverage of the carbon backbone (Fig. 2).

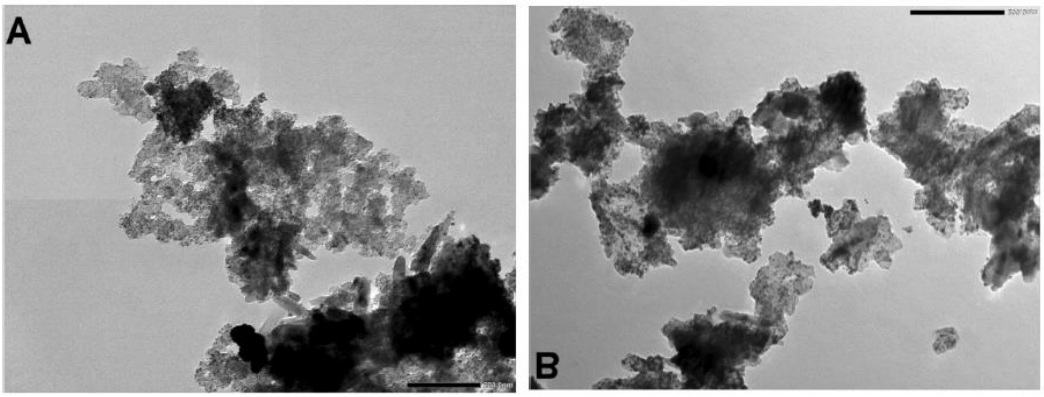


**Fig. 2** TEM images of selected composite supported catalysts. (a) TiBP and (b) TiGO.

Long-term stability tests carried out in the potential range 50 < E < 1000 mV showed that the effect of the composite support is limited in terms of catalyst stability and that this mainly depends on the properties of the active phase (e.g. Pt NPs). However, the Pt/TiGO-derived sample showed higher ORR activity than the Pt/TiBP-derived sample. Based on the decrease in electrochemical surface area, the order of stability was as follows: Pt/C< Pt/TiBP < Pt/TiGO.

*References*

1. Z. F. Pan, L. An, T. S. Zhao and Z. K. Tang, „Advances and challenges in alkaline anion exchange membrane fuel cells", Prog. Energy Combust. Sci., 66, 141–175 (2018)
2. U. B. Demirci, „Direct liquid-feed fuel cells: Thermodynamic and environmental concerns", J. Power Sources, 169, 239–246 (2007)
3. S. Neatu, F. Neatu, I.M. Chirica, I. Borbath, E. Talas, A. Tompos, S. Somacescu, P. Osiceanu, M.A. Folgado, A.M. Chaparro, M. Florea, „Recent progress in electrocatalysts and electrodes for portable fuel cells", J. Mater. Chem. A, 9, 17065–17128 (2021)
4. L. Navarrete, M. Florea, P. Osiceanu, J.M. Calderon-Moreno, M.M. Trandafir, S. Somacescu, J.M. Serra, "NiO/Sr doped Ce0.85Pr0.10Er0.05O2-δ mesoarchitectured: assessing as catalyst for partial oxidation of CH4 and IT-SOFC anode fueled by H2", Microporous and Mesoporous Materials, 323, 111171 (2021)
5. I. Ayyubov, I. Borbáth, Z. Pászti, Z. Sebestyén, J. Mihály, T. Szabó, E. Illés, A. Domján, M. Florea, D. Radu, A. Kuncser, A. Tompos, E. Tálas, "Synthesis and Characterization of Graphite Oxide Derived $TiO_2$-Carbon Composites as Potential Electrocatalyst Supports", Topics in Catalysis, (2021)

# Cation replacement in hybrid perovskite to enhance the stability of solar cells

**S. Derbali,[a,b] K. Nouneh,[b] L.N. Leonat,[a] V. Stancu,[a] A.G. Tomulescu,[a] A.C. Galca,[a] M. Secu,[a] L. Pintilie,[a] M. Ebn Touhami,[c] F. Neațu,[a] V. Toma,[a] S. Neațu,[a] A.M. Rostas,[a] C. Beșleagă,[a] R. Pătru,[a] I. Pintilie,[a] Mihaela Florea,[a]**

[a]National Institute of Materials Physics, Atomistilor 405 A Street, 077125 Magurele, Romania
[b]Laboratory of Materials Physics & Subatomics, Department of Physics, Ibn Tofail University, 14000 Kenitra, Morocco
[c]Laboratory of Materials and Environment Engineering: Modeling and Application, Department of Chemistry, Ibn Tofail University, 14000 Kenitra, Morocco

The finding that hybrid perovskites own exquisite semiconductor properties has opened up a new horizon in the field of thin-film solar cells: perovskite based solar cells (PSCs). Among the most important photo-physical properties that have attracted attention to the study of these materials we underline: the capability to collect photons from the visible solar spectrum as they possess an optimum direct band gap of ~1.5 eV,[1] they have a high absorption coefficient > $1.5 \times 10^4$ $cm^{-1}$,[2] which coupled with a small exciton binding energy allows an easy separation of charges at low temperatures (~50 meV),[3] and they show a high carrier mobility (12.5 $cm^2\ V^{-1}\ s^{-1}$ for electron and 7.5 $cm^2\ V^{-1}\ s^{-1}$ for holes)[4]. The general chemical formula of these perovskites follows a $ABX_3$ pattern, where A is a monovalent cation such as methylammonium ($MA^+$), formamidinium ($FA^+$), cesium ($Cs^+$), rubidium ($Rb^+$) or potassium ($K^+$); B is a divalent metal cation such as $Pb^{2+}$, $Sn^{2+}$ or $Sb^{2+}$ and X is an anion such as $Cl^-$, $Br^-$, or $I^-$.[5]

Although the power conversion efficiency (PCE) record of PSCs lately surpassed 24%,[6] considerable efforts are still needed to solve their stability issues and thus, many reports revealed that with a proper composition tuning, via substitution or by doping either the A-site, B-site or X-site ions, the stability and the device performances can be improved.[5] In this concern, herein two strategies for enhancement of the stability and photovoltaic performance of perovskite based solar cells were employed.

The first strategy implies the incorporation of $K^+$ into $K_xFA_{0.80-x}MA_{0.20}PbI_{2.8}Cl_{0.2}$ (x = 0 and 0.10) perovskite films fabricated by one-step spin coating method. The extend of the partial substitution of $FA^+$ with $K^+$ is expected to modulate the morphology, the optoelectronic properties, prevent the chemical decomposition of FA-MA film and also stabilize the α-phase of $FAPbI_3$.[7] Thus, within this study, some of the authors have checked the changes in the morphological, structural and optoelectronic properties of triple cations and mixed halide perovskite synthesized films. In this context, the experimental scanning electron microscopy analyses demonstrate that the films with potassium have uniform morphology and large grains. Following the synthetic route presented in ref. 7, different solar cells with n-i-p mesoporous structure of FTO/Compact-$TiO_2$/mesoporous-$TiO_2$/$K_xFA_{0.80-x}MA_{0.20}PbI_{2.8}Cl_{0.2}$/Spiro-OMeTAD/Au were fabricated (Fig. 1(a)). As illustrated in Fig. 1(b), the PCE values of the FAMA-K10% based devices exhibit a tighter distribution compared to pristine FAMA-based devices. Moreover, the stability of non-encapsulated PCSs with and without potassium was evaluated periodically by measuring the PCEs of these cells over 850 h shelf storage in a low-humidity environment without encapsulation. It was shown that, after 864 h, the PCE of the FAMA device reduces up to almost 71% of the starting value, while the PCE of the FAMA-K10% device retained 70% of the initial efficiency (data not shown here for brevity, but that can be accessed from ref. 7).

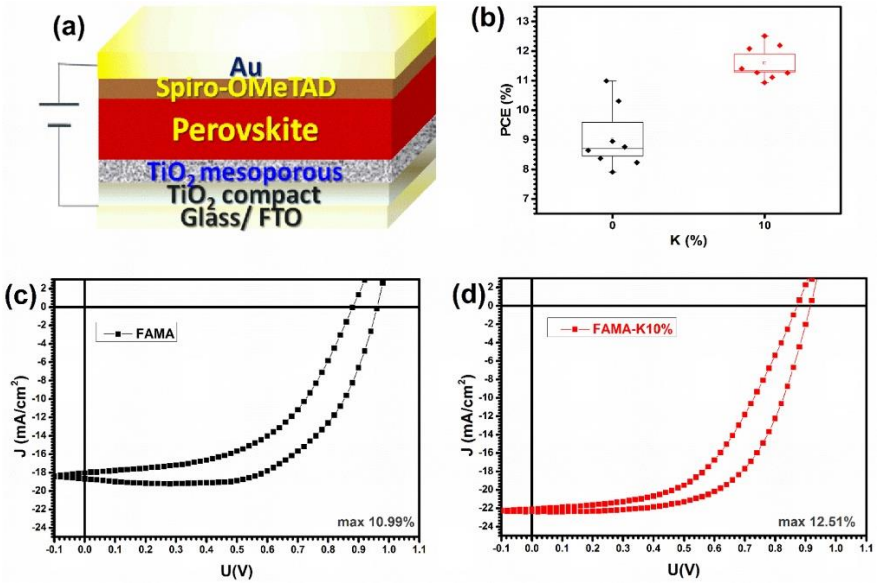


**Fig. 1** Schematic illustration of mesoscopic solar cells configuration (a), Power conversion efficiencies of solar cells with doped potassium and undoped perovskite films (b), Forward and reverse J–V curves of champion cells with FAMA (c) and FAMA-K10% (d) measured in ambient air without encapsulation under 1.5 G illumination.[7]

Such stability might be assigned to the intrinsic properties of the triple cation perovskite layer, i.e. fewer defects and high structural stability due to the incorporation of potassium. As shown, the incorporation of potassium inhibits the formation of the yellow non-perovskite δ-phase, which is inefficient in photovoltaic applications as it possesses very poor optoelectronic properties, and thus increasing the structural stability at room temperature of the photoactive α-phase. Moreover, the large grains that compose the FAMA-K10% perovskite film minimize permeability to oxygen and moisture through the grain joints, and thus, the overall stability of the solar cell is improved.

As a conclusion of the potassium corporation: the perovskite film quality is improved, while the overall stability and PCE values increase also (see Fig. 1(c) and (d)). Furthermore, the potassium doped devices exhibit reduced hysteresis and provide remarkable shelf stability by retaining more than 70% of the initial efficiency with low humidity over 850 h.

In an attempt to further improve the photovoltaic performances and stability of the hybrid perovskite solar cells, in a second strategy, some of the authors have doped the $CH_3NH_3PbI_{2.6}Cl_{0.4}$ mixed halide perovskite with imidazolium ($C_3N_2H_5^+$, denoted IM) on the "A site" position of a perovskite.[8] Thus, the effect of gradual replacement of $MA^+$ with $IM^+$ upon structural, optical and electronic properties of the perovskite films was investigated. Different compositions of organic-inorganic perovskites based on MA and IM solutions ($MA_xIM_{1-x}PbI_{2.6}Cl_{0.4}$, with x = 0 to 1) were synthesized and thoroughly characterized by using different characterization techniques, such as: X-ray diffraction, Atomic Force Microscopy, Scanning Electron Microscopy, UV–Vis, X-ray Photoelectron and Electron Paramagnetic Resonance spectroscopies, Impedance Spectroscopy and Incident Photon-to-Electron Conversion Efficiency. Based on the XRD data of such doped cells, the calculated new tolerance factors according to the "globularity factor" were experimentally proved and for doping concentrations greater than 20% the 3D structure is no longer obtained. Thus, following the doping process, an optimal IM incorporation percent was found to be 6%.

The monitoring of the stability of these solar cells was done by performing photovoltaic measurements on 10 cells (5 pristine and 5 with IM6 respectively), over 2000 h shelf storage in a low humidity environment (<10%) (see Fig. 2). As shown, the pristine devices degrade much faster than their IM6 doped counterparts. Thus, after 2000 h, the IM6 cells retain, on average, 70% of their original efficiency while the pristine cells preserve only 40% of their initial PCE or even become short-circuited, corresponding to a two-fold increase of the degradation speed.[8] This indicates that the perovskite with 6% IM is more stable compared with MAPI, the $MA_{0.94}IM_{0.06}PbI_{2.6}Cl_{0.4}$ structure being more resilient to degradation.

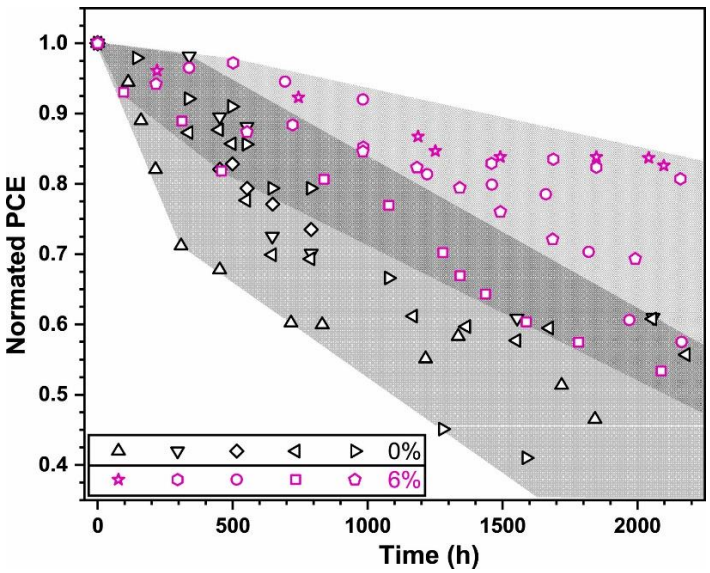


**Fig. 2** Solar cells efficiency over 2000 h shelf storage.[8]

As a conclusion of the second strategy, although the doping with IM did show a slightly lower efficiency than that of the pristine, this study proves that the stability for the IM containing solar cells devices increases over time. Thus, this study confirms once again that obtaining higher PCE value is not everything, especially if sacrificing a small percentage of efficiency improves the stability of perovskite film. Finally, we believe that following this design strategy, by introducing aromatic molecules like IM in the perovskite structure, might represent a new route to the obtaining of highly stable PSC devices.

*References*

1. S. De Wolf et al., "Organometallic Halide Perovskites: Sharp optical Absorption Edge and Its Relation to Photovoltaic Performance," J. Phys. Chem. Lett. 5(6), 1035-1039 (2014)
2. W. Ke et al., "Perovskite Solar Cell with an Efficient $TiO_2$ Compact Film," ACS Appl. Mater. Interfaces 6(18), 15959-15965 (2014)
3. L. J. Phillips et al., "Maximizing the optical performance of planar $CH_3NH_3PbI_3$ hybrid perovskite heterojunction stacks," Sol. Energy Mater. Sol. Cells 147, 327-333 (2016)
4. L. K. Ono et al., "Temperature-dependent hysteresis effects in perovskite-based solar cells," J. Mater. Chem. A 3, 9074-9080 (2015)
5. J. Albero, A. M. Asiri and H. Garcia, "Influence of the composition of hybrid perovskites on their performance in solar cells," J. Mater. Chem. A 4, 4353-4364 (2016)
6. M. A. Green et al., "Solar cell efficiency tables (Version 55)," Prog. Photovoltaics Res. Appl. 28(1), 3-15 (2020)
7. S. Derbali et al., "Potassium-containing triple-cation mixed-halide perovskite materials: Toward efficient and stable solar cells," J. Alloy. Compd. 858, 158335 (2021)
8. A. G. Tomulescu et al., "Enhancing stability of hybrid perovskite solar cells by imidazolium incorporation," Sol. Energy Mater. Sol. Cells. 227, 111096 (2021)

# Recent Progress in Phase Stability of Novel Nanocomposite Magnets

**Ovidiu Crisan,[a] Cristina Bartha,[a] Alina Daniela Crisan,[a] Aurel Leca,[a] Ioan Dan[b]**
[a]National Institute for Materials Physics, PO Box MG-7, 077125, Magurele, Romania
[b]R&D Consulting and Services S.R.L., 023761 Bucharest, Romania

Recent progress regarding phase stability in MnAl-based nanocomposite magnets has been achieved, in several studies involving complex structural dynamic, temperature-dependent characterization. It is known that not only the stoichiometry plays a role in forming the hard magnetic τ – MnAl phase but also microstructural arrangements of grains upon casting the alloy and the thermodynamic equilibrium. Two main pathways for obtaining τ - MnAl have been explored; a) ultra-rapid quench of equilibrium ε - phase successively followed by thermal treatment, b) slow cooling of the parent disordered ε - phase. In order to better understand the effects of carbon addition on the magnetic performances and especially on the signature of the ε – τ phase transformation as manifested in the temperature dependent magnetization measurements, we have synthesized two melt spun alloys having nominal composition $Mn_{52}Al_{46}C_2$ and respectively $Mn_{53}Al_{45}C_2$. Structural studies by means of X-ray diffraction have shown [46] that for the two ribbons in the as-cast state, the ε hexagonal phase predominates. This result confirms the hints we have got from the scanning electron microscopy images, i.e. that the two samples are mostly single phased. However, after the annealing at 700°C, the ε phase transforms into the tetragonal τ phase which becomes predominant.

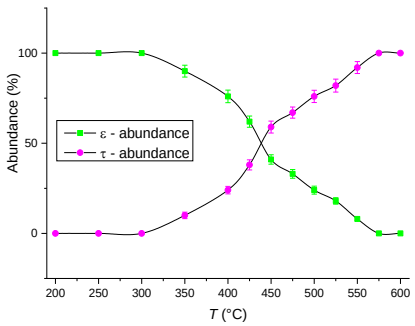


**Fig. 1** Relative abundance of ε and τ – MnAl, respectively, vs. temperature of the measurement.

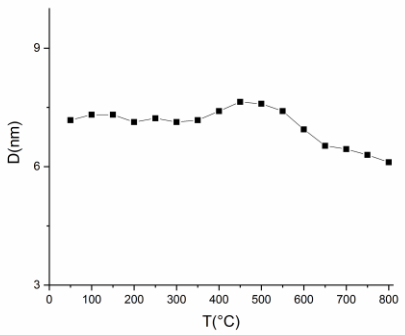


**Fig. 2** Average crystallite size of $Mn_{52}Al_{46}C_2$ sample vs. temperature of the measurement.

For a better estimation of the structural effects and of the parameters that govern the ε – τ structural phase transition, to determine the path to formation of the tetragonal phase as well as to estimate its stability with the temperature, a temperature-dependent structural study has been undertaken on the two samples. For this purpose, the samples were subjected to measurements using the synchrotron X-ray diffraction facility at the Paul Scherrer Institute, Villigen, Switzerland. This facility allows to obtain X-ray diffractograms at various temperatures, ranging from 50 to 800 °C. In our experimental protocol, the samples were measured at temperatures starting from 50 °C until 800°C, in steps of 50°C for each measurement. The resulting diffractograms have been analyzed using the full-profile, Rietveld-type MAUD software. This analysis allowed us to determine both the nature of the crystalline phases observed in the samples and the relative abundances of both ε and τ – MnAl phases, during the continuous ε – τ structural phase transition over the investigated temperature range. Figure 1 comparatively shows the relative abundances of the two phases, ε respectively τ – MnAl, as a function of temperature of measurement. It can be seen that below the ε - τ transition temperature, the abundance of the ε phase in $Mn_{52}Al_{46}C_2$ sample is 100%, as this phase is predominant in the as-cast state, until 300°C. Above this value, the τ – MnAl phase starts to be observed, in relatively low proportions (10 – 25%, until the measurement temperature of about 400°C). This indicates that the ε – τ structural phase transition is a gradual one, occurring over a large temperature range, at high heating rates, as the ones used during our synchrotron XRD measurement protocol. The abundance

of the τ – MnAl phase continues to grow, until it becomes equal to the one of the precursor ε phase, at about 450°C. Above this value, the abundance of the τ – MnAl grows further and becomes predominant, in such a way that by the end of the analyzed temperature range (700°C – 800°C) this phase reaches 100% abundance in both the analyzed samples. Through our experiment we have thus confirmed that the ε – τ phase transition occurs gradually. Figure 2 shows the temperature dependence of the average crystallite size of τ – MnAl nanograins, a size which was calculated from the full profile analysis of the synchrotron X-ray diffractograms, using the integral breadth method. It is interesting to notice that the average crystallite size for all the investigated temperatures oscillates slightly but is kept at low values, between 6 and 7.6 nm, The fact that the average crystallite size does not increase significantly with increasing the temperature, even at the highest investigated temperatures (700°C – 800°C) brings solid proof that the τ – MnAl has strong structural stability, an issue of high importance when it comes to contemplating potential applications of this material as magnets in extreme conditions of operation. The structural characterization of the as-cast and annealed alloys was done by X-ray diffraction at room temperature. XRD patterns have been recorded for both as-cast and annealed samples. Comparative XRD patterns are represented for $Mn_{53}Al_{45}C_2$ samples (Fig. 3).

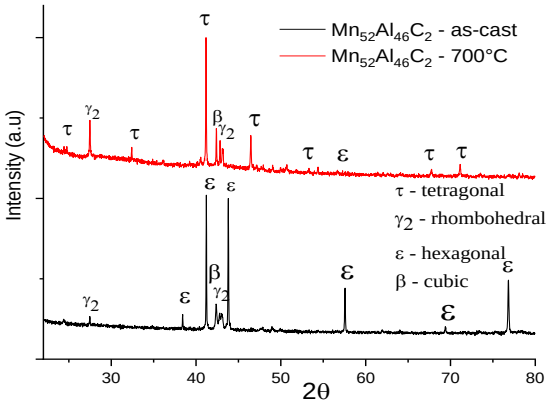


**Fig. 3**. X-ray diffractograms for samples $Mn_{53}Al_{45}C_2$ as-cast and annealed at 700 °C.

The $Mn_{53}Al_{45}C_2$ *as-cast* sample exhibits polycrystalline behavior, having well-formed, sharp Bragg peaks, mostly assigned to hcp ε-phase. The full-profile analysis provided the lattice parameters of the *hcp* crystal structure: a = 2.684 Å and c = 4.336 Å. Based on the fitting parameters resulted from MAUD, peak angular positions and shape, full-width-at-half-maximum (FWHM), we estimated the grain size, understood here as being the weighted volume, crystallographically-coherent, domain size. We have thus obtained a mean grain size of around 185 ± 12 nm for the hcp ε-phase. Besides the formation of the ε-phase, which is predominant in the as-cast samples, we detected also the presence of $\gamma_2$-rhombohedral and β cubic phases, in much smaller proportions. The $Mn_{53}Al_{45}C_2$ sample annealed at 700°C shows quite different features. The strong diminution, even disappearance of the Bragg peaks of ε-phase is observed, new diffraction lines of significant intensity appear, lines that are indexed as belonging to the τ-phase The relative proportion of the new τ-phase is very high, found to be around 88%. The remaining 12% abundance consists of rhombohedral $\gamma_2$ phase and primitive cubic β-phase. Correlating this value with the disappearance of the Bragg lines of the hcp ε-phase, we can conclude that indeed, after the 700 °C annealing, the $Mn_{53}Al_{45}C_2$ alloy undergo an almost full ε-τ structural phase transformation.

Using MAUD results of the full-profile analysis, it is possible to estimate the preferential orientation of crystals of the τ-phase by investigating the texture coefficient. This coefficient defines each corresponding Bragg reflection, their integral intensity as determined by numerical fitting of XRD pattern. In Table 1 we present the texture coefficient results for the samples annealed at 700 °C for the three most prominent *(hkl)* reflections of the tetragonal τ-phase: (110), (111), and (200). It can be seen that while the texture coefficient of the main (111) peak of the tetragonal phase is slightly below 1, the two superlattice peaks (110) and (200) show both a texture coefficient which is larger than 1.

This indicates a slight *in-plane* preferential orientation for the formation of the crystallites of the τ-phase.

**Table 1.** Texture coefficient results for the samples annealed at 700 °C.

| Sample | Texture Coefficient | | |
|---|---|---|---|
| | **(110)** | **(111)** | **(200)** |
| $Mn_{53}Al_{45}C_2$ | 1.04 | 0.83 | 1.08 |
| $Mn_{52}Al_{46}C_2$ | 1.11 | 0.79 | 1.03 |

We can conclude that in the case of ribbons in the as-cast state, the ε hexagonal phase predominates. Following the annealing at 700 °C, the ε phase has been almost completely transformed into the tetragonal τ phase which becomes predominant. The microstructure of the annealed samples is completed by rhombohedral $\gamma_2$ and cubic β phases that coexist (small abundance) with the predominant τ phase.

*References*


1. Alina Daniela Crisan, Aurel Leca, Ioan Dan and Ovidiu Crisan, "Thermal Stability, Blocking Regime and Superparamagnetic Behavior in Mn-Al-C Melt Spun Ribbons, Nanomaterials 2021, 11(11), 2898
2. Alina Daniela Crisan, Aurel Leca, Cristina Bartha, Ioan Dan and Ovidiu Crisan, "Magnetism and ε-τ Phase Transformation in MnAl-Based Nanocomposite Magnets, Nanomaterials 2021, 11(4), 896

# The functionalization of the carbon nanoparticles for multifunctional applications

**A.Udrescu,[a] M.Daescu,[a] M.Stroe,[a] M.Daescu,[a] S. Florica,[a] M.Chivu,[a] L. Stingescu,[a] E. Matei,[b] C. Negrila,[c] I. Mercioniu,[d] L.C. Cotet,[e] I. Anghel,[f] I.E. Sofran,[f] L. Baia,[e] S.N. Fejer,[g] M. Baibarac,[a,*]**

[a] National Institute of Materials Physics, Lab. Optical Processes in Nanostructure Materials, Atomistilor str. 405 A, Magurele, Romania, 77125

[b] National Institute of Materials Physics, Multifunctional Materials and Structures Laboratory, Atomistilor str. 405 A, Magurele, Romania, 77125

[c] National Institute of Materials Physics, Nanoscale Condensed Matter Laboratory, Atomistilor str. 405 A, Magurele, Romania, 77125

[d] National Institute of Materials Physics, Laboratory of Atomic Structures and Defects in Advanced Materials, Atomistilor str. 405 A, Magurele, Romania, 77125

[e] Babes-Bolyai" University, Faculty of Chemistry and Chemical Engineering, Department of Chemical Engineering, Arany Janos 11, , Cluj-Napoca, Romania, 400028

[f] "Alexandru Ioan Cuza" Police Academy, Fire Officers Faculty, Morarilor str.3, Bucharest, Romania, 022451

[g] Pro-Vitam Ltd., Muncitorilor street 16, Sfantu Gheorghe, Romania

In the last year, our effort was focused on three composite materials for applications in the field of: i) fire retardant agents [1], ii) electrochemical sensors for the detection of epidermal growth factor receptor (EGFR) [2] and iii) catalysts for the rhodamine B photodegradation [3]. In this context, poly(vinyl chloride) (PVC) spheres were prepared by the interaction of the PVC grains of Aldrich purity with hexyl ethyl cellulose and lauroyl peroxide, at 60 $^0$C. The PVC spheres coated with graphene oxide (GO) sheets were obtained by the adding of GO sheets in dimethylformamide to above reaction mixture [1]. According to the scanning electron microscopy studies a decrease in the size of the PVC spheres from 3.5 □m to 0.7 □m (Fig.1) was reported when the GO concentration in the PVC/GO composite mass increases from 0.5 to 5 wt.% [1]. As shown by Raman scattering and FTIR spectroscopy, this chemical method involves the emergence of new -COO- and C-OH bonds onto the GO sheets surface [1] The micro-scale combustion calorimetry (MCC) analysis have highlighted that the PVC/GO composites with a GO concentration of 5wt.% show the lower value of – the heat release capacity (HRC), the results highlight these composites, which allow us to conclude that these composites can be promising retardant flame agents [1].

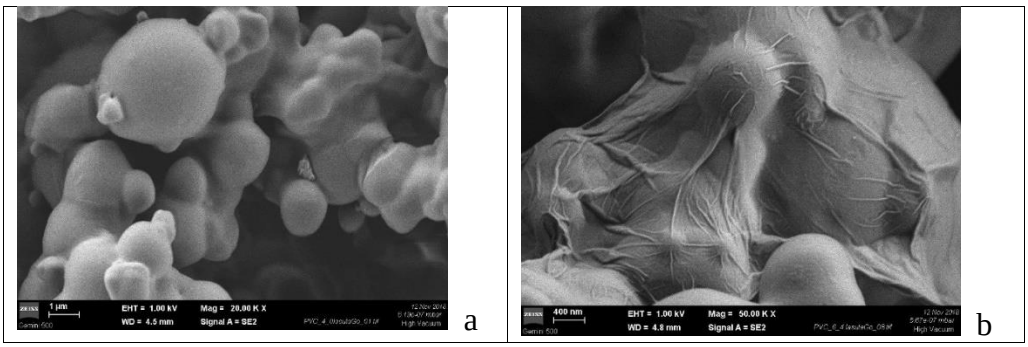


**Fig.1** SEM images of PVC and the PVC/GO composite with a GO concentration of 4wt.% [1]

In the electrochemical sensors field, a special attention has been given to the monitoring by Raman scattering and FTIR spectroscopy of the assembling of the sensors based on reduced graphene oxide (RGO) and polydiphenylamine (PDPA) for the EGFR. We have demonstrated that the assembling process of the RGO sheets electrofunctionalized with PDPA occurs in three stages, as follows: i) a chemical adsorption of 1,4-phenylene diisothiocyanate (PDITC) onto the RGO-PDPA sheets surfaces, ii) the incubation of the RGO-PDPA/PDITC sheets with protein G in phosphate buffer (PB) solution and iii) the interaction of RGO-PDPA/PDITC/protein G with EGFR antibodies solution, the final molecular structure being shown in Scheme 1[2]. The preliminary testing of the sensors based

on screen printed carbon electrodes modified with RGO sheets (SPCE-RGO) and SPCE-RGO/PDPA-PDITC-G-anti-EGFR/EGFR are shown in Fig.2 [2].

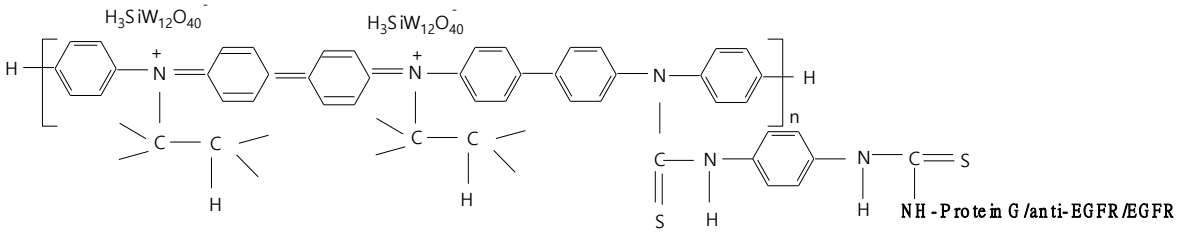


**Scheme 1**. Molecular structure of the sheets of RGO-PDPA/PDITC/protein G/anti-EGFT/EGFR

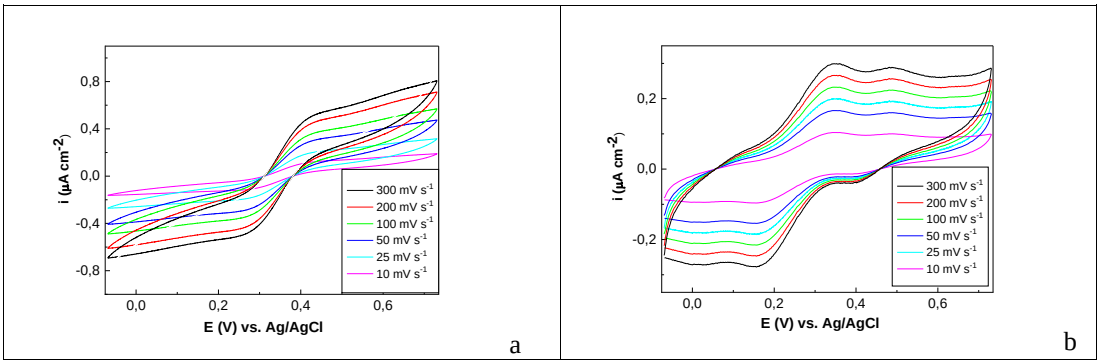


**Fig. 2** Cyclic voltammograms of the electrodes of SPCE-RGO (**a**) and SPCE-RGO/PDPA-PDITC-G-anti-EGFR/EGFR (**b**) in 5 mM $K_3[Fe(CN)_6]$/ $K_4[Fe(CN)_6]$ solution and 0.1 M PB with pH = 7.4. [2]

According to Fig. 2, the ratio between current densities of the anodic and cathodic peaks is equal approximately with 1 and the difference between the anodic and cathodic peaks potential is different of 56.5/n, where n corresponds to the number of electrons involved in the electrochemical process [2]. This fact indicates that an irreversible process occurs at the electrode/electrolyte interface [2]. This process was explained considering the electrostatic interaction between the positively charged amine entities of the SPCE-RGO/PDPA-PDITC-G-EGFR antibodies/EGFR platform and negative charges of $[Fe(CN)_6]^{3-/4-}$ [2].

Concerning the applications in the catalysts field, our attention has been given to the mixtures based on nitrogen doped titanium dioxide ($TiO_2$:N) and carbon nanotubes (CNTs) type of single -walled carbon nanotubes (SWNTs), double-wall carbon nanotubes (DWNTs), multi-wall carbon nano-tubes (MWNTs), and single-walled carbon nanotubes functionalized with carboxyl groups (SWNT-COOH) having various concentrations of CNTs [3]. The studies by UV-VIS spectroscopy have demonstrated that for the rhodamine B (RhB) photodegradation the best results were obtained for samples containing $TiO_2$:N and 2.5 wt.% SWNTs-COOH, when ~ 85% of dye removal during 300 min. of UV irradiation [3]. In the case of catalysts containing $TiO_2$:N and CNTs of the type of SWNTs, DWNTs, and MWNTs, ~ 70% of RhB removal was reported [3]. According to Fig. 3, the exposure to UV light up to 300 min of the RhB solutions in the presence of the $TiO_2$:N/CNT catalysts containg SWNTs, DWNTs, MWNTs and SWNT-COOH to induce a down-shift of the RhB absorption band from 554 nm to 524 nm, 533 nm, 518 nm and 551 nm, respectively [3], This result was interpreted as a proof of the adsorption of RhB onto the $TiO_2$:N particles surface [3].

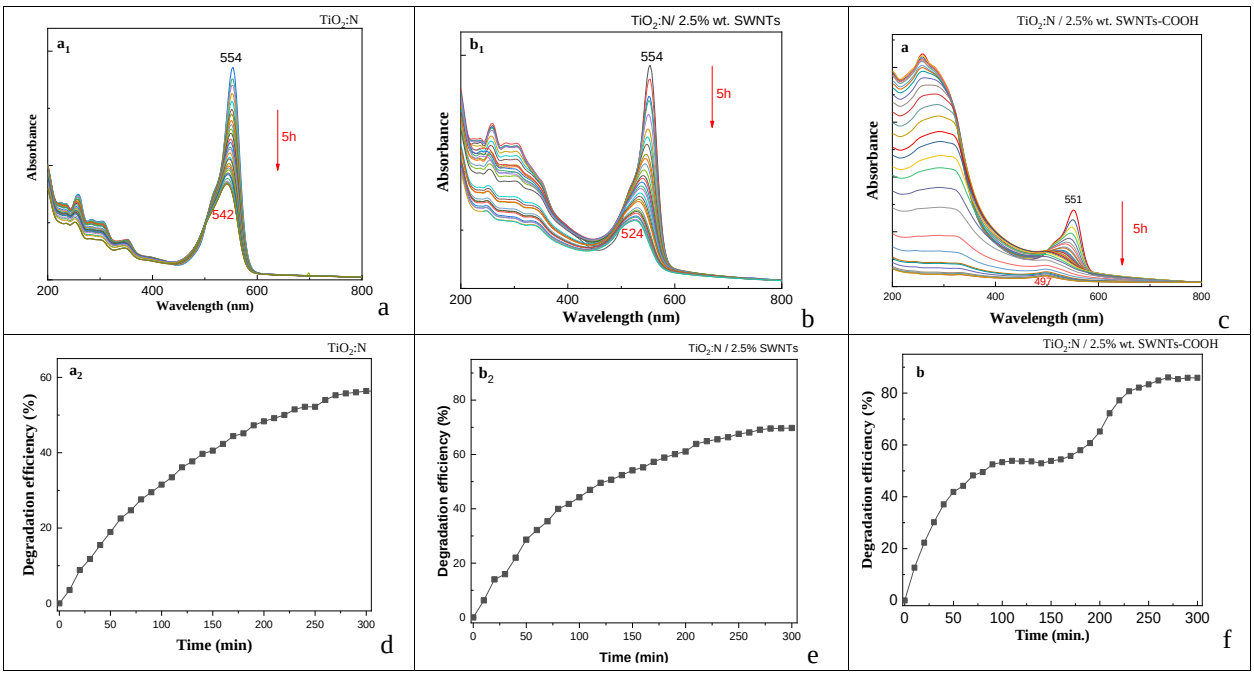


**Fig 3.** UV–VIS absorption spectra of the RhB aqueous solution containing as catalyst $TiO_2$:N (a), $TiO_2$:N/2.5 wt.% SWNTs (b) and $TiO_2$:N/2.5 wt.% SWNTs-COOH (c). Figs. d, e and f show the RhDdegradation efficiency as a function of the UV irradiation time in the case of catalysts $TiO_2$:N, $TiO_2$:N/2.5 wt.% SWNTs and $TiO_2$:N/2.5 wt.% SWNTs-COOH, respectively. [3]

The reaction kinetics of RhB aqueous solutions in the presence of $TiO_2$:N/CNT blends followed a first-order kinetic model, the higher photodegradation efficiency of RhB in the case of $TiO_2$:N/CNT blends than $TiO_2$:N being a consequence of the fact that CNTs act as adsorbent and dispersing agent and allow capture the photogenerated electrons of $TiO_2$:N hindering the electron–hole recombination. Summarizing these results, we can conclude that: i) the PVC/GO composite is a promising retardant flame agent; ii) the Raman scattering and FTIR spectroscopy are two valuable tools in monitoring the assembling of the sensorial platforms SPCE-RGO/PDPA-PDITC-G-EGFR antibodies/EGFR; and iii) the RhB photodegradation can be carried out using blends based on $TiO_2$:N and CNTs, a dye removal of ~ 85% being reported in the case of the $TiO_2$:N/ 2.5 wt.% SWNTs-COOH mixture after 300 min. of UV irradiation.

*References*


1. M. Baibarac, L. Stingescu, M. Stroe, C. Negrila, E. Matei, L.C. Cotet, L. Anghel, I.E. Sofran, L. Baia, "Poly(vinyl chloride) spheres coated with graphene oxide sheets: from synthesis to optical properties and their applications as flame-retardant agents", Polymers. 13, 565 (2021)
2. M. Baibarac, M. Daescu, S. Fejer, "Optical evidence for the assembly of sensors based on reduced graphene oxide and polydiphenylamine for the detection of epidermal growth factor receptor," Coatings. 11, 258 (2021)
3. A. Udresu, S. Florica, M. Chivu, I. Mercioniu, E. Matei, M. Baibarac, "Rhodamine B photodegradation in aqueous solutions containing nitrogen doped $TiO_2$ and carbon nanotubes composites," Molecules 126, 237 (2021)